COMPUTATIONAL INVESTIGATIONS ON THE STRUCTURE AND REACTIVITY OF NANOMATERIALS

By

NARESH KUMAR JENA

(CHEM01200604003)

BHABHA ATOMIC RESEARCH CENTRE, MUMBAI

A thesis submitted to the

Board of Studies in Chemical Sciences

In partial fulfillment of requirements
For the Degree of
DOCTOR OF PHILOSOPHY

of

HOMI BHABHA NATIONAL INSTITUTE

MARCH, 2012

Homi Bhabha National Institute

Recommendations of the Viva Voce Board

As members of the Viva Voce Board, we certify that we have read the dissertation prepared by **Naresh Kumar Jena** entitled "**Computational Investigations on the Structure and Reactivity of Nanomaterials**" and recommend that it may be accepted as fulfilling the dissertation requirement for the Degree of Doctor of Philosophy.

Tulsi Mukherjee **Date:** 31 - 08 - 2012
Chairman- Prof. Tulsi Mukherjee

Swapankumar Ghosh **Date:** 31-8-2012
Guide / Convener- Prof. Swapan K. Ghosh

Date: 31-8-2012
External Examiner- Prof. M. Durga Prasad

Tapan Kr Ghanty **Date:** 31-8-2012
Member 1- Dr. T. K. Ghanty

Date: 31-8-2012
Member 2- Dr. A. K. Samanta

Date: 31-8-2012
Member 3- Dr. K. R. S. Chandrakumar

Final approval and acceptance of this dissertation is contingent upon the candidate's submission of the final copies of the dissertation to HBNI.

I hereby certify that I have read this dissertation prepared under my direction and recommend that it may be accepted as fulfilling the dissertation requirement.

Date: 31-8-2012 **Guide:** Swapankumar Ghosh

Place: Mumbai

STATEMENT BY AUTHOR

This dissertation has been submitted in partial fulfillment of requirements for an advanced degree at Homi Bhabha National Institute (HBNI) and is deposited in the Library to be made available to borrowers under rules of the HBNI.

Brief quotations from this dissertation are allowable without special permission, provided that accurate acknowledgement of source is made. Requests for permission for extended quotation from or reproduction of this manuscript in whole or in part may be granted by the Competent Authority of HBNI when in his or her judgment the proposed use of the material is in the interests of scholarship. In all other instances, however, permission must be obtained from the author.

Naresh Kumar Jena

Naresh Kumar Jena

DECLARATION

I, hereby declare that the investigation presented in the thesis has been carried out by me. The work is original and has not been submitted earlier as a whole or in part for a degree / diploma at this or any other Institution / University.

Naresh Kumar Jena

Naresh Kumar Jena

DEDICATION

Darkness was so rampant,
Trading the Transcendental path,
Was not an easy task.
Riddled with obstacles,
And uncertainties that galore;
Inconceivable was,
The Source and Force.
With a sunken mind,
In a disparate path,
A feeling got stronger,
With each passing day;
“To keep walking restlessly,
And no getting away.”
The stones and pebbles,
That I started to stumble,
Made me endearing and humble.
Every passer-by I came across,
Illuminated me,
With their tiny spark.

I *dedicate* this,

To All of them…

“The stones and pebbles,
For defining Opportunity and Impediment,
The passer-by,
For Being Kind and Benevolent,
The Force
As the insatiable curiosity,
The Source,
As the,
All pervasive Almighty.”

Who have kept me afloat.

ACKNOWLEDGEMENTS

Foremostly, I would like to acknowledge and owe my deep sense of indebtedness to my supervisor, **Prof. Swapan K. Ghosh** for all the care, help, support, and other countless reasons which I cannot enumerate in its full verbosity. He has been my source of inspiration and role model and in my endeavor to follow his footprints, although I could not inherit his erudite, the trail of his nobleness and virtuosity that I carry forward is certainly a priceless treasure trove for the rest of my life. My acknowledgements deservedly find a name as **Dr. K. R. S. Chandrakumar,** for giving shape to my scientific intuition and research aptitude in the formative years of my career and being there as a friend, philosopher and guide all through. I would also like to acknowledge my other collaborators **Dr. Alok Samanta**, **Dr. Tusar Bandopadhayay**, **Manoj K. Tripathy**, **K. Srinivasu**, **Dr. Mahesh Sundararajan, Dr. Malaya K. Nayak** and **Dr. Y. Sajeev** for sharing their knowledge and experiences with me. I also thank all the members of Theoretical Chemistry Section for their unalloyed support. The list of my friends who have stood before me thick and thin can be very exhaustive, however, I would like to acknowledge some of them; **Siba**, **Deepak**, **Tapas**, **Rajubahi**, **Biswajit**, **Rajib**, **Lucky**, **Pradeep**, **Ganesh**, **Suranjan**, **Priyambada**, **Bani** and **Maneeshadidi** who have been phenomenal in their help and support.

I sincerely acknowledge the Department of Atomic Energy for providing the fellowship for my research. I would also like to acknowledge the financial support received from DST-JC Bose fellowship through Prof. Swapan K. Ghosh**.** The supercomputing facility of Bhabha Atomic Research Center is also gratefully acknowledged for providing the computational resources that underpin my research work.

Finally, I acknowledge my caring family and loving parents for my being and becoming.

……..Naresh

CONTENTS

SYNOPSIS

HOMI BHABHA NATIONAL INSTITUTE

Ph. D. PROGRAMME

1. **Name of the Student:** **Naresh Kumar Jena**
2. **Name of the Constituent Institution:** **Bhabha Atomic Research Centre**
3. **Enrolment No. :** **CHEM01200604003**
4. **Title of the Thesis:** **Computational Investigations on the Structure and Reactivity of Nanomaterials**
5. **Board of Studies:** **Chemical Sciences**

Synopsis

If we were to categorize the material world we live in and which encompasses us on the basis of length-scale of size and shape, we can safely put ourselves in the macroscopic or continuum domain. Beyond the comprehension of our senses, a top down approach will lead our way through the regimes of mesoscale, atomistic and finally to the level of quantum along the ladder of length-scale. The latter two regimes is the fertile playground of what the modern day nano-world means to us. Literally “nanometer” is defined by one billionth of a meter- a length scale where a few atoms or molecules assume their significance. The exploration of structure and reactivity and all other aspects related to the nanomaterials might have gathered momentum due to the intense research activity spanning over the last two decades. However, the knowledge of nanomaterials and their unique properties can date back to ancient times when these materials found applications in medicines, dyes, pigments, glasses etc. Mother Nature in its intelligent creations also employs nanomaterials in an efficient manner which cannot be matched even by our most scientifically and technologically proliferated endeavors. An apt example can be efficient functioning of Photosystems in plants which converts solar energy to chemical energy with efficiency and complexity.

The types of nanomaterials can be vast and vivid in their structure, electronic properties and reactivity. Investigation on the structure and reactivity of these nanomaterials is a challenging task as it requires advanced techniques and instrumentations. Last few years have witnessed an unprecedented advancement in instrumental techniques such as Transmission Electron Microscopy (TEM), Scanning Electron Microscopy (SEM), and Atomic Force Microscopy (AFM) etc. which gives us detailed information about the shape, size and morphology of nanomaterials. On a parallel track, advancement in the electronic structure calculation methods which strongly hinges on the tremendous advancement in the computational resources enables us to investigate the nitty-gritty of the electronic structure and properties of nanomaterials. Use of Density Functional Theory (DFT) based methods for few hundred atoms has been a common practice amongst the computational physicists/chemists.

The classification of nanomaterials on the basis of structure, function or reactivity can be a tantalizing task. Similarly any investigations which aim at probing the diversity and complexity of these nanomaterials either by employing experimental or theoretical methods can also be an intensive and rigorous exercise. Therefore, from the vast and expansive pool of nanomaterials, the present thesis pulls out some of the important nanomaterials which are at the center-stage of current research interests. Employing diverse computational methods, the thesis aims at providing some important insights into the electronic structure and reactivity of these nanomaterials. The thesis is organized in the form of 7 chapters.

Chapter 1

This introductory chapter deals with several general aspects of nanomaterials. It starts with a brief genesis of the nanomaterials, explaining how the properties of nanomaterials can be distinctly different from that of the bulk materials. When size approaches nanometer length, quantum-size effects start appearing. These effects cannot be predicted from the behavior of matter in bulk form. It also describes the challenges that can come in the way of detailed exploration of structure, property and reactivity of nanomaterials both by experimental and theoretical techniques. The importance of computational methods have been outlined which provides some of the most valuable information which experiments cannot provide. Brief introduction to the existing computational methods have been provided. Employing these computational methods, the scope of the thesis is to investigate some important nanomaterials namely (1) carbon nanotubes (CNT) (2) fullerenes (3) gold nanoclusters and (4) nanomaterials for energy applications. Importance of the aforementioned nanomaterials is briefly described with a clear objective of what the present investigations aim at exploring their electronic structure and reactivity.

Chapter 2

Chapter 2 deals with the electronic properties and reactivity of carbon nanotubes employing model systems. This chapter is divided into two parts. Part one describes the electronic properties of nanotubes in the light of model systems which are analogue of the single unit of nanotubes. Local nanoscale curvature is demonstrated to be a key parameter in describing the electronic properties like ionization potential, electron affinity, HOMO-LUMO gap and polarizability of the nanotubes. Moreover, it has also been shown that this local curvature plays a discerning role in the interaction of atomic species like hydrogen and aluminium with the nanotubes. We have proposed the generality of this concept of curvature to correlate with several properties as well as reactivity of the nanotubes.

Part two of this chapter deals with investigations on the electronic properties of water molecule under the confinement of CNT. It is well known that water present in the nanoscale confined medium like the hydrophobic interior of the CNT extols unique properties that depart largely from their behavior in the bulk form. In a manner analogous to the first part of this chapter, here also, we consider suitable model systems which structurally resemble single unit of the CNT, and demonstrate that two unique parameters, namely the local nanoscale curvature and the confinement length, are in general of paramount importance in governing the structural and electronic properties of water molecule present inside CNT. It has been shown that these two parameters also play a key role in governing the significant variations in the interaction energy, structural parameters, Mulliken charges and red and blue shift in the O-H vibrational frequencies of the encapsulated water molecule. More importantly, interplay between curvature and confinement in deciding the electronic property of water in the nanoscale confinement has also been emphasized.

Chapter 3

The scope of Chapter 3 encompasses the investigations on the structure and electronic properties and reactivity of C_{60} fullerene. This chapter is again subdivided into two parts. The first part deals with the structure and electronic properties of fullerene C_{60} and its N-atom doped counterpart called azafullerene ($C_{60-x}N_x$). The bucky-ball fullerene, an allotrope of carbon, since its serendipitous discovery from the mass-spectrometric studies of carbon vapors has resulted in the emergence of fascinatingly new domain of research activities. In recent past, a considerable amount of work has been done to understand the structural, electronic and optical properties of fullerenes[1]. One obvious strategy to modulate the electronic properties of C_{60} fullerene is doping. The cage structure of fullerene entails three types of doping namely- endohedral, exohedral and substitutional doping. Azafullerenes are of special importance as they exhibit variable electronic properties which enable them to be potential candidates for various device applications such as materials with tunable optical properties (TOPs)[2, 3] In this part of the chapter, we have computed several electronic properties, viz. atomization energy, ionization potential, electron affinity, vibrational frequencies, nuclear independent chemical shift (NICS) and polarizabilities of these fullerenes. We have considered several possible isomers for particular azafullerene and put forward some general criterion for the stability of these fullerenes.

In the second part of the chapter, we have considered the reactivity of C_{60} fullerene towards the uranyl ion (UO_2^{2+}). The binding and speciation of this cation is extremely important not only from the perspective of nuclear waste management but also from environmental issues. In our computational investigations, we have considered several binding modes of the bare uranyl cation with fullerene molecule. To realistically describe solvent effects on the binding energies, we have also considered explicit solvent molecules as well as continuum solvation model (COSMO) in our calculations. Apart from the binding of uranyl with bare fullerene, this part of the chapter also deals with interaction of uranyl with functionalized fullerene, particularly C_{60} functionalized with malonate groups. The importance of functionalization in improving the solubility of the fullerene as well as enhancing its binding affinity with uranyl ion has been put forward based on our results.

Chapter 4

This chapter starts with a systematic investigation on the electronic structure and properties of pristine gold nanoclusters Au_n as well as the corresponding alkali metal and hydrogen atom doped counterparts $Au_{n-1}X$, where n = 2-8 and X = Li, Na, and H. The dopant atoms are interesting from the perspective that they have similar outer electronic configuration in the form of a single valence electron like the gold atom. Electronic properties such as ionization potential, electron affinity, binding energy, HOMO-LUMO gap, and hardness parameters are found to exhibit a regular odd-even oscillatory pattern with variation of the cluster size. Our results reveal that the role of the hydrogen atom in modulating the structural and electronic properties of gold clusters is antagonistic to that of the alkali-metal atoms. The HOMO-LUMO gaps for the hydrogen-doped gold clusters are found to be much higher than the pristine and the alkali-metal-atom-doped gold clusters. In addition, we have also made an extensive study to investigate the important role of the impurity atoms, viz. hydrogen and alkali-metal atoms, on the adsorption of CO molecules by the doped gold clusters. An enhancement of the CO-adsorption energy has been observed for the gold clusters doped with a hydrogen atom rather than for the corresponding alkali-metal-doped ones and the enhancement is found to be more pronounced for the higher clusters in the series. It has been observed that there is as high as a 5-fold increase in the interaction energy of CO with Au_7H cluster as compared to its pristine counterpart Au_8. Contingent upon this observation, we have also considered adsorption of the former two gold clusters on top of the surface of carbon nanomaterials. We have considered three different substrate surfaces viz. planar, concave and convex which represent respectively the surfaces of graphene, outer surface of CNT and inner cavity of CNT. The adsorption of CO molecule on gold clusters adsorbed on these surfaces is also considered. We have demonstrated that the modulation of local electronic environment of gold cluster by H-atom doping largely governs the CO binding energy to these clusters. Its implications to nanocatalysis and sensory applications have been highlighted in this investigation. This chapter ends with a note on further exploring these interesting observations on reactivities of gold clusters towards their possible applications in nanocatalysis.

Chapter 5

Exploration of the catalytic properties of gold clusters is the central theme of this chapter. It has been shown that gold nanoclusters are efficient catalysts for CO oxidation reaction at low temperatures[4]. This reaction is important in connection with control of environmental pollution as CO constitutes a major part of the automobile emission. Oxidation of CO is also important for fuel cells where CO-poisoning limits the efficiency. In the beginning of this chapter, we have considered the effect of doping the gold cluster Au_8 with a single H-atom. It is observed that the otherwise closed shell neutral pristine gold cluster which is known to have weaker binding with O_2 molecule, exhibit remarkable enhancement in the molecular oxygen binding energy, on doping, i.e. for the doped cluster Au_7H. Accordingly, we have also demonstrated the activation of O_2 characterized by appreciable increment in the O-O bond length and concomitant red shift in vibrational frequency, on account of a single hydrogen atom doping. It has also been highlighted that H-doped gold cluster reduces the barrier height for environmentally important reaction of CO oxidation to CO_2 as compared to the pristine cluster. We have asserted that these observations may lead towards the design of cost-effective and efficient catalyst by doping gold clusters with a cheaper element like hydrogen. The origin of this catalytic enhancement is viewed from the perspective of charging effect of gold clusters in presence of H atom. From the Mulliken Charge analysis, we have found that H atom in gold clusters carries higher negative charge and it induces highly cationic gold centers on the adjacent sites which act as active sites. Following this analogy, in the latter part of this chapter, we have made a systematic investigation on the effect of impurities in the gold cluster on their catalytic performance. We have considered several impurity atoms of varying degree of electronegativities such as C, N, B, Li, Na, K, F etc. From our important observations we have concluded that the local electrostatic effects play a governing role for CO oxidation reaction on gold clusters.

Towards the end of this chapter, we have considered the complex of gold cluster (Au_3) with DNA-bases as a catalytic model for CO oxidation reaction. DNA is known to be a programmable assembler for bottom-up synthesis of nanomaterials and hence these kinds of complexes can serve the purpose of ideal nanomaterials with tuneable functionality and applications. We have demonstrated that oxidation of CO on DNA base-gold cluster complex is more facile (in terms of reduction of activation barrier) as compared to the pristine cluster and hence we propose that DNA-gold complexes can be an active model nanocatalyst.

Chapter 6

Some important nanomaterials which are relevant for renewable energy applications are the subject matter of this chapter. With burgeoning world population and declining fossil fuel reserves, a time has arrived to look for some alternative energy sources which are green, non-polluting as well as abundant. To this end, the emergence of hydrogen energy has been recognized world over. Two important aspects of utilizing hydrogen as an alternative energy sources are (1) generation of hydrogen either by photochemical or electrochemical splitting of water and (2) storage of hydrogen for mobile energy applications. Accordingly, this chapter is subdivided into two major parts. In the first part, we have discussed several nanomaterials for dissociation of water. Firstly, we have started with study of dissociation of water molecule on gold clusters. We have computed the barrier height for water splitting on gold cluster Au_8. It has been shown that for pristine cluster the barrier is as high as ~2.0 eV. As a step forward, we have also considered gold cluster Au_8 supported on a defective CNT which acts as a substrate for investigations of water splitting. At this point we have concluded that the effect of substrate manifests in terms of significant reduction of activation barrier of water dissociation, particularly CNT. We propose CNT-Au system as a possible nanostructure for water dissociation. We then moved to another system, namely Ti atom adsorbed on BN nanotube (BNT) as a possible candidate for water splitting. For this system, we have shown that the dissociation of a single water molecule proceeds with a lower activation barrier of ~0.2 eV. More interestingly, we have also demonstrated that subsequent dissociation of an additional water molecule leading to release of H_2 molecule becomes almost barrierless. We have thus proposed that Ti-decorated BNT can be one of the potential nanomaterial based catalysts for water dissociation.

In the second part of this chapter we have considered nanomaterials for storage of hydrogen. Herein, we have investigated hydrogen adsorption properties of silicon-lithium binary clusters. We have considered three different clusters viz. $Si_5Li_5^-$, Si_5Li_6 and $Si_5Li_7^+$. In all the minimum energy isomers of the three clusters considered, two of the lithium atoms are found to be situated in the axial positions and the remaining lithium atoms are in the equatorial position in the Si_5 plane. The lithium atoms which are in Si_5 plane are bonded to the Si-Si edge through a bridge bonding instead of a corner of the Si_5 ring. From the calculated atomic charges, it is found that there is charge transfer from lithium to silicon leaving a partial positive charge on the Li atoms and the axial lithium atoms are more charged as compared to the remaining lithium atoms. In the case of Si_5Li_6 and $Si_5Li_7^+$, the Li sites can trap a total of 14 and 17 H_2 molecules respectively, with each bridge bonded Li site adsorbing three H_2 molecules and each axial Li adsorbing one H_2 molecule which corresponds to a gravimetric density of 13.33 wt% and 15.25 wt% respectively.

Chapter 7

This is the concluding chapter of the thesis. This gives a brief outline about the possible future directions that can be charted out from the present investigations on various aspects of structure and reactivity of diverse nanomaterials that have been discussed in the present work.

References

(1) Dresselhaus, M. S.; Dresselhaus, G.; Eklund, P. C. *Science of fullerenes and carbon nanotubes*; Academic: NewYork, 1996.

(2) Xie, R.H.; Bryant, G.W.; Zhao, J.; Smith Jr., V.H.; Di Carlo, A.; Pecchia, A. *Phys. Rev. Lett.* **2003**, *90*, 206602 .

(3) Xie, R.H.; Bryant, G.W.; Sun, G.; Kar, T.; Chen, Z.; Smith Jr., V.H.; Araki, Y.; Tagmatarchis, N.; Shinohara, H.; Ito, O. *Phy Rev B*, **2004**, *69*, 201403(R).

(4) Haruta, M.; Kobayashi, T.; Sano, H.; Yamada, N. *Chem. Lett.* **1987**, *16*, 405.

LIST OF FIGURES

LIST OF TABLES

CHAPTER 1

Introduction

Chapter 1: Introduction

1.1: Nanomaterials: a Prelude

Since the dawn of human civilization, mankind's obstinate conviction to unravel the inner details of the material world that surrounds us epitomizes its triumphant spirit. Mankind's insatiable quest for knowledge and curiosity to see through and see par, is cardinal point to all the advancement in modern day science and technology. When science was at its infancy, the material world that encompasses us seemed uncanny yet triggering all our fascination to explore it in its fullest details. Limited by our senses and perceptions, the part of the world encountered by early thinkers was only confined to a domain of length scale and time scale that our ordinary sensory perceptions can feel. The ability to envision what happens to the material world at the reductionist level comprising of atoms, molecules etc. as well as the maximalist limits consisting of the astronomical objects, was a task beyond comprehension. The only reason was, we lacked well-equipped instruments. If we consider Rene Decartes's profound statement, "I think, therefore I am" as emblematic of western rationalism, the present avatar of science firmly based on rational thinking, careful observations, precise experiments, and logical interpretations can be considered to be expeditions of last few centuries. Thanks to the developments in the field of modern-day science and technology, which is an eventful journey of last one century having produced its glorious episodes in last few decades, we have moved from an era of perception to an era of reality.

In the early part of 20th century, British physicist Dirac famously said, the fundamental physical laws of nature are fully understood. His impression might have been in relation to the physical world that we encounter in our day to day life. To understand the laws of nature that govern at the level of atomic and molecular or cellular level on one extreme and the celestial objects on the other, still pose a challenge to our rational intelligence. There have been some attempts to formulate string theory that might be applicable for massive black-holes and condensed matter physics on the same bench. However, such attempts have met with only marginal success providing no solid ground for the so called "Theory of Everything".

If we were to categorize the material world we live in and which encompasses us on the basis of length-scale of size and shape, we can safely put ourselves in the macroscopic or continuum domain. Beyond the comprehension of our senses, a top down approach will lead our way through the regimes of mesoscale, atomistic and finally to the level of quantum across the ladder of length-scale. The latter two regimes are the fertile playgrounds of what the modern day nano-world means to us. Literally the word "nano" has been derived from Greek word "*nanos*" meaning dwarf. On a discerning note, "one nanometer" is nothing but a billionth of a meter- a length scale where a few atoms or molecules assume their significance. The exploration of structure and reactivity and all other aspects related to nanomaterials might have gathered momentum due to the intense research activity spanning over the last two decades. However, the knowledge of nanomaterials and their unique properties can date back to ancient times when these materials found applications in medicines, dyes, pigments, glasses etc. Mother Nature in her intelligent creations also employs nanomaterials in an efficient manner which cannot be matched even by our most scientifically and technologically proliferated endeavors. An apt example can be efficient functioning of photosystems in plants which converts solar energy to chemical energy with efficiency and complexity.

1.2: The Nanoworld in a Nutshell

In the beginning of the nineteenth century, John Dalton, an Englishman, to the utmost awe and skepticism of his fellow scientific community, asserted that materials are built of atoms and every atom of a given chemical element is identical. Furthermore, these interchangeable atoms combine and recombine to form the vast array of objects we come across in our everyday life. His profound insight came nearly two centuries before the individual atoms or at least the outer electronic configurations were mapped by an imaging device called STM (Scanning Tunneling Microscope). In the latter part of that century, the genius in the Czech Monk Gregor Mendel from his careful observations on the transmittance of some special kind of traits in the pea plants in his garden from parents to offspring generation laid the foundation stone of modern genetics. The nanometer-sized humble DNA that constitutes the gene had to wait nearly a century and half to mark its presence amongst the scientific community. The emergence of modern day Nanotechnology is believed to be inspired from a thought provoking lecture delivered by Richard Feynman to the American Physical Society in the year 1959. In his lecture, without making any obvious mention of the word nanoscience or nanotechnology, he envisioned manipulating matter at the level of atoms or molecules by putting forward his oft quoted lines "There is plenty of room at the bottom". However, many researchers owe the credit to Eric Drexler for laying the foundation stone of Nanotechnology as an ever exciting and independent area of research in his book "*Engines of Creation*". [1] If we were to provide a elaborative definition of Nanotechnology, the National Nanotechnology Initiative defines nanotechnology as "working at the atomic, molecular and supramolecular levels, in the length scale of approximately 1–100 nm range, in order to understand and create materials, devices and systems with fundamentally new properties and functions because of their small structure" (www.nano.gov).

1.3: A Brief Classification

It is often said that diversity is the law of nature. This diversity not only exists in the material world we come across in our day-to-day life but also it can exist in the Nanoworld. For the sake of completeness we can classify the Nanoworld into the following major categories.

- Fullerene
- Nanotubes
- Gas Phase Nanoclusters
- Self Assembled Monolayers
- Semiconductor Quantum Dots
- Nanoshells
- Monolayer-protected Metal Nanoparticles
- Core-Shell Nanoparticles

Although this classification gives an overview of several possible types of Nanomaterials, it is important to note that this list is not exhaustive. The development of Nanotechnology is a story of last two to three decades and the path of advancement in this field is being constantly enriched with many new discoveries day by day.

It is a tantalizing task to discuss, even briefly, the structure, function or reactivities of these Nanomaterials spanning over a large spectrum. The present thesis primarily focuses on several interesting aspects of the first three types of nanomaterials viz. Fullerene, Carbon Nanotube (CNT) and Nanoclusters. We will briefly mention some of the very basic general features of the above three types of Nanomaterials before going to discuss the objective of the present work.

1.3.1: Fullerenes

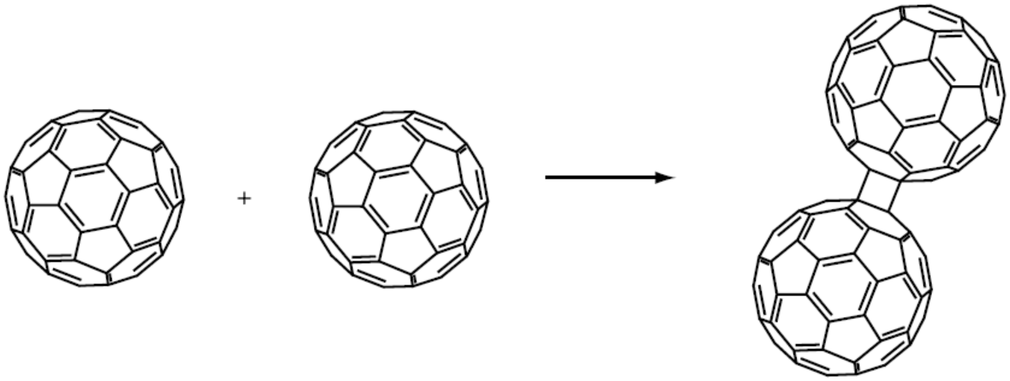

Figure 1.1: Geometry of Fullerene C_{60} and its dimer formed by [2 + 2] cycloaddition.

The discovery of fullerene[2] C_{60}, a hollow carbon cluster with highly symmetric I_h geometry (Figure 1.1), added a new dimension to the allotropic forms of carbon. The production[3] of fullerenes in bulk amount has fuelled active research in understating the physical and chemical properties of fullerenes. Although the fullerene family encompasses several other analogues starting from lower members like C_{20}, C_{32} to higher counterparts like C_{70}, C_{70}, C_{76}, C_{84} etc., the bucky-ball fullerene C_{60} is the most widely explored member. Some of the very unique features of fullerene C_{60} such as (1) abundant production in carbon soot by arc discharge of graphite, (2) highly symmetric icosahedron I_h structure with all the sixty carbon atoms being chemically equivalent, (3) less expensive (4) relatively inert under mild conditions and (5) negligible toxicity, make it an attractive molecule for physicists and chemists. Interestingly, C_{60} fullerene has a closed shell electronic structure where 60 p electrons are filled in 30 bonding molecular orbitals.[4] The completely filled highest occupied molecular orbital (HOMO) is fivefold degenerate (h_u) and the corresponding lowest unoccupied molecular orbital (LUMO) is highly delocalized with threefold degeneracy. The HOMO-LUMO gap ranges between 1.5-2.0 eV. The threefold-degeneracy, along with the low-energy possession of the LUMO, makes C_{60} a fairly good electron acceptor with the ability of reversibly gaining up to six electrons upon reduction. [5,6] On the other hand, the oxidation of C_{60} fullerene is difficult and only first three reversible oxidation states have been observed. [7] This unique electronic structure of C_{60} fullerene forms the basis for extensive studies on its electronic, optical, magnetic, semiconducting and superconducting properties.[8-13]

The fullerene chemistry is more diversified by virtue of the functionalization. The chemical reactivity of fullerenes resemble that of strained electron deficient polyalkenes, as a consequence of which it favorably reacts with nucleophiles. The chemistry of fullerenes is primarily governed by cycloaddition reactions. The preferred position for the cycloaddition reaction is junction of two hexagons ([6, 6] ring junctions) where the electron density is more as compared to [6, 5] ring junctions. Wide range of cycloaddition reactions viz. cyclopropanation, Diels–Alder ([2 + 2] and [3 + 2] have been employed to explore the diverse chemistry of functionalized fullerenes.[14] The primary advantage of functionalization of fullerene is due to the enhancement of solubility of fullerenes. The diverse physical and chemical properties of added functional groups open up new avenues for designing materials with broad range of applications.

1.3.2: Nanotubes

If we consider fullerene as the 0D form of carbon nanostructure, carbon nanotube (CNT) can be considered its 1D counterpart. CNTs were discovered as a byproduct of fullerene synthesis in the year 1991.[15] This novel crystalline form of carbon in the form a hollow carbon filament resembles a nano-tube like structure. Last three decades have witnessed a plethora of literature reports on this wonder material which has captivated physicists, chemists, material scientists as well as biologists for the promise it holds based on the diversity of its structure and applications. The unique properties of carbon nanotubes are due to their distinctive structure, which is composed of C-C bonds more closely related to those in graphite than to those in diamond. That is, while diamond has a coordination number of four with sp^3 hybridization, graphite involves three-coordinated carbons, in which three electrons are in sp^2 hybridization and one is delocalized. Fullerenes and nanotubes also have carbon bonds with sp^2 hybridization as graphite, but unlike the graphite structure, which is made up of a flat planar honeycomb, the structures of fullerenes and nanotubes involve a high degree of curvature. A flat graphene sheet is idealized as a single layer of carbon atoms packed in a hexagonal honeycomb structure and is typically used to describe the structure of sp^2 carbon materials such as graphite and nanotubes. Structurally, single-walled carbon nanotube (SWCNT) can be visualized as a rolled up sheet of graphene can be uniquely characterized in terms of a chiral vector (n, m) perpendicular to its axis which is in turn defined by two base vectors a_1 and a_2. The magnitude of this chiral vector, $C_h = n\ a_1 + m\ a_2$ is circumference of the nanotube. Based on the indices (n, m), there can be three different types of nanotubes namely, armchair, zig-zag, and chiral which are shown in Figure 1.2. The $n = m$ tubes are of the armchair structure, whereas the $n = 0$ or $m = 0$ tubes are of the zigzag structure, otherwise the structure is chiral. Apart from SWCNT, there can also be multi-walled carbon nanotube (MWCNT) which consists of several concentric SWCNTs with varying diameter. Although nanotubes of carbon are exhaustively explored in the literature, there are also reports of other nanotubes viz. BN, BCN, SiC, metal dichalcogenides etc.

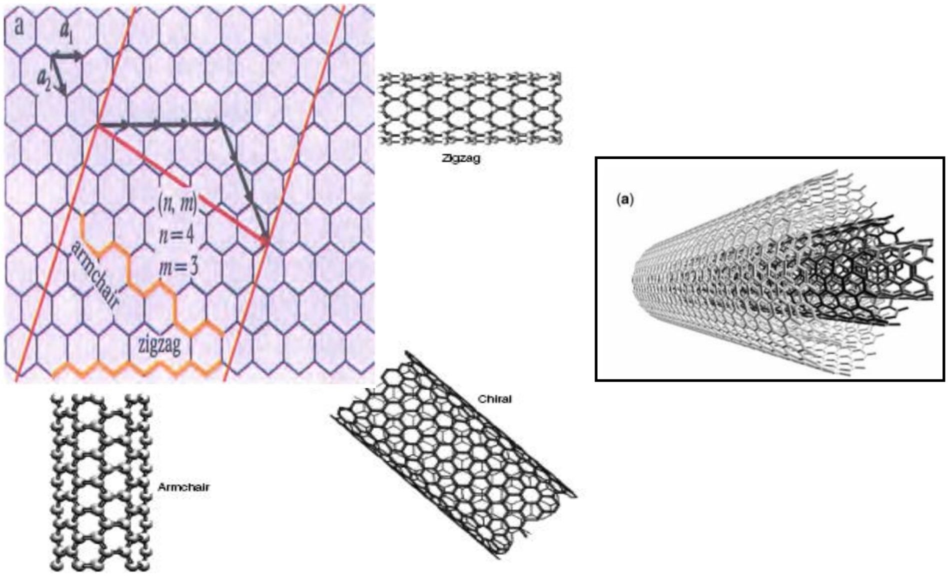

Figure 1.2: Construction of the SWCNT from a graphene sheet (inset: MWCNT).

The fascination of the researchers for carbon nanotubes hinges strongly on the unique structural, electronic, thermal, optical and mechanical properties. Electronically, the extended π electrons present in the CNT like the planar graphene makes them important candidates for opto-electronic applications. The indices (*n*, *m*) can give us clues about the nature of the CNT. If *n*=*m* or *n*-*m* is a multiple of 3, then the nanotube is metallic, otherwise it is semiconducting. One of the most admirable properties of CNTs are their extremely high mechanical strength which is based on the intrinsic strength of sp^2 C-C bond. Theoretically CNTs can be stronger and stiffer than any known substance. The measured or predicted value of Young's Modulus is ~1000 Gpa by several groups. [16,17] The wide range of application of nanotubes has also opened up new dimensions for their commercial uses, a brief description of which is presented in Figure 1.3.

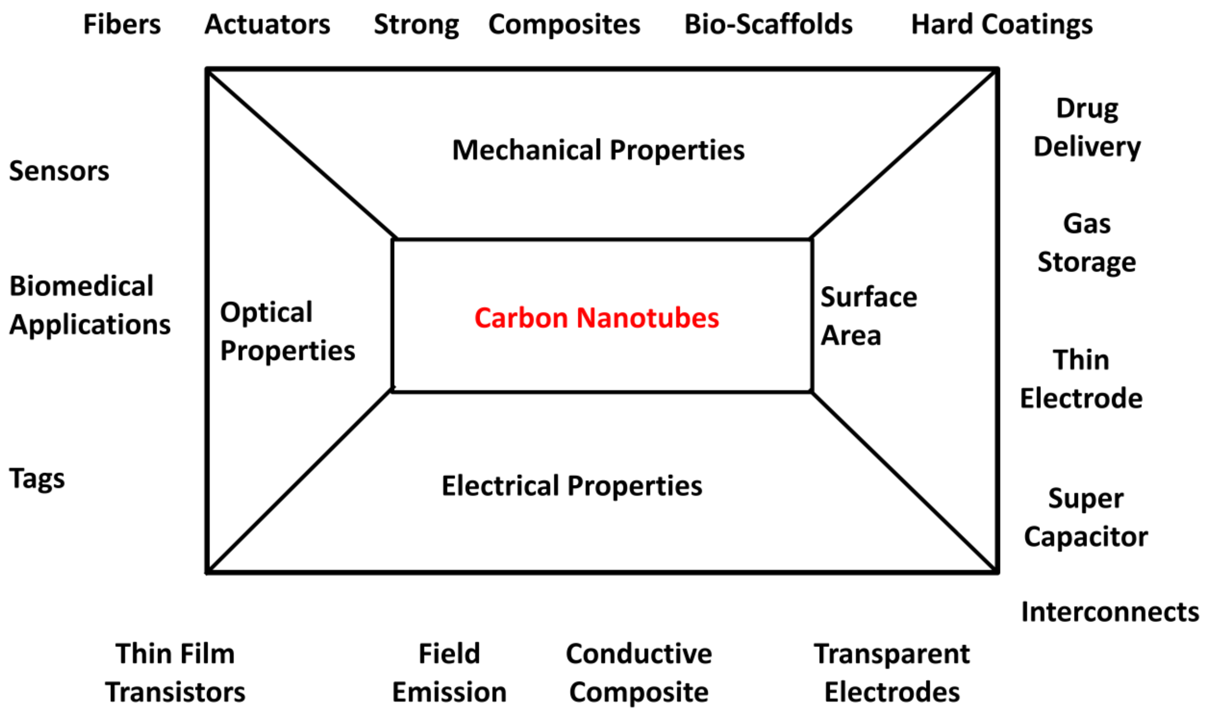

Figure 1.3: Properties and possible applications of carbon nanotubes.

1.3.3: Gas Phase Clusters

With the reduction of material size, interesting variations in the material properties start appearing. In past few decades, understanding the physical or chemical properties of matter with change in size, shape or dimensionality has grabbed the attentions of the researchers. For matter with diameter 10-100 nm, usually called nanoparticles consisting of several 100 atoms, the material property is often scalable with particle size. However, for material dimensions ranging between 1-10 nm (usually called clusters consisting of usually 1 to 100 atoms), the material property can be very much dependent on the size of the clusters and this constitute the non-scalable size range. As an illustration, the vertical detachment energies (VDE) of anionic Au_N^- clusters with the variation of the cluster size is presented in Figure 1.4. [18]

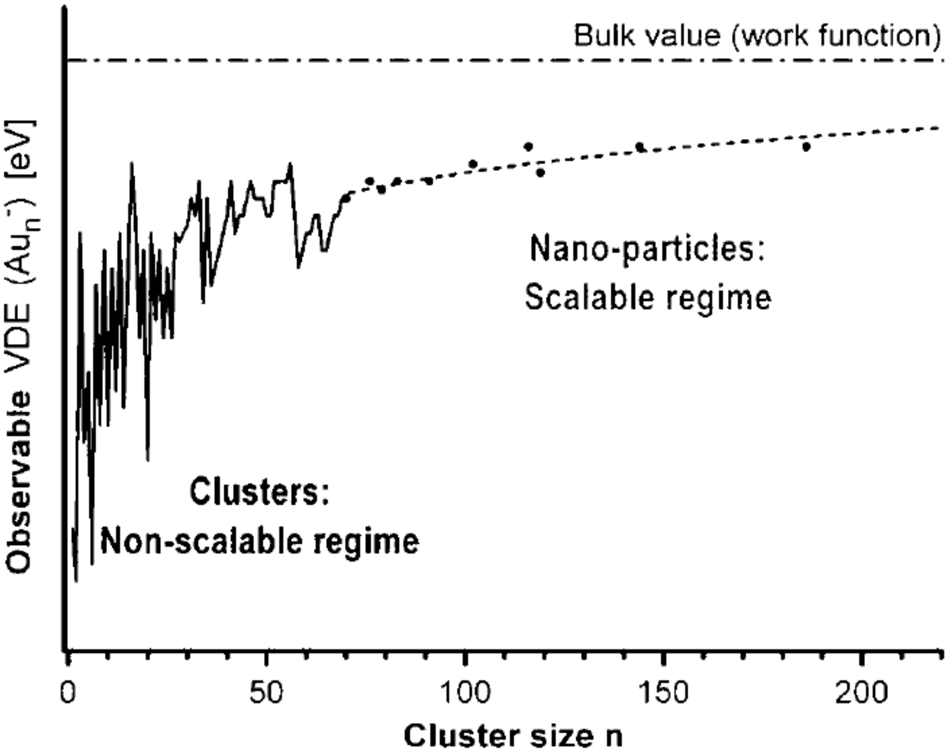

Figure 1.4: Physical property of nanoclusters as a function of size. Here the observable is VDE of anionic Au_N^- clusters.

In the scalable size range, the physical properties of nanoparticles as a function of size scale with that of the bulk value. This particular regime can be useful for nanotechnology applications as by changing the dimension of the particles its intrinsic properties can be altered. In the non-scalable size range, on the other hand, slight variation in the size leads to significant effect on the properties as we can clearly see from the variation of VDE (Figure 1.4) for anionic gold clusters comprising of 30 or fewer atoms. In this region, the properties of matter are predominantly controlled by quantum size effects and are not predictable from the information of its bulk counterparts.

Starting in the 1980s, the study of size-dependent properties of Na clusters in the non-scalable size range by the group of Schumacher [19,20] and subsequently by the group of Knight [21,22] have led the foundations of the study of size-dependent properties of clusters. From the observations of discontinuities in the mass spectra and ionization potential at magic number clusters (n= 2, 8, 20 etc.), they have demonstrated the importance of electronic shell structure in deciding the reactivity of small alkali metal clusters. In recent years, understanding the structure and electronic properties of gas phase clusters and exploring their possible applications have advanced tremendously.

With the advent of intense cluster sources [23], the chemical reactions of gas phase clusters have recently become an active field of research. Isolated mass-selected metal clusters are extremely important model systems to understand the chemical reactions, and catalysis in particular, as they act as catalytically active particles. In the above mentioned non-scalable size range, model catalysts of metal clusters supported on oxides have offered much insightful information related to catalysis and a host of important factors namely size, shape, charge state, nature of substrate etc. have been found to govern the processes. Although, the gas-phase cluster studies might not account for the precise mechanisms in the applied catalysis, these studies conducted under well controlled conditions can provide some of the atomistic details of the elementary steps of the catalytic reactions and also the important influencing factors. Complemented by *ab initio* computational investigations, gas-phase studies of cluster can provide details of the mechanisms, energetics and kinetics of catalytic reactions. Based on this knowledge, the performance of several potentially important catalysts can be screened as well as many unexplored catalysts can also be standardized.

A very recent and emerging example of importance of the size effect of matter on their properties is the catalytic activity of highly dispersed supported gold nanoparticles and clusters. Nano-meter sized gold supported on oxides has been shown to act as active catalysts for the oxidation of CO even at low temperatures, where the performance of other catalysts systems are marginal. [24-29] This observation is counterintuitive considering the fact that bulk gold is noble and thus inert whereas nano-scale gold exhibits pronounced catalytic activity. Following these reports, a burgeoning field research has stemmed up pertaining to reactivity of small gold clusters and their applications in catalysis.

1.4: Tools of the Trade

The phenomenal development of Nanotechnology primarily rests on the development of instrumentation, particularly, microscopy in recent years. Two types of electron microscopy, scanning electron microscopy (SEM) and transmission electron microscopy (TEM), utilize electron beam rather than light to achieve angstrom level resolution of matter. TEM can be visualized as a process in which a beam passes through the sample and the image is projected on screen. On the other hand, SEM technique is equivalent to a shinning a flashlight on the matter and getting the information about the topography. Although, the later technique have the resolution limitations on the nanometer length scale, it is sometimes more informative as it provides topographical information. In addition to electron microscopy techniques, developments in scanning probe microscopies have also allowed visualization and even manipulation of matter at a new level. This class of microscopies acquires data by using a physical probe to scan the surface. Generally, the probe is moved mechanically across the surface providing line by line data of the probe location and the interaction with the surface. The two most common types of scanning probe microscopy are atomic force microscopy (AFM) and scanning tunneling microscopy (STM). The schematic depiction of the above mentioned techniques are presented in Figure 1.5.

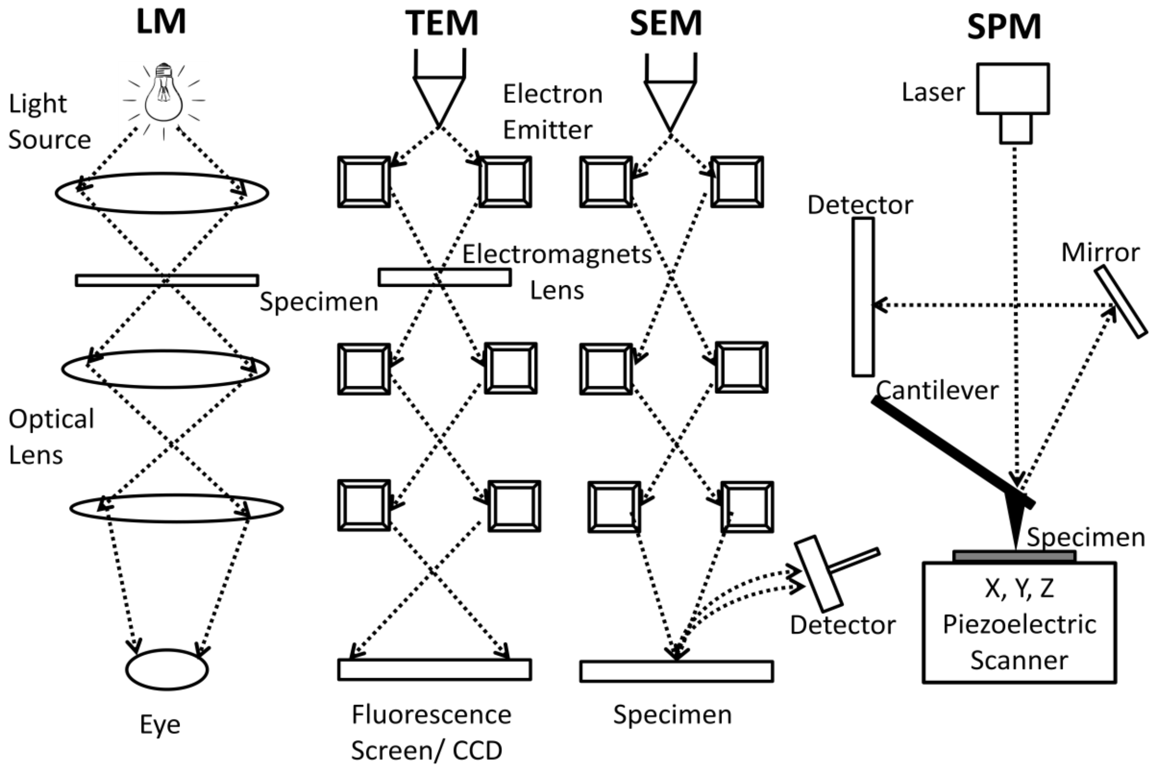

Figure 1.5: Schematic depiction of conventional light microscopy (LM), transmission electron microscopy (TEM), scanning electron microscopy (SEM), and scanning probe microscopy (SPM).

In the description of the structure, function and phenomena at the nanoscale, the experiments sometimes provide incomplete picture. These loop holes can be plugged in by theoretical and computational methods. Relying on the unprecedented rise in the computing ability in last two decade, use of computational tools for the in-depth investigations of nanoscale materials has become a common practice among the scientific community. However, there are also practical impediments in employing theory/computation for the nanomaterials as the system of interest can be large and the time scale can be long. This pose challenges in applying accurate atomistic methods. On the other hand, the continuum methods which are more suitable for matter at the length scale of micro-meter cannot give an accurate description of the structure/function of nano-scale materials. Despite all these challenges, some theoretical methods particularly the density functional theory (DFT) has become increasingly popular among the scientific community because of its computational cost-effectiveness and reasonably good accuracy. In the following section, we will provide a brief summary of the computational methods.

1.4.1: Theoretical Background

1.4.1.1: The Schrödinger Equation

Unambiguously, quantum mechanics can be regarded as one of the major scientific breakthrough of the twentieth century. At the heart of this theory lies the Schrödinger equation that deals with collective motion of electrons in the environment of nuclei and asserts us the ground state energy of any given collection of atoms. The primary prescription in quantum mechanics is to obtain the solution of the Schrödinger equation, in its time independent non-relativistic form, written for the i-th eigen state as:

$$\hat{H}\Psi_i(\vec{x}_1,\vec{x}_2,\ldots,\vec{x}_N,\vec{R}_1,\vec{R}_2,\ldots,\vec{R}_M) = E_i\Psi_i(\vec{x}_1,\vec{x}_2,\ldots,\vec{x}_N,\vec{R}_1,\vec{R}_2,\ldots,\vec{R}_M). \tag{1.1}$$

In the above equation $\hat{H}$ is the Hamiltonian operator for a system of M nuclei and N electrons and represents the total energy operator which can be written (in atomic units) as:

$$\hat{H} = -\frac{1}{2}\sum_{i=1}^{N}\nabla_i^2 - \frac{1}{2}\sum_{A=1}^{M}\frac{1}{M_A}\nabla_A^2 - \sum_{i=1}^{N}\sum_{A=1}^{M}\frac{Z_A}{r_{iA}} + \sum_{i=1}^{N}\sum_{j>i}^{N}\frac{1}{r_{ij}} + \sum_{A=1}^{M}\sum_{B>A}^{M}\frac{Z_A Z_B}{R_{AB}} . \tag{1.2}$$

In the above expression A and B run over the M nuclei and i and j over the N electrons of the system. Z_A and M_A represent the charge and mass of the A-th nuclei in atomic units. The first two terms define the kinetic energy of the electron and nuclei respectively. The latter three terms represent the potential energy part of the Hamiltonian, where the first term represents the attractive interaction between the nuclei and the electrons while the last two terms represent the repulsive interaction, electron-electron and nucleus-nucleus respectively. The Laplacian operator ∇_q^2 can be defined as:

$$\nabla_q^2 = \frac{\partial^2}{\partial x_q^2} + \frac{\partial^2}{\partial y_q^2} + \frac{\partial^2}{\partial z_q^2} \quad . \tag{1.3}$$

1.4.1.2: Born-Oppenheimer Approximation

Based on the fact that the nuclei are much heavier than the electrons, the Schrödinger equation can be further simplified. Due to this large mass difference between the nuclei and electrons, it is approximated that electrons move in the field of fixed nuclei which is known as the Born-Oppenheimer approximation. This approximation makes the kinetic energy term of the nuclei in (1.1) as zero and nucleus-nucleus repulsive potential energy as a mere constant. Hence the Hamiltonian in (1.2) reduces to only the electronic Hamiltonian as:

$$\hat{H}_{elec} = -\frac{1}{2}\sum_{i=1}^{N}\nabla_i^2 - \sum_{i=1}^{N}\sum_{A=1}^{M}\frac{Z_A}{r_{iA}} + \sum_{i=1}^{N}\sum_{j>i}^{N}\frac{1}{r_{ij}} = \hat{T} + \hat{V}_{Ne} + \hat{V}_{ee} \, . \tag{1.4}$$

Hence, the electronic wavefunction Ψ_{elec} only depends on the electronic coordinates and does not explicitly depend on nuclear coordinates which appear only parametrically in the wave function. Hence we can write

$$\hat{H}_{elec}\Psi_{elec} = E_{elec}\Psi_{elec} \tag{1.5}$$

$$E_{tot} = E_{elec} + E_{nuc} \, . \tag{1.6}$$

1.4.1.3: The Variational Principle

By solving equation (1.5), one has to find out eigenfunction Ψ_i corresponding to eigenvalue E_i of $\widehat{H}$. Once Ψ_i are determined, all other properties of the system can be obtained by evaluating the expectation values of desired operators using the wavefunctions. However, the above equation cannot be solved exactly for any atomic or molecular systems of practical importance. The variational principle gives us a recipe for systematically approaching the ground state eigenfunction Ψ_0 which gives the ground state energy E_0 as the operator $\widehat{H}$ is applied on it. The variational principle states that the energy obtained as the expectation value of the Hamiltonian $\widehat{H}$ using any trial wave function Ψ_{trial} is always an upper bound to the true ground state energy. This statement can be written as:

$$\left\langle \Psi_{trial} \middle| \hat{H} \middle| \Psi_{trial} \right\rangle = E_{trial} \geq E_0 = \left\langle \Psi_0 \middle| \hat{H} \middle| \Psi_0 \right\rangle . \tag{1.7}$$

1.4.1.4: The Hartree-Fock Approximation

Although the variational principle gives us some clue about how to approach the ground state eigenfunction and eigenvalue of a particular system, it does not provide any information on how to select the trial wave function Ψ_{trial}. In the Hartree-Fock (HF) approximation, the N-electron wave function of the system consisting of N electrons is approximated by an antisymmetrized product of N-one electron wave functions $\chi_i(\vec{x_i})$. This product is termed as a Slater determinant ϕ_{SD}, given by

$$\Phi_{SD} = \frac{1}{\sqrt{N!}} \begin{vmatrix} \chi_1(\vec{x}_1) & \chi_2(\vec{x}_1) & \cdots & \chi_N(\vec{x}_1) \\ \chi_1(\vec{x}_2) & \chi_2(\vec{x}_2) & & \chi_N(\vec{x}_2) \\ \vdots & \vdots & & \vdots \\ \chi_1(\vec{x}_N) & \chi_2(\vec{x}_N) & \cdots & \chi_N(\vec{x}_N) \end{vmatrix} , \tag{1.8}$$

which can be alternatively represented in a short-hand notation as:

$$\Phi_{SD} = \frac{1}{\sqrt{N!}} \det\{\chi_1(\vec{x}_1) \quad \chi_2(\vec{x}_2) \ldots \chi_N(\vec{x}_N)\} \quad . \tag{1.9}$$

In the above expressions, the one electron wave functions $\chi_i(\vec{x_i})$ are called spin-orbitals which are composed of spatial orbitals Φ_i $(\vec{r})$ and either of the spin functions $\alpha(s)$ or $\beta(s)$. The expectation value of the Hamiltonian operator applied on the Slater determinant will give us the HF energy E_{HF}, as

$$E_{HF} = \left\langle \Phi_{SD} \middle| \hat{H} \middle| \Phi_{SD} \right\rangle = \sum_{i}^{N} (i \mid \hat{h} \mid i) + \frac{1}{2} \sum_{i}^{N} \sum_{j}^{N} (ii \mid jj) - (ij \mid ji) \quad . \tag{1.10}$$

The first term in the above expression defines the contribution due to the kinetic energy and nucleus-electron attraction, as

$$(i \mid \hat{h} \mid i) = \int \chi_i^*(\vec{x}_1) \left\{ -\frac{1}{2}\nabla^2 - \sum_{A}^{M} \frac{Z_A}{r_{1A}} \right\} \chi_i(\vec{x}_1)\, d\vec{x}_1 \tag{1.11}$$

while the following two terms represent the Coulomb and exchange integrals given by,

$$(ii \mid jj) = \iint \left|\chi_i(\vec{x}_1)\right|^2 \frac{1}{r_{12}} \left|\chi_j(\vec{x}_2)\right|^2 d\vec{x}_1 d\vec{x}_2 \tag{1.12}$$

$$(ij \mid ji) = \iint \chi_i(\vec{x}_1)\, \chi_j^*(\vec{x}_1) \frac{1}{r_{12}} \chi_j(\vec{x}_2)\, \chi_i^*(\vec{x}_2)\, d\vec{x}_1 d\vec{x}_2 \quad . \tag{1.13}$$

The variational principle is applied for minimizing E_{HF} which is a functional of spin orbitals by choosing an orthonormal set of orbitals. The resulting Hartree-Fock equations can be written as:

$$\hat{f}\,\chi_i = \varepsilon_i\,\chi_i\,,\ i = 1, 2, \ldots, N. \qquad (1.14)$$

In the above expression $\hat{f}$ is the Fock operator and ε_i are the Lagrangian multipliers, which have the physical representation as the orbital energies.

1.4.1.5: Electron Correlation

According to the variational principle, we will always get E_{HF} larger than the exact ground state energy E_0. The difference between these two energies is called as the correlation enrgy.

$$E_{corr} = E_0 - E_{HF}\,. \qquad (1.15)$$

The instantaneous repulsion of electrons which is not included properly in the HF scheme is the main origin of this correlation energy. There can be two types of correlations namely dynamic and static. There have been prescriptions to obtain the correlation energy using multi-configuration wavefunction and related other technique.

1.4.1.6: Electron Density

Before we start the discussion about the density functional theory (DFT) in furtherance of our discussion, it is pertinent to introduce the concept of electron density at this point. The wave function Ψ introduced in the previous section may itself does not have any physical significance, but the square of the wave function is an observable quantity given as the probability function,

$$P\,(\vec{x}_1, \vec{x}_2, \ldots \vec{x}_N) = \left|\Psi\,(\vec{x}_1, \vec{x}_2, \ldots \vec{x}_N)\right|^2. \qquad (1.16)$$

The normalization condition for the system of N electrons leads to the equation

$$\int\cdots\int \left|\Psi(\vec{x}_1,\vec{x}_2,\ldots,\vec{x}_N)\right|^2 d\vec{x}_1 d\vec{x}_2 \ldots d\vec{x}_N = 1 . \quad (1.17)$$

A physical observable that is related to eqn. (1.16) is known as the electron density which can be experimentally determined by techniques like X-ray diffraction, etc. We can define the single particle electron density $\rho(\vec{r})$ as:

$$\rho(\vec{r}) = N\int\cdots\int\left|\Psi(\vec{x}_1,\vec{x}_2,\ldots,\vec{x}_N)\right|^2 ds_1 d\vec{x}_2 \ldots d\vec{x}_N . \quad (1.18)$$

The quantity $\rho(\vec{r})d\vec{r}$ defines the probability of finding any one of the N electrons in a volume element within $\vec{r}$ and $\vec{r} + d\vec{r_1}$ with an arbitrary spin while remaining (N-1) electrons have arbitrary spin and spatial positions. We can clearly have

$$\int \rho(\vec{r})\, d\,\vec{r} = N. \quad (1.19)$$

1.4.1.7: The Thomas-Fermi Model

The concept of wavefunction that we have discussed in the previous section is a complicated quantity of 4N (3 spatial and 1 spin for each electron) variables that cannot be probed experimentally. To simplify this situation, there have been attempts to use the electron density rather than the wavefunction as a basic variable to extract information about the atomic or molecular systems. One of such earliest attempt was made by Thomas and Fermi in 1927. Their model is essentially a quantum statistical model representing a system of uniform electron gas of constant electron density which takes into account of a quantum mechanical approach for the kinetic energy while treating the nucleus-electron and electron-electron interactions classically. The kinetic energy of such a system is given by,

$$T_{TF}[\rho(\vec{r})] = \frac{3}{10}(3\pi^2)^{2/3}\int \rho^{5/3}(\vec{r})d\vec{r} \ . \tag{1.20}$$

Combining the above expression for kinetic energy with classical expressions for nucleus-electron attractive potential and electron-electron repulsive potential, one obtains the Thomas-Fermi expression for energy of an atom as:

$$E_{TF}[\rho(\vec{r})] = \frac{3}{10}(3\pi^2)^{2/3}\int \rho^{5/3}(\vec{r})d\vec{r} - Z\int \frac{\rho(\vec{r})}{r}\, d\vec{r} + \frac{1}{2}\int\int \frac{\rho(\vec{r}_1)\rho(\vec{r}_2)}{r_{12}}\, d\vec{r}_1 d\vec{r}_2 \ . \tag{1.21}$$

The major shortcomings of the above expression, however, are that the expression of kinetic energy is a rather crude approximation to the actual kinetic energy and exchange and correlation effects are neglected completely.

1.4.1.8: The X_α Method

In the Hartree-Fock scheme, the exchange term is non-local and complicated in nature. The exchange term arising out of the anti-symmetric nature of the wavefunction can be expressed as an interaction between the electron density corresponding to the same spin and the Fermi hole for the same spin as:

$$E_X = \frac{1}{2}\int\int \frac{\rho(\vec{r}_1)h_X(\vec{r}_1;\vec{r}_2)}{r_{12}}\, d\vec{r}_1 d\vec{r}_2 \ . \tag{1.22}$$

In the approximation by Slater, the exchange hole is considered to be spherically symmetric with constant exchange-hole density (equal to minus of $\rho(\overrightarrow{r_1})$) within the sphere and zero outside it. The radius of the exchange hole r_S, also called Wigner-Seitz radius, is given by:

$$r_S = \left(\frac{3}{4\pi}\right)^{1/3} \rho(\vec{r}_1)^{-1/3} . \tag{1.23}$$

The Hartee-Fock exchange energy can be approximated as:

$$E_X[\rho] \cong C_X \int \rho(\vec{r}_1)^{4/3} \, d\vec{r}_1 . \tag{1.24}$$

In the above expression the exchange term is only local that depends on the electron density and C_X is a numerical constant. In Slater's approximation, a semiempirical parameter α (value varies between 2/3 to 1) was introduced into the constant factor C_X and the approach is famously known as X_α method or the Hartree-Fock-Slater method, with the exchange energy given by

$$E_{X\alpha}[\rho] = -\frac{9}{8}\left(\frac{3}{\pi}\right)^{1/3} \alpha \int \rho(\vec{r}_1)^{4/3} \, d\vec{r}_1 . \tag{1.25}$$

1.4.1.9: The Hohenberg-Kohn Theorems

The practical implementation of DFT is based on two important theorems proposed by Hohenberg and Kohn and derivation of subsequent set of equations by Kohn and Sham in the mid-1960s. The so called Hohenberg-Kohn (H-K) theorem gives us a prescription for the construction of a rigorous many-body theory employing electron density as a fundamental quantity. The first H-K theorem states that: *The ground-state energy of many-electron system characterized by an external potential* $V_{ext}(\vec{r})$ *is a unique functional of its electron density* ($\rho(r)$)

and the second theorem states that: *The electron density that minimizes the energy of the overall functional* (E[ρ(r)]) *is the true electron density corresponding to the full solution of the Schrödinger equation*. One of the important ramifications of these theorems is that the ground-state electron density uniquely determines all properties, including the energy and wave function, of the ground state. The ground state energy of any atomic or molecular system can be expressed as:

$$E_0 = \min_{\rho \to N} \left(F[\rho] + \int \rho(\vec{r})\, V_{ext}\, d\vec{r} \right) \tag{1.26}$$

where the universal functional F[ρ] contains contributions from the kinetic energy, classical Coulomb interaction and the non-classical terms such as exchange and electron correlation effects. We thus have

$$F[\rho(\vec{r})] = T[\rho(\vec{r})] + J[\rho(\vec{r})] + E_{ncl}[\rho(\vec{r})]\,. \tag{1.27}$$

Out of all the terms present in the above equation, only J[ρ] is known explicitly. Therefore, suitable approximations have to be developed for the kinetic energy and the non-classical exchange correlation energy density functionals.

1.4.1.10: The Kohn-Sham Method

In the previous discussion of the HF method, it has been shown that the N-electron wave function can be approximated by a single Slater determinant Φ_{SD} constructed from N spin orbitals. The Φ_{SD} can be considered as the exact wave function corresponding to a system of of N non-interacting electrons moving in an effective potential V_{HF}. Using the same analogy, one can express the kinetic energy of a system of non-interacting electrons, moving in some potential, as

$$T_{kin} = -\frac{1}{2}\sum_i^N \langle \chi_i|\nabla^2|\chi_i\rangle. \tag{1.28}$$

In analogy to the HF expression for energy given by

$$E_{HF} = \min_{\Phi_{SD}\to N} \left\langle \Phi_{SD} \middle| \hat{T} + \hat{V}_{Ne} + \hat{V}_{ee} \middle| \Phi_{SD} \right\rangle \tag{1.29}$$

one can, in principle, construct a Hamiltonian for a non-interacting reference system with an effective local potential $V_S(\vec{r})$, as

$$\hat{H}_S = -\frac{1}{2}\sum_i^N \nabla_i^2 + \sum_i^N V_S(\vec{r}_i)\,. \tag{1.30}$$

The ground state wave function of the above Hamiltonian can also be expressed as a Slater determinant (Θ_S) which consisting of spin orbitals (φ_i), the so called Kohn-Sham (K-S) orbitals, viz.

$$\Theta_S = \frac{1}{\sqrt{N!}}\begin{vmatrix} \varphi_1(\vec{x}_1) & \varphi_2(\vec{x}_1) & \cdots & \varphi_N(\vec{x}_1) \\ \varphi_1(\vec{x}_2) & \varphi_2(\vec{x}_2) & & \varphi_N(\vec{x}_2) \\ \vdots & \vdots & & \vdots \\ \varphi_1(\vec{x}_N) & \varphi_2(\vec{x}_N) & \cdots & \varphi_N(\vec{x}_N) \end{vmatrix} \tag{1.31}$$

where φ_i's are the solution of the one-electron K-S equation, i.e.

$$\hat{f}^{KS}\ \varphi_i = \varepsilon_i \varphi_i \tag{1.32}$$

$$\hat{f}^{KS} = -\frac{1}{2}\nabla^2 + V_S(\vec{r})\ . \tag{1.33}$$

In the above expressions, $\hat{f}^{KS}$ is the one-electron Kohn-Sham operator. The fictitious non-interacting system described above is connected to a real system of interest by choosing the effective potential V_S such that the density corresponding to this potential equals the ground state density of the real system, i.e.

$$\rho_S(\vec{r}) = \sum_{i}^{N} \sum_{s} \left|\varphi_i(\vec{r}, s)\right|^2 = \rho_0(\vec{r}) \,. \tag{1.34}$$

As discussed earlier, the Thomas-Fermi model corresponds to the local density approximation of the kinetic energy. The Thomas-Fermi model as well as several other extensions of this method where the kinetic energy is an explicit functional of electron density, however fail miserably beyond some qualitative considerations when applied for real atomic or molecular systems. The main reason for this disagreement lies in the error involved in the kinetic energy expression. In the path breaking approach by Kohn-Sham, they tackled this problem in a way where the kinetic energy is calculated as much accurately as possible and approximating the remaining part of the energy functional. In their approach, the exact kinetic energy of the non-interacting reference system is obtained by taking the same density as the real interacting system as:

$$T_S = -\frac{1}{2} \sum_{i}^{N} \left\langle \varphi_i \middle| \nabla^2 \middle| \varphi_i \right\rangle . \tag{1.35}$$

The functional F [ρ] can now be expressed as

$$F[\rho(\vec{r})] = T_S[\rho(\vec{r})] + J[\rho(\vec{r})] + E_{XC}[\rho(\vec{r})] \tag{1.36}$$

where the term E_{XC} is called exchange-correlation energy and can be given by,

$$E_{XC}[\rho] \equiv \left(T[\rho] - T_S[\rho]\right) + \left(E_{ee}[\rho] - J[\rho]\right) = T_C[\rho] + E_{ncl}[\rho]\,. \tag{1.37}$$

In the above expression, T_C represents the kinetic energy contribution to correlation energy and the remaining part is a non classical electrostatic contribution. Now, the energy of the real interacting system can be expressed as:

$$\begin{aligned} E[\rho(\vec{r})] &= T_S[\rho] + J[\rho] + E_{XC}[\rho] + E_{Ne}[\rho] \\ &= T_S[\rho] + \frac{1}{2}\iint \frac{\rho(\vec{r}_1)\,\rho(\vec{r}_2)}{r_{12}}\, d\vec{r}_1 d\vec{r}_2 + E_{XC}[\rho] + \int V_{Ne}\rho(\vec{r})d\vec{r} \\ &= -\frac{1}{2}\sum_i^N \left\langle \varphi_i \middle| \nabla^2 \middle| \varphi_i \right\rangle + \frac{1}{2}\sum_i^N \sum_j^N \iint \left|\varphi_i(\vec{r}_1)\right|^2 \frac{1}{r_{12}} \left|\varphi_j(\vec{r}_2)\right|^2 d\vec{r}_1 d\vec{r}_2 \\ &\quad + E_{XC}[\rho(\vec{r})] - \sum_i^N \int \sum_A^M \frac{Z_A}{r_{1A}} \left|\varphi_i(\vec{r}_1)\right|^2 d\vec{r}_1 \quad . \end{aligned} \tag{1.38}$$

In the above expression, E_{XC} does not have any exact form. The variational principle can be applied to solve the above expression by choosing a set of KS orbitals (φ_i) so that the energy can be minimized. The resulting equations are called KS equations given by,

$$\begin{aligned} &\left(-\frac{1}{2}\nabla^2 + \left[\int \frac{\rho(\vec{r}_2)}{r_{12}} d\vec{r}_2 + V_{XC}(\vec{r}_1) - \sum_A^M \frac{Z_A}{r_{1A}}\right]\right)\varphi_i \\ &= \left(-\frac{1}{2}\nabla^2 + V_{eff}(\vec{r}_1)\right)\varphi_i = \varepsilon_i \varphi_i\,. \end{aligned} \tag{1.39}$$

We have,

$$V_S(\vec{r}) \equiv V_{eff}(\vec{r}) = \int \frac{\rho(\vec{r}_2)}{r_{12}} d\vec{r}_2 + V_{XC}(\vec{r}_1) - \sum_A^M \frac{Z_A}{r_{1A}}\,. \tag{1.40}$$

Here, V_{XC} is the exchange-correlation potential which can be expressed as the functional derivative of E_{XC} with respect to ρ, i.e.

$$V_{XC} \equiv \frac{\delta E_{XC}}{\delta \rho} . \tag{1.41}$$

The strength of the K-S approach is that it is, in principle, exact. However, the only approximation enters in deciding the explicit form of E_{XC} and V_{XC}. Providing better approximation to these two quantities is one of the most sought after tasks in modern density functional theory.

1.5: Scope of the present Study

The classification of nanomaterials on the basis of structure, function or reactivity can be a tantalizing task. Similarly any investigations which aim at probing the diversity and complexity of these nanomaterials either by employing experimental or theoretical methods can also be an intensive and rigorous exercise. Therefore, from the vast and expansive pool of nanomaterials, the present thesis pulls out some of the important nanomaterials which are at the center-stage of current research interests. Employing diverse computational methods, the thesis aims at providing some important insights into the electronic structure and reactivity of these nanomaterials. The main work on the electronic structure and reactivity of nanomaterials encompassing this thesis has been presented in five chapters: 2-6 and the final chapter (chapter 7) presents an overview of the possible future directions contingent upon the results of the present thesis. In the following section, a brief objective of different chapters is discussed.

Chapter 2

Chapter 2 deals with the electronic properties and reactivity of carbon nanotubes employing model systems. This chapter is divided into two parts. Part one describes the electronic properties of nanotubes in the light of model systems which are analogue of the single unit of nanotubes. Local nanoscale curvature is demonstrated to be a key parameter in describing the electronic properties like ionization potential, electron affinity, HOMO-LUMO gap and polarizability of the nanotubes. Moreover, it has also been shown that this local curvature plays a discerning role in the interaction of atomic species like hydrogen and aluminium with the nanotubes. We have proposed the generality of this concept of curvature to correlate with several properties as well as reactivity of the nanotubes.

Part two of this chapter deals with investigations on the electronic properties of water molecule under the confinement of CNT. It is well known that water present in the nanoscale confined medium like the hydrophobic interior of the CNT extols unique properties that depart largely from their behavior in the bulk form. In a manner analogous to the first part of this chapter, here also, we consider suitable model systems which structurally resemble single unit of the CNT, and demonstrate that two unique parameters, namely the local nanoscale curvature and the confinement length, are in general of paramount importance in governing the structural and electronic properties of water molecule present inside CNT. It has been shown that these two parameters also play a key role in governing the significant variations in the interaction energy, structural parameters, Mulliken charges and red and blue shift in the O-H vibrational frequencies of the encapsulated water molecule. More importantly, interplay between curvature and confinement in deciding the electronic property of water in the nanoscale confinement has also been emphasized.

Chapter 3

The scope of Chapter 3 encompasses the investigations on the structure and electronic properties and reactivity of C_{60} fullerene. This chapter is again subdivided into two parts. The first part deals with the structure and electronic properties of fullerene C_{60} and its N-atom doped counterpart called azafullerene ($C_{60-x}N_x$). The bucky-ball fullerene, an allotrope of carbon, since its serendipitous discovery from the mass-spectrometric studies of carbon vapors has resulted in the emergence of fascinatingly new domain of research activities. In recent past, a considerable amount of work has been done to understand the structural, electronic and optical properties of fullerenes[1]. One obvious strategy to modulate the electronic properties of C_{60} fullerene is doping. The cage structure of fullerene entails three types of doping namely- endohedral, exohedral and substitutional doping. Azafullerenes are of special importance as they exhibit variable electronic properties which enable them to be potential candidates for various device applications such as materials with tunable optical properties (TOPs)[2, 3] In this part of the chapter, we have computed several electronic properties, viz. atomization energy, ionization potential, electron affinity, vibrational frequencies, nuclear independent chemical shift (NICS) and polarizabilities of these fullerenes. We have considered several possible isomers for particular azafullerene and put forward some general criterion for the stability of these fullerenes.

In the second part of the chapter, we have considered the reactivity of C_{60} fullerene towards the uranyl ion (UO_2^{2+}). The binding and speciation of this cation is extremely important not only from the perspective of nuclear waste management but also from environmental issues. In our computational investigations, we have considered several binding modes of the bare uranyl cation with fullerene molecule. To realistically describe solvent effects on the binding energies, we have also considered explicit solvent molecules as well as continuum solvation model

(COSMO) in our calculations. Apart from the binding of uranyl with bare fullerene, this part of the chapter also deals with interaction of uranyl with functionalized fullerene, particularly C_{60} functionalized with malonate groups. The importance of functionalization in improving the solubility of the fullerene as well as enhancing its binding affinity with uranyl ion has been put forward based on our results.

Chapter 4

This chapter starts with a systematic investigation on the electronic structure and properties of pristine gold nanoclusters Au_n as well as the corresponding alkali metal and hydrogen atom doped counterparts $Au_{n-1}X$, where n = 2-8 and X = Li, Na, and H. The dopant atoms are interesting from the perspective that they have similar outer electronic configuration in the form of a single valence electron like the gold atom. Electronic properties such as ionization potential, electron affinity, binding energy, HOMO-LUMO gap, and hardness parameters are found to exhibit a regular odd-even oscillatory pattern with variation of the cluster size. Our results reveal that the role of the hydrogen atom in modulating the structural and electronic properties of gold clusters is antagonistic to that of the alkali-metal atoms. The HOMO-LUMO gaps for the hydrogen-doped gold clusters are found to be much higher than the pristine and the alkali-metal-atom-doped gold clusters. In addition, we have also made an extensive study to investigate the important role of the impurity atoms, viz. hydrogen and alkali-metal atoms, on the adsorption of CO molecules by the doped gold clusters. An enhancement of the CO-adsorption energy has been observed for the gold clusters doped with a hydrogen atom rather than for the corresponding alkali-metal-doped ones and the enhancement is found to be more pronounced for the higher clusters in the series. It has been observed that there is as high as a 5-fold increase in the interaction energy of CO with Au_7H cluster as compared to its pristine counterpart Au_8.

Contingent upon this observation, we have also considered adsorption of the former two gold clusters on top of the surface of carbon nanomaterials. We have considered three different substrate surfaces viz. planar, concave and convex which represent respectively the surfaces of graphene, outer surface of CNT and inner cavity of CNT. The adsorption of CO molecule on gold clusters adsorbed on these surfaces is also considered. We have demonstrated that the modulation of local electronic environment of gold cluster by H-atom doping largely governs the CO binding energy to these clusters. Its implications to nanocatalysis and sensory applications have been highlighted in this investigation. This chapter ends with a note on further exploring these interesting observations on reactivities of gold clusters towards their possible applications in nanocatalysis.

Chapter 5

Exploration of the catalytic properties of gold clusters is the central theme of this chapter. It has been shown that gold nanoclusters are efficient catalysts for CO oxidation reaction at low temperatures[4]. This reaction is important in connection with control of environmental pollution as CO constitutes a major part of the automobile emission. Oxidation of CO is also important for fuel cells where CO-poisoning limits the efficiency. In the beginning of this chapter, we have considered the effect of doping the gold cluster Au_8 with a single H-atom. It is observed that the otherwise closed shell neutral pristine gold cluster which is known to have weaker binding with O_2 molecule, exhibit remarkable enhancement in the molecular oxygen binding energy, on doping, i.e. for the doped cluster Au_7H. Accordingly, we have also demonstrated the activation of O_2 characterized by appreciable increment in the O-O bond length and concomitant red shift in vibrational frequency, on account of a single hydrogen atom doping. It has also been highlighted that H-doped gold cluster reduces the barrier height for environmentally important reaction of CO oxidation to CO_2 as compared to the pristine cluster. We have asserted that these observations may lead towards the design of cost-effective and efficient catalyst by doping gold clusters with a cheaper element like hydrogen. The origin of this catalytic enhancement is viewed from the perspective of charging effect of gold clusters in presence of H atom. From the Mulliken Charge analysis, we have found that H atom in gold clusters carries higher negative charge and it induces highly cationic gold centers on the adjacent sites which act as active sites. Following this analogy, in the latter part of this chapter, we have made a systematic investigation on the effect of impurities in the gold cluster on their catalytic performance. We have considered several impurity atoms of varying degree of electronegativities such as C, N, B, Li, Na, K, F etc. From our important observations we have concluded that the local electrostatic effects play a governing role for CO oxidation reaction on gold clusters.

Towards the end of this chapter, we have considered the complex of gold cluster (Au_3) with DNA-bases as a catalytic model for CO oxidation reaction. DNA is known to be a programmable assembler for bottom-up synthesis of nanomaterials and hence these kinds of complexes can serve the purpose of ideal nanomaterials with tuneable functionality and applications. We have demonstrated that oxidation of CO on DNA base-gold cluster complex is more facile (in terms of reduction of activation barrier) as compared to the pristine cluster and hence we propose that DNA-gold complexes can be an active model nanocatalyst.

Chapter 6

Some important nanomaterials which are relevant for renewable energy applications are the subject matter of this chapter. With burgeoning world population and declining fossil fuel reserves, a time has arrived to look for some alternative energy sources which are green, non-polluting as well as abundant. To this end, the emergence of hydrogen energy has been recognized world over. Two important aspects of utilizing hydrogen as an alternative energy sources are (1) generation of hydrogen either by photochemical or electrochemical splitting of water and (2) storage of hydrogen for mobile energy applications.   Accordingly, this chapter is subdivided into two major parts. In the first part, we have discussed several nanomaterials for dissociation of water. Firstly, we have started with study of dissociation of water molecule on gold clusters. We have computed the barrier height for water splitting on gold cluster Au_8. It has been shown that for pristine cluster the barrier is as high as ~2.0 eV. As a step forward, we have also considered gold cluster Au_8 supported on a defective CNT which acts as a substrate for investigations of water splitting. At this point we have concluded that the effect of substrate manifests in terms of significant reduction of activation barrier of water dissociation, particularly CNT. We propose CNT-Au system as a possible nanostructure for water dissociation. We then moved to another system, namely Ti atom adsorbed on BN nanotube (BNT) as a possible candidate for water splitting. For this system, we have shown that the dissociation of a single water molecule proceeds with a lower activation barrier of ~0.2 eV. More interestingly, we have also demonstrated that subsequent dissociation of an additional water molecule leading to release of H_2 molecule becomes almost barrierless. We have thus proposed that Ti-decorated BNT can be one of the potential nanomaterial based catalysts for water dissociation.

In the second part of this chapter we have considered nanomaterials for storage of hydrogen. Herein, we have investigated hydrogen adsorption properties of silicon-lithium binary clusters. We have considered three different clusters viz. $Si_5Li_5^-$, Si_5Li_6 and $Si_5Li_7^+$. In all the minimum energy isomers of the three clusters considered, two of the lithium atoms are found to be situated in the axial positions and the remaining lithium atoms are in the equatorial position in the Si_5 plane. The lithium atoms which are in Si_5 plane are bonded to the Si-Si edge through a bridge bonding instead of a corner of the Si_5 ring. From the calculated atomic charges, it is found that there is charge transfer from lithium to silicon leaving a partial positive charge on the Li atoms and the axial lithium atoms are more charged as compared to the remaining lithium atoms. In the case of Si_5Li_6 and $Si_5Li_7^+$, the Li sites can trap a total of 14 and 17 H_2 molecules respectively, with each bridge bonded Li site adsorbing three H_2 molecules and each axial Li adsorbing one H_2 molecule which corresponds to a gravimetric density of 13.33 wt% and 15.25 wt% respectively.

Chapter 7

This is the concluding chapter of the thesis. This gives a brief outline about the possible future directions that can be charted out from the present investigations on various aspects of structure and reactivity of diverse nanomaterials that have been discussed in the present work.

CHAPTER 2

Carbon Nanotubes: Insights into the Electronic Structure and Reactivity from Model Systems

Chapter2: Carbon Nanotubes: Insights into the Electronic Structure and Reactivity from Model Systems

This chapter discusses several aspects of electronic structure and reactivity of carbon nanotubes (CNTs). Our approach for addressing the above problem is by considering simpler model systems rather than considering actual CNTs. This chapter is organized into two parts. In the first part, we exclusively consider several electronic properties of CNTs in relation to a unique parameter called nanoscale curvature inherent in its structure. In part 2 of this chapter, we discuss the interaction of a single molecule with CNT model systems. In recent years, there has been several insightful reports revealing startling properties of nano-confined water and the interior of CNT is a demonstrative example of nano-confined medium which can manifest a host of interesting properties for the entrapped water. In this part of our study, we have identified two important factors namely confinement and curvature which largely govern the property of water molecule.

2.1: Importance of Curvature in CNT

As we make a futuristic foray into a hyper-evolved world of science and technology, nanotechnology in particular has been at the helm of the affairs for the last few years. All poised to impart a distinct impact on the life and living of the society, nanotechnology manifests itself in the form of multitudes of technological advancements to varied real-life applications. Much to the delight of researchers, this field of activity has also captured their imaginations which is evident from the plethora of scientific literature available. When we talk about nanomaterials, carbon nanomaterials in particular dominate the current research trends. Ranging from honeycomb graphene[30] to its hydrogenated counterpart graphane[31], from the buckyball fullerenes[2] to carbon nanotubes[15], they cover a broad spectrum of applications. However, carbon nanotubes deserve special mention because of their fascinatingly new properties and potentially promising applications,[32] thus irresistibly prompting some researchers to aptly term them as “materials for the new century”.

Carbon nanotubes exist in different types namely, armchair, zigzag and chiral nanotubes depending upon the chiral vectors *n* and *m*, which are dictated by the pattern of rolling and the properties of these nanotubes can be different from each other, viz. metallic, semi-conductor or insulator. The essential building blocks for both the forms, SWCNT and graphene, remain the six-membered ring of carbon, such as a benzene ring (without H atoms which are not the part of either SWCNT or graphene). However, both the materials manifest distinctly different behavior. For the SWCNT, the building block is not the simple planar six-membered ring, but a ring with an intrinsic curvature, a bent one. Hence, it follows that as we bend the planar benzene ring introducing a local curvature, this seemingly simple and straightforward concept can offer us some clue about the reactivity difference between planar graphene and SWCNT at its crudest level.

This nanoscale curvature has been known to play a crucial role in discerning the reactivity of nanomaterials. From a practical point of view, synthesis of a truly flat sheet of graphene has always been a difficult task until recently[33]. In fact, graphene produced by various methods were the corrugated ones with the inherent curvature on them. This curvature will bring about noticeable change in the properties of graphene and may not make it as suitable a candidate for electronic applications as its flat analogue. Another important consequence of this curvature effect is that the curved graphene tends to be more reactive and facilitates spontaneous hydrogenation to form graphane[31], the completely hydrogenated counterpart of graphene. This essentially underlines the importance of the effect of curvature arising from the corrugation of the surface (global curvature).

The global curvature inevitably alters the physical properties of the material leading to new properties which are not observed in the planar structure. From an experimental observation point of view,[34,35] it has been established that the temperature of superconducting transition T_c of SWCNTs increases as the curvature of the graphene layers (decrease of diameter of nanotubes) increases. In SWCNT of diameter $d = 10$ A^0, one observes[34] Tc ≈ 1K and for $d = 4$ A^0, one has[35] Tc ≈ 16K. Recently, Jeong et al.[36] have demonstrated that the geometric curvature can enhance the spin-orbit coupling in carbon nanomaterials, thus making them more suitable for spintronics applications. In another interesting finding, Periera et al.[37] have suggested that artificial curved structures of graphene may facilitate device applications. In all the above studies, the diameter of the nanotubes can be directly correlated with the curvature. Morokuma and co-workers[38] have found a linear relationship between the reaction energy of the CH_2/NH/O exo and endo additions to armchair (n,n) SWCNTs and the inverse tube diameter (1/d) measuring sidewall curvature.

Although some of the earlier studies[39-44] have provided some indirect evidences for the role of diameter or side-wall curvature in relating some aspects of the chemical and physical properties of the nanotubes, the discerning role of the local curvature in determining the electronic properties and their reactivity of the different kinds of nanotubes has not been explored in a generalized manner. In order to have a deeper understanding of the attributes and manifestations of nanoscale curvature, one needs to consider several systems ranging from graphene to various SWCNTs differing in diameter and chirality and calculate the electronic properties. Conversely, one can approach this ostensibly straightforward but computationally expensive exercise in a rather intelligent way by choosing suitable model systems. All these findings, therefore, nudged us to view this important problem from an entirely different standpoint which is rather simplistic in approach. Our objective is to establish a correlation between the electronic properties as well as the reactivity of the nanotubes with the variation of local curvature through the model systems.

Electronic properties of carbon nanomaterials are of immense theoretical and practical interest. For our model system, we have made an attempt to compute the electronic properties like ionization potential (IP), electron affinity (EA), HOMO-LUMO gap (HL) which are central to the understanding of the reactivity of these materials. In general, the optical response properties of the carbon nanomaterials essentially rely on the polarizability at the molecular level which in turn, depends on their atomic structure and chirality[45]. Accordingly, there have been many studies in evaluating the polarizability of CNTs using various theoretical methods[46-49]. Invoking model systems for such calculations, however, has not been attempted earlier and no effort has been made in relating the local nanoscale curvature (from the perspective of its very origin into the surface curvature of the nanotube) to the electronic properties and chemical reactivity of the nanotubes. In the present study, we have demonstrated that the results obtained through these model systems strike a right chord with some of the reported literature results and also with those obtained for some of the actual nanotube candidates taken into consideration. Our methodologically straightforward approach leads to gain rational insights as well as meaningful conclusions for the description of the electronic properties and reactivity of carbon nanomaterials in terms of local nanoscale curvature inherent in the nanotubes.

2.1.1: Model and Method

We have envisioned a model system which is a logical representative of a building block of particular type of nanotube. We start with the simplest planar benzene ring, representing a single repeating unit of honeycomb lattice of graphene, as our model system. On the other hand, we can consider the inherent structure of nanotube as a mere repetition of six-member carbon ring with some degree of curvature. To exactly reproduce the single repeating unit of nanotube, curvature has been introduced in the model ring and the dangling bonds have been saturated with H atoms. The curvature has been introduced intuitively by lifting two diagonally opposite carbon atoms out of the plane of the original benzene ring. The degree of departure from planarity is the amount of local curvature introduced in the system. The way curvature angle (θ) has been defined here is shown schematically in Figure 2.1.

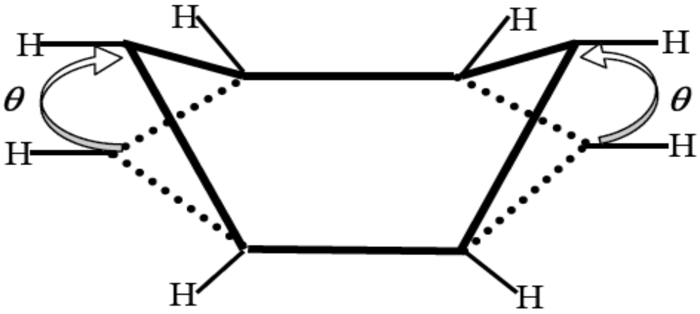

Figure 2.1: The model system depicting the local curvature (θ).

We have varied the curvature from 0^0 (planar) to 10^0, 15^0, 20^0, 25^0 and 30^0 to make curved benzene rings of corresponding curvatures. There has been some kind of intriguing relationship between the curvature of a particular CNT and its diameter. In general, the observed fact is that for smaller diameter nanotubes, the curvature on the ring is higher and vice-versa. The selection of this maximum curvature of 30^0 is also reasonable from the consideration that in very small diameter CNTs this is the approximate maximum value of the curvature introduced in the ring. Another point which is worth mentioning is that, this curvature as viewed from the surface of CNT can be of two types, namely concave and convex. This consideration, however, will not change the model system because by simply flipping the ring we can make a transition from concave surface to convex surface, thus essentially keeping the basic structure of the model system fixed for a particular degree of curvature.

We have used density functional theory (DFT) based methods for electronic structure calculation using the software GAMESS[50] for all the model structures. The split-valence basis set with diffuse and polarization functions namely, 6-31++G(d, p) has been employed for C and H atoms. All the electronic property calculations have been performed by keeping the geometries of the model systems frozen. We have used M06 exchange-correlation energy density functional as proposed by Zhao and Truhlar[51,52]. The M06 functional is a hybrid *meta*-GGA exchange-correlation functional, which has been shown to be quite successful for the accurate calculation of thermo-chemical parameters, non-covalent interactions and excited states[51-54] Apart from the above DFT based method, we have also employed the second order Moller-Plesset (MP2) perturbation method for all the model system calculations. In order to compare the electronic properties like IP, EA, and HL of the model systems with those of real nanotubes, four different candidate nanotubes with chirality (n and m) namely (3, 3), (6, 6), (10, 10) and (15, 15) have been considered in the present study. These actual nanotubes considered here are represented as finite segments consisting of three translational unit cells long with their peripheral C atoms saturated by H atoms. The total number of (C, H) atoms in the nanotubes (3, 3), (6, 6), (10, 10) and (15, 15) are (36, 12), (72, 24), (120, 40) and (180, 60) respectively. Calculations for these real nanotubes have been performed at the level of B3LYP/DFT employing a reasonably good basis set def2-TZVP for C and H atoms using the electronic structure calculation program TURBOMOLE[55]. The initial structures of the model systems and that of real nanotubes have been obtained by using the graphical software Gabedit[56]. Our approach to the calculation of polarizability relies on the finite-field method[57], which essentially involves on finite differencing of the energy values, and hence works for all *ab initio* wavefunctions. In this study, the average linear polarizability[58] (α) is calculated using the following expression.

$$\alpha = \frac{1}{3}\left(\alpha_{xx} + \alpha_{yy} + \alpha_{zz}\right). \tag{2.1}$$

2.1.2: Role of Nanoscale Curvature on the Electronic Properties and Reactivity of Carbon Nanotubes

In the following sections, in order to have an impression of how pertinent a parameter the concept of local curvature can be, to modulate the electronic properties and reactivity of CNT, we will discuss each property separately.

2.1.2.1: Nanoscale Curvature vs Diameter of the Nanotubes

We begin our discussion by simply observing the variation of this intrinsic curvature of a CNT with its chirality. This is accomplished by focusing on a single six-membered (6-m) carbon ring on nanotubes of different chiral vectors *n* and *m* comprising of both arm-chair and zigzag types and measuring the curvature induced in the ring. We present, in Table 2.1, the trend of local curvature (θ) with changing chirality of various CNTs.

Table 2.1: Variation of local curvature and diameter of nanotubes with chiral vectors *n* and *m*.

Armchair			Zigzag		
(n, m)	Curvature(θ^0)	Diameter (A^0)	(m, n)	Curvature(θ^0)	Diameter (A^0)
3, 3	16.02	4.05	3, 0	30	2.34
4, 4	12.42	5.4	4, 0	22.49	3.12
5, 5	10.09	6.75	5, 0	17.99	3.9
6, 6	8.48	8.1	6, 0	15	4.68
7, 7	7.31	9.45	7, 0	12.85	5.46
8, 8	6.42	10.8	8, 0	11.25	6.24
9, 9	5.72	12.15	9, 0	10	7.02
10, 10	5.15	13.5	10, 0	8.99	7.8
15, 15	3.45	20.26	15, 0	6	11.7

From these results several important conclusions can be drawn. Firstly, for a particular type of CNT (either arm-chair or zigzag), the degree of curvature uniquely specifies the chiral vectors *n* and *m*. It can also be seen from Table 2.1 that the variation in curvature for the CNTs having lower indices of *n* and *m* is larger as compared to the members with higher *n* and *m*, for which the curvature tends to vary rather marginally. It also indicates that with increase in diameter of the zigzag/armchair type of the nanotubes, the 6m-ring becomes flattened. In general, an increase in the chiral vector, *n* and *m* values of CNTs is associated with a decrease in the corresponding curvature. The difference between the zigzag and arm-chair types of nanotubes can be easily seen from Figure 1 and it can also be mentioned that for a particular value of the chiral vector n and diameter, the curvature of the zigzag type is more than that of arm-chair type. One interesting feature of SWCNTs is that given the chiral vectors n and m, one can calculate their diameter by using the expression[59]: $d = \left(\sqrt{3}/\pi\right) a_{cc}\ (m^2 + mn + n^2)^{1/2}$, where a_{cc} is the nearest-neighbor carbon atom distance of 1.42 A^0. The calculated values of diameters of various nanotubes are also presented in Table 1. The corresponding variation of curvature with diameter is presented in Figure 2.2 for armchair and zigzag nanotubes.

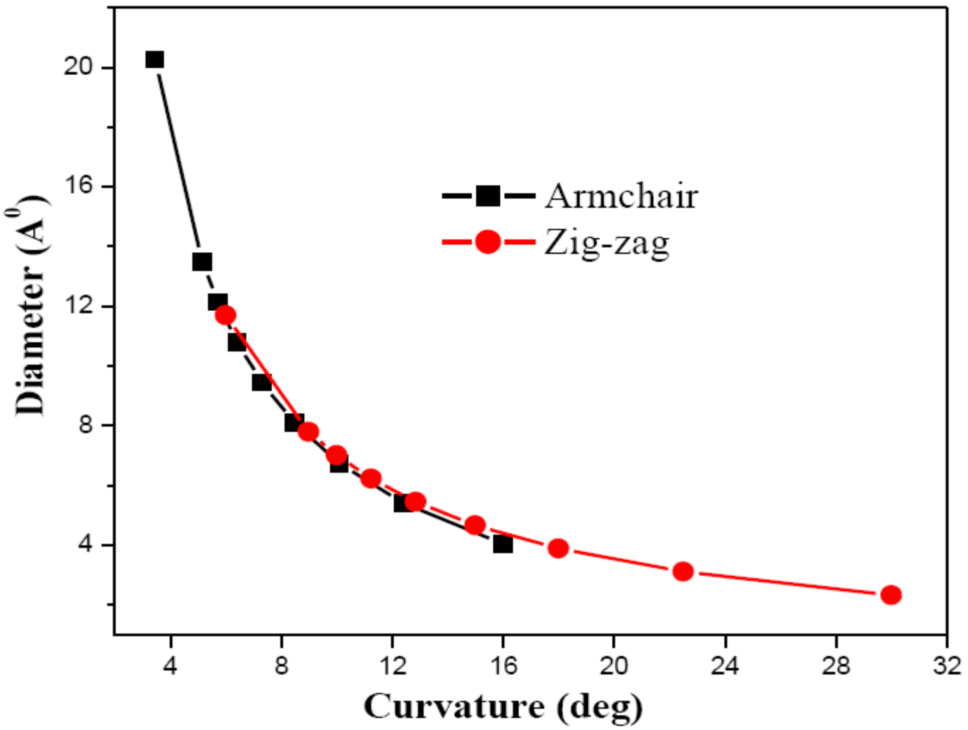

Figure 2.2: Variation of diameter with local curvature for arm-chair and zigzag nanotubes.

We observe, most strikingly, from these figures that the diameters of the nanotubes, be it armchair or zigzag, show same kind of behavior. It is also evident from these figures that the diameters of nanotubes are smooth varying functions of their curvature and the former decreases as we increase the latter. What is worthwhile to remind here is the fact that, this curvature from the consideration of our model ring is nothing but the bending introduced in that ring. Another interesting point is that there can have two different CNTs that correspond to nearly comparable value of curvature; CNT (5, 5) and CNT (9, 0), for instance, have curvature nearly equal to 10^0, but a careful observation of the structures of a finite segment of both types of nanotubes will tell us that although the magnitude of curvature remains the same, the nature of curvature (i.e. concave or convex) sets them apart. From these considerations, the model systems with a certain amount of curvature and with the information on whether it is concave type or convex type can be thought of as a fingerprint of a particular nanotube, defining uniquely the chiral vectors *n* and *m* and also their diameters which in turn decide their electronic properties. The preceding arguments justify our selection of the model system to investigate further their electronic properties.

2.1.2.2: Nanoscale Curvature vs Electronic Properties

Having set a firm footing on the rationale for the need and suitability of such model systems, we now proceed to the discussion of various electronic properties computed for these model systems. The knowledge of electronic properties like IP and EA is very helpful in deciding the reactivity and stability of the system. Most of the theoretical studies on CNTs are centered around *ab initio* calculations[60-62] of the work function (WF) rather than on IP and EA. There are also a very few studies[63] pertaining to the IP and EA of the nanotubes which are directly related to the WF. The calculations of WF as adopted in the above studies are suitable for extended periodic systems. Since our model system is an isolated molecular system, the IP and EA have been computed using the definitions, IP = $E(N-1) - E(N)$ and EA = $E(N) - E(N+1)$, where $E(N)$, $E(N+1)$ and $E(N-1)$ are the total ground-state energies in the neutral, single negatively charged and single positively charged configurations containing *N*, *N+1* and *N-1* electrons respectively. This approach for calculations of IP and EA is common for isolated systems such as molecules and nanocrystals[64,65]. To begin with, the variation of IP with curvature has been shown in part (a) of Figure 3. It is clear from this plot that as the curvature changes from 0^0 in case of planar system to the highly curved counterpart corresponding to local curvature of 30^0, there is steady decrement of the IP values. Up to a curvature of 15^0, the decrease in IP is relatively slower and beyond this point the curves steeply bend down. The trend of decreasing IP is in well accord with the observed fact that as the SWCNT becomes narrower i.e. its diameter becomes smaller, the reactivity increases.[66]

The imperativeness of the model systems can be judged if comparisons of any particular electronic property for the model systems can be made with that of real SWCNTs. The IP of the real SWCNTs can exhibit variable trends with respect to either diameter or length. The diameter dependence of real nanotubes can be directly correlated with the curvature of the model systems. However, length dependence of nanotube should also be taken into consideration for computing any electronic property of SWCNT. This length dependence is however limited by the computational cost in terms of taking larger lengths of SWCNTs. In a related study, Galano[67] has addressed the length and diameter dependence of several electronic properties of SWCNTs theoretically. As a comparison, we have taken the IP values corresponding to the largest lengths of several arm-chair SWCNTs considered in the above report and the trend of IP with respect to curvature has been presented as an inset in Figure 2.3 (a). We can qualitatively compare the similarity in the trend for the model and real systems. This observation tells us that the model systems can be as informative as the real SWCNTs in terms of qualitative prediction of property like IP.

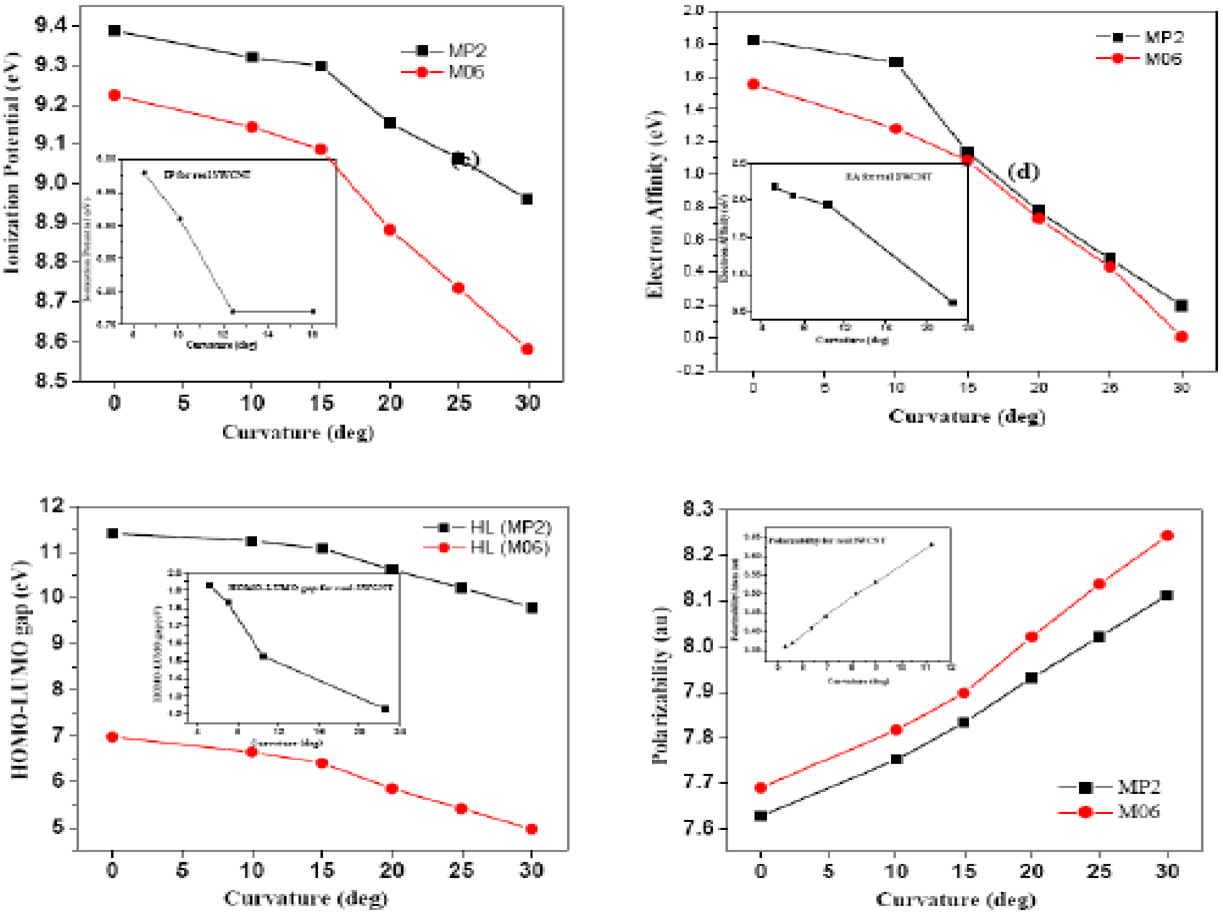

Figure 2.3: Variation of (a) Ionization Potential, (b) Electron Affinity, (c) HOMO-LUMO gap and (d) Polarizability for the model systems with respect to local curvature (θ) (inset shows the same for real SWCNT). The calculated values for the model systems correspond to $\theta = 0^0$, 10^0, 15^0, 20^0, 25^0 and 30^0.

The other property, that we consider for discussion is the EA. Part (b) of Figure 2.3 shows the variation of EA with curvature. EA, like IP, is also an indicator of the stability and reactivity of many-electron systems. The above figure illustrates the linear decrease in EA with the increase of curvatures for the model systems. On a discernible attempt to see how the EA of real nanotubes behave with curvature, we computed this property for four different nanotubes as mentioned in the model and method section. Very interestingly, the trend observed for representative nanotubes, presented as an inset of Figure 2.3 (b), show uncanny resemblance with that of model systems exhibiting a linear decrease with curvature. The qualitative agreement of model calculations, for EA, thus parallels with those of real nanotubes. Driven by our curiosity to obtain further insight into similarity of the trends obtained in Figure 2.3 (b) and that of the inset one, we have attempted to look for quantitative agreement, if any, between these two figures. We calculated the values of EA for representative nanotubes corresponding to local curvature values of 10^0, 15^0 and 20^0 from the plot and found the values to be 1.94 eV, 1.45 eV and 0.87 eV respectively. The corresponding values obtained from calculations (MP2) for the model systems are 1.75 eV, 1.31 eV and 0.77 eV for the above three values of curvatures respectively. This clearly demonstrates that the EA values obtained for model systems differ from that of real nanotubes within 0.1 to 0.2 eV. This observation, very emphatically indicates that a model system considered here, in essence, is in quantitative agreement with the real nanotubes in reliable estimate of EA values of the latter. More than IP and EA, the gap between the HOMO and LUMO energy levels (HL), which is the counterpart of the band-gap for periodic solids, is considered to be another important parameter to describe the reactivity of molecular systems and clusters.[68] The systems with higher HL gap correspond to higher degree of stability. Part (c) of Figure 2.3 describes the corresponding trend of HL gap with curvature. Conspicuously, from this figure, we find a linear dependence of the HL gap depicting a decrease of the former as the curvature values increase or in another terms the diameters decrease. From this figure, one can infer that the model rings tend to become more reactive as the curvature increases. Although the trends of the HL gap, thus obtained by MP2 and M06 methods, are similar in nature, the former method yields larger values as compared to the latter. In connection to the stability of SWCNTs, our interpretations in terms of computation of IP or HL for the model rings corroborate nicely with some of the previous results.[66,69,70] To further strengthen these observations, we have also estimated how the real nanotubes behave regarding the variation of HL gap as a function of curvature. The computed trend of the HL gap values for different nanotubes at the level of B3LYP/DFT with respect to change in curvature is shown as an inset in Figure 2.3 (c). This inset figure clearly demonstrates, for the real nanotube, the decreasing trend of HL gap values with increase in curvature, which is in qualitative agreement with that of the model systems, very similar to the trend of EA. It has already been predicted, in some of the earlier studies,[69,70] that nanotubes with very small radii are energetically unstable. The smaller values of the HL gap for very short diameter model rings as compared to their larger diameter counterparts clearly confirm this fact. A recent study by Torrens,[66] which employed a combined approach of a group-theoretical and geometric study along with calculations of standard heat of formation per C atom for SWCNTs, has inferred that wider infinite SWCNTs will be relatively more stable than the narrower counterparts. From these discussions, we can conclude that the diameter-dependence of the reactivity of SWCNTs is at least qualitatively interpreted by considering the model systems with varying curvature. Thus, to summarize, as the curvature becomes more pronounced, the corresponding diameter of the representative SWCNT becomes smaller. This manifests into an increase in reactivity which varies linearly with the amount of curvature as evinced from the trends of various electronic properties discussed in the preceding paragraphs. More pragmatically, the computed values for the model systems can be of immense importance in predicting the qualitative nature of reactivity for real nanotubes.

Carbon nanomaterials like carbon nanotube, by virtue of their extended delocalization of π-electrons are important in the context to their applications in optical harmonic generation and ultrafast optics and photonics. Interestingly, many of the unusual optical properties of SWCNTs are due to their ultra-small diameter and large curvature. Properties like polarizabilities can be of immense importance in understanding the non-linear optical properties of SWCNTs. We have presented in part (d) of Figure 2.3, the trend of polarizabilities with change of local curvature for the model systems. The linearly increasing trend with curvature essentially conveys that the model systems with larger curvature values are more polarizable and ideal for non-linear optical properties. To know what can be the relationship of polarizabilities of real SWCNTs, we have taken the corresponding polarizabilities per atom values obtained by Yaghobi[71] for several semiconducting SWCNTs and its variation with curvature has been shown as an inset to the above figure. Very interestingly, we find a similar linear relationship for the model and the real systems. This excellent corroboration of properties of the model systems with real SWCNTs give enough confidence to our proposed model and choice of the local curvature as a key parameter.

It is pertinent, at this point, to note that in order to claim that our model system yields reasonable qualitative trend of properties, we need to correlate them with some existing literature results. From the prediction of Benedict et al.,[46] by employing a simple tight binding method, the longitudinal polarizability per unit length was shown to be proportional to the radius directly and the square of the band gap inversely. Guo et al.[47] in their results for static polarizability (α), using a local spin density approximation (LSDA), have shown α to be proportional to square of the radius. From these two results, the dependence of polarizability on the radius seems to have no unanimity. A point worth mentioning, here, is that in our results, the dependence of polarizability has been shown with respect to the global (or surface) curvature and not the radius or diameter. However, in the initial part of our discussion we have shown that these two parameters are related inversely. In the calculation of polarizability by Torrens[66] using the induced dipole polarization model, the value of α is shown to increase monotonically with radius.

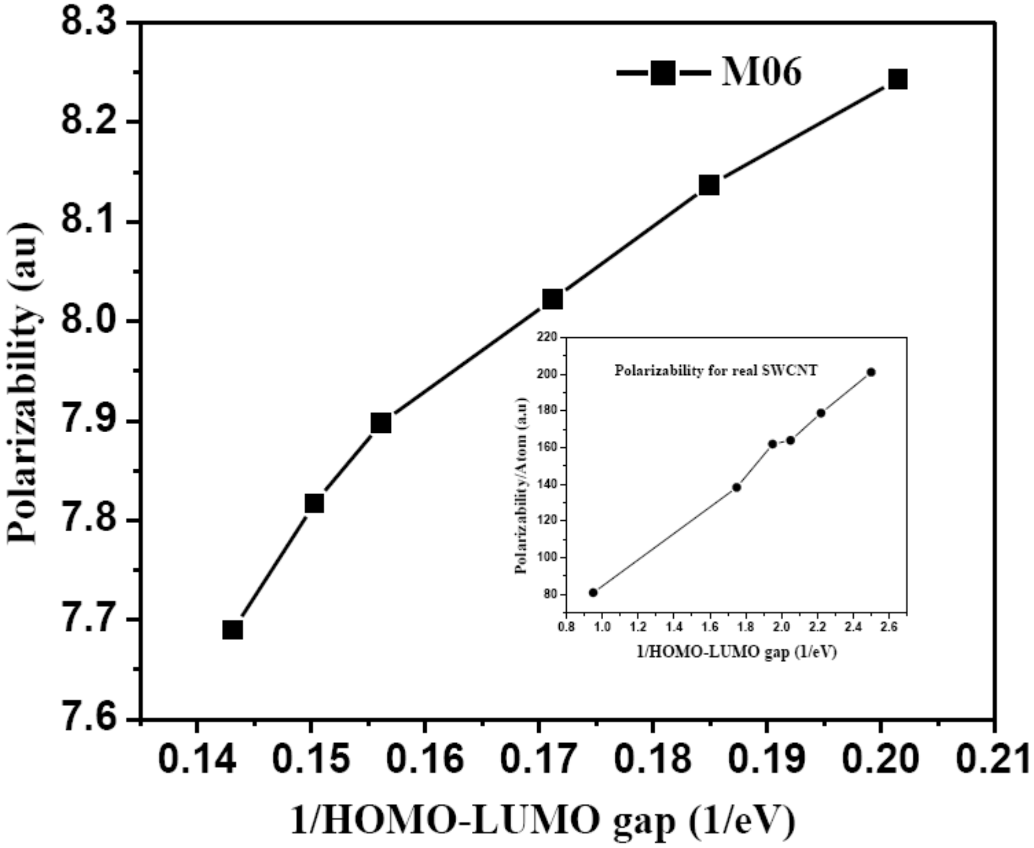

Figure 2.4: Variation of polarizability with inverse HOMO-LUMO gap obtainedM06 method for the model systems.

These results apparently suggest that as the curvature increases, i. e. as radius decreases, the polarizability should decrease which is not in accordance with our observed trend of α with curvature. From the results of Torrens,[66] it is also shown that for small R (radius) SWCNTs, the value of α varies smoothly with R^{-1}, which is, however, in qualitative agreement with the trend shown by our model calculations. In a more recent calculation, using first principles DFT methods, Brothers et al.[49] in a very interesting finding have shown that the polarizability per atom of nanotubes creates a universal relationship, showing a linear trend as a function of the inverse of band gap. In analogy to this, to check, whether our calculated HL gap values follow any such kind of trend or not, what we present in Figures 2.4 and inset (obtained from Ref:[49]) to this figure, is the corresponding variation of α versus inverse of HL gap for the model and the real SWCNTs respectively. For the model systems, in the above figure, we have presented only the M06 result for comparison with the real ones, because the MP2 results also show similar trend. We observe, most strikingly, that α yields nearly the linear trend with HL inverse in both the cases. Therefore, emphatically, we can argue at this point that although our system is a mere model system, with the inclusion of a very unique parameter as the local curvature, its results are able to go hand in hand with the existing literature results in predicting some of the correct trends of the electronic properties of carbon nanotubes.

2.1.2.3: Nanoscale Curvature vs Reactivity of the Nanotubes

In general, one of the important questions in chemistry is to find a relationship between the reactivity of molecular systems and their properties. Accordingly, the reactivity has been related to many concepts, such as the nature of the frontier molecular orbitals, valency, charges, aromaticity, electron density, Fukui function, hard-soft acid-base principle, etc. Although these concepts have been partially successful for predicting the nature of a particular reaction, the validity of these principles/concepts can have limited applications for the prediction of reactivity of the CNT-based materials. Accordingly, herein, we demonstrate the applicability of the concept of local curvature as a first step to understand the reactivity of SWNT with different species.[72] In this regard, Gülseren et al.[73] have investigated the reactivity of different types of carbon nanotubes and showed that the interaction of hydrogen and aluminum atoms can be tuned efficiently with respect to the radius of the nanotube. To describe the reactivity of model systems, we have also considered the interaction of H and Al atoms with our model systems and calculated the binding energies of these two atoms. The results are shown in Figure 2.5 and it is evident that as the local curvature increases, the interaction energy of the atomic species with the curved structure increases remarkably. The most striking results are the interaction energies of the hydrogen atom with the model curved benzene ring, which change from 0.0 to -55 kcal/mol and the corresponding changes in the shortest bond distance between the hydrogen atom and one of the carbon atoms are 3.465 A^0, 3.343 A^0, 1.154 A^0, 1.133 A^0, 1.121 A^0, and 1.112 A^0 respectively for the increasing values of curvature shown in the figure. This observation suggests that towards the higher curvature range, although the increment in the shortest H-C bond length seems negligible, the binding energy shows appreciable increase with curvature variation. It is inferred from this observation that, the interaction of atomic species is largely governed by the local nanoscale curvature at the site of interaction. Evidently, from the similarity in the nature of interaction of atomic H with the real nanotube and the model system, the larger role of nanoscale curvature as a suitable descriptor of reactivity can be realized.

We have also shown the relationship between the local curvature and binding energy (BE) of the aluminum atom in Figure 2.5. From this figure, one can indeed find a good correlation between the curvature and binding energy, and the correlation is found to be quadratic in nature ($\mathrm{BE} = a + b\theta + c\theta^2$). (It may, however, be noted that the correlation with other electronic properties is somewhat linear in nature). The corresponding correlation coefficient is 0.993 for the values obtained for the case of aluminum. This can be considered to be an important observation because the above results can provide a way to understand the nature of interaction from the values of the curvature. Another interesting aspect is the spontaneous (gradual) ionization of the aluminum atom upon binding with the curved benzene structure. The charge on the aluminum atom as obtained from natural population analysis are 0.002, 0.295, 0.475, 0.592, 0.646, and 0.698 au corresponding to the bending angle variation from 0^0, 10^0, 15^0, 20^0, 25^0 and 30^0 respectively.

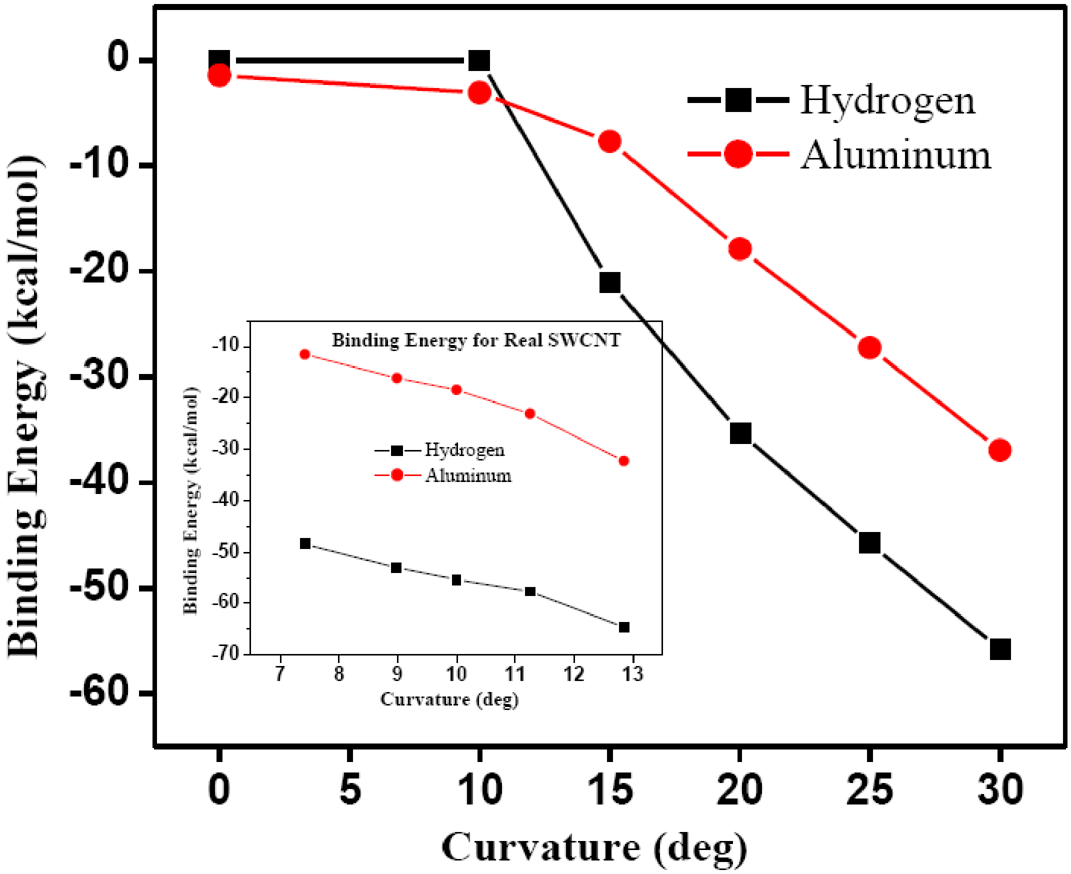

Figure 2.5: Binding energy of H and Al atom with the model systems (Inset Figure shows the corresponding trend for real SWCNT) with respect to local curvature.

A slight increase in curvature (~10^0) results in to a charge transfer of ~0.3 au from Al atom to the curved model carbon ring. This result can have very important implications in view of the fact that the charged atom can now interact more strongly with any incoming molecule, as compared to either the aluminum atom or planar carbon ring surface. The corresponding trend for real SWCNTs as obtained from the results of Gülseren et al.[73] is also presented as an inset figure and these results show that the interaction of hydrogen atom is weaker than aluminum. More interestingly, this fine modulation of the interaction energy is captured by the model system. Essentially, both the figures clearly demonstrate similar behavior with the variation of local curvature in spite of the fact that the model system consists of one repeating unit of the nanotube. This surprising result clearly indicates that each hexagonal ring of the nanotube behaves like disconnected benzenes, and the reactivity is highly localized at the individual ring, as is evident from the values of the binding energy of the species. This observation, in the same line with the previous cases, unequivocally indicates the realism in taking the model systems as a representative case of SWCNTs and concomitantly demonstrating a one to one correspondence of several electronic properties computed for the model systems and real nanotubes as a function of local curvature. Thus, from the above results, it is clear that the interaction is predominantly governed by the local curvature present in the carbon ring, and hence, the latter can be considered as one of the important parameters in determining the reactivity of the carbon surface. It is also important to note that the enhanced reactivity of the carbon surface can be similar to the effects due to the presence of vacancy, interstitial defects, or even any chemical modifications created on the molecular or solid surfaces. The increase in reactivity may be associated with the change in the electronic structure of the curved benzene system. In benzene molecule, all the atoms are arranged in a planar manner with sp^2 hybridization and the electrons are delocalized around the ring which will, however, be reduced along the ring if the bending angle (curvature) is increased. This will lead to the localization of the p_z-electron density partially on each carbon atom present in the benzene ring and it will also cause some changes in the nature of hybridization from pure sp^2 to quasi sp^2-sp^3 type. The partially localized electrons can act as a neutral free-radical center which can enhance the interaction with other molecules effectively. Thus, the reactivity of the curved systems will be significantly different from the conventional planar systems (with pure sp^2 hybridization) like graphite or graphene sheets. It should, however, be noted that in real systems, the bending or curvature is observed not only in the single ring but also between the rings (intra and inter, respectively). In general, different types of curvature can occur together in most of the carbon based nanomaterials, such as nanotubes and fullerenes, and hence, the electronic properties and reactivity of these systems will heavily depend on the resulting effect arising from the different types of curvatures (both the inter and sidewall curvature). The results derived from the present study will be useful in understanding how the various electronic properties and adsorption phenomena differ simply by changing the structure and/or size of different carbon-based nanomaterials.

2.2: Water inside CNT: A Brief Genesis

The all-pervasive water in all its forms and manifestations has been the cynosure of innumerable scientific investigations for its distinctly unique properties. Behavior of water under the confined environment of nano-channels is a fascinating field of research as it extols some different new phenomena not witnessed for water in bulk systems. The role of water in the nonpolar cavities of proteins and other biological systems is of fundamental importance. Some recent studies have established the role of water as mediator for proton transfer through the nonpolar interior channels of biological importance.[74,75] The dynamics of water permeation through membrane channel protein aquaporin has also been investigated by several groups.[76-78] In this case a narrow hydrophobic channel has been shown to facilitate the facile single-file water transport through the core of protein. The energetics and thermodynamic aspects of water interaction in these cavities are very poorly understood avenues.

Carbon nanotube (CNT), in recent years, has emerged as a potential candidate for its applications to store or transport fluids in nanoscale precision, apart from its mechanical, optical, thermal, electrical or biomedical applications. Some recent experiments[79,80] have established that CNTs facilitate pressure driven transport of gas, ion and water. These experiments also demonstrate significant enhancement of water flow inside the tube, thereby widening the scope of using CNTs as obvious candidates for fabrication of nanopore structures. The hydrophobic interior of CNT can be considered as functionally similar to that of proteins. From these considerations, study of water interaction in the channel of CNT is an important problem to address. The initial reports by Hummer et al. [81] on the burst transmission of water in the hydrophobic channel of CNT have inevitably spurred an active research dealing with several aspects of water under the confinement of CNT. [82,83] The experimental results of Holt et al. [80] reveal that the flow rate of water through a CNT of radius 1 to 2 nm is more than three orders of magnitude faster than the conventional hydrodynamic flow. In addition, Sood and co-workers [84] have demonstrated that the flow of a liquid on single-walled carbon nanotube bundles can induce a voltage in the sample along the direction of the flow. Water inside nanotubes under the application of axial pressure has been shown to exhibit a first-order freezing transition to hexagonal and heptagonal ice nanotubes and a continuous phase transformation into solid-like square or pentagonal ice nanotubes. [85] It has also been conjectured that liquid confined in the nanotube can exhibit very interesting behavior like solid-liquid critical point beyond which the distinction between solid and liquid phases becomes difficult. [86] A recent review article highlights some of the recent advancements in our understating pertaining to this unique system viz. water inside nanotube. [87]

Structurally, CNT can be thought of a rolled planar sheet of graphene. The building block of honeycomb graphene is none other than the six-membered carbon ring as present in, say benzene. On the contrary, if we examine meticulously, the repeating unit of CNT is not the simple benzene ring, but a bent counterpart of the benzene ring with some inherent degree of curvature. Some of the previous studies have demonstrated the influencing role of curvature in governing the reactivity and property of nanotubes. [38,41,88] The usefulness of this concept has been demonstrated in one of the studies by Chandrakumar et al. [89] for the rational design of carbon based nanomaterials for hydrogen storage. Thus, it is also expected that the curvature and confinement due to the nanotube can influence the properties of water present inside CNT. However, investigations based on these two factors have not been addressed so far in the literature to describe the behavior of encapsulated water molecule in a generalized manner. The classical molecular dynamics simulations can essentially shed light on the dynamical aspects of water conduction in CNT. The electronic structure methods, on the other hand, can supplement with nitty-gritty of structural and electronic properties that are essential for understanding the properties of the confined systems. However, first principles based investigations[90-92] to explore the structural, electronic and vibrational properties of confined water are rather scarce in the literature. In our present study, using density functional theory based first principle methods, we have attempted here to explore the structural and electronic properties of water under the confinement of CNT.

Accordingly, our standpoint to address this very important problem is, however, a bit different in the sense that instead of considering actual CNT, we have chosen suitable models that can mimic the effect of CNT. From the rationale followed in the preceding discussion that a bent benzene ring can be thought of as the single repeating unit of CNT, we have taken this model system to represent the CNT and proceeded further in our investigation of interaction with the water molecule. In this study, we envision that the curvature on the model systems, i. e. benzene rings with a certain degree of curvature, has a direct correlation with the diameter of the CNT. For CNTs with smaller diameters, the curvature introduced on the model rings is higher and vice-versa. As we approach from the planar benzene ring to its counterpart with some degree of curvature, essentially we start probing the effect of moving from planar graphene to the CNTs with increasing curvature or in other words decreasing diameter. The ways in which we define this curvature and model system have been explicitly mentioned in the following (model and method) section. To gain insight into this effect of variation of curvature we have considered model rings of different curvatures and studied its interaction with water molecule. More importantly, in order that the water molecule feels the effect of confinement, we have modeled our systems such that water molecules are sandwiched between two model rings where the confining distances as well as the curvatures are varied. These two apparently simplistic terms, confinement and curvature can be two imperative parameters to decide the structural and electronic properties of water inside CNT. From our model system calculations, we are able to conclude about the combined effect of confinement and curvature on the structure and electronic and vibrational properties of water molecule present inside CNT.

2.2.1: Model and Method

To mimic the effect of confinement, the model system that we have considered in our study is essentially two benzene rings separated by some distance which we treat as the confinement distance. While this can produce the effect of confinement, in order to really mimic the curvature effect of the hydrophobic surfaces, we have judiciously introduced some finite curvature on the benzene rings. The rationale for selecting this kind of curved benzene rings can be justified if we carefully have a zoom-in view of a single building block of carbon nanotube which has been demonstrated in part (a) of Figure 2.6. The curved carbon rings in CNT are structurally similar to our model curved rings with the difference that in our model rings the C-atoms are saturated with H atoms and the rings are not interconnected. Since the electronegativity of hydrogen atom is comparable with that of carbon and it does not affect the electron delocalization inside the carbon ring, hydrogen has been used to saturate the carbon ring. The way we define the two important parameters, namely the confinement and the curvature in these model systems, has been illustrated in part (b) of Figure 2.6. Water molecule is placed between the two model rings marked as C1-C2-C3-C4-C5-C6 in the above figure. The confinement is defined by the distance between the base planes formed by C1-C2-C4-C5 atoms on both the rings. The curvature is defined here in terms of the acute angle between the base plane and the plane formed by atoms C2-C3-C4. The curvature values considered here are 0^0, 10^0, 15^0, 20^0, 25^0 and 30^0 in our calculations. This variation of curvature, interestingly, has direct correlation with the diameter of the CNT. For the CNT with smaller diameter, the model ring deviates significantly from the planarity and consequently the curvature is larger and vice-versa. Hence, as we approach from the planar benzene ring to its counterpart with some degree of curvature, essentially we start probing the effect of moving from planar graphene to the CNTs with increasing curvature or in other words decreasing diameter. For our calculations, the confinement is varied from 4 to 8 Å. This situation is analogous to two diametrically opposite carbon rings in the real CNT where the distance between them represents the diameter. For simplicity, the effect of curvature and confinement on water with benzene rings is designated as W-DB-CV-CF, where W, DB, CV and CF are referred as water, double benzene rings, curvature (degree) and confinement length (Å), respectively. Similarly, the terminology, "W-SB-CV" denotes the system consisting of a water molecule and single benzene ring with varying curvature.

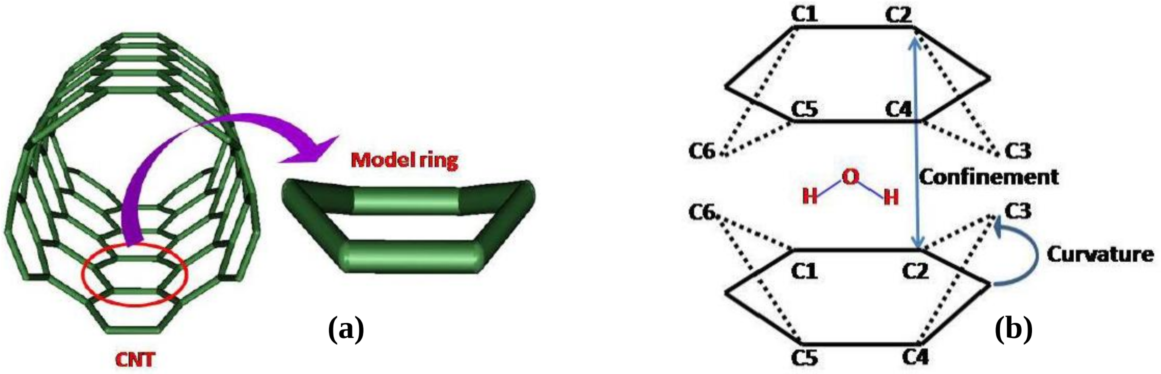

Figure 2.6: (a) A zoom-in view of a single unit of CNT showing the model structure , **(b)** model ring depicting the confinement and curvature.

All the calculations have been carried out with GAMESS[50] electronic structure package. The split-valence basis set with diffuse and polarization functions namely, 6-31+G(2d, 2p) have been used for all the atoms. We have employed the second order Moller-Plesset (MP2) perturbation method for all the calculations. Apart from this, we have also employed the full Hartree-Fock exchange functional along with the Lee-Yang-Parr (LYP) correlation functional in the density functional calculations (HLYP method) as well as the popular hybrid functional B3LYP and the hybrid *meta*-GGA exchange-correlation functional M06 as proposed by Zhao and Truhlar[51] for comparison of performance of various methods and functionals. During optimization, the positions of the two model rings have been kept frozen so as to maintain the desired confinement and curvature value and only the water molecule is subjected to geometry optimization. For some representative cases, the vibrational spectra of water have been computed using the

Turbomole[93] package at the level of BP86/def2-SV(P) with the already obtained MP2 optimized structures.

2.2.2: Effect of Confinement and Curvature on Water Molecule Encapsulated in Carbon Nanotube Model Systems

In this section, the interaction of water molecule with single and double benzene rings with different curvature as well as confinement is discussed separately. Let us first consider the interaction of a water molecule with single benzene ring and its curved counterparts. The interaction energy of the system W-SB-CV (CV is curvature in degree) evaluated by the MP2 method has been presented in Figure 2.7.

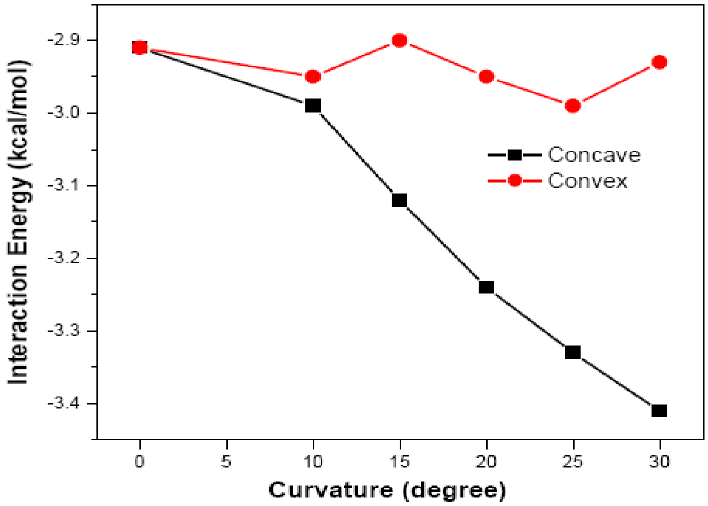

Figure 2.7: Trend of interaction energy of water with variation of curvature (W-SB system).

In this model system, the water molecule is placed on the concave side of the model ring as we vary the curvature. Herein, it may be noted that the water molecule experiences the effect of only the curvature on the ring and there is no confinement effect. The most important point about the water and benzene system is that it exemplifies an ideal case of hydrogen bonding interaction to the π-acceptor (benzene ring in this case) and such type of systems have been addressed in great details by both theoretical and experimental methods. [94-98] Moreover, for this kind of systems the correlated *ab initio* methods like MP2 are known to describe the binding energies in a fairly accurate manner. [99] Both the hydrogen atoms of the water molecule are always found to orient towards the π-electrons of the carbon ring with the concave surface and the minimum distance between the center of mass of the carbon ring and hydrogen is found to be 3.06 Å. We have also studied the water molecule interaction with convex surface of the curved carbon ring and the corresponding energy values are also presented in Figure 2.7. Herein, we note that the interaction energy does not vary significantly with respect to the curvature of the carbon ring and the increment in the interaction energy is only ~ 3 % whereas for the concave surface it is ~ 17 %. As the curvature is introduced in the carbon ring, the effect of π-electron density due to the four carbon atoms (C1-C2-C4- C5) lying on the convex surface, experienced by the incoming water molecule is not altered significantly. In addition, only one of the hydrogen atoms of the water molecule is found to interact with the carbon atom of the convex surface and the shortest carbon-hydrogen distance also does not change appreciably. Hence, it appears that the convex surface is less interactive than the concave surface due to the above reasons.

For the case of planar benzene-water system, the experimental distance[96] and the CCSD(T)/CBS[99] values are 3.35 and 3.21±0.03 Å respectively. The estimate of the interaction energy of flat benzene (curvature=0^0) with water is found to be ~2.9 kcal/mol and the previous reported benchmark calculation[99] with MP2/IB (infinite basis set limit) predicts the same to be 3.66 kcal/mol. The lesser magnitude of interaction energy in our case can be attributed mainly to (1) smaller basis set and (2) the fact that here the geometries of the benzene ring and its curved counterparts are frozen and only the water is allowed to be optimized. In a related study, Jenness and Jordan[100] employed density functional theory-symmetry-adapted perturbation theory for studying the interaction of water molecules with different sizes of aromatic benzene rings and their results revealed that the interaction energy of water with benzene is found to be -3.14 kcal/mol and it is gradually reduced to -2.48 kcal/mol with respect to increase in the number and size of the aromatic benzene rings. More interestingly, the energy decomposition analysis revealed that there is a 50% reduction in the electrostatic energy term and 10% increase in the dispersion energy term due to the increase in the number of π-hydrogen bond interactions. Similarly, Prakash et al. [98] have studied the interaction of water clusters with benzene ring, where they predicted that the presence of π-hydrogen bond interaction in all the clusters adds to the stability of water clusters. These results clearly signify the effect of the inclusion of more number of water molecules and benzene rings on the binding strength of water with planar benzene ring and the results exhibit a noticeable variation in the binding strength.

Let us now discuss the effect of curvature on the interaction of water molecule with the curved carbon ring. It can be seen from Figure 2.7 that the magnitude of interaction energy of W-SB increases with increase in the curvature on the ring and the increment is interestingly significant. The binding energy of the W-SB system corresponding to curvature of 30^0 is ~3.4 kcal/mol. The difference in interaction energy with water for a truly flat benzene and the one with highest degree of curvature amounts to be ~20%. Since the present system is an ideal case of weakly interacting systems, the increment observed in this case should be considered to be very significant. The important rationale learnt from this observation is that, the variation of curvature can have significant influence on the interaction of water with surface of carbon nanomaterials having inherent curvature associated with different types of carbon ring networks. In general, such systems are controlled by the π-hydrogen bonding involving the dispersion, electrostatic, polarization (induction), and charge transfer interactions. Especially, the long-range dispersion interaction contributes significantly to the interaction energy of water and carbon-rings.

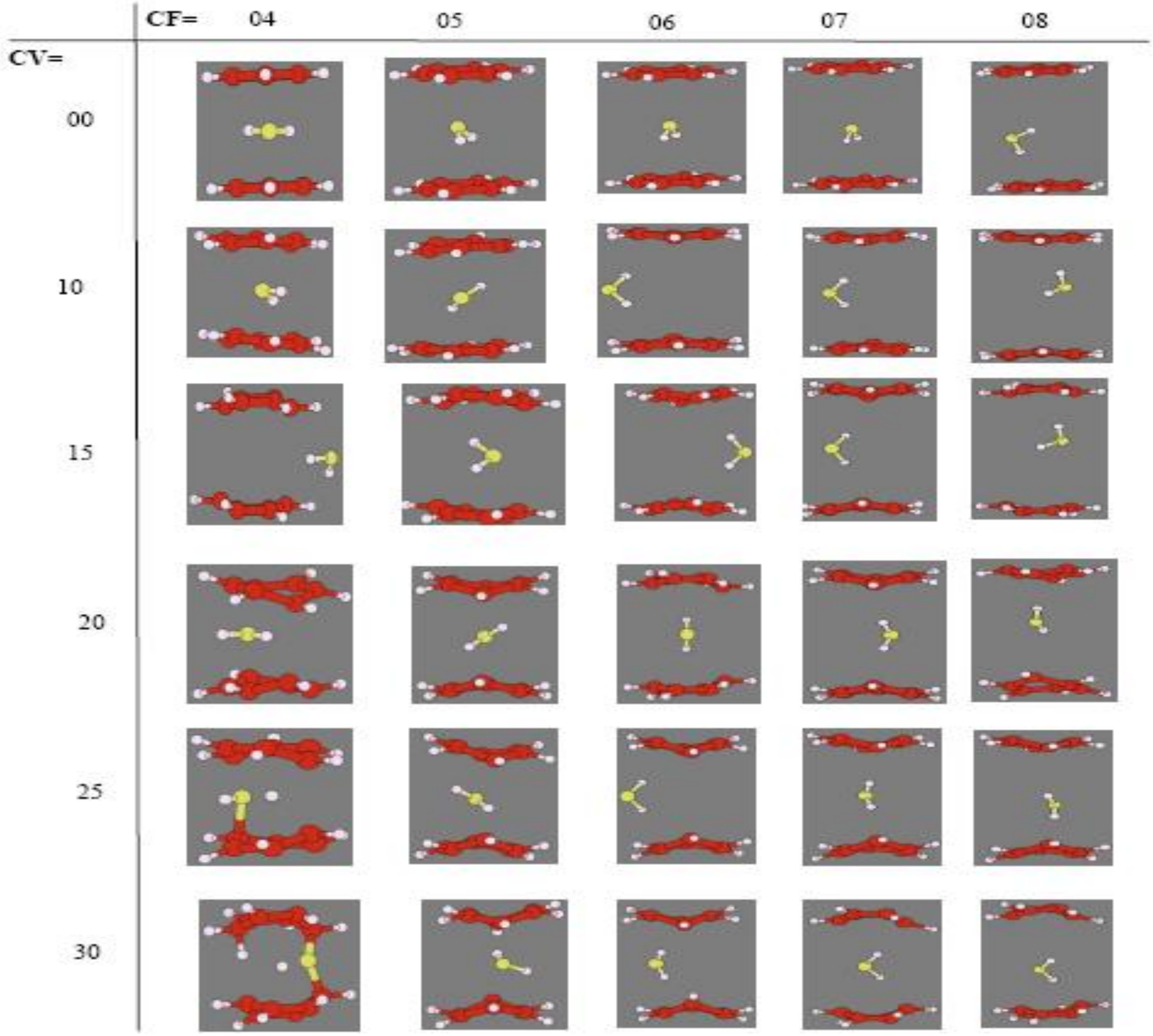

Figure 2.8: MP2 optimized geometries of water molecule with different curvature and confinement values, W-DB-CV-CF system.

Based on our results, we indeed find that for the W-SB case, the electronic and geometric properties of the water molecule like the H-O-H bond angle, O-H bond length and Mulliken charge on O and H atoms for the W-SB system change marginally with respect to the different values of curvature.

We will now discuss about the structure and electronic properties of a water molecule placed between two benzene rings which we refer as Water-Di-Benzene (W-DB) system. In particular, the effect of two important parameters, namely the confinement and curvature on the properties of encapsulated water has been focused on. Also, results pertaining to MP2 as well as various DFT methods have been discussed to firmly establish our arguments. The MP2-optimized geometries of W-DB-CV-CF (CV=curvature in degree and CF= confinement distance in Å) systems have been presented in Figure 2.8. From this figure we observe that, as we increase the confinement distance between the two rings, keeping the curvature fixed the water molecule changes from an initial position where the molecular plane is parallel to the base plane (horizontal) of the benzene rings to a position (vertical) where the two H atoms are pointing towards the ring. This observation suggests that when the confinement is more, water molecule is forced to adopt a horizontal orientation with respect to the rings and as the confinement gradually decreases it adopts a vertical structure. The interplay between confinement and curvature seems to govern the structure and orientation of water molecules. More interestingly, where the effect of confinement predominates and the curvature is larger, for instance in case of W-DB-25-04 and W-DB-30-04 systems, the water molecule is in a dissociated form with significant lengthening of O-H bond. However, on slight increase of the confinement distance as in the cases of W-DB-25-05 and W-DB-30-05, the water molecule attains regular geometry. An important rationale that we can derive from this observation is that, if the water molecule is placed in between highly confining hydrophobic surfaces where the surface is also curved, water molecule can be dissociated. This kind of dissociated structure of the water molecule, in turn can also affect the dynamical properties of water like diffusion as well as the strength and orientation of the hydrogen bonding. Our results can shed light into the understanding of the manner in which water is transported in membrane proteins like aquaporin, where the water molecules pass through a narrow constriction, in a biological environment. Very interestingly, it has been demonstrated that in the protein channel of aquaporin 1, the narrowest part (~5-8 Å in diameter) of pore which is formed by aromatic and arginine residues has a decisive role in maintaining single file flow of water molecules across the pore. [76] Moreover, we can also extend our argument to the case of water inside CNT and argue that if water is allowed to pass through extremely narrow diameter ~4-5 Å, the properties can exhibit a marked difference from the water confined in larger diameter CNTs.

In furtherance of our discussion, we now elaborate on the energetics of the water molecule placed between two model rings. The variations of interaction energy of the water molecule with curvature have been presented in Figures 2.9(a)-(e) for different confinement distances ranging from 4-8 Å. Apart from the MP2 results, the results for different functionals have also been superimposed on these figures. From Figure 2.9(a), we observe that when the confinement is more prominent (CF=4 Å), the interaction energy of water varies drastically. Up to curvature 10^0, the water molecule is unfavorably bound as the interaction energy is positive. However, with a slight variation of curvature from 10^0 to 15^0, there is a significant dip in the interaction energy, revealing the discerning role of curvature in stabilizing the encapsulated water molecule. This variation in interaction energy of water is as high as ~ 80 kcal/mol for the MP2 method. DFT methods such as HLYP, B3LYP and M06 predict even larger variations in interaction energy (~100 kcal/mol) as we move from curvature 10^0 to 15^0. The water molecule attains its most energetically favorable orientation for curvatures 15^0-20^0 where the interaction energy is negative and then it again shoots up for higher curvatures. *This observation is indeed fascinating from the perspective that under highly confining media, although the water molecule experiences energetically a highly unfavorable situation, a miniscule variation of one parameter, namely, the curvature of the ring brings about a remarkable change in the stabilization energy of the water molecule.* A change in energy of ~ 80-100 kcal/mol (depending upon the methods chosen) itself, emphatically reflects this fact. Now we move to a case where the confinement distance is 5Å (Figure 2.9(b)). It is expected that as the confinement effect tends to disappear gradually, the stability of the water molecule can be enhanced in a significant manner. The results obtained by different methods in this case show some discrepancy in the trend of the interaction energy. The MP2 method predicts the water interaction energy to be positive, varying within a range of 5 kcal/mol across all the curvatures. However, the DFT methods predict trends similar to the case of confinement within 4 Å. As was the situation with the previous case, here also for initial smaller curvatures, the interaction energy is positive (but with lower magnitude than the 4 Å case) indicating that the water molecule is unbound. The water molecule attains minimum energy configuration with negative interaction energy for curvature beyond 15^0. In this case, the variation in interaction energy shows a sudden dip in the curve with values between 15-25 kcal/mol. This observation is in the same spirit as seen for the 4 Å case highlighting the effect of curvature on the energetics of water molecule for smaller confinement lengths.

More strikingly, on further increase in the confinement distance to 6 Å (Figure 2.9(c)), it is observed that the interaction energy of the water molecule is always negative across the variation of curvature. This suggests that the water molecule is now in an energetically favorable environment with confinement being eased up leading to net stabilization energy. Focusing on the results obtained by different DFT methods, a linear trend is observed for the stabilization energy of water as the curvature changes. This observation suggests that the effect of curvature practically becomes irrelevant as there is almost no variation in the interaction energies with change in the curvature. Only the MP2 method predicts that as we move from curvature 0^0 to 10^0 the stabilization energy changes by ~ 4 kcal/mol and remains nearly constant thereafter. Figures 2.9 (d) and (e) represent the cases where the confinement corresponds to a distance of 7 Å and 8 Å respectively. These two plots also show a behaviour qualitatively similar to that in the 6 Å case. The stabilization energy is always negative and this has minimal effect from variation of curvature.

To have a better illustration of the combined effect of interplay of confinement and curvature on the water interaction energy, we have presented the trend of variation of the latter as a function of confinement and curvatures in Figures 2.9 (f) and (g). For the sake of clarity, we have presented only the B3LYP results as the results based on other methods have similar qualitative nature. We are able to make some important observations. There seem to be three regimes, viz., 0-15^0, 15-25^0, 25-30^0 of curvatures wherein the water molecule experiences the effect of curvature in a distinct way and there is a noticeable change in the energetics of the water molecule. For the two extreme regimes (lower and higher) of curvature, the stabilization energies of water molecule under highly confined situations, especially below a confinement distance of 6 Å, are found to be highly positive. Strikingly, there is an abrupt decline in stabilization energy for the intermediate curvature regime, i.e. 15-25^0 and this sharp downward jump is as high as 100 kcal/mol. Beyond a confinement distance of 6 Å, the variation of stabilization energy with curvature is marginal and it is also noted that the water molecule is always stabilized for all the curved structures. The important rationale that we derive from this observation is that for smaller and larger curvature cases, confinement indeed can be a factor of paramount importance. A confinement distance of 6 Å is believed to be at the borderline below which the water molecule interaction is energetically highly unfavourable (for the two extreme regimes), with the stabilization energy depending significantly on the curvature and beyond this the water interaction energy remains almost unchanged and curvature has a minimal effect on it. Secondly, for intermediate range of curvatures (15^0-20^0), the effect of confinement becomes insignificant as there is negligible change in the stabilization energy of water as is evident from the above two figures. However, this curvature range significantly induces a stabilization energy favorably inside the nanotube, implying that the water molecule prefers these curvatures for an energetically stable conformation thereby nullifying another important parameter of confinement which governs the energetics of water for rest of the curvature values.

Apart from the interaction energy of the water molecule, other structural and electronic properties like H-O-H bond angle, O-H bond distance and Mulliken charges on O and H atoms (q_{O}, q_{H1} and q_{H2}) of water molecule under confinement can provide important information on the nature of water molecule under nano-confinement. These essential properties have been presented in Table 2.2 (MP2 results) for all values of confinement and curvatures. As we have already mentioned, there are some cases where the water molecule undergoes dissociation (marked as DIS in the table), the H-O-H bond angle, O-H bond distance becomes insignificant and have not been given in the Table. The H-O-H bond angle for the free water molecule is 104.30^0 which almost matches with the experimental value[101] of 104.45, thus validating the present level of theory. One of the most note-worthy observations is that the bond angle for the confined water either shrinks or expands and the value varies between 101-105^0. In cases where the interaction energy is positive, it is observed that the H-O-H bond angle shrinks (101^0 -102^0)

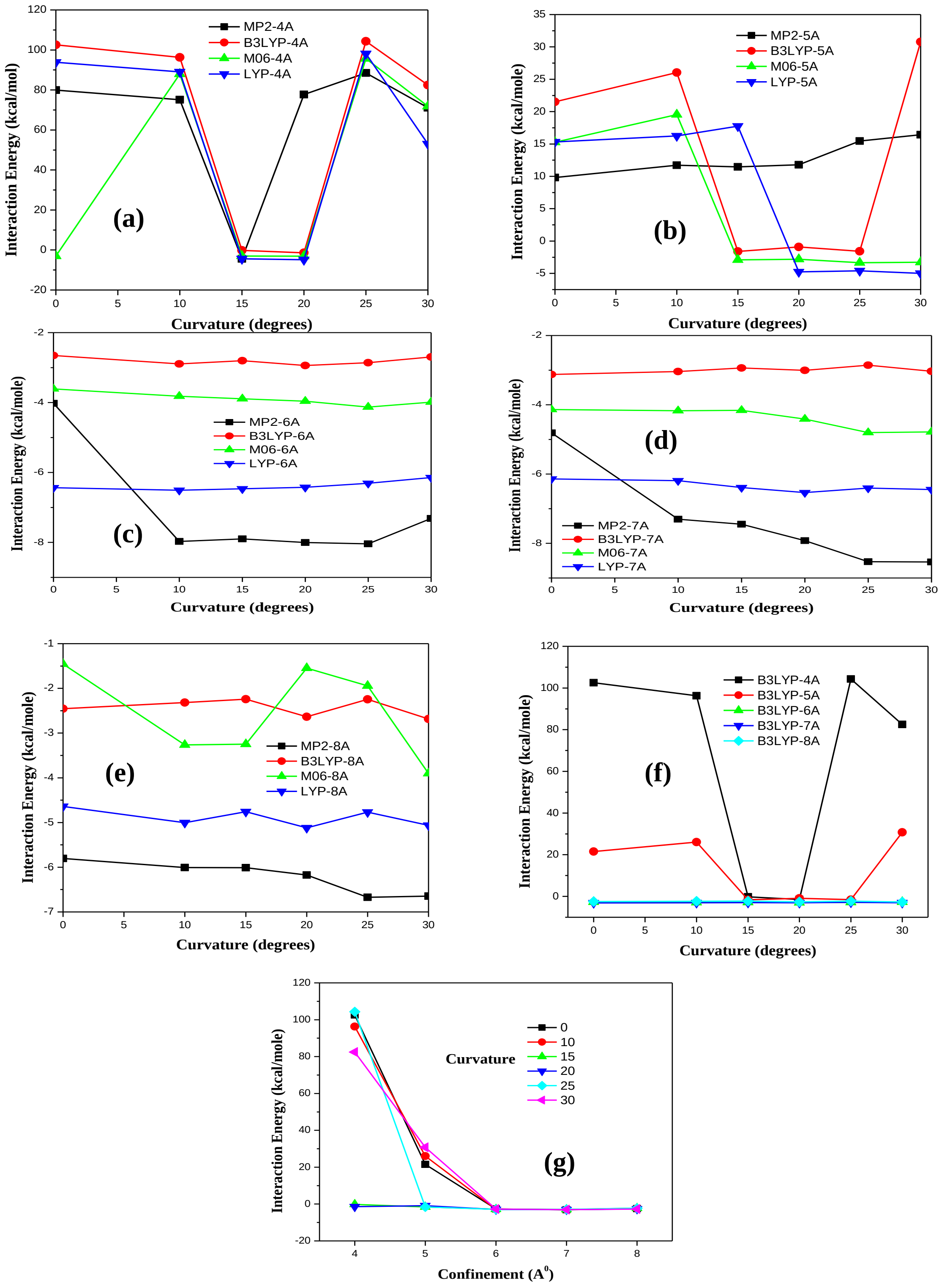

Figure 2.9: (a)-(e) Variation of Interaction energy of water as a function of curvature for W-DB system for different confinement distances 4-8 A^0, **(f)** Interaction energy as a function of curvature for different confinement distances and **(g)** Interaction energy as a function of confinement distances for different curvatures.

as compared to that of the isolated water molecule. In majority of the cases where the stabilization energy of water is favorable (negative), the bond angle marginally changes as compared to the free water molecule. Exception to this general trend is the case of W-DB-00-06 and W-DB-00-07 wherein the bond angle is ~101^0 with the net stabilization of energy being -4.02 and -4.81kcal/mol respectively. This deviation of ~3^0 from the usual bond angle suggests that, in fact, the confinement can have a pertinent role in deciding the structure and bonding of nano-confined water molecules. In our calculations, we have found the O-H bond distance for the free water molecule to be 0.957 Å which is in good agreement with the experimental value[101] of 0.958 Å. On careful observation of the O-H bond length, we find that in almost all cases, the bond distance is increased from its initial value (free water) of 0.957 Å to ~0.960 Å for the encapsulated water molecule. The increment of about 0.014 Å in bond distance, although seems to be quite small, can have pronounced effect on the vibrational spectra of water. For encapsulated water, vibrational spectroscopy[102-107] is a sensitive indicator to probe the confinement effect as well as the strength and orientation of hydrogen bonding. It is well known that lengthening of the bond leads to a decrease in the stretching frequency, and thus it is expected that the O-H stretching frequency in confined water will have a red shift as compared to that of the free water molecule. This red shifting of O-H stretching frequency, in principle, can act as a direct probe for the water under confinement. To quantify the above arguments, we have calculated the vibrational spectra of water for three representative cases, the free water molecule, W-DB-00-06 and W-DB-20-06 model systems. For the latter two cases, the stabilization energy is negative indicating the systems to be energetically stable. Furthermore, the W-DB-00-06 system represents the case of only confinement with H-O-H bond angle and O-H bond distance both appreciably deviating (101.765^0 and 0.961 Å respectively) and the W-DB-20-06 system represents the case of both

Table 2.2: Interaction energy, H-O-H bond angle, O-H bond length and Mulliken charges for water molecule with different curvature and confinement values, W-DB-CV-CF system.

System Name	ΔE (Kcal/mol)	H-O-H (degree)	O-H (Å)	Charge (MULLIKEN) (a.u.)		
				q_O	q_{H1}	q_{H2}
H2O		104.304	0.957, 0.957	-0.496	0.248	0.248
W-DB-00-04	79.93	103.231	0.943, 0.943	-0.315	0.180	0.184
W-DB-00-05	9.81	102.473	0.957, 0.957	-0.364	0.209	0.205
W-DB-00-06	-4.02	101.765	0.961, 0.961	-0.390	0.214	0.215
W-DB-00-07	-4.81	101.951	0.961, 0.961	-0.421	0.223	0.223
W-DB-00-08	-5.80	104.699	0.959, 0.962	-0.466	0.235	0.249
W-DB-10-04	75.10	103.235	0.950, 0.954	-0.352	0.181	0.229
W-DB-10-05	11.72	103.905	0.958, 0.960	-0.367	0.198	0.218
W-DB-10-06	-7.97	104.752	0.962, 0.962	-0.460	0.244	0.243
W-DB-10-07	-7.30	105.427	0.961, 0.961	-0.448	0.241	0.240
W-DB-10-08	-6.00	104.604	0.962, 0.959	-0.454	0.248	0.229
W-DB-15-04	-4.40	104.572	0.962, 0.959	-0.417	0.223	0.225
W-DB-15-05	11.45	102.654	0.962, 0.960	-0.364	0.224	0.198
W-DB-15-06	-7.89	104.587	0.962, 0.962	-0.462	0.241	0.246
W-DB-15-07	-7.44	105.549	0.961, 0.962	-0.438	0.236	0.240
W-DB-15-08	-6.01	104.570	0.959, 0.963	-0.461	0.231	0.259
W-DB-20-04	77.69	101.090	0.972, 0.989	-0.267	0.238	0.268
W-DB-20-05	11.79	102.707	0.962, 0.961	-0.308	0.194	0.190
W-DB-20-06	-8.00	104.567	0.962, 0.962	-0.460	0.242	0.241
W-DB-20-07	-7.92	105.264	0.963, 0.962	-0.444	0.241	0.237

W-DB-20-08	-6.17	104.879	0.959, 0.963	-0.455	0.23	0.263
W-DB-25-04	88.50	DIS	DIS	-0.271	0.247	0.297
W-DB-25-05	15.45	102.175	0.967, 0.961	-0.312	0.218	0.186
W-DB-25-06	-8.04	104.511	0.962, 0.962	-0.452	0.239	0.235
W-DB-25-07	-8.52	104.876	0.963, 0.963	-0.439	0.238	0.243
W-DB-25-08	-6.67	104.669	0.960, 0.964	-0.451	0.232	0.249
W-DB-30-04	71.11	DIS	DIS	-0.123	0.133	0.253
W-DB-30-05	16.43	102.544	0.961, 0.974	-0.321	0.194	0.253
W-DB-30-06	-7.31	104.821	0.961, 0.965	-0.420	0.224	0.224
W-DB-30-07	-8.53	104.813	0.963, 0.964	-0.429	0.241	0.236
W-DB-30-08	-6.64	104.667	0.965, 0.960	-0.451	0.249	0.231

confinement and curvature with only sizeable change of bond length (0.961 Å) with the bond angle 104.567^0 remaining practically unaffected from that of the isolated water molecule case. For the free water molecule, we have obtained three normal modes of vibration as 3811 cm^{-1} (symmetric stretching), 3932 cm^{-1} (asymmetric stretching) and 1539 cm^{-1} (bending) which are in close agreement with the reported experimental values[108] of 3832 cm^{-1}, 3943 cm^{-1} and 1648 cm^{-1} for the three modes respectively. For the W-DB-20-06 system, our calculated vibrational frequencies are 3772 cm^{-1}, 3874 cm^{-1} and 1546 cm^{-1} respectively for the above three modes. In this case, the bond angle hardly changes from that of the free water molecule case which is also reflected in minimal change in the frequency for the bending mode (1546 cm^{-1} against 1539 cm^{-1} for free water). However, the O-H bond length increases for the W-DB-20-06 model system and correspondingly the symmetric stretching and asymmetric stretching frequencies decrease by 39 cm^{-1} and 58 cm^{-1} respectively. On the other hand, for the W-DB-00-06 case, our results are 3799 cm^{-1}, 3888 cm^{-1} and 1567 cm^{-1}, which clearly demonstrate the effect of change in bond angle and bond lengths on the vibrational frequencies of water due to the confinement. Our analysis of vibrational frequencies of O-H stretching mode indicates a red shift of the frequency for the encapsulated water molecule as compared to free water molecule. This observation is in good agreement with the result obtained by Wang et al. [90] for water chains encapsulated in a CNT, thereby justifying the suitability of our model systems.

In a related study, Sathyamurthy and coworkers[109] have demonstrated that confinement induced by C_{60} fullerene cage leads to blue shift of the O-H frequency. It may however, be noted that we also observe blue shift in O-H frequency for model systems where the confinement effect felt by the water molecule is very large and the stabilization energy is positive. To demonstrate this, we have considered three cases namely, W-DB-00-04, W-DB-00-05 and W-DB-10-04 where the net stabilization energy of the water molecule is positive. The calculated symmetric stretching, asymmetric stretching and bending frequencies for the above three cases are as follows: 4007, 4105, 1593; 3848, 3931, 1572; and 3829, 3976, 1539 in cm^{-1} units, respectively. From these values, it is clearly evident that the blue shift in the symmetric and asymmetric frequencies is relatively much larger for the case of highly confined water with a confinement length of 4 Å. For a slight increase in the confinement length from 4 to 5 Å, the observed blue shift is found to be reduced and the symmetric frequency shifts from 4007 to 3848 cm^{-1} which is higher than that of the free water molecule. Upon further increase in the confinement length beyond 6 Å, as we discussed earlier, red-shift in the vibrational frequency is observed. From the above results, it appears that the molecule initially goes through a blue-shift by shortening of the O-H bond length and thereafter further increase in confinement length leads to a red-shift. Comparing the result of Sathyamurthy and coworkers[109] for the real system, the blue shift due to the fullerene molecule whose diameter is ~6 Å, is in good agreement with our results corresponding to the model case, viz. W-DB-00-05. Hence, it is inferred that the blue or red-shift in the vibrational frequencies of encapsulated water is governed by a fine balance between the curvature and confinement effects.

Finally, we now discuss the results on Mulliken charges on the O and H atoms of the encapsulated water molecule and all the values of charges are presented in Table 2.2. As an illustrative case, the plot for the variation of atomic charge on oxygen atom due to the curvature and confinement is presented in Figure 2.10.

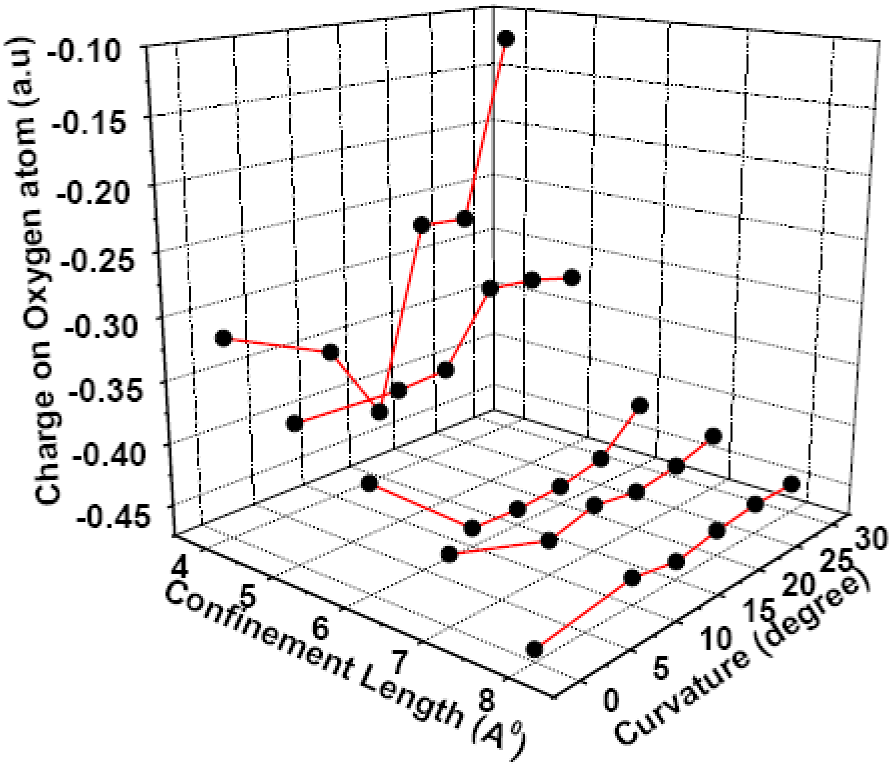

Figure 2.10: Variation of Mulliken charge of oxygen atom of the encapsulated water molecule as a function of curvature with different confinement distances (4-8 Å).

It is clear from Figure 2.10 that for highly confined regions with high curvature (CV and CF are 30^0 and 4 Å, respectively), the charge on the oxygen atom is found to be very less, -0.123 a.u. while for the case of free water molecule it is -0.496 a.u. Such a remarkable change in the charge separation is accompanied by the dissociation of water molecule. We have discussed earlier that for the case of stabilization energy for which the confinement distance of 6 Å seems to be at the borderline. Following the same line of arguments, one can rationalize the charge separation which also varies dramatically below 6 Å and above this border line, although the variation is marginal with respect to curvature. Another striking result is that the magnitude of the charge on oxygen atom is not same as the sum of the charges on hydrogen atoms in water. This result reveals that there is a significant amount of charge transfer from the water molecule to the carbon rings and hence, the encapsulated water molecule exists with a small amount of partial positive charge. Further, it is also evident from Table 2.2 that the charge on both the hydrogen atoms is not necessarily the same (unlike to the case of free water molecule) and the difference between the charge on the two hydrogen atoms becomes prominent for the case of highly confined and curved model systems. Considering the remarkable variation in the geometrical parameters and atomic charges of the confined water molecule, we can conclude that the hydrogen bonding characteristics of water under confinement will also differ to a large extent. Concomitantly, this observation is also in support of the different properties that the nano-confined water may exhibit as compared to free water. The preceding discussions lead us to conclude that nano confinement and also curvature are two crucial parameters which can influence the structure, electronic properties as well as vibrational properties of water.

2.3: Summary of the Work

To summarize the first section of this chapter, we have made an attempt to generalize the nanotubes with different properties, the local curvature present inside a single unit of six-membered carbon ring is identified to be a suitable descriptor for correlating their electronic property and reactivity. Our results reveal that there is a one-to-one correspondence between the variation of electronic properties (ionization potential, electron affinity, polarizability and HOMO-LUMO gap) and reactivity of the nanotubes with the curvature locally present in each hexagonal unit of the nanotube. These results obtained from the model systems demonstrate the effect of the structural deformation within the ring on the electronic properties and reactivity of the nanotube. The nature of the interactions (weak to strong) and properties of different kind can be induced or tuned by merely introducing a curvature inside the carbon materials. It can be concluded that the presence of local curvature accounts for the large difference in the properties and reactivity of the carbon nanotubes or fullerenes and graphite or graphene sheets.

More importantly, we assert that, (i) the properties (electronic as well as reactivity) of the nanomaterials are mostly locally driven due to the curvature inherently present in the nanostructures, (ii) tuning the curvature can, in principle, modulate the properties of these nanomaterials in a desired manner. Unambiguously, the curvature, which is a simple yet staggering concept, is central to the correlation with the properties of the nanostructures. The usefulness of the model systems is worth appreciating from the perspective that "part" (model systems) can lead to predictable estimate of "full" (SWCNTs) which is accomplished by identifying the governing role played by the local curvature. In addition, the results derived from the model structures can have wider ramifications in terms of exploring the diverse properties of the nanotubes and their interactions with other systems in a generalized perspective. Thus, we hope that the present results would provide valuable insights in designing and understanding new materials based on the concept of the different types of curvatures.

In the second part of this chapter, our *ab initio* theoretical studies attempt to explore the behavior of water molecule under confinement. Considering model systems which involve only one/two unit/s of CNT, i.e. curved 6-membered carbon ring, we have investigated the structural, electronic and vibrational properties of water molecule encapsulated in the model system. The interaction of a water molecule with a single model structure (W-SB) with inherent curvature reveals that the stabilization energy of the water molecule increases with increasing curvature. Similarly, for the case of confined system (W-DB), we note that although the water molecule is held in an energetically unfavorable situation, a slight change in curvature can bring about significant change in the interaction energy of water (~100 kcal/mol for 4 Å case) leading to an favorable configuration. For lower (0^0-15^0) and higher (20^0-30^0) curvature values, the interaction energy shows drastic variation with the confinement distance. However, for the curvature values ranging from 15^0 to 20^0, the interaction energy is almost constant over the variation of the confinement distance and the energy is negative suggesting a favorable interaction. Another important outcome of the present study is that the confinement distance of 6 Å seems to mark a borderline below which the curvature has a pronounced effect on the stabilization energy of water. Beyond the confinement distance of 6 Å, curvature plays a lesser significant role and for these cases, the behavior of water is similar to that of free water (gas phase). It is therefore inferred that water molecule can be favorably encapsulated between two moderately curved surfaces of curvature 15^0-20^0. The dissociation of water is also observed for higher values of curvature and lower values of confinement distance which is worth mentioning. In addition, we have demonstrated that the two parameters, curvature and confinement, play a key role in governing the significant variations in the structural parameters, Mulliken charges and vibrational frequencies of the encapsulated water molecule. Encapsulation leads to slight elongation or shortening of the O-H bond length which in turn is reflected in the red or blue shift in the O-H stretching mode depending on the two important parameters, i.e. the amount of curvature and confinement length. This kind of observation is in corroboration with some of the earlier results for water inside CNT or fullerene systems.[90,109] Hence, we conclude that the conjunction of the two important factors namely the confinement distance and the curvature of the model system, seem to manifest very interesting trend on the nature of confined water molecule. The interplay between these two parameters in deciding the electronic properties of water in the nanoscale confinement is of paramount importance.

CHAPTER 3

Electronic Properties, Reactivity and Possible Applications of Fullerenes

Chapter 3: Electronic Properties, Reactivity and Possible Applications of Fullerenes

In the introductory chapter 1, we have briefly mentioned about the important contributions of fullerenes to modern nanoscience and technology. In furtherance of the exhaustive literature results related to the study of several aspects of structure and reactivity of fullerenes which has established the subject in its full bloom, we try to capitalize on two differently unique aspects of fullerenes as the theme of this chapter. Firstly, based on the extended electronic delocalization of fullerenes, these were mooted as potential candidates for applications involving nonlinear optical (NLO) properties. To this end, the experimental characterizations of N-doped fullerene, where one or more C-atoms in the C_{60} fullerene molecule was replaced with N atoms added new paradigms as these structures exhibited enhanced NLO. With this initial motivation, in the first part of this chapter, we have discussed the structure and electronic properties of N-doped fullerenes. We have carried out systematic investigations on the structures of several possible N-doped fullerenes. We have identified some important factors that decide the stability of these fullerenes. The second part of this chapter deals with one specific application of pristine fullerenes. In this section, we have considered the functionalization of C_{60} fullerene which is a powerful strategy based on which the fullerene chemistry has expanded in recent years as means to explore the binding of uranyl ion, a key species in the radioactive nuclear wastes. Such an investigation will help us design strategies for effective nuclear waste management.

3.1: Introduction to Azafullerenes

The serendipitous discovery of C_{60} fullerene by Kroto et al. [2] has resulted in the emergence of fascinatingly new and large swathe of research activities in the field of carbon fullerenes. Apart from C_{60} there are many fullerenes with closed cage structures consisting of twelve pentagons and variable number of hexagons depending on the number of carbon atoms which is equal to (n-20)/2 in fullerene C_n. The isolated pentagon rule is one of the rules in carbon nanomaterials proposed by Kroto[110] which states that the neighboring pentagons in a carbon nanostructure are energetically unstable. C_{20} is the smallest fullerene with twelve pentagons and zero hexagons whereas C_{60} is the smallest fullerene to follow the isolated pentagon rule with twelve pentagons and twenty hexagons. In recent past, a considerable amount of work has been carried out to understand the structural, electronic and optical properties of fullerenes. [111] One obvious strategy to modulate the electronic properties of C_{60} fullerene involves doping with hetero atoms. The cage structure of fullerene entails three types of doping, namely endohedral, exohedral and substitutional doping. [111-116] There are many reports on the synthesis of heterofullerenes by replacing few carbon atoms of C_{60} with boron and nitrogen atoms. Nitrogen-doped carbon nonmaterials are of special importance as they exhibit variable electronic properties, which enable them to act as potential candidates for various device applications such as metal free catalyst[117-119], hydrogen storage[120-122], materials with tunable optical properties (TOPs) [115,116] etc.

First indications of fullerene like structures with the composition C_{60-2n} N_{2n} came from Glenis et al. [123] In 1995, reports of N-doped fullerene by Hummelen et al. [113] in the dimeric form, has sparked off immense interest amongst the researchers. Subsequent experimental works have resulted in the isolation of several nitrogen-doped heterofullerenes. [124-130] On a parallel track, there has also been several theoretical investigations on the structural and stability aspects of heterofullerene $C_{60-n}X_n$ (X = N and B, n= 1-2) as well as their electronic properties. [131,132] Later on, employing semiempiricial methods like MNDO, AM1, PM3 and the Hartee-Fock method

Chen et al. [133-135] investigated several other heterofullerenes corresponding to n= 2, 4 , 6 , 8 and also extension to $C_{57}X_3$ and $C_{56}X_4$. The possible structures of $C_{48}N_{12}$ were investigated by Stafstörm[136] using density functional theory (DFT) calculations and it was inferred that the most stable structure is the one where the nitrogen substitutes the carbon atoms in the para-positions of six-membered rings in C_{60} fullerene leading to a S_6 symmetry. In contrast to this structure, Manaa et al.[137] reported another $C_{48}N_{12}$ structure with S_6 symmetry that is energetically more stable by 13.1 kcal/mol than the previously reported one and the extra stability is attributed to the extended local aromaticity in that particular structure with eight all-carbon hexagonal rings. Xie et al.[138] have carried out a comparative study of the structural, electronic, vibrational and magnetic properties of $C_{48}N_{12}$ and C_{60} and demonstrated that $C_{48}N_{12}$ has second order hyperpolarizability which is about 55 % larger than that of the C_{60}. This result was indicative of the fact that azafullerenes can have higher and better NLO properties and may thus find potential applications in photonic devices and in molecular electronics. DFT studies of Hou et al.[139] has shed light on the chemical stability of oxygenated and hydrogenated $C_{48}N_{12}$ and $C_{58}N_{12}$. The possibility of using $C_{48}N_{12}$ and $C_{48}B_{12}$ as a donor-acceptor pair for molecular electronics applications has been shown by Manaa.[140] Ewels et al.[141] have shown that the presence of nitrogen stabilizes the fullerenes with neighboring pentagons to overcome the conventional isolated pentagon rule. Majority of the studies addressing the structure and stability of azafullerenes, takes into account only even number of N atoms. In a very recent *ab initio* investigation, Sharma et al.[142] have carried out a systematic study of the structural, electronic and vibrational properties of nitrogen-doped fullerenes $C_{60-n}N_n$ for n =1-12. To the best of our knowledge, any investigation pertaining to nitrogen-doped fullerenes where the number of N atoms is larger than 12 has not been attempted thus far. In this context, one of the earliest mass spectrum result by Glenis et al.[123] clearly demonstrates the existence of several azafullerenes with high N-content, like $C_{44}N_{16}$, $C_{40}N_{20}$, $C_{38}N_{22}$, $C_{34}N_{26}$, $C_{30}N_{30}$, $C_{26}N_{34}$, $C_{44}N_{16}$, $C_{20}N_{40}$ and $C_{14}N_{46}$ amongst others, all belonging to the series $C_{60-2n}N_{2n}$. Hence, exploration of the structural and electronic properties of azafullerenes having higher number of N atoms is of fundamental importance.

In the present study, we have employed DFT methods to systematically investigate the structural, electronic and vibrational properties of a series of even numbered nitrogen-doped fullerenes $C_{60-2n}N_{2n}$ for $n = 1\text{-}12$. Furthermore, banking upon the literature reports that azafullerenes are of immense importance from the perspective of NLO properties, we have also computed the polarizabilities and hyperpolarizabilities of these azafullerenes and compared them with that of bare C_{60}. One important consideration in studying the structural and electronic properties of azafullerenes is that as the number of N atoms increase, the possible numbers of low lying isomers also increase. Based on our chemical intuition and reasoning, we have started with several possible isomers for a given azafullerene and considered only the most stable one for detailed investigations. The stability of all the azafullerenes can be judged from our vibrational frequency calculations with higher minimum frequency.

3.1.1: Electronic Structure, Stability and Non-Linear Optical Properties of Nitrogen Doped Fullerenes $C_{60-2n}N_{2n}(n=1\text{-}12)$

We have optimized the geometry of C_{60} as a reference system and the minimum energy structure is found to have Icosahedral symmetry with two different sets of C-C bond lengths of 1.398 Å and 1.460 Å which are in good agreement with the earlier reported results.[138,142] As Glenis et al.[123] had shown that with the exception of $C_{59}N$, only even-numbered ratios of C to N atoms are present in their mass spectra, we have considered here only the even numbered nitrogen substituted species here. The minimum energy isomers of all the considered systems are given in Figures 3.1 (a) to (l) and all the different isomers with energy difference are given in Figures 3.2 (a) to (l). In the case of $C_{58}N_2$, we considered three different isomers as shown in Figure 3.2 (a). Out of these three isomers, one with two nitrogen atoms placed in para position to each other in a hexagon as shown in Figure 3.1 (a), is found to be the lowest energy isomer which is in agreement with the earlier reported results.[142] The isomer having nitrogen atoms in meta position to each other (-N-C-N- fragment) is the next lower energy one and is found to be 22.6 kcal/mol higher in energy as compared to the minimum energy isomer. The other isomer with the nitrogen atoms placed at maximum possible distance with S_2 symmetry is found to be 30.1 kcal/mol higher in energy as compared to the minimum energy isomer. The energy of the isomer with nitrogen atoms at meta position to each other can be expected to be higher as compared to the one having para positioned nitrogens because of the repulsions between the lone pairs on both the nitrogen atoms. Though the nitrogen-nitrogen distance is maximum (6.811 Å) in the other isomer, the energy is found to be higher. It can be explained based on the concept of extended local aromaticity of all-carbon hexagonal rings as given by Manaa et al.[137] In the lowest energy isomer, there are seventeen all-carbon hexagonal rings (ACHR) whereas in the isomer with maximum N-N distance, sixteen such rings are possible.

In the case of $C_{56}N_4$ also, we considered three different isomers as shown in Figure 3.2 (b). The isomer shown in Figure 3.1 (b) with fifteen ACHR is found to be the lowest energy one which is also in agreement with the minimum energy isomer of Sharma et al.[142] All the four nitrogen atoms are placed in a single corannulene part of C_{60} and connected to the C_5 ring so that the nitrogen atoms are separated by at least two carbons. The other two isomers with fourteen and twelve ACHR are found to be higher in energy by 15.4 kcal/mol and 60.5 kcal/mol respectively as compared to the minimum energy isomer. In all three isomers considered, nitrogen atoms are separated by at least two carbon atoms. The minimum energy isomer of $C_{54}N_6$ is found to have thirteen ACHR as shown in Figure 3.1 (c), which is lower in energy by 5.8 kcal/mol as compared to the other isomer with 12 ACHR and one –N-C-N- fragment, reported to be the minimum energy isomer by Sharma et al. [142] Five of the six nitrogens are arranged within a corannulene ring and the remaining nitrogen is separated from the corannulene nitrogen by at least two carbons. The third isomer considered with eight ACHR is found to be 29.8 kcal/mol higher in energy as compared to the minimum energy isomer. In the case of $C_{52}N_8$ as well, the minimum energy isomer we obtained, with eleven ACHR as shown in Figure 3.1 (d), is found to be lower in energy as compared to the earlier reported one[142] with six ACHR by 9.7 kcal/mol. In the minimum energy isomer, five of the eight nitrogens are within a corannulene moiety and the other three nitrogens are arranged in another corannulene opposite to the corannulene containing five nitrogens. The other isomer considered with five ACHR is found to be 15.2 kcal/mol higher in energy as compared to the minimum energy isomer and none of the three isomers considered is found to consist of the –N-C-N- fragment.

The minimum energy isomer of $C_{50}N_{10}$ is shown in Figure 3.1 (e) and is found to be highly symmetric with D_{5d} symmetry with ten ACHR which is just 1.3 kcal/mol lower in energy as compared to the one reported earlier[142] with three ACHR. Five of the ten nitrogen atoms are placed in a corannulene unit and the remaining are in other corannulene unit opposite to the first corannulene unit. The third isomer considered is 8.8 kcal/mol higher in energy as compared to the minimum energy structure. The next member of this series is $C_{48}N_{12}$ which is well studied and the minimum energy structure is found to have S_6 symmetry with eight ACHR which is consistent with the earlier studies by Manaa et al. [137] and is shown in Figure 3.1 (f). Though there are six –N-C-N- fragments, this structure is found to be more stable by 24.6 kcal/mol as compared to the other geometry with two ACHR and no –N-C-N- fragments. This shows that the aromatic stabilization due to the eight ACHR is more prominent in comparison to the destabilization due to the nitrogen-nitrogen repulsion coming from the –N-C-N- fragments.

For the next member of this series, viz. $C_{46}N_{14}$, we have considered three different isomers and found that the structure with four ACHR and ten –N-C-N- fragments is found to be the minimum energy structure as shown in Figure 3.1 (g). Interestingly, in this case, it is found that isomers with five and six ACHR are found to be higher in energy. The isomer with five ACHR and eight –N-C-N- fragments is found to be 8.7 kcal/mol higher in energy as compared to the minimum energy isomer. The next higher energy isomer is found to have six ACHR and twelve –N-C-N- fragments and is 35.7 kcal/mol higher in energy. In the case of minimum energy isomer, though there are only four ACHR, it has four more six membered rings which are substituted by only one nitrogen (C_5N rings) which might be stabilizing factor as compared to the next higher energy structures where all the substituted hexagons are having at least two nitrogens (C_4N_2 rings). In the case of the third isomer with six ACHR, destabilization due to the –N-C-N- fragments is found to be predominant over the stabilization by ACHR. This shows that at higher concentration of nitrogen, nitrogen-nitrogen repulsion is dominating over the aromatic stabilization by C_6 ring which is opposite to the case at lower concentration of nitrogen ($C_{48}N_{12}$). Similarly, in the case of $C_{44}N_{16}$, we have optimized different possible isomers and the lowest energy isomer is found to be the one with four ACHR and fourteen –N-C-N- fragments as shown in Figure 3.1 (h). The next higher energy isomer is with two ACHR and ten –N-C-N- fragments. We have also optimized other possible isomers with four ACHR and sixteen or eighteen –N-C-N-fragments (shown in Figure 3.2) and the energy difference is found to be very high due to the increased nitrogen-nitrogen repulsions.

The minimum energy isomer of all three isomers of $C_{42}N_{18}$ considered here is found to have three ACHR in such a way that there is no C_6 ring adjacent to another C_6 ring and the optimized structure is shown in Figure 3.1 (i). We have also considered another structure with same number of ACHR but all three connected to each other, and found it to be 35.5 kcal/mol higher in energy. This shows that the isomers with more evenly substituted nitrogen are more stable. The next isomer considered is with two ACHR and is found to be 91.3 kcal/mol higher in energy as compared to the minimum energy isomer. In the case of $C_{40}N_{20}$ also, we have considered three different isomers and the isomer with two ACHR is found to be the lowest energy isomer as shown in Figure 3.1 (j). The next higher energy isomer is found to be 19.5 kcal/mol higher in energy and has no ACHR. The third isomer is with two ACHR bur higher in energy by 40.6 kcal/mol. For $C_{38}N_{22}$, we have considered two possible isomers as shown in Figure 3.2 (k) and the minimum energy isomer, shown in Figure 3.1 (k), is found to have one ACHR. The second isomer considered is 65.3 kcal/mol higher in energy and with no ACHR. In the case of $C_{36}N_{24}$, there is only one possible isomer without any N-N bonds and the structure is found to be highly symmetric with T_h symmetry group as shown in Figure 3.1 (l).

From all the above results on structural aspects, it is clear that the presence of undisturbed C_6 rings (ACHR) will improve the stability due to the aromatic nature of the C_6 rings whereas the presence of -N-C-N- fragments will destabilize the structure because of the N-N repulsion. Out of these two mutually opposite factors, the stabilization due to C_6 ring is found to be predominant at lower concentration of doping and as the doping level increases, the destabilizing effect due to N-N repulsion becomes more important.

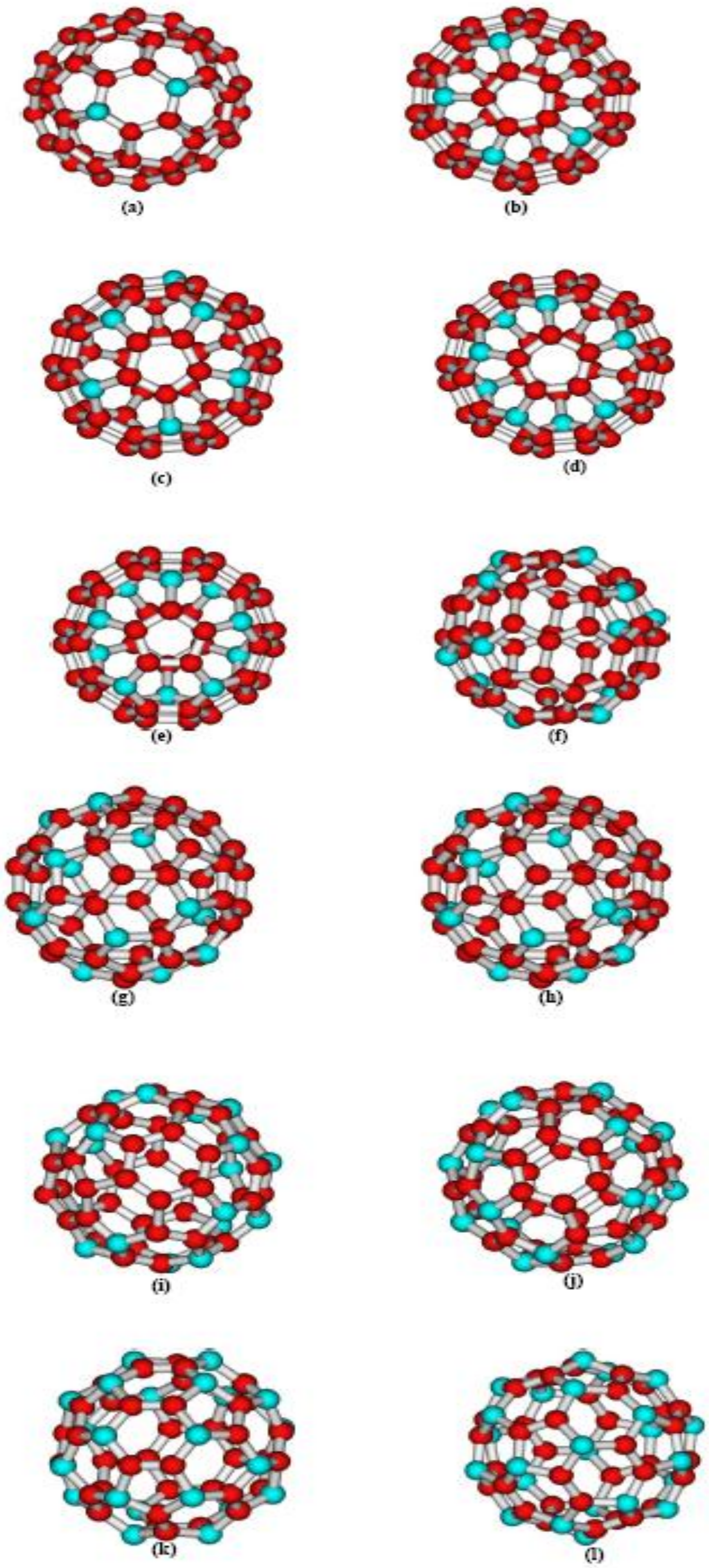

Figure 3.1: Lowest energy structure of azafullerenes (a) $C_{58}N_2$, (b) $C_{56}N_4$, (c) $C_{54}N_6$, (d) $C_{52}N_8$, (e) $C_{50}N_{10}$, (f) $C_{48}N_{12}$, (g) $C_{46}N_{14}$, (h) $C_{44}N_{16}$, (i) $C_{42}N_{18}$, (j) $C_{40}N_{20}$, (k) $C_{38}N_{22}$ and (l) $C_{36}N_{24}$.

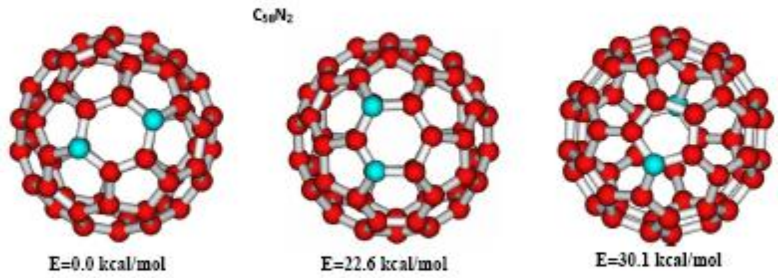
$C_{58}N_2$
E=0.0 kcal/mol
E=22.6 kcal/mol
E=30.1 kcal/mol

(a)

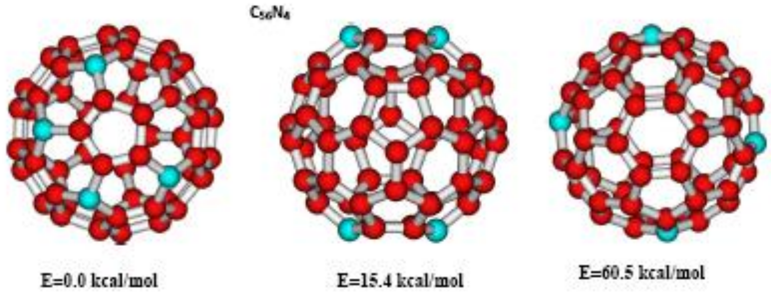
$C_{56}N_4$
E=0.0 kcal/mol
E=15.4 kcal/mol
E=60.5 kcal/mol

(b)

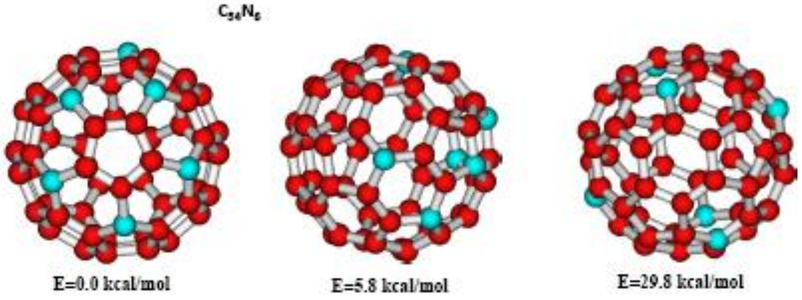
$C_{54}N_6$
E=0.0 kcal/mol
E=5.8 kcal/mol
E=29.8 kcal/mol

(c)

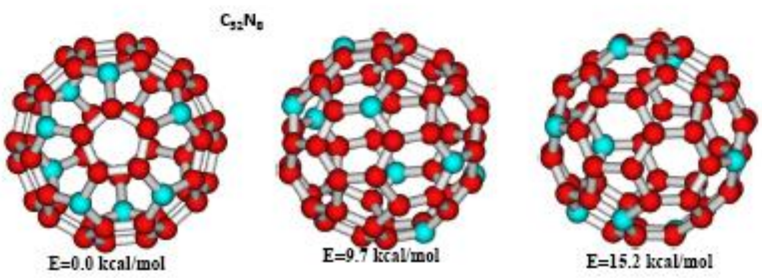
$C_{52}N_8$
E=0.0 kcal/mol
E=9.7 kcal/mol
E=15.2 kcal/mol

(d)

$C_{50}N_{10}$

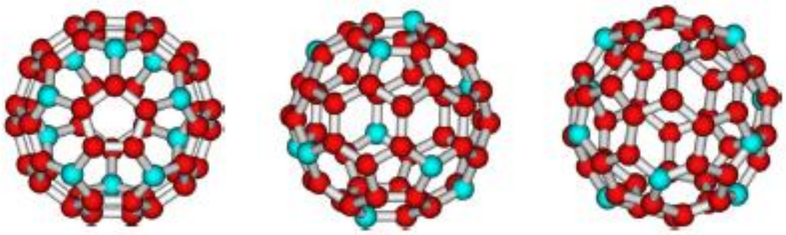

E=0.0 kcal/mol E=1.3 kcal/mol E=8.8 kcal/mol

(e)

$C_{48}N_{12}$

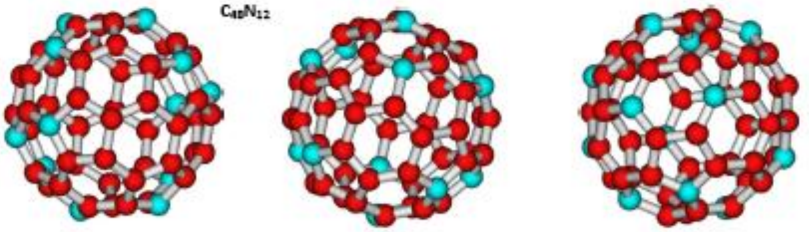

E=0.0 kcal/mol E=24.6 kcal/mol E=56.5 kcal/mol

(f)

$C_{46}N_{14}$

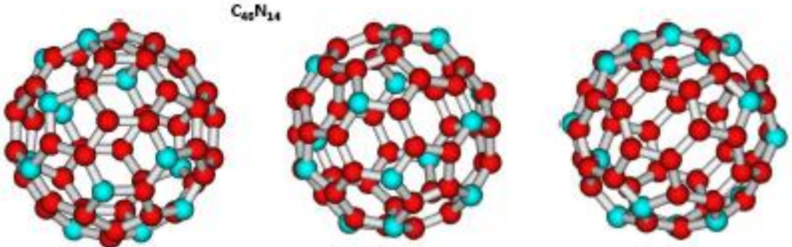

E=0.0 kcal/mol E=8.8 kcal/mol E=27.0 kcal/mol

(g)

$C_{44}N_{16}$

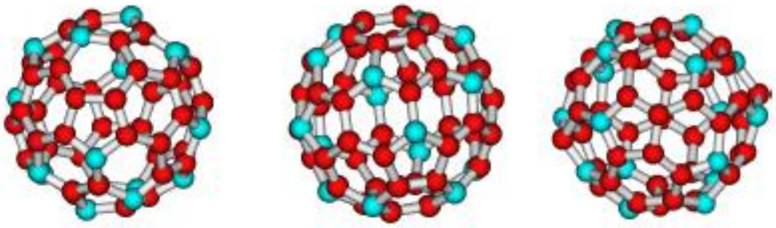

E=0.0 kcal/mol E=49.4 kcal/mol E=69.5 kcal/mol

(h)

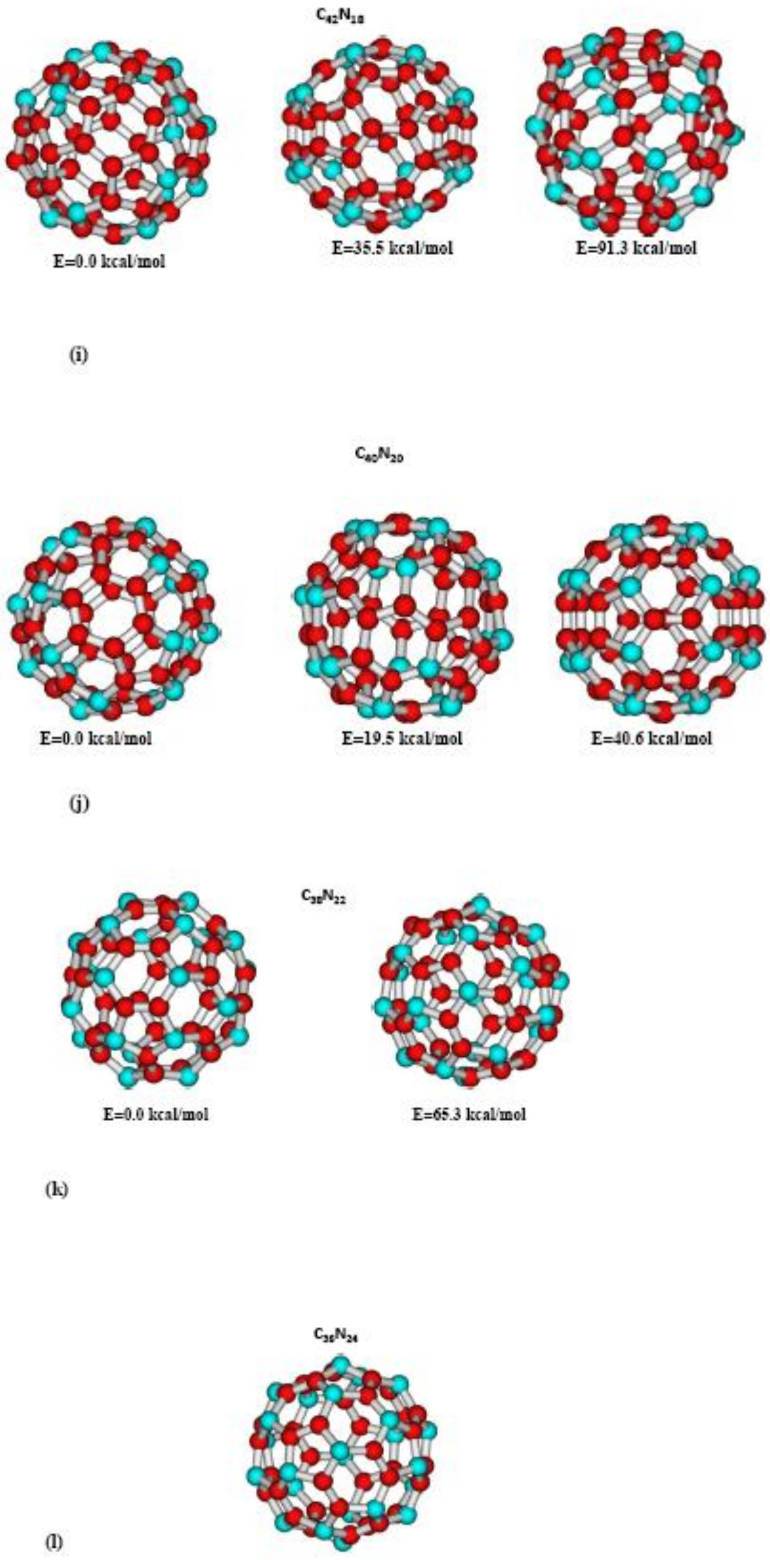

Figure 3.2: Possible isomers of azafullerenes (a) $C_{58}N_2$, (b) $C_{56}N_4$, (c) $C_{54}N_6$, (d) $C_{52}N_8$, (e) $C_{50}N_{10}$, (f) $C_{48}N_{12}$, (g) $C_{46}N_{14}$, (h) $C_{44}N_{16}$, (i) $C_{42}N_{18}$, (j) $C_{40}N_{20}$, (k) $C_{38}N_{22}$ and (l) $C_{36}N_{24}$.

Table 3.1. Average atomization energy per atom, HOMO-LUMO gap, minimum IR frequency, vertical ionization potential (IP), vertical electron affinity (EA) and NICS (0) values calculated for azafullerenes $C_{60-2n}N_{2n}$.

System	Average Atomization energy (eV)	HOMO-LUMO gap (eV)	Minimum IR frequency	IP	EA	NICS(0)
C_{60}	-8.667	2.87	270.12	7.390	2.057	-1.03
$C_{58}N_2$	-8.58	1.64	264.48	6.334	2.165	-1.93
$C_{56}N_4$	-8.51	1.64	261.87	6.460	2.317	-10.02
$C_{54}N_6$	-8.42	1.62	261.46	6.305	1.946	-29.46
$C_{52}N_8$	-8.34	1.59	255.42	5.870	2.243	-18.95
$C_{50}N_{10}$	-8.26	1.49	244.80	5.993	1.965	-0.94
$C_{48}N_{12}$	-8.18	2.72	253.59	6.295	1.022	-3.30
$C_{46}N_{14}$	-8.06	1.53	222.33	6.045	1.064	-3.62
$C_{44}N_{16}$	-7.95	1.02	188.64	7.842	0.185	-0.71
$C_{42}N_{18}$	-7.83	1.45	248.79	7.632	0.721	+0.67
$C_{40}N_{20}$	-7.74	2.63	246.09	7.909	0.513	-5.52
$C_{38}N_{22}$	-7.63	2.45	248.71	6.050	0.964	-4.90
$C_{36}N_{24}$	-7.51	3.06	248.79	5.969	1.201	-2.53

Table 3.2: Calculated values of dipole moment (μ), polarizability (α), first hyperpolarizability (β) and second hyperpolarizability (γ) of the azafullerene systems $C_{60-2n}N_{2n}$.

System	μ	α (Å**3)	β (10^{-30} esu)	γ (10^{-36} esu)
C_{60}	0.0	78.547	.00009	27.305
$C_{58}N_2$	1.75	79.044	5.81	35.670
$C_{56}N_4$	3.54	78.794	9.89	41.742
$C_{54}N_6$	5.73	81.121	16.54	42.172
$C_{52}N_8$	8.18	82.175	34.87	84.080
$C_{50}N_{10}$	0.51	83.95	2.38	47.600
$C_{48}N_{12}$	0.0	76.84	.002	35.607
$C_{46}N_{14}$	2.81	76.09	2.90	28.613
$C_{44}N_{16}$	0.0	74.99	0.002	34.537
$C_{42}N_{18}$	2.86	74.02	3.76	32.342
$C_{40}N_{20}$	0.0	73.41	.0009	30.955
$C_{38}N_{22}$	10.25	75.61	27.46	125.145
$C_{36}N_{24}$	0.0	71.924	0.006	18.920

To verify the stability of these azafullerenes, we have calculated the Hessian for all the minimum energy isomers considered. As it is known from the literature, to designate any complex as stable one, it should not only have all real vibrational frequencies but the minimum vibrational frequency should be considerably large.[143] From the results shown in Table 3.1, one can see that all of the azafullerenes considered here are having considerably higher minimum vibrational frequencies. This shows that the studied structures are the stable ones and correspond to one of the local minima on the potential energy surface. We have also calculated the vertical ionization potentials and electron affinities for all the minimum energy isomers and reported the results in Table 3.1. The large ionization energy and lower electron affinities also signifies the stability of these structures. We have also calculated the HOMO-LUMO gap and the presence of large gaps in all these structures indicate the stability. To verify the aromatic nature of these fullerenes similar to C_{60}, we have calculated the NICS parameter and found that all of them are having negative NICS values as shown in Table 3.1. This negative NICS values demonstrate the aromatic nature of the studied azafullerenes.

As the azafullerenes and nitrogen doped carbon nanotubes are well known for their non linear optical properties,[144,145] we have also calculated the dipole moment, static polarizability (α), first order hyper polarizability (second harmonic generation, β) and second order hyper polarizability (third harmonic generation, γ) of all the minimum energy isomers and the corresponding results are reported in Table 3.2. The permanent dipole moments of all the highly symmetric structures like C_{60}, $C_{50}N_{10}$, $C_{48}N_{12}$, $C_{36}N_{24}$ etc. are found to be nearly zero. The static polarizability calculated for C_{60} is found to be 78.55 $Å^3$ which is in good agreement with the experimental value.[146] Since the β is the coefficient of the square term in the expansion, its value should be zero for centro-symmetric systems. The calculated first hyperpolarizability values for systems with inversion symmetry viz. C_{60} (Ih), $C_{48}N_{12}$ (S_6), $C_{44}N_{16}$ (D_{2h}) $C_{40}N_{20}$ (C_{2h}) and C36N24 (T_h) are also found to be nearly zero as compared to the other systems without inversion symmetry. The calculated γ value is found to be 27.3 x 10^{-36} esu which is also in good agreement with some of the earlier reported values. [147,148] Out of all the structures studied, $C_{50}N_{10}$ is found to have the highest polarizability of 83.95 $Å^3$ and $C_{38}N_{22}$ is found to have the largest γ value of 125.1 x 10^{-36} esu. On observing the variation of α and γ, one can see that though there is no systematic variation with doping concentration, there is a lot of variations in both the polarizability and second order hyperpolarizability. These results show that it is possible to tune the optical properties of carbon fullerenes by varying the concentration of the hetero atom substitution which can have good applications in designing new photonic devices.

3.2: Widening the Scope of Applications of Fullerenes: Implications in Nuclear Waste Management

To cater to the need of the ever increasing demand for energy, nuclear energy is emerging as an indispensible source of alternate energy. Uranium, Neptunium and Plutonium are commonly encountered elements in the nuclear fuel cycle. The generation of nuclear power, however, comes with the penalty in the form of challenges associated with the disposal of radioactive nuclear wastes from the spent fuel. The radiation and toxicity generated from such nuclear waste contaminate the aquatic and geological systems which are of primary concern.

However, there exist alternate ways of converting the toxic highly soluble U^{VI} species to insoluble U^{IV} species by means of electron transfer mechanisms. In fact, cytochrome c_7 type bacteria present in *D. Acetoxitans*, [149] iron-sulfur containing mineral surfaces (hematite) [150] and humic acids[151] derived from natural organic matter does convert U^{VI} to U^{IV} in an efficient manner via electron transfer processes.

Fullerene chemistry grew very rapidly during the last two decades due to the remarkable redox and energy storage properties associated with it. [111,152,153] Furthermore, fullerene derivatives can be used as biologically active compounds in medicinal chemistry. Due to the poor solubility of C_{60}, its application involving aqueous phase chemical processes has been hindered. Major efforts have, however, been invested to improve the solubility of C_{60} fullerene in aqueous phase. To this end, chemical functionalization bearing hydrophilic functional groups, [154] encapsulation of C_{60} within γ-cyclodextrin[155] and incorporation of C_{60} in micelles[156] have improved the solubility in aqueous environment.

On the theoretical side, there has been a large increase in the number of computational investigations of actinide complexes, particularly those of uranium.[157-166] The electronic structure and molecular geometry of the di-oxo cation of the three elements U, Np, and Pu have been studied at the Hartree Fock (HF),[161] density functional theory (DFT)[158,159,162,164] as well as correlated *ab initio* levels.[157,163] In addition to the requirement of using high level of theory and basis sets, modelling actinide ions is also quite challenging because of the need to account for solvation and relativisitic effects at some level. Fortunately, the DFT approach, with incorporation of relativistic effect via small core pseudo-potentials in conjunction with continuum solvation model seems to be sufficient and cost-effective. As far as the accuracy of the results is concerned, calculations at this level are at least semi-quantitative.[164]

To this end, theoretical studies have also modelled these cations, especially uranyl, using various methods for the inclusion of aqueous solvation effects including variants of continuum models as well as by explicitly including the solvent molecules. The most studied structures are those which arise when the uranyl ion is hydrated, with the penta-aqua form being generally preferred to be the dominant species. [160] The effect of bulk solvent is usually included *via* a continuum model, but there is an increasing interest in considering the actual nature of interaction with the nearest solvent molecules. [164,165] Vazquez et al. [166] modeled the uranyl acetate, carbonate and malonate complexes of uranyl in solution using DFT. We have recently investigated the interaction of uranyl with functionalized carbon nanotubes and found that the binding of uranyl is strong in the functionalized case than the unfunctionalized counterpart. [167]

Hence, there is need for further calculations in order to understand in more details the binding behavior of uranyl with nanostructures, which might help us in designing new nanomaterials that can be efficiently used for nuclear waste management. In this work, we investigate the structures, vibrational frequencies and binding affinities of uranyl to malonate functionalized C_{60} in 1:1 and 1:2 ratio of functionalized C_{60} (malonate:uranyl) through DFT based calculations.

3.2.1: Interaction of Uranyl with Bare and Functionalized Fullerenes

We will discuss the interactions of uranyl cation with bare as well as functionalized fullerenes separately in the following sections.

3.2.1.1: Binding of Uranyl with Bare C_{60}

We first present our results on binding of uranyl to bare C_{60} prior to considering functionalization. In Figure 3.3, we have shown the five different binding sites of uranyl to C_{60}. The first two binding sites are at the hexagonal carbon rings, where the uranyl can bind in two different orientations which is either parallel ($\mu^{2-\parallel}$) or perpendicular ($\mu^{2-\perp}$) with respect to the C-C bond at the junction of two hexagons of C_{60} (Figure 3.3). Similarly, we have made attempts to optimize the structures of the uranyl bound at the pentagonal carbon in both $\mu^{2\text{-}\perp}$ and $\mu^{2\text{-}\parallel}$ modes with respect to the junction of the hexagon-pentagon bond of C_{60}. However, the minimum energy structures are obtained only for the $\mu^{2\text{-}\perp}$ binding site, which will be discussed hereafter. In the fourth binding site, the uranyl ion can bind symmetrically to the pentagonal ring (μ^5) of the carbon atoms. Finally, we have also confined the uranyl inside the C_{60} cage.

For both hexagon and pentagon $\mu\text{-}^{2\perp}$ binding, the calculated U=O bond lengths (~1.766 Å) and O=U=O (~174.0^0) bond angle are very similar. However, for the uranyl binding at the hexagon $\mu\text{-}^{2\parallel}$ binding mode, a strong bending of O=U=O (162.8^o) is noted which is rather surprising. Within the three $\mu\text{-}^2$ coordination, the U-C bond lengths are somewhat shorter (by 0.06 Å) when uranyl binds at the pentagonal ring system (pentagon $\mu\text{-}^{2\perp}$) as compared to the hexagons. Further, the two U-C bond lengths are symmetric for the $\mu\text{-}^{2\perp}$ binding mode at both hexagons and pentagon ring systems.

For the μ^5-binding, the uranyl bond lengths and bond angles are slightly elongated (~0.002 Å) and more bent (by 4^o) as compared to the three μ^2-binding sites. The distances between U and C (of C_{60}) for all the above four binding modes (excluding the encapsulation mode) have also been presented in Figure 3.3. Between $\mu\text{-}^2$ and $\mu\text{-}^5$, the U-C bond strength for the latter species is weaker as indicative from their bond lengths. Attempts were even made to optimize the structure of the uranyl at the hexagonal ring system with $\mu\text{-}^6$ binding. Unfortunately, we were unable to get the minimum energy species, due to the spontaneous formation of $\mu\text{-}^2$ coordination mode with the hexagons. Finally for the uranyl encapsulated species, the linear uranyl is much more elongated (1.798 Å) and very strongly bent (81.1^o) as compared to the other three binding sites.

All the four structures are characterized as minima and we find that the calculated vibrational spectra (symmetric (ν_{sym}) as well as asymmetric (ν_{asym})) are slightly red shifted as compared to the penta-aqua-uranyl complex (Table 3.3). For instance, the calculated ν_{sym} and ν_{asym} of μ^5 is about 20-25 cm^{-1} lower in energy as compared to the penta-aquo uranyl complex. For the encapsulated uranyl adduct, this stretching is further reduced (854 cm^{-1} and 923 cm^{-1}) due to U=O bond elongation. For the μ^2 binding motifs, the calculated vibrational spectra are only slightly downshifted as compared to the penta-aquo uranyl complex.

Binding energies are calculated using the following equation,

$$[UO_2]^{2+} + C_{60} \rightarrow \quad [UO_2\text{-}C_{60}]^{2+} .$$

Between the four species, pentagon-$\mu^{2-\perp}$ binding is the most stable species and the binding energy (COSMO-B3LYP) is found to be -6.27 kcal mol^{-1}. Hexagon-μ^{2}-$^{\parallel}$ is the least stable amongst the four binding patterns considered and the binding energy is estimated to be + 4.93 kcal mol^{-1}. It is also noted that hexagon-μ^{2}-$^{\parallel}$ is less stable by 12.28 kcal mol^{-1} in comparison to the most preferred structure (pentagon-$\mu^{2-\perp}$). For the encapsulated adduct, the binding energy is found to be 100.45 kcal mol^{-1} and the species is less stable by 66.45 kcal mol^{-1} from the pentagon-$\mu^{2-\perp}$ structure. Further, the calculated binding is marginally favorable for hexagon-μ^{2}-$^{\perp}$ (-2.21 kcal mol^{-1}) and unfavorable for pentagon-μ^5 (+2.55 kcal mol^{-1}). The weak binding of uranyl to C_{60} can be attributed to the inability of C_{60} to donate the charge to the lowest unoccupied molecular orbital (LUMO) of uranyl. As the charges on the carbons are very small (-0.001 to -0.005 au), the cation binding is very weak. Further, the binding efficacy of uranyl at various sites of bare C_{60} can be attributed to the extent of charge transfer from uranyl to C_{60}. Indeed, it is known that in the case of metal atom-C_{60} interactions, charge transfer usually occurs from the metal centre to the C_{60} moiety, thus the metal atom attains partial ionic character. [44] This concept has been successfully utilized in the field of hydrogen storage using metal decorated fullerenes. [44] However, in our case, due to the di-positive charge of the uranyl species, further electron transfer from uranyl to C_{60} is highly unlikely. We find that the electron flow is from C_{60} fullerene to the uranyl species. Our Mülliken charge analysis does confirm the above statement. For instance, as compared to bare uranyl, the positive charge on the uranyl moiety for the most stable pentagon-$\mu^{2-\perp}$ species is smaller (1.28e^-) as compared to the least stable hexagon-$\mu^{2-\parallel}$ species (1.36e^-). The electron accepting nature of the C_{60} fullerene predominantly governs the fullerene chemistry, where the fullerene acts as a dienophile (electron acceptor) and forms favourable addition adducts with electron rich molecules like dienes.[168] For these cases, the most preferable site of additions is at the junctions of two hexagons [6,6]. Conversely, in our case, we find that the [6,5] junction is the preferable site of binding to uranyl. This signifies the basic differences between the interactions of C_{60} fullerene with different species.

As uranyl ion exists in aqueous phase with five water molecules, we have optimized a structure of uranyl with three water molecules bound to C_{60} (considering the most stable structure pentagon-$\mu^{2-\perp}$). The calculated uranyl bond lengths (1.783Å) are found to be lengthened due to the additional coordination of water molecules. However, the uranyl binding energies are unfavorable by more than 40 kcal mol^{-1}, probably because the solvation energy of uranyl ion is very high prior to C_{60} binding as compared to the adduct. We have also made attempts to optimize the structure of uranyl binding to C_{60} by keeping all five water molecules. Although the binding energies have reduced from 40 kcal mol^{-1} to ~18 kcal mol^{-1}, the relative trend is still the same. We note that the equatorial penta-coordination is only preferred over the heptacoordination. The two additional water molecules are only interacting via hydrogen bonding with the coordinated water molecules (of the first coordination sphere).

Further, for effective separation, uranyl ion will be in aqueous phase and C_{60} will be in organic phase of the system. By attaching C_{60} with organic functional groups (such as malonate), one can increase the solubility of C_{60} and make it a better binder for uranyl in aqueous phase. From this part of the discussion, it is quite clear that interaction of bare uranyl (along with explicitly hydrated species) with C_{60} is unfavorable. Hence, in the forthcoming sections, we focus on binding of uranyl with malonate functionalized C_{60}.

3.2.1.2: Binding of Uranyl to Functionalized C_{60}

Functionalization of C_{60} with carboxylic group such as malonic acid can improve the solubility and the strength of uranyl binding affinity to C_{60}.[169] We have functionalized C_{60} with a dicarboxylic acid, (malonic acid) and considered the uranyl binding to neutral, anionic and dianionic form of malonate functionalized C_{60}. All the three types of complexes which differ in the protonation states of carboxylic acid group are expected to be formed at different pH conditions. At low pH (pH=1-3), both the carboxylate functional groups will be protonated, and in semi-acidic pH (pH=3-6), either of the functional groups is expected to be protonated (mono-anionic form), whereas at high pH (7-10), both the carboxylates will be deprotonated creating a di-anionic form.[170]

We have considered uranyl binding to mono-dentate (neutral), bi-dentate (in both anionic forms) or chelate (all three forms) binding motifs of malonate functionalized C_{60} (Figures 3.4, 3.5, and 3.6). For uranyl binding to neutral malonate functionalized C_{60} (Figure 3.4), we find that the U=O axial bond length is slightly longer for the chelate binding mode as compared to the mono-dentate binding mode. Similarly, the O=U=O bond angle is somewhat more bent (by 1^o) in the chelate mode as compared to the same in mono-dentate binding. For mono-dentate carboxylate binding, during geometry optimization, we find that one water molecule is automatically detached from uranyl (2.751Å) and now forms hydrogen bonding with the carboxylate group of malonic acid if we consider tetra-aquo uranyl with penta-coordination mode. Hence, we have considered only tetra coordination site of uranyl (tri-aquo complex) with the mono-dentate carboxylate binding. This structure is characterized as minima (Figure 3.4) and the geometrical parameters are given in Table 3.3.

For the mono-dentate carboxylate binding, the equatorially coordinated water molecule is hydrogen bonded (1.965 Å) to the carboxylate group, whereas in the case of chelate binding, no such weak interactions are noticed (Figure 3.4). Further, asymmetric binding of two carboxylate oxygens to uranyl (2.404Å and 2.465Å) is noticed for chelating binding mode. Further, out of the monodentate and chelate modes, the latter uranyl binding mode is more favorable by ~10 kcal mol^{-1}.

For both mono-anionic and di-anionic species, we have considered two types coordination modes, one is of chelate type which we refer as μ^2-chelate and the other is through the symmetric bidentate carboxylate site denoted as μ^2-carboxylate. The notation carboxylate or chelate μ^2 arises from whether the bonded oxygen comes from the same carboxylic acid moiety or from two different carboxylic acids present in malonate.

As compared to the neutral malonic acid, the U=O bond lengths are slightly weaker by 0.01Å for both μ^2 binding modes in the case of corresponding mono-anionic form. Similarly, the O=U=O bond angle is also more bent by 2^o in the latter binding sites. Between the two coordination modes, μ^2-carboxylate binding site is somewhat more stable by ~3 kcal mol^{-1} as compared to the μ^2-chelate binding site. Here again, we find the asymmetric U-O bond length (2.197Å and 2.470Å) for chelate binding site due to the differing charges present on the oxygen atoms of the two carboxylates. Due to the strong coordination of malonate to uranyl, the coordinated water molecules become weakly bound (2.497-2.549Å). At high pH conditions, the coordination of uranyl will be at the completely deprotonated sites of malonate. Similar to the mono-anionic form, here we have two μ^2- forms which are either bi-dentate μ^2-carboxylate or μ^2-chelate binding modes. Due to the double negative charge of the ligand, the binding of uranyl is expected to be stronger. Indeed, the U=O bond length is more elongated (by 0.01 Å as compared to the mono-anionic form and 0.02Å with respect to neutral malonate form). Between the two binding sites, the μ^2-chelate binding is stronger and energetically more favorable by ~17 kcal mol^{-1} as compared to the μ^2-carboxylate binding mode. The stronger binding of asymmetric μ^2 mode to uranyl is also reflected in the O=U=O bond angle, which is more bent (167^o) as compared to the μ^2 carboxylate binding. Due to the strong coordination of negative charged ligand, we find that the water molecules are loosely bound (2.512Å-2.586Å).

If the concentration of uranyl is high, then the binding of uranyl to functionalized C_{60} in 1:2 (C_{60}: uranyl) is possible. We have optimized the geometry of this species (Figure 3.6 (c)), where the two uranyl ions bind via μ^2-bidentate carboxylate functional groups of malonate. As compared to the μ^2-carboxylate binding of malonate to one uranyl, we find that the binding of uranyl is somewhat weak which are reflected in the reduction of of U=O bond length (1.792Å) and the extent of bending of O=U=O bond angle being small (173.4^o).

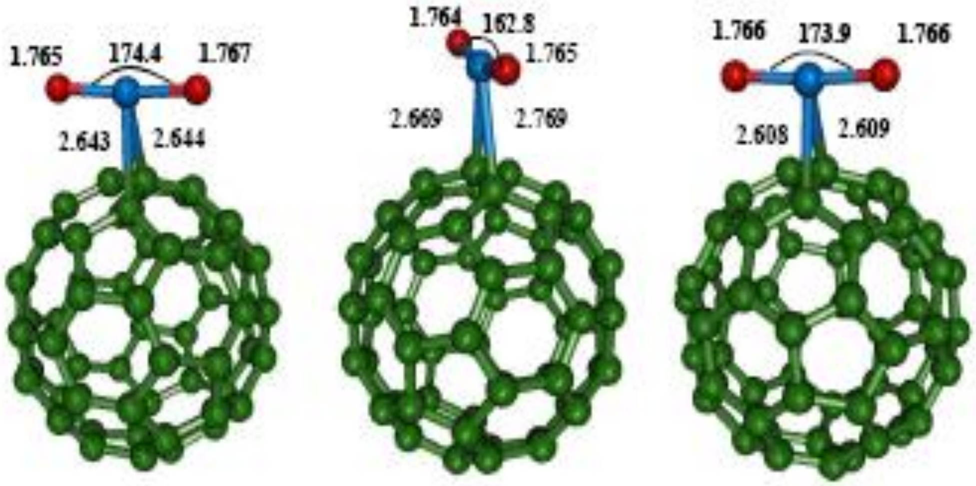

(a) Hexagon-μ^2-$^{\perp}$ **(b) Hexagon-μ^2-$^{\parallel}$** **(c) Pentagon-μ^2-$^{\perp}$**

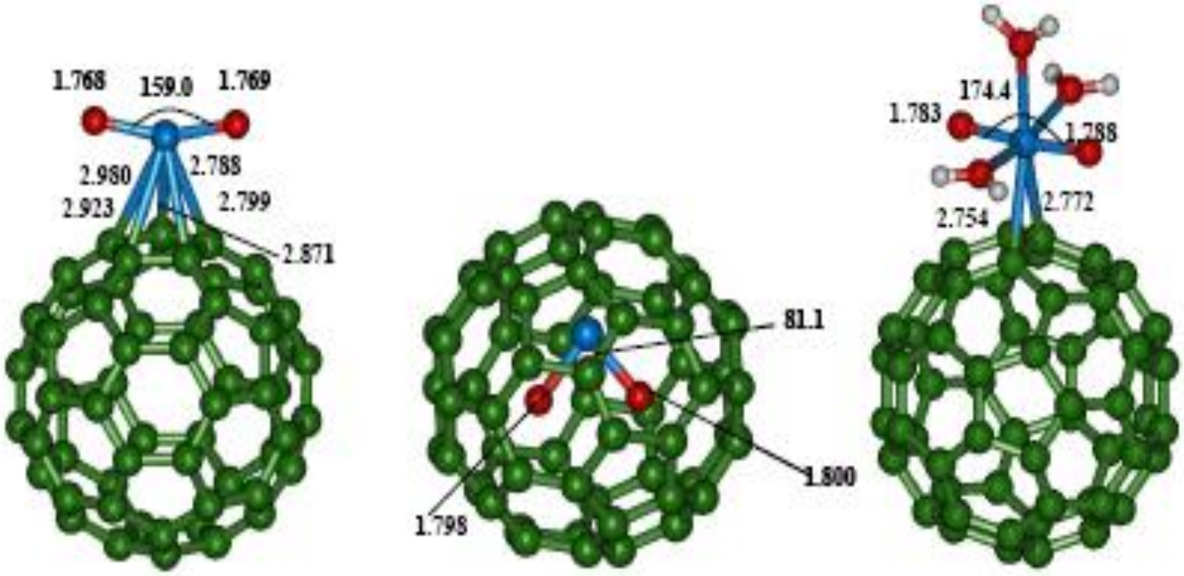

(d) Pentagon-μ^5 **(e) Encapsulation** **(f) Pentagon-μ^2-$^{\perp}$-$(H_2O)_3$**

Figure 3.3: Binding of uranyl at various sites to bare C_{60} fullerene.

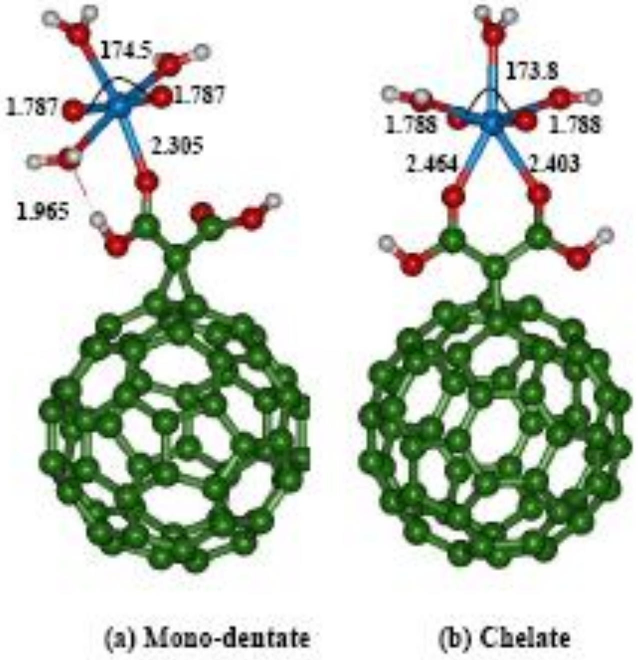

(a) Mono-dentate (b) Chelate

Figure 3.4: Binding of uranyl with neutral malonic acid functionalized C_{60} fullerene.

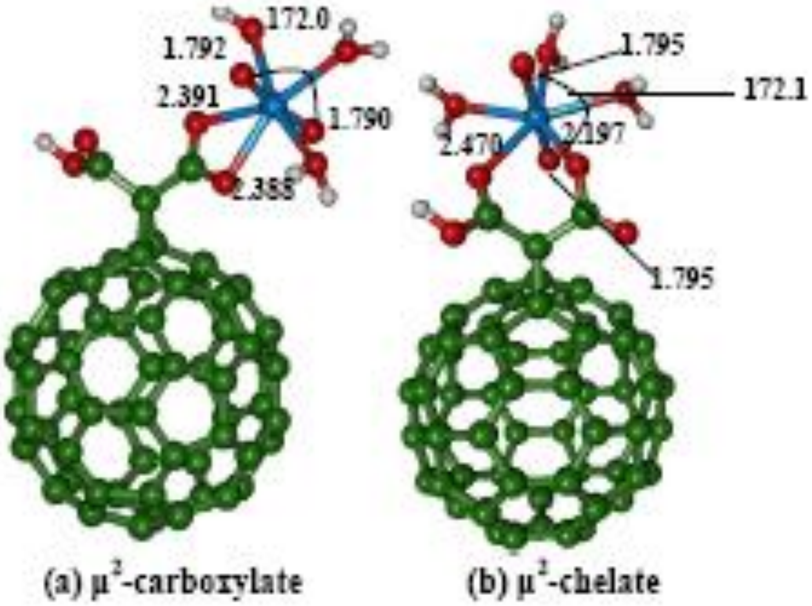

(a) μ^2-carboxylate (b) μ^2-chelate

Figure 3.5: Binding of uranyl with mono-anionic malonate functionalized C_{60} fullerene.

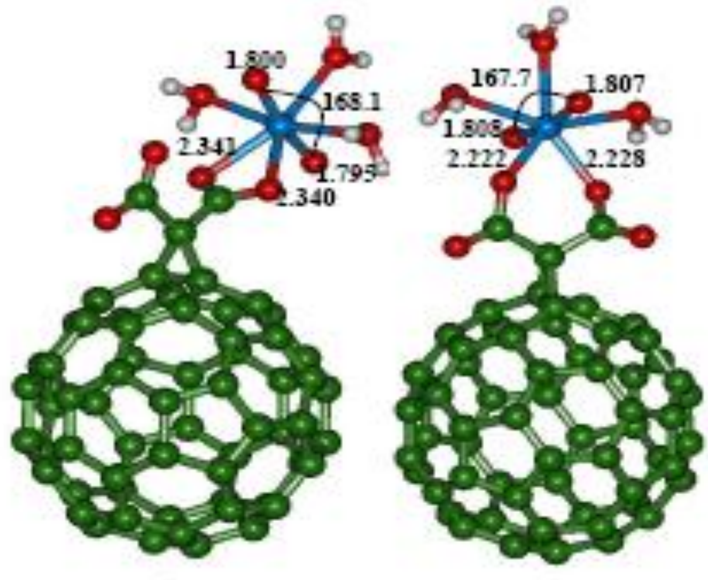

(a) μ^2-carboxylate (b) μ^2-chelate

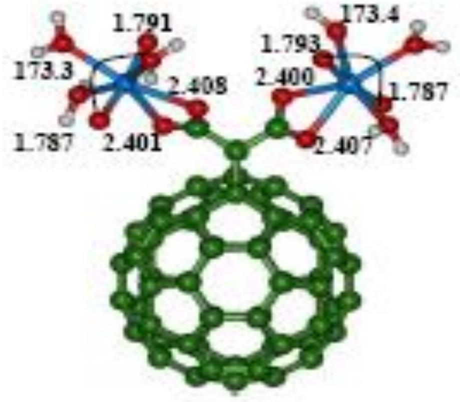

(c) $(\mu^2)_2$-carboxylate

Figure 3.6: Binding of uranyl with di-anionic malonate functionalized C60 fullerene.

3.2.1.3: Vibrational Frequencies

The favourable binding of functionalized C_{60} to uranyl will lead to elongation of U=O bond as compared to penta-aqua uranyl complex, and this weakening in the bond strength will be reflected in the vibrational frequencies corresponding to symmetric (ν_{sym}) and asymmetric (ν_{asym})

stretching of the U=O bond. For all the complexes, the calculated U=O ν_{sym} and ν_{asym} stretching modes (Table 3.3) are red-shifted as compared to the penta-aqua-uranyl complex. However, the extent of red-shift of the malonate-uranyl complex varies depending on the protonation state of the carboxylate group of the malonate.

Hence, at high pH (fully deprotonated), the uranyl bond lengths are elongated by more than 0.02Å as compared to low pH (doubly protonated). Correspondingly, the uranyl stretching frequencies are downshifted by more than 25 cm^{-1}. Between the two bidentate coordination modes, (carboxylate and chelate binding modes), both υ_{sym} and υ_{asym} μ^2-binding are red shifted by nearly 20 cm^{-1}. Hence, the vibrational frequencies of the uranyl bond can be used as a *"fingerprint"* to identify the type of coordination mode and the protonation state of malonate ligand can be understood at least semi-quantitatively.

3.2.1.4: Binding Energies

The binding energy for the functionalized C_{60} to uranyl is evaluated using the following equation,

$$[UO_2(H_2O)_5]^{2+} + [Mal\text{-}H_n\text{-}C_{60}]^{n-2} \rightarrow [UO_2\text{-}Mal\text{-}H_nC_{60}\text{-}(H_2O)_3]^{n} + (H_2O)_2 .$$

We note that the formation of $[UO_2(H_2O)_3]^{2+}$ from $[UO_2(H_2O)_5]^{2+}$ is an endothermic process (36 kcal mol^{-1}). The calculated binding energies (B3LYP/COSMO) for the neutral malonic acid to uranyl are unfavorable for both mono-dentate (19.1 kcal mol^{-1}) and chelate (9.5 kcal mol^{-1}) binding modes. However, for the case of mono-anionic and dianionic malonate species (which are considered to be present in semi-neutral and high pH), the uranyl affinities are strongly favorable. For instance, for the mono-anionic malonate binding to uranyl, the calculated binding energies are -14.6 kcal mol^{-1} and -12.0 kcal mol^{-1} for μ^2-carboxylate and chelate modes respectively. For the di-anionic species, the uranyl binding energies are strongly favorable for both μ^2-carboxylate (-28.8 kcal mol^{-1}) and chelate modes (-46.0 kcal mol^{-1}). In analogy to our earlier discussion, the possibility of binding of uranyl with all five water molecules and malonate is also tested. We again find that two water molecules detached from uranyl and are weakly interacting with the coordinated water molecules. Further, the overall stabilization energy is not altered significantly. Hence, only penta-coordination mode of uranyl (with three water molecules) is favoured for both functionalized and bare C_{60}. Finally, in the case of 2:1 uranyl complex with deprotonated malonate, we find the binding energies to be somewhat weak (20 kcal mol^{-1} per uranyl) as compared to 1:1 ratio (28 kcal mol^{-1}). Hence, we propose that favorable and efficient uranyl binding to malonate functionalized C_{60}, is possible at high pH conditions.

We now compare our results with those of the recent experimental study using spectrophotometric measurements. Rao et al.[171] carried out experiments (EXAFS) on complexation behavior of uranium (VI) with malonate at different temperatures and at differing pH (3.5 and 5.2). Our geometric predictions of uranyl bond lengths are in close agreement with those of the experimental data. Particularly, the calculated U=O bond lengths from low pH (3.5) to semi-acidic pH (5.2), we find the elongation of 0.01Ǻ to be in close agreement with the experimental findings. In agreement with the experimental proposal, our calculations also suggest that chelate type binding with three equatorial water molecules is favoured. In the case of free malonate, more than one malonate molecule can interact with uranyl molecule. However, due to the presence of C_{60} molecule, steric hindrance restricts the formation of such species which is again consistent with the experimental data.[172]

Table 3.3: Structural parameters and vibrational frequencies of uranyl complex bound to malonate functionalized C_{60}.

	Binding Mode	U=O **(Å)**	O=U=O **(Degree)**	U-O_{Mal} **(Å)**	U-O_{H2O} **(Å)**	$^{U=O}\nu_{sym}$ **(cm^{-1})**	$^{U=O}\nu_{asym}$ **(cm^{-1})**
$[U^{VI}O_2(C_{60}\text{-Mal-}H_2)(H_2O)_3]^{2+}$	μ^1-carboxylate	1.787	174.5	2.305	2.437-2.603	836.2	930.5
$[U^{VI}O_2(C_{60}\text{-Mal-}H_2)(H_2O)_3]^{2+}$	μ^2-chelate	1.788	173.9	2.404, 2.465	2.473-2.485	836.2	930.2
$[U^{VI}O_2(C_{60}\text{-Mal-H})(H_2O)_3]^{1+}$	μ^2-carboxylate	1.792	172.0	2.389, 2.391	2.482-2.497	831.4	926.2
$[U^{VI}O_2(C_{60}\text{-Mal-H})(H_2O)_3]^{1+}$	μ^2-chelate	1.795	172.1	2.197-2.470	2.497-2.549	825.4	918.7
$[U^{VI}O_2\ (C_{60}\text{-Mal})(H_2O)_3]^0$	μ^2-carboxylate	1.801	168.1	2.341	2.504-2.530	821.5	909.3
$[U^{VI}O_2\ (C_{60}\text{-Mal})(H_2O)_3]^0$	μ^2-chelate	1.809	167.7	2.222, 2.228	2.512-2.586	809.1	891.5
$[(U^{VI}O_2)_2(C_{60}\text{-Mal})(H_2O)_3]^{2+}$	$(\mu^2)_2$-carboxylate	1.792, 1.788	173.4	2.400-2.408	2.479-2.486	829.6, 836.5	927.2, 929.2

3.3: Computational Details

In the first section of this chapter where we have discussed the structure and electronic properties of azafullerenes, we have carried out all the geometry optimizations and energy calculations using the density functional theory (DFT) methods implemented in the GAMESS software.[50] Becke's three-parameter exchange functional and Lee-Yang-Parr correlation (B3LYP)[173] DFT functional has been used for all the calculations. The split-valence basis sets, 6-31 has been employed for all the calculations. For all the minimum energy isomers, Hessian has been calculated analytically. The highest occupied molecular orbital (HOMO)-lowest unoccupied molecular orbital (LUMO) gap is calculated as the energy difference between the corresponding orbitals. All the nucleus-independent chemical shifts (NICS) parameter[174,175] calculations are carried out using the Amsterdam Density Functional (ADF) package 2007[176,177] at B3LYP/TZP level of theory. For an N electron system, ionization potentials (I) are obtained as the energy difference between the positive ion and the neutral system at the neutral geometry and electron affinities (A) are calculated as the energy difference between the negative ion and the neutral system at the neutral geometry, viz.

$$I = E(N-1) - E(N)$$

$$A = E(N) - E(N+1) .$$

All the polarizability calculations have been performed using semi-empirical quantum chemistry package MOPAC2009. [178] This uses more accurate PM6 parametrization which has been developed from extensive experimental and *ab initio* calculation results.[178] The keyword "POLAR" has been used for the polarizability calculations. It may be noted that, the accuracy of polarizability prediction by the above method has been tested for several neutral molecules and the results nicely agree with experimentally obtained values with the average absolute error of 2.1%.

For the latter section of this chapter dealing with interaction of uranyl cation with functionalized fullerenes, all the geometries are optimized using BP86 functional in conjunction with def-TZVP basis set for uranium, def2-TZVP basis set for oxygen (of UO_2) and def2-SV(P) basis set for the remaining atoms. For uranium, the core electrons are modeled with def-MWB pseudopotential. For energetics, we have used B3LYP functional with the same basis sets. Solvation effects are incorporated using COSMO continuum solvation model (using $\varepsilon=80$) as implemented in TURBOMOLE. [179] Such a cost effective strategy saves computational time and the predicted structures, vibrational spectra and redox properties are comparable to the experimental data. [164]

3.4: Summary of the Work

In the first section of this chapter, we have discussed the possible minimum energy isomers for different azafullerenes with a formulae of $C_{60-2n}N_{2n}$ (n=1-12). The structural studies reveal that the presence of an undisturbed C_6 ring enhances the stability of the fullerene whereas the presence of a –N-C-N- fragment destabilizes the system. At lower level of nitrogen concentration, the stabilization by C_6 ring is more important and on increasing the doping concentration, the N-N repulsion becomes more important. All the minimum energy isomers are found to have large HOMO-LUMO gaps, large IP and lower EA values apart from having considerably large minimum vibrational frequencies which show the stability of these structures. Some of the structures studied are found to have large NLO coefficients which can be useful in designing new photonic materials.

To summarize the second section of this chapter, we have considered the interactions between C_{60} and uranyl using DFT based calculations. The effect of pH is incorporated by carrying out calculations by varying the protonation states of malonate. Our calculations suggest that uranyl binding with bare C_{60} is not possible due to unfavorable binding energies. Upon functionalizing with malonate, the uranyl binding strength is improved upon increasing the pH of the medium. Further, we propose that chelate type binding is more favorable as compared to carboxylate binding. Our calculated geometries are also in close agreement with the experimental data. Although the formation of 2:1 and 3:1 ratio of malonate with uranyl are possible, it is highly unlikely to be formed in the case of malonate functionalized C_{60} due to steric hindrance. Functionalized fullerenes can be considered as an ideal building block for the design of materials and our study demonstrates that favourable binding of uranyl species with functionalized fullerenes may chart the road map for developing materials for effective nuclear waste management.

CHAPTER 4

Structure and Electronic Properties of Small Pristine and Doped Gold Clusters

Chapter 4: Structure and Electronic Properties of Small Pristine and Doped Gold Clusters

This chapter is divided into two main sections. In the first section, we have discussed the structure and electronic properties of small pristine and doped gold clusters. Also, as a first step towards understand their catalytic properties; the adsorption of CO molecule is studied. In the latter section of the chapter, we have investigated the CO adsorption on the supported gold clusters.

4.1: Importance of Structure and Electronic Properties of Gold Clusters

The glitter of metal gold seems to have obsessed mankind for centuries. For the scientific community, it is the “noblest” of all metals. The physical and chemical properties of gold in the bulk phase are, however in sharp contrast as well as unusually different from the material at the nanoscale regime. The properties in this regime strongly depend on the size and shape of the nanoparticles. Many interesting phenomena involving nanomaterials have been observed during the past decade due to the increasing availability of highly sophisticated experimental techniques and also improved understanding and prediction has been possible with the availability of the high-quality electronic structure calculation methods. Traditionally, gold clusters have also played an important role in the ancient medicines, dyes and colloidal chemistry. The reactivity of gold nanoparticles towards CO oxidation far below the room temperature has been initially shown by Haruta et al. [180] in late eighties**.** Subsequently, the unusual size dependence of the low-temperature catalytic oxidation of carbon monoxide using gold clusters ranging in diameter from 1 to 6 nanometers has been recently demonstrated by Goodman and co-workers. [25] In one of the most recent studies, the high catalytic activity for CO oxidation is correlated with the presence of bilayer clusters which contain nearly ten gold atoms. [181] The size and structure sensitivity of this reaction is related to the quantum size effect with respect to the thickness of the gold islands with two layers of gold which are effective for catalyzing the oxidation of carbon monoxide. These results suggest that the nanoclusters, in general, may have unusual catalytic properties as one of the dimensions of the cluster becomes smaller than the corresponding three-dimensional systems. Following these initials reports of the reactivity of gold nanoparticles, the stage has been perfectly set for study of the nanoscale gold catalysis leading to upsurge of activities on structural aspects, electronic properties of gold clusters and their potential applications in nanocatalysis. [25,29,180-194] The intriguing properties of these clusters originate from their finite-size effect, quantum effect and large surface-to-volume ratio. In spite of these studies, some of the important issues are yet to be resolved. For instance, questions dealing with how the surface structure and features with nanometer dimensions affect the reactivity in metallic and model bimetallic catalyst surfaces and heterogeneous systems and also how the various factors like presence of low coordinated atoms, electronic confinement, particle shape and more importantly effect of the substrate, mainly govern the catalytic properties of gold nano particles require immediate attention. [195]

Apart from the study of pristine gold clusters, the role of dopant atoms offering chemical versatility in fine tuning the structural and electronic properties is another important aspect. In most of the studies involving the doped gold clusters, the dopant atom has been primarily the transition metal atoms. The first highly stable doped gold cluster predicted from density functional theory (DFT) based investigations by Pyykkö and Runeberg[196] and also confirmed by using photoelectron spectroscopy (PES) by Li et al.,[197] was a closed-shell icosahedral $W@Au_{12}$. Subsequent PES studies[198] revealed the I_h symmetry of the V, Nb and Ta doped Au_{12}. In another theoretical study, Gao et al.[199] showed that Au clusters doped with a foreign metal atom tend to form core-shell structures when the number of Au atoms exceeds nine. Wang et al. [200] provided the first experimental evidence of endohedral doping of the gold cages by Cu in $Cu@Au_{16}^-$ and $Cu@Au_{17}^-$. Wang et al.[201] have also studied the doping effect of gold cage Au_{16}^{-} with Si, Ge and Sn. Chen et al. [202] have used DFT calculations to study the stability of Ti doped gold clusters. In general, transition metal doped gold clusters have been widely explored in these highly stable gold-caged structures for their novel physical and chemical properties like large HOMO-LUMO (HL) gap. [196-198,203] Hence, in most of these reported literatures on doped gold clusters, the dopant atoms have been transition metals. The main focus, so far, however has been the size dependent geometric evolution from planar structure to 2D or stabilizing the cage structure of gold with endohedral dopant atoms. Any systematic study pertaining to alkali metal atom or hydrogen doped gold clusters is really missing.

Having known the important role of gold nanoclusters in various catalytic reactions and keeping in mind the fact that the doping can play a pivotal role in modifying the electronic property, any attempt to further enhance the catalytic property of these clusters by introduction of suitable dopant atoms is a well deserved exercise. In other words, we intend to investigate how the reactivity of the gold clusters towards CO adsorption can be enhanced by choosing proper dopant atoms. In order to address these issues, in the present work, we have endeavored to study the structure and electronic properties of doped small gold clusters $Au_{n-1}X$ (n=2-8, X=H, Li and Na) along with their pristine counterparts Au_n (n=2-8). With particular reference to oxidation of CO, we have also made an attempt to study the interaction of CO with these doped gold clusters along with the pristine ones. Although a few previous works[204] have reported the structures and electronic properties of gold clusters of varying sizes and charge states, a comparative study of pristine clusters vis-à-vis monovalent atom dopants will be of great importance. It will also be quite fascinating to study the monovalent atom doped gold clusters not only from the perspective of electronic structure but also keeping in mind their overwhelmingly important role in catalysis. Recently, a critical review article[204] has discussed the theoretical developments on heterogeneous gold catalysis which covers various pertinent issues of gold catalysis.

One of the important reasons for selecting the hydrogen and alkali-metal atoms as the dopant atoms is that gold, alkali metal and hydrogen atoms have similarity in electronic configuration in having one electron in the valence shell. In addition, the electronegativity of hydrogen and gold is very close to each other. Most recently, Kiran *et al.* [205] have demonstrated that the chemistry of gold has significant resemblances to that of the hydrogen atom for specifically chosen systems. In Au-alloy clusters, the gold and hydrogen analogy is a general phenomenon and can add a new dimension to the expanding chemistry of Au. Several recent theoretical works[206,207] have also further explored the similar analogy. Our objectives for the present work have been to investigate (a) whether these monovalent dopants induce any structural change in pure undoped clusters, (b) the effect of doping in modifying the electronic properties (c) the energetics of CO adsorption and also (d) whether there is any chemical activation of gold clusters as a consequence of doping. We are also interested in calculating the electronic properties of the pristine and doped gold clusters, like ionization potential (IP), electron affinity (EA), HOMO-LUMO (HL) gap, binding energy per atom (BE) and chemical hardness η, especially to investigate the stability and reactivity of these clusters.

We hope that the outcome of this particular work would stimulate further research in this area, particularly in designing materials involving the doped gold clusters by exploiting the nature of similarity in their electronic structure, as investigated here. Thus, a molecular-level understanding of the present study is expected to provide a better understanding of the structure-reactivity relations in the nanosurface-catalyzed reactions.

4.1.1: Electronic Structure and Properties of Hydrogen and Alkali Metal Atoms Doped Gold Clusters and CO Adsorption

In this part of the chapter we will discuss our results pertaining to structural aspects as well as several electronic properties of small gold clusters. The effects of doping in these gold clusters on the modulation of the electronic properties have also been addressed. We have also discussed the adsorption CO molecules on these clusters.

4.1.1.1: Structural and Electronic Properties

In general, most of the theoretical methods predict that small neutral gold clusters tend to favor planar geometry up to the cluster size *n*=11.[208,209] The relativistic effects seem to play a major role in governing the planar geometries.[210] In the present work, the geometries optimized by HLYP method for pristine gold clusters for sizes *n*=2-8 are given in **Figure 4.1 (a)**. Similarly, equilibrium structures obtained by M06 method are shown in **Figure 4.1 (b)**. The geometries obtained by the HLYP as well as the M06 methods are found to yield similar structures, with only marginal difference in the geometrical parameters. Out of the several minimum energy structures for a given cluster size, the lowest-energy isomer has been chosen for studying the effect of doping the hydrogen and alkali-metal atoms. We have also compared all the lowest-energy structures with the already existing reports and it is found that the structures are similar to those already predicted[209] except for sizes *n*=7 and 8. For the cluster size corresponding to *n*=3, the lowest-energy structure obtained by the HLYP and M06 method is of linear and bent (V-shaped) geometry, respectively. The complete active space self consistent field (CASSCF) calculations of Balasubramanian and Lio[211], show that the cluster Au_3 adopts an isosceles triangle with an apex angle of 54°. However, use of PW91 functional with scalar relativistic projector augmented wave (PAW) core states predicts that D_{3h} and C_{2v} structures are also energetically comparable with an energy difference of only 0.05eV.[212] Our result for Au_3 shows that the HLYP method predicts the Au-Au bond lengths for the linear structure to be 2.78 A^0 and 2.57 A^0.

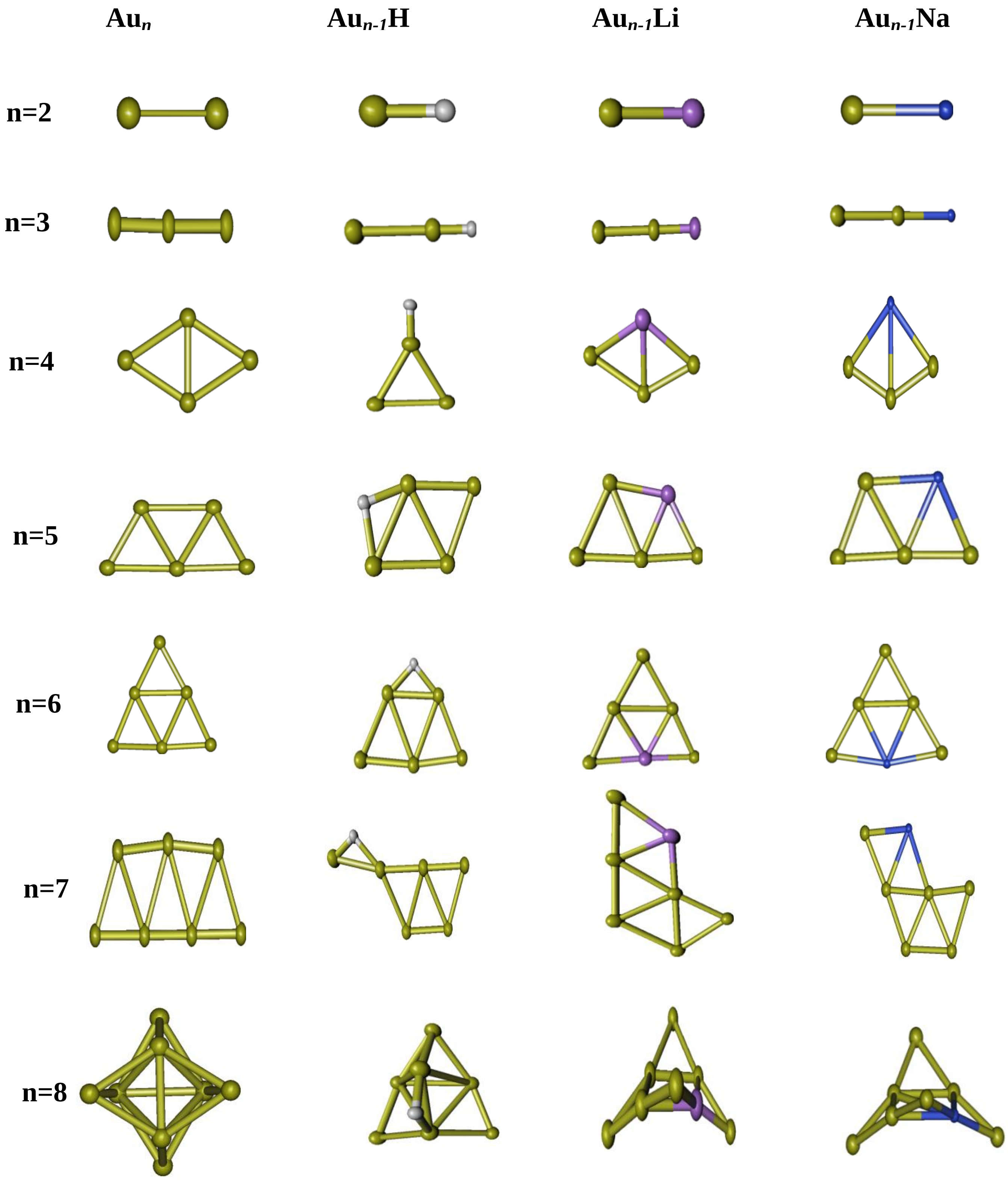

Figure 4.1 (a): Optimized geometries of pristine and doped gold clusters obtained by using HLYP based DFT method.

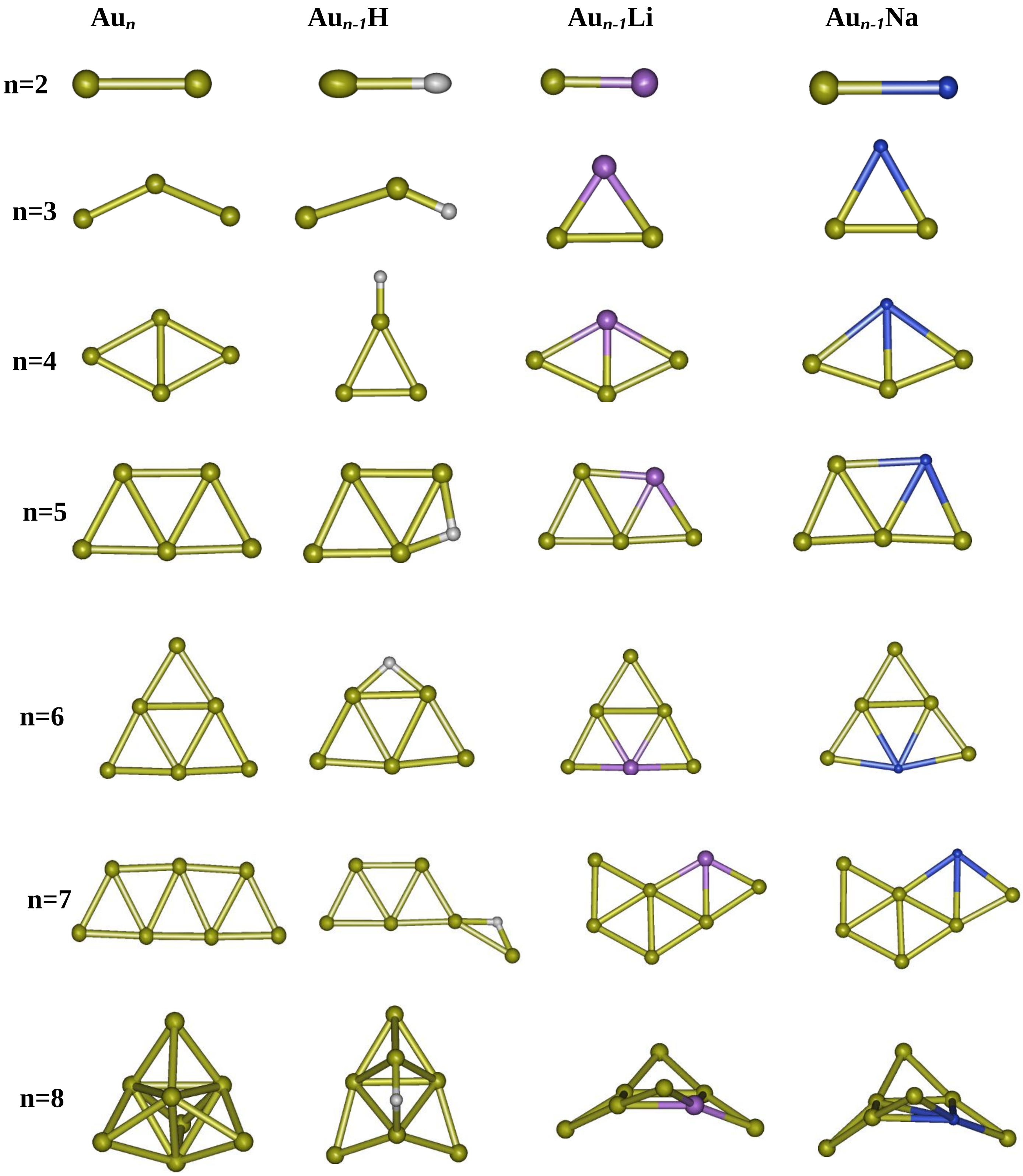

Figure 4.1 (b): Optimized geometries of pristine and doped gold clusters obtained by using M06 based DFT method.

On the other hand, M06 predicted geometry has both the Au-Au distance as 2.65 A^0 with an angle of 131.71^0. For the cluster size n=7, the energy minimized geometry is planar, but the structure differs slightly from that given in Ref. 209. There have been many reports discussing the 2D and 3D structures for the cluster Au_8. For instance, Olson *et al.* [213] have shown that the DFT methods predict planar geometries while the second order Moller-Plesset (MP2) perturbation method as well as CCSD(T) predict the lowest isomers to be non-planar with D_{2h}, D_{2d}, C_{2v} and T_d symmetry. Our result obtained by both HLYP and M06 methods shows that the lowest-energy isomer of Au_8 is having a 3D geometry with T_d symmetry which is in good agreement with the most stable structure obtained by the CCSD(T) method.

Let us now discuss the effect of the dopant atoms on the structure of gold clusters. It should be mentioned that there can be several equivalent positions for the dopant atoms in a given cluster geometry, and considering all the possible cases, the energetically lowest isomer of the doped geometry for a particular cluster size has been considered for further study. Accordingly, we have replaced one of the gold atoms in the cluster Au_n by the dopant atom X, (X = H, Li and Na), and among the several possible geometries, the lowest energy structures obtained by HLYP method are shown in **Figure 4.1 (a)**. **Figure 4.1 (b)** depicts the structures of doped gold clusters obtained by the M06 method apart from the pristine gold clusters obtained by the same method. It can be seen from **Figures 4.1 (a)** and (**b)** that upon doping with H atom, the distortion from the corresponding initial planar structure of pristine gold clusters is marginal for the clusters Au_nH (n=1-6). The structure of Au_7H, although not of perfect T_d symmetry, is cage like and is slightly distorted from its undoped counterpart Au_8. For the Li and Na atom doped gold clusters, there is a slight deviation from the initial planar structure in most of the cases for Au_nX (n=1-6). Although the structures of Au_7Li and Au_7Na are found to be similar to each other, they differ drastically from the initial T_d symmetry structure of Au_8 and they retain their 3D geometry. Let us now compare the geometrical parameters such as bond length for the cluster size *n*=2 obtained by both the methods. HLYP method predicts bond lengths of 2.56 A^0, 1.54 A^0, 2.32 A^0 and 2.60 A^0 for the bonds Au-Au, Au-H, Au-Li and Au-Na respectively. On the other hand, M06 predicted values for the same bond lengths are 2.59 A^0, 1.56 A^0, 2.34 A^0 and 2.64 A^0 respectively. This suggests that both the methods are quite consistent in predicting nearly similar structural parameters for both the doped and pristine gold clusters. We have earlier discussed that for the cluster Au_3, the methods HLYP and M06 yield different geometry. The same can be seen for the doped clusters Au_2X. In the HLYP case the geometry of the doped cluster is essentially linear like their pristine counterpart with Au-Au and Au-X (X=H, Li, Na) bond lengths as 2.85 A^0 and 1.55 A^0, 2.78 A^0 and 2.36 A^0, and 2.70 A^0 and 2.67 A^0 respectively for the clusters Au_2H, Au_2Li, and Au_2Na. For this cluster size, bent geometry is predicted by M06 for the doped gold clusters. In Au_2H, the Au-Au and Au-H bond distance is 2.71A^0 and 1.58 A^0 respectively with the Au-Au-H bond angle being 138.47^0. The geometry of Au_2Li is like an isosceles triangle with Au-Au and Au-Li bond lengths as 2.80 A^0 and 2.51 A^0 respectively, and the apex angle (Au-Li-Au) as 67.76^0. The geometry of the cluster Au_2Na is almost like an equilateral triangle with Au-Au and Au-Na bond distances having values of 2.79 A^0 and 2.82 A^0 respectively. The apex angle is 59.34^0 and the other two bond angles are 60.29^0 each.

One of the important electronic properties computed in the present study is IP for the pristine and doped clusters and the calculated results are presented in **Figure 4.2 (a)**. The variation of IP with size n, as plotted in **Figure 4.2 (a)**, shows an odd-even oscillatory behavior. It is also evident that the IP values of H-atom doped clusters are higher than that of pristine gold clusters and their Li and Na-atom doped counterparts, except for the cluster size, *n*= 7. Interestingly, the IP trend for alkali metal doped (Li and Na) gold clusters shows nearly similar kind of fluctuating behavior with slightly higher values for the Li doped clusters than their corresponding Na doped counterparts. Hence, it can be mentioned that the alkali metal doped gold clusters behave similarly whereas pristine gold clusters and their H doped counterparts show considerable difference in their size-dependence behavior. For the latter two types of clusters, the first member in the series corresponds to the highest value of IP which decreases with increase in cluster size up to n=5 with the only exception of the cluster Au_4H. This suggests that the clusters with size n=2 i.e. clusters Au_1H and Au_2 are more stable than other members in the series. It is clear from the IP trend that the even-numbered and closed shell Li and Na doped gold clusters have higher IP values than their neighboring clusters. The observed trend for higher stability of Au_nNa and Au_nLi clusters can be attributed to the presence of even number of delocalized electrons.

The trend of variation of EA with varying cluster sizes is shown in **Figure 4.2 (b)**. Odd-even oscillations, as found in the case of IP plot, are also observed here. The higher values of EA for clusters with odd n can be understood from the fact that, they require one additional electron to form the closed electronic shell. This occurrence of maxima at the odd-numbered cluster sizes for all the doped gold clusters also goes along the same line with the reported literature [18] for pristine gold clusters. The most striking result is that the values of IP and EA for the cluster, Au_4H, is significantly higher than that of pristine and alkali metal doped gold clusters and it is almost comparable to that of the halogen atoms. It also indicates that the cluster size of 5 may be in short of one electron to fill their outermost orbitals to form a closed electronic shell. This can be realized from the fact that the value of EA of the next cluster size, Au_5H, is almost half of that of Au_4H. In contrast to the H-atom doped gold clusters, the EA of Li and Na doped ones is very less and it is almost half of that of the H-doped counterpart. Based on this result, it can be mentioned that the exceptional property of H-doped gold clusters can have important consequences in the field of catalysis and it can act as an effective electron acceptor or Lewis acid. As observed previously for the IP plot, the EA trend for both the alkali metal atom doped clusters also match very closely to each other and deviate considerably from the pristine and H atom doped clusters. The chemical hardness parameter η is also a good descriptor for chemical reactivity as well as stability. The hardness variation with the cluster size is presented in **Figure 4.2 (c)**. Odd-even alternation can be seen for η, and for the odd n clusters, the values are less as compared to their corresponding neighbors. This fact also supports the view that clusters with odd number of valence electrons are more reactive and tend to attain closed electronic shell for greater stability. More importantly, the higher values of η for H-atom doped clusters as compared to their alkali metal atom doped counterparts, as seen from the Figure 4.2 (c), suggest the higher stability.

Another related parameter is the HL gap, a parameter suitable for describing the relative stability for these clusters. It can be mentioned that higher the value of HL gap, more stable is the cluster than the neighboring clusters and vice-versa. From the trend of HL with cluster size as shown in **Figure 4.2 (d)**, the odd-even staggering is conspicuous. In most of the cases, the HL gap for clusters having H-atom as the impurity is higher as compared to those having Li and Na as the doping atoms. This result reflecting the higher stability of H atom doped clusters sounds promising from a better catalyst point of view.

Finally, **Figure 4.2 (e)** describes the trend of BE with varying cluster size. The odd-even oscillation here is not very pronounced like HL variation with size. An important observation is that for all the doped clusters, the BE increases as compared to the pristine ones. Higher BE for these doped gold clusters can be regarded as a good indication that these clusters can be even potentially better catalysts than the pristine gold clusters. It can also be seen from the plot that for all the series of clusters considered, the stability corresponding to the sizes 6 and 8 are much higher than their neighbors.

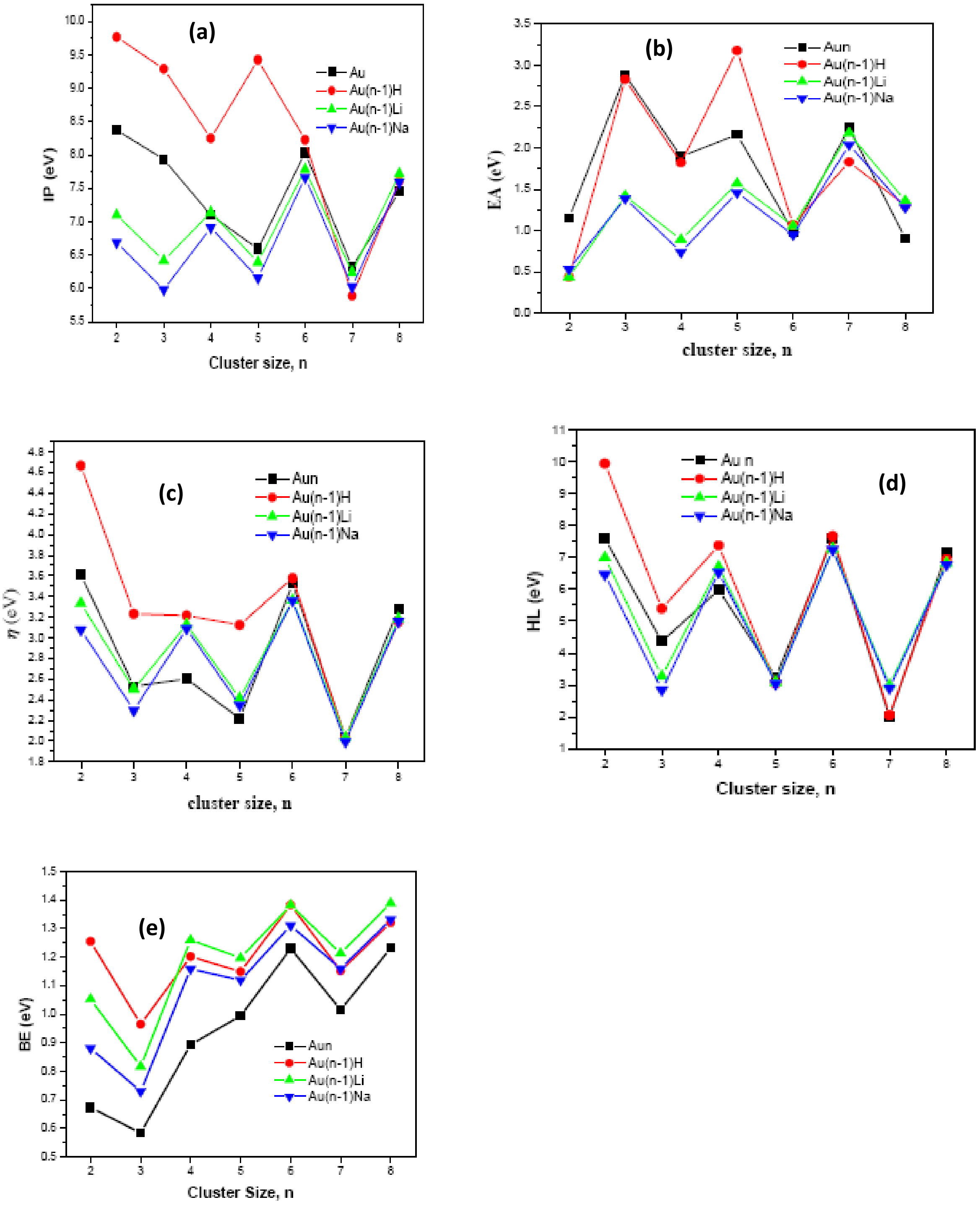

Figure 4.2: Variation of ionization potential (a), electron affinity (b), hardness parameter (c), HOMO-LUMO gap (d) and binding energy per atom (e) of pristine and doped gold clusters with cluster size.

From all the figures described so far, one common point that can be emphasized is that the alkali metal atom doped gold clusters show identical features. Similarly, pronounced modifications in the electronic properties for the H-atom doped clusters as compared to the pristine gold clusters can also be an important point. It has already been reported in the literature by Buckart et al. [214] that the spectra of anionic clusters, Au_n and $Au_{n-1}H$, show almost identical features for the sizes $n > 2$ and it was concluded that a single H atom in the environment of a gold cluster behaves like metal atom. However, our results reveal that although the hydrogen dopant atom does not induce any major structural modifications in the pristine gold clusters, the electronic properties are modified by a considerable extent. The calculated values of electronic properties, such as IP, BE and HL gaps for the hydrogen atom doped gold clusters are higher than that of pristine clusters. Other electronic properties are also modified by the introduction of H-atom in the gold cluster. In contrast to this observation, we also notice that the alkali metal atom doped gold clusters show almost similar electronic properties and these properties also differ appreciably from that of pristine and hydrogen doped gold clusters.

4.1.1.2: Adsorption of CO Molecule

The energetics of CO adsorption on unsupported gold clusters has been investigated by a number of workers. [215] [216] [217] It has been reported that the usual mode of interaction of CO to transition metals involves CO → metal electron donation and metal → CO back donation. The covalent component of Au-CO bond is very small and the major contribution comes from electrostatic interactions. In the present study, we have considered mainly two types of CO adsorption patterns, vertical and horizontal to the plane of the gold clusters. In addition, a number of adsorption patterns have been chosen for clusters having 3D geometry, to study the CO interaction. Since the number of adsorption sites is increased for the bigger clusters, we have chosen some of the most stable complexes. The optimized structures of CO adsorbed complexes obtained by HLYP as well as M06 methods are shown in **Figures 4.3 (a)** and **and 4.3 (b)** with the variation of cluster size from 2 to 8.

From our initial studies, we find that CO can bind to the pristine as well as doped clusters through two ways, CO mode (interaction is through C atom) and OC mode (O is the interacting atom). It is also observed that the preferred mode of interaction for all the pristine gold clusters and their H-atom doped counterparts is Au-C bond (CO mode) which has been found to be in good agreement with the earlier reports. [217] On the contrary, it is interesting to note that for Li and Na doped clusters, although the predominant mode of interaction is Au-C, in some clusters, interaction through O-atom of CO (OC mode) is found to favor the stability of the complex. However, we have, herein, exclusively discussed the CO mode of interaction with the different types of clusters. In general, it has been observed that for clusters doped with H atom, the gold atom adjacent to H atom (α-position) favorably interacts with CO. In contrast to this, in the Li and Na doped gold clusters, the alkali atom shows some propensity for CO molecule by directly interacting with it in the adsorbed complexes.

Regarding the approach of CO molecule in the adsorbed complex, it can be inferred that it prefers a planar approach exclusively up to cluster size n=7 for H-doped and pristine gold clusters. On the contrary, Li and Na doped clusters do not seem to show any preference for planar orientation of CO for all cluster sizes under consideration. Up to the cluster size n=6, there is negligible distortion from the initial geometry of the cluster upon CO adsorption for Au_n -CO and Au_{n-1} -HCO systems while Li and Na-doped complexes induce some distortion in the initial planar geometry. It may be noted that in the CO-adsorbed complex Au_7HCO, the initial 3D geometry of the Au_7H cluster completely collapses to a planar structure. Let us now discuss the stability as well as the nature of interaction of CO with the gold clusters.

4.3 (a)

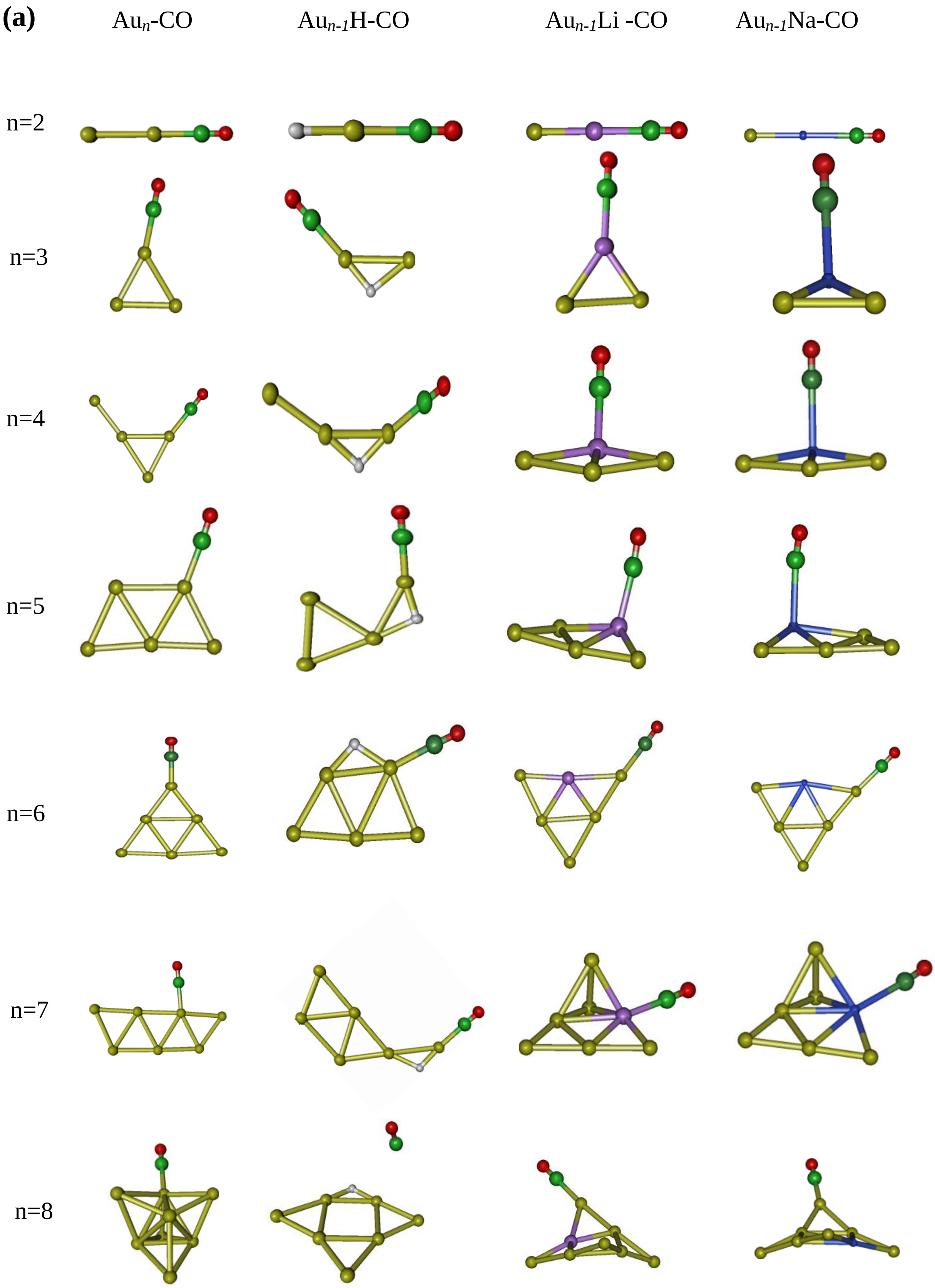

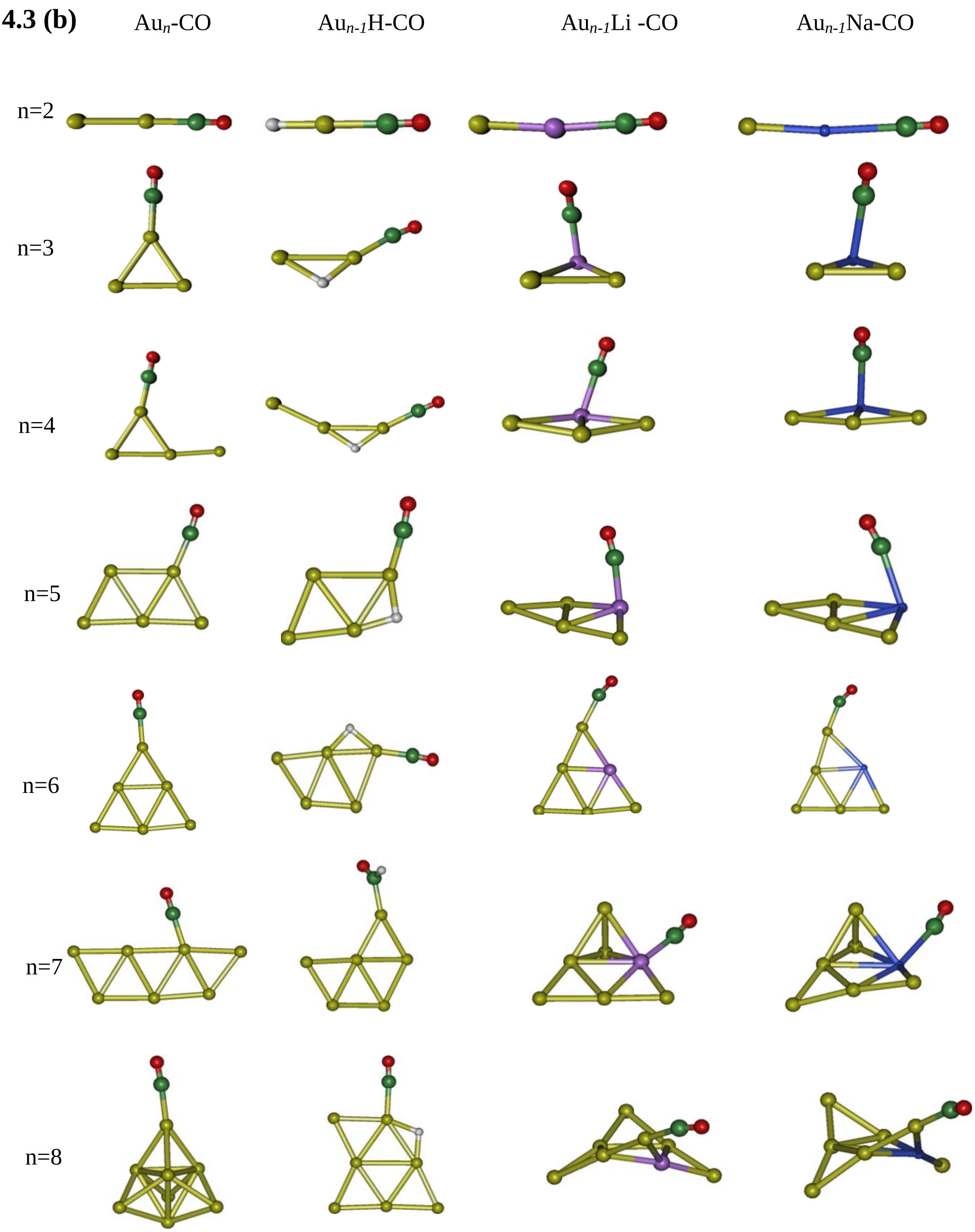

Figure 4.3: Optimized geometries of CO-adsorbed pristine and doped gold clusters obtained with HLYP (a) and M06 (b) method.

The interaction energies of these CO adsorbed complexes for all the clusters are presented in **Table 4.1.** The corresponding trend of interaction energy with cluster size is shown in **Figures 4.4 (a)** and **(b)**. For pristine gold clusters, by comparing our results with those available in the literature [217], we find that at the present level of theory, these values are generally smaller. The apparent discrepancy may be due to different levels of theory used and also the functional PW91 used by Wu et al. [217] tending to overestimate the energy.

It may be noted that the stability of the CO complexes formed with the pristine clusters is in good agreement with the earlier reports, especially for the cluster size up to $n = 5$. Au_6CO system deserves special mention and in our study we find this system to be feebly interacting. HLYP predicts the interaction energy to be -7.42kcal/mol and the same is improved to -13.27kcal/mol by M06 method. The reported value for Au_6CO by Wu *et al.* [217] is -20.87kcal/mol. For this geometry, we have calculated the single point interaction energy by employing the MP2 method which turns out to yield a value of -22.50 kcal/mol. This suggests that the stability of this adsorbed complex matches closely with the literature reports. The reported adsorption energy [218] for Au_7CO and Au_8CO is also higher than our computed values, calculated at a different level of theory but the trend can be said to be the same with the results reported in the present study.

On the basis of these results presented in **Table 4.1**, two pertinent comments can be made. Firstly, it can vividly be seen that the influence of the hydrogen atom doping on the CO adsorption is much stronger than the pristine gold as well as the lithium metal-doped gold clusters. Another very interesting and striking observation is that the Na metal doping surprisingly, does not play any role in enhancing the CO adsorption energy and we also find that for Na doped gold clusters, OC mode of interaction is more favored in comparison to the CO mode. Let us now discuss the variation of interaction energy with cluster size in details. For the HLYP case, one common observation is that for the cluster size $n<6$, the H atom doped gold cluster favorably interacts with the CO molecule as compared to the pristine and alkali metal atom doped clusters, as shown in **Figure 4.4 (a)**. However, the only exception is the cluster size *n*=3 where Au_2Li has the interaction energy of -24.19 kcal/mol. The cluster size *n*=6 is a special case where the pristine gold cluster Au_6 interacts more favorably than all its doped counterparts. For higher cluster sizes i.e. *n*=7, 8, the interaction energy for H doped gold cluster is appreciably larger than the pristine ones. For instance, the interaction energy increases from -10.53 kcal/mol for the complex Au_7CO to -25.95 kcal/mol for Au_6HCO. More interestingly, we observe nearly fivefold increase in interaction energy from -4.9495 kcal/mol to -25.839 5kcal/mol as we move from the complex Au_8CO to Au_7HCO. Even, for these two higher cluster sizes, the alkali metal doped clusters show higher interaction energy than the pristine gold clusters. Almost similar kind of variation of interaction energy is obtained with M06 functional which is shown in the **Figure 4.4 (b)**. We find that clusters with *n*=3 and 6 are the two cases where the pristine clusters manifest higher interaction energy than their H atom doped counterpart. In all other cases, clusters doped with H atom correspond to higher interaction energy than pristine clusters. Significant enhancement in interaction energy for the higher clusters particularly, *n*=7, 8 is also observed as was the case with HLYP functional. It is also worth mentioning from the results derived from the M06 functional, that the alkali metal atom doped clusters seem to show no enhancement in the interaction energy and the values were found to be lower than those of both the pristine and H doped gold clusters. The important point that can be made is that except for cluster size 6, there is remarkable enhancement in interaction energy for H-doped gold clusters as compared to their pristine and Li doped counterparts. We can also find enhancement of adsorption energy for Li-doped clusters as compared to the pristine ones for cluster size corresponding to 3 and 7. However, for cluster size 6 we find the pristine cluster to correspond to higher adsorption energy as compared to the H and Li/Na doped ones. For computing the interaction energy, we have also used the M06 functional and the corresponding values are reported in **Table 4.1**. This functional also predicts the enhancement of interaction energy for H doped clusters for all sizes under study. Although there is very little enhancement in adsorption energies for the smaller clusters up to size 4, there is significant enhancement for larger clusters in the series. In all the cases the interaction energy as given by the M06 functional is higher than their corresponding HLYP counterparts. Nevertheless these values are more close to the earlier reported values using PW91 functional.

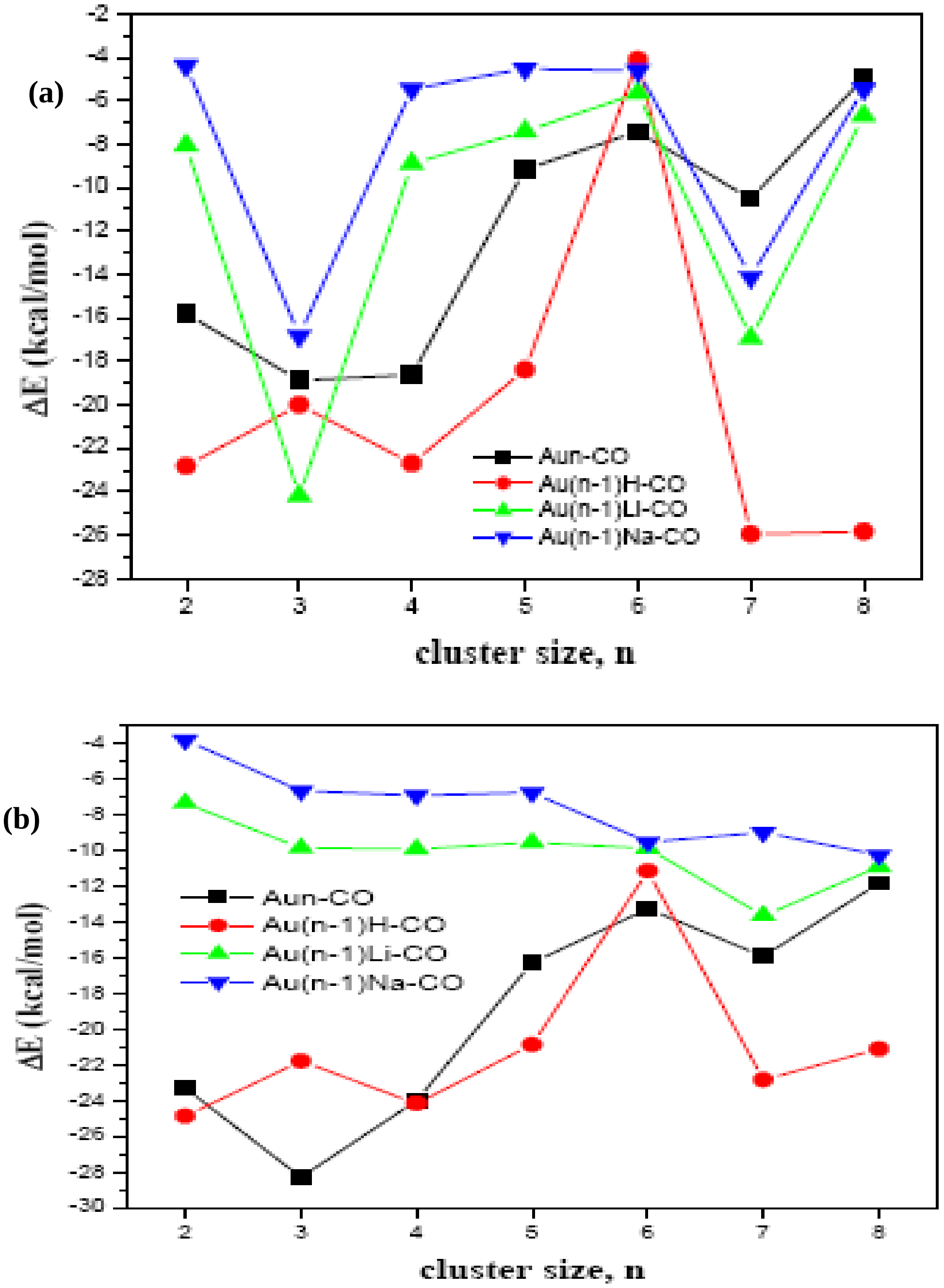

Figure 4.4: Variation of CO interaction energy of pristine and doped gold clusters obtained by using HLYP (a) and M06 (b) methods with cluster size.

Table 4.1: Variation of interaction energy (kcal/mol) of pristine and doped gold clusters with cluster size.

Cluster size (n)	Au_nCO		$Au_{n-1}HCO$		$Au_{n-1}LiCO$		$Au_{n-1}NaCO$	
	HLYP	**M06**	**HLYP**	**M06**	**HLYP**	**M06**	**HLYP**	**M06**
2	-15.80	-23.30	-22.81	-24.88	-8.06	-7.35	-4.38	-3.82
3	-18.87	-28.31	-20.00	-21.80	-24.19	-9.86	-16.82	-6.66
4	-18.62	-24.00	-22.69	-24.17	-8.90	-9.92	-5.46	-6.91
5	-9.15	-16.29	-18.38	-20.87	-7.40	-9.55	-4.52	-6.76
6	-7.42	-13.27	-4.12	-11.15	-5.65	-9.89	-4.61	-9.54
7	-10.53	-15.93	-25.95	-22.84	-16.94	-13.64	-14.12	-8.99
8	-4.94	-11.82	-25.83	-21.12	-6.69	-10.91	-5.45	-10.26

Table 4.2: Mulliken charges on the dopant atoms of the doped gold clusters.

Cluster size (*n*)	Charge on H	Charge on Li	Charge on Na
2	0.0333	0.2449	0.4115
3	0.0945	0.4890	0.7510
4	0.0070	0.6378	0.8049
5	0.1827	0.7356	0.8018
6	0.1784	0.9478	0.6998
7	0.2033	0.7492	0.8116
8	0.2764	1.0329	0.8464

The most strikingly important point that emerges out from the above discussion is that gold clusters doped with H atom favorably interact with CO molecule as compared to the pristine clusters particularly for the higher members in the size range. This can be thought of as the chemical activation of gold clusters towards CO adsorption. The cluster Au_8 in particular has been extensively explored for the catalytic oxidation of CO and very recently Hakkinen et al. [219] in their temperature-programmed reaction (TPR) measurements of CO oxidation reaction have shown that the smallest gold cluster that catalyzes the reaction is Au_8. They have also outlined that nature of bonding and the activation largely govern the remarkable chemical size-sensitivity of this reaction. To illustrate the potential role a dopant atom can play they have shown that while Au_4 is catalytically inert, the doped cluster Au_3Sr is active. [219] This kind of observation can give new impetus to our results. The multiple enhancement in the interaction of CO for Au_7H than the pristine Au_8 is certainly an indication of activation by the introduction of the H atom. In fact, this might act as a better candidate for the CO oxidation reaction as well.

To have a deeper understanding of our observation, we have examined the Mulliken charge values of the dopant atoms. Our results reveal that for the Mulliken charges obtained by HLYP method, there is no consistency in the sign of the charge value on the H, Li or Na in the gold cluster before the interaction and also in the gold cluster-CO complexes. On the other hand, M06 yields charge values quite consistent and hence, we have considered only the M06 based results which are reported in **Table 4.2**. These results indicate that in the H-doped cluster, the H atom carries positive charge and its neighboring interacting Au atom carries negative charge. A known phenomenon for hydrogen in metals [220--222] is that it is present in an “anionic” form. The positive charge on H atom is reminiscent of its anomalous behavior as reported by Buckart et al. [214] The charge on Li or Na atom in doped clusters is positive which is expected as it is an electropositive metal. However, Li/Na atom carries a higher value of positive charge than the H atom in the doped clusters. From this observation, one may conclude that lower positive charge on the doped H atom plays some role in the enhancement of interaction. Recently, Wim et al. [223] have discovered that short-range electrostatic effects were significant in tailoring the O_2 dissociation process which was crucial for CO oxidation. Given the fact that CO adsorption is largely governed by electrostatic interaction, a detailed investigation is really needed to comment on the role of H atom in the gold clusters. Another important reason can be the electronegativity difference. Au and H atoms have nearly comparable electronegativity values (Au=2.4, H=2.2) whereas alkali metal atoms Li and Na have much smaller values.

4.2: Role of Substrates for Gold Clusters

In the first section of this chapter, we have discussed the structure and electronic properties of pristine and doped gold nanoclusters. It is pertinent to understand, as a first step, the CO adsorption behavior of these nanoclusters to assess their catalytic properties. Following this line of thought, we have already discussed the adsorption of CO molecule on the bare clusters. Now, we will consider the effect of carbon nanostructure surface on the adsorption of CO molecule on gold clusters supported on these surfaces.

In general, the surfaces that have been explored both theoretically and experimentally for supported nanocatalysis by gold clusters are high surface area oxides like MgO or TiO_2. [204] Apart from that, in recent times carbon based nano materials are emerging as exceptionally better choices as surfaces for supported catalysis by nanoparticles. Carbon based nanomaterials relevant to our discussion essentially mean the planar (2D) honeycomb sheet graphene[224-226] and its rolled counterpart carbon nanotube[15] (CNT). This fascinating material graphene has grabbed much attention of researchers for its interesting electronic and photonic device applications. Adding a new dimension to the vast and vivid horizons of diverse applications, very recently graphene supported transition metal catalysis has attracted considerable interest. Carbon nanotube, on the other hand, has been at the focal point of modern day research in nanoscience and nanotechnology for its pluralistic properties and applications. [227] Nanoparticles decorated CNT (NP-CNT) are also emerging as promising candidates for application like gas sensing and catalysis and bio-medical applications. [228-235] In a very recent study, in an attempt to fortify the idea of sensory applications of NP-CNT system, Kauffman et al. [236] based on their combined theoretical and experimental investigations have concluded that Au nanoparticles decorated CNT can be a potential gas sensor for CO. More importantly, in their interesting observations, they concluded that while the bare CNT does not respond to CO gas Au-NP-CNT system shows remarkable affinity for CO. Underlining the importance of NP-CNT interface, from their electronic structure calculations, they have also indicated dramatic variation in the charge density at the interface. Hence, it follows that the surface of carbon nanomaterials, viz. graphene and nanotubes are excellent supports for anchoring nanoclusters and facilitating their gas sensing as well as catalytic activities. Apart from the surface of the CNT, the interior of it can also be thought as a nanochannel that can promote several chemical transformations. The confinement of CNT as a medium conducive for various reactions has thus attracted immense interest. There has been very fascinating reports that nanoparticles anchored inside the CNT act as an efficient catalyst system for the production of methanol. [237]

Galvanized by these intriguing findings, we plan to study the importance of surface effects of aforementioned carbon nanomaterials on the adsorption of nanoclusters and their consequence on catalysis or sensor responses. From the rationale obtained from the preceding discussions, we envision three different types of surfaces, namely a planar sheet of graphene, a convex surface and a concave surface, where the later two representing the exterior and interior of CNT. In our previous study, we have made an attempt to study the doping effects of alkali metal atoms along with H on small gold clusters in the size range 2-8.[238] Consequent upon this, we have also studied adsorption of CO on these clusters. In our interesting findings, we have observed great enhancement of CO binding with the corresponding H-doped gold clusters as compared to its un-doped pristine counterpart. This enhancement was more prominent for cluster size of 8. Interestingly, we have also demonstrated that H atom in the environment of gold clusters also leads to activation of oxygen molecule and concomitant reduction in barrier height for CO oxidation reaction.[239] With these encouraging initial results, in the present study, we further attempt to investigate the effect of the aforementioned three different types of surfaces of carbon nanomaterials on the adsorption of gold cluster Au_8 and its H-atom doped counterpart Au_7H. Also, we have attempted to study the adsorption of CO molecule on these supported nano clusters. Our study is the first step in the process of overall exploration of supported gold clusters on carbon nanomaterials and pertinent role in the burgeoning field of catalysis and sensors.

From the detailed analysis of adsorption energies and charge transferred to gold clusters, we derive important conclusions relevant to the real world of catalysis. On the comparison of gold cluster Au_8 with its doped counterpart Au_7H we observe great enhancement of CO adsorption for the H-doped cluster as compared to the pristine one. These results are of endearing importance to the understanding of effect of doping, effect of surface curvature to the field of cluster assisted nanocatalysis at large. Furthermore, our studies also underpin the importance of nanoparticles and carbon nanomaterials-surface system for sensing applications.

4.2.1: CO Adsorption on Supported Gold Clusters

In this section, we will discuss our results under two different heads focussing adsorption of bare clusters on the surface and subsequent CO adsorption on the supported clusters.

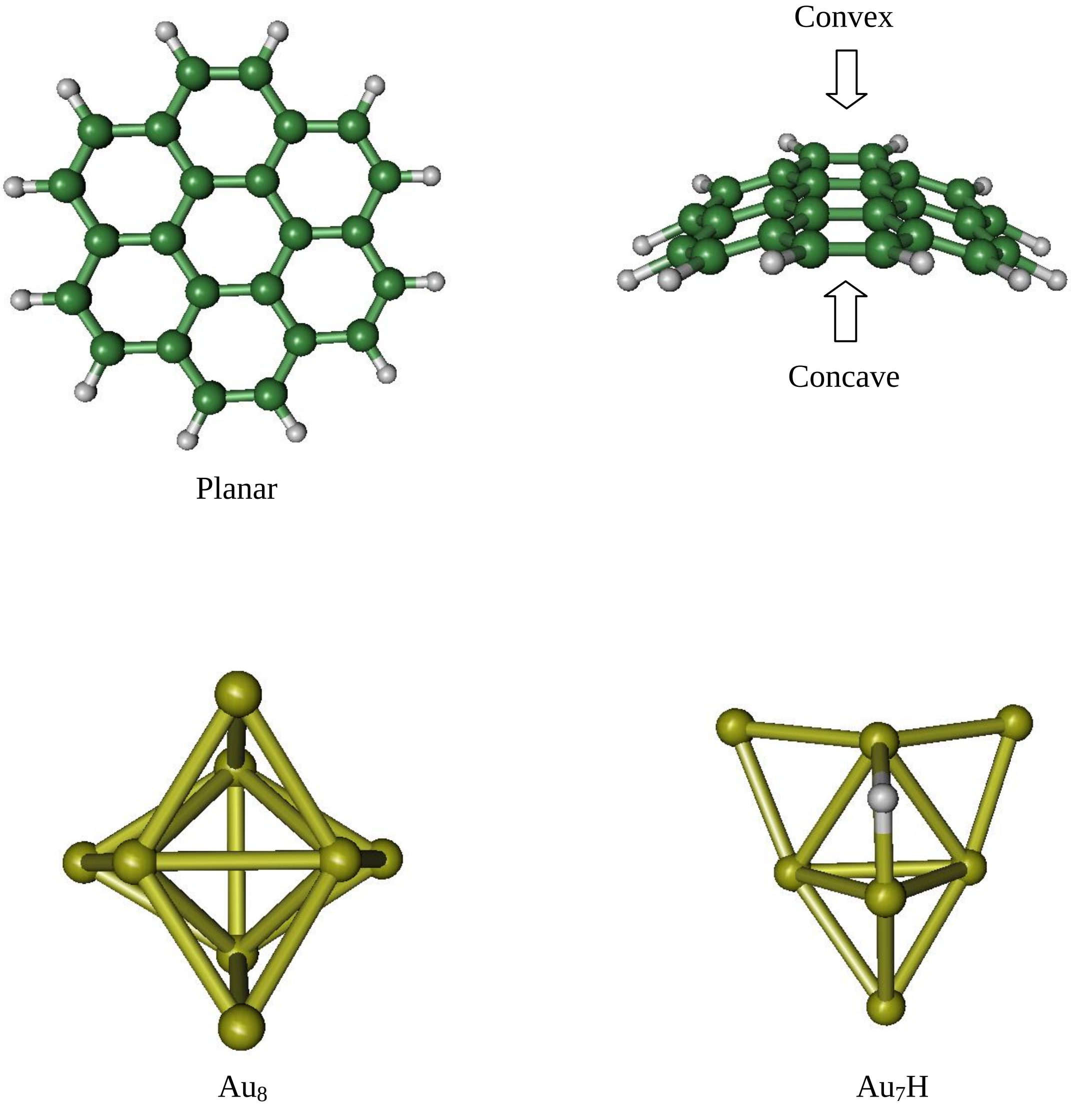

Figure 4.5: Optimized geometries of clusters Au_8 and Au_7H and three types of surfaces; planar, concave and convex of carbon nanostructures considered in the study.

4.2.1.1: Adsorption of Clusters on the Model surfaces

Model structures that represent the surface of graphene and carbon nanotube have been illustrated in Figure 4.5. The planar structure is part of the graphene and the curved surface is taken from CNT. The structures of the two different clusters namely pristine Au_8 and its H-atom doped counterpart Au_7H considered in the present study are also presented in Figure 4.5. The geometries of these two clusters have been the same as considered in our previous study. To begin with, let us consider the adsorption of clusters Au_8 and Au_7H on the three different surfaces namely planar, concave and convex. The optimized geometries of the clusters adsorbed on the three different types of surfaces have been presented in Figure 4.6. The adsorption energy of the clusters on the surface E_{ads} is nothing but the difference in energies between the adsorbed cluster systems and the individual constituents (surface and the cluster). These values are presented in Table 3. We observe, from these results that for the pristine cluster Au_8, E_{ads} is the minimum for the convex surface and maximum for the concave surface, having the values -5.37 and -9.83 kcal/mol respectively. For the planar graphene, the adsorption energy is intermediate having a value of -7.22 kcal/mol. From these observations it is inferred that pristine gold cluster Au_8 preferentially bind to the concave surface. The binding energy for concave surface, however, is also nearly twice that of the convex surface. Turning our attention to the doped cluster Au_7H we find that the adsorption energies are nearly the same for plane and convex surfaces. The adsorption of this particular cluster is favored for the concave surface where E_{ads} is the maximum. On comparing the adsorption energies of both the clusters, we find that for a particular type of surface considered, doped gold cluster Au_7H preferentially adsorbs on the surface. Furthermore, comparing the binding tendencies of different types of surfaces, it is found that a concave surface favorably binds the clusters. These results lead us to many important conclusions.

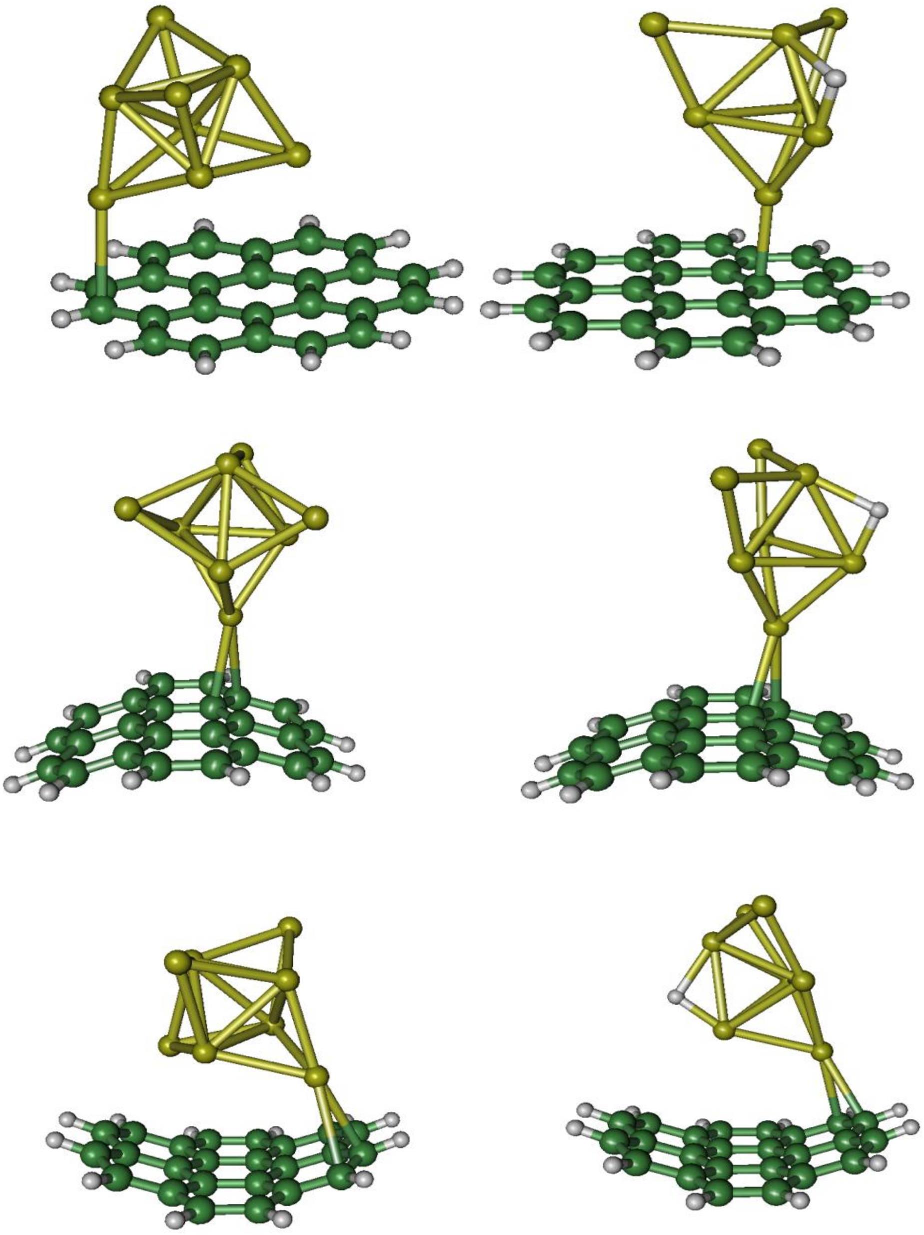

Figure 4.6: Adsorption of the clusters Au_8 and Au_7H on the planar, convex and concave surfaces of carbon nanostructures.

Firstly, on doping the pristine gold cluster with a single H-atom, the H-doped gold cluster turns out to be a better candidate for catalysis or sensor applications in terms of their favorable adhesion to the surface of carbon nanomaterials. More importantly, the highest adsorption energies for a concave surface towards these clusters essentially indicate that the interior of the CNT can have a profound role in promoting chemical transformations as evinced form a simple model calculations.

4.2.1.2: CO Adsorption on Supported Gold Clusters

In furtherance of our discussion, we now consider the adsorption of CO molecule on these pre-adsorbed gold clusters on the three different types of surfaces mentioned in the previous section. In practice, the CO molecule is made to adsorb on the same clusters Au_8 and Au_7H that has already been adsorbed on the model surfaces as presented in Figure 4.6. The CO molecule can have multiple adsorption sites in a given cluster. Based on the preliminary knowledge from our previous investigations, we have considered several possible CO adsorption sites for a particular cluster and the energetically most stable one, out of several possibilities for a particular surface-cluster combination, has been chosen for further discussion. The optimized structures of cluster-CO complex along with the surface have been presented in Figure 3. In general, it has been observed that CO preferentially interacts with a low coordinated peripheral Au-atom in the case of pristine cluster Au_8. Conversely, for the doped cluster Au_7H, gold atom directly attached to the dopant H-atom shows favorable adsorption of CO molecule, an observation consistent with our previous study. On a careful look at the structures of the CO-adsorbed clusters, we find that for the pristine cluster, there is very little change in the geometry of the cluster consequent upon the adsorption of CO molecule for the three different types of surfaces under investigation. The doped cluster Au_7H, on the other hand, undergoes significant distortion in its geometry in the CO adsorbed complex. As illustrated in Figure 4.7, we can see that in structures of Au_7H-CO complex adsorbed on the planar and concave surfaces, one of the Au-H bond in the cluster is elongated whereas the other shrinks when compared to the corresponding structures without CO adsorption. This suggests the fluctionality in the structure of the doped cluster upon CO adsorption. This observation is also in tune with our earlier reports of significant change in structure of bare Au_7H cluster from its initial 3D structure to a planar 2D one after the adsorption of CO molecule. In the current study, however, due to the effect of the surface, the structural distortion for the doped cluster Au_7H is not as dramatic as in the previous case. Considering, next, the energetics of CO adsorption, the calculated adsorption energies have been presented in Table 4.3.

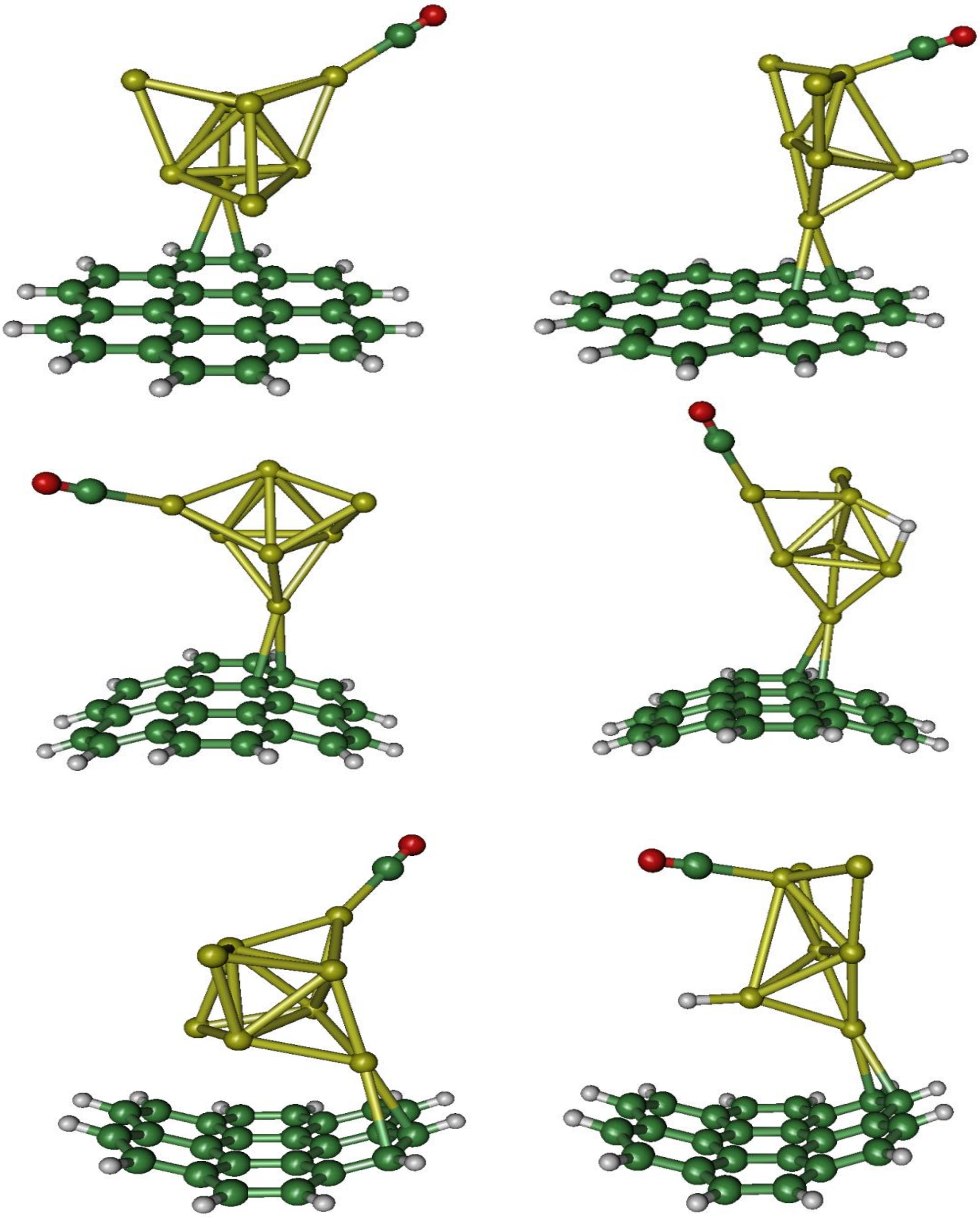

Figure 4.7: Adsorption of CO molecule on clusters Au_8 and Au_7H held on the planar, convex and concave surfaces of carbon nanostructures.

Table 4.3: Adsorption energies of clusters Au_8 and Au_7H on three types of surfaces of carbon nanostructures, adsorption energies of CO on supported clusters and charges on the cluster and CO molecule.

Type of Surface	E_{ads} in kcal/ mol^{-1} (surface+cluster)		E_{ads} in kcal/ mol^{-1} (surface+cluster+CO)		Q (in e) on cluster (surface+cluster)		Q (in e) on cluster (surface+cluster+CO)		Q (in e) on CO	
	Au_8	Au_7H	Au_8	Au_7H	Au_8	Au_7H	Au_8	Au_7H	Au_8	Au_7H
plane	-7.22	-7.32	-3.33	-10.10	-0.25	0.04	-0.31	-0.10	0.05	0.07
convex	-5.37	-7.96	-6.45	-9.9	-0.02	-0.03	-0.14	-0.07	0.08	0.06
concave	-9.83	-11.02	-3.11	-10.35	-0.32	-0.21	-0.36	-0.24	0.05	0.07

For the pristine cluster Au_8, we find the adsorption energy is nearly the same for the planar and concave surface. Strikingly, the E_{ads} for the pristine cluster is almost doubled for the convex surface. The pertinent conclusion we make from this observation is that, pristine gold cluster Au_8 adsorbed on the surface of CNT can be a better choice for catalyst for the CO oxidation reaction. Also, this cluster-nanotube surface system can be a suitable candidate for sensing molecules like CO which exhibits the highest binding affinity. The results for the doped cluster Au_7H are equally interesting. We find, for this doped cluster that the CO adsorption energy of three different types of surfaces is nearly the same which is around 10.0 kcal/mol. This signifies that, in contrast to the pristine gold cluster, its doped counterpart is a better choice for catalysis or sensor irrespective of the nature of the surface of carbon nanomaterials considered. On a careful comparison of CO adsorption energy for both the clusters for a particular type of surface under consideration, we always find a significant enhancement of E_{ads} for the doped cluster. For the planar and concave surfaces, the CO adsorption energy of Au_7H cluster is three times that of the pristine cluster. For the convex surface, E_{ads} for Au_7H is nearly twice as that for the cluster Au_8.

To get deeper insights into the adsorption of clusters and subsequent CO adsorption on them, we have computed the net charge transferred to the cluster (in units of electronic charge e) and to CO molecule. These results have been presented in Table 4.3. In the absence of CO, the net charge transferred to Au_8 carries higher negative values for plane and concave surfaces, as compared to that for the Au_7H. For the convex surface, the net charges transferred to both the above clusters are comparable. It is also observed that the charge transferred to the clusters, Au_8 and Au_7H, is the maximum for concave surface as compared to that of convex and planar surfaces. It follows from this observation that charging effects of the clusters will be more prominent for the clusters encapsulated inside the CNT. This observation is also supported by the enhancement of binding energies of clusters for concave surfaces. On a careful observation of the effect of H-atom doping on charging of clusters and their subsequent CO adsorption, we notice that doping makes the clusters more positively charged as compared to the pristine clusters. In turn, the lesser negative charge on Au_7H manifests itself in the form of increased binding energy of CO molecule. For instance, the charge transferred to cluster changes from -0.25 to 0.04 for the planar surface as we move from the cluster Au_8 to Au_7H. This significant variation in the charge is also reflected in threefold enhancement in CO adsorption energy from -3.33 to -10.1 kcal/mole. This fact underlines the effect of charging of gold clusters by suitable doping with H-atoms. Turning our attention to the charge transferred to clusters after CO adsorption, we notice that adsorption of this molecule leads to a more negative charge on the clusters. This observation indicates that there is partial transfer of electrons from CO molecule to the cluster on its adsorption. Moreover, on comparison of the three types of surfaces it is found that the concave surface induces significant charging effects on the clusters. Finally the charge on CO molecule has also been presented in Table 1 for comparison. It is, however, observed that there is not much variation in the charge on CO where the value ranges between 0.05-0.08.

4.3: Computational Details

The geometry of all the clusters have been optimized without any symmetry constraints at the level of density functional theory based methods using the electronic structure program GAMESS. [240] The split-valence basis set with diffuse and polarization functions namely, 6-31++G(d, p) have been employed for C, O, H, Li and Na. We have used the LANL2DZ[241-243] effective core potential (ECP) for Au. The charge on each atom has been obtained by the Mulliken population analysis. In the following discussion, IP and EA refer to the vertical ionization potential and vertical electron affinity, respectively and it is assumed that the lowest-energy structure of the charged state is same as that of the neutral cluster. IP is calculated as the difference of total energy of the neutral species and its positively charged counterpart. Likewise, EA represents the difference of total energy of the negatively charged cluster and its neutral counterpart. Binding energy per atom (BE) of the cluster is defined as,

$$E_b\,[\mathrm{Au}_{n-1}\mathrm{X}] = ((n-1)E[\mathrm{Au}] + E[X] - E[\mathrm{Au}_{n-1}\mathrm{X}])\,/\,n$$

where X is the dopant atom. And finally, the parameter η describing the chemical hardness can be defined as $\eta \approx (\mathrm{IP-EA})/2$. [244, 245] The adsorption energy of CO, $E_{\mathrm{ads},}$ with all the gold clusters are calculated using the expression,

(1) for pristine gold clusters, $E_{\mathrm{ads}} = E(\mathrm{Au}_n\,\mathrm{CO}) - (E(\mathrm{Au}_n) + E(\mathrm{CO}))$

and (2) for doped gold clusters $E_{\mathrm{ads}} = E(\mathrm{Au}_{n-1}\mathrm{X}\,\mathrm{CO}) - (E(\mathrm{Au}_{n-1}\mathrm{X}) + E(\mathrm{CO}))$

where the first, second and the third terms in both the expressions correspond to the calculated energies for CO-Au-cluster complex, the bare/doped cluster and the CO molecule, respectively. We have employed the full Hartree-Fock exchange functional along with the Lee-Yang-Parr (LYP) correlation functional in the density functional calculations.

Since CO adsorption is weak in nature, proper inclusion of the electron correlation effect is important for its prediction. The performance of DFT-based exchange-correlation functional, although, is satisfactory in most cases, is not good enough for the description of weak interactions. Hence, we have used a new exchange-correlation energy density functional, M06, proposed by Zhao and Truhlar. [51-52] The M06 functional is a hybrid *meta*-GGA exchange-correlation functional, which has been shown to be quite successful for the accurate calculation of thermochemical, noncovalent interactions and excited states. [51-54] In particular, the overall performance for weakly interacting cases and π-π stacking systems are shown to be better with the M06-based functional than conventional DFT methods. [53, 54, 246] Hence, apart from using LYP correlation, we have also employed M06 functional to calculate the interaction energies of all the CO adsorbed complexes. The optimized geometries as given by HLYP method have been used as the initial geometries for the M06 level of calculation with basis functions for both the methods remaining the same. We have tried to critically evaluate the performance of this newer functional M06 for the prediction of interaction energy. All the initial structures for the gold clusters have been made by using graphical software Gabedit. [247]

For the second part of this chapter, the geometries of the two clusters considered in the work namely Au_8 and its H-atom doped counterpart Au_7H are essentially taken from the previous section of the chapter. The geometry of all the clusters have been optimized without any symmetry constraints at the level of density functional theory based methods using the electronic structure program GAMESS. [240] The split-valence basis set with diffuse and polarization functions namely, 6-31++G(d, p) have been employed for C, O and H. We have used the LANL2DZ[242,243] effective core potential (ECP) for Au. We have employed the full Hartree-Fock exchange functional along with the Lee-Yang-Parr (LYP) correlation functional in the density functional calculations. The three different types of surfaces representing surfaces of graphene and interior and exterior of CNT essentially have a total of 24 C-atoms and 12 H-atoms in common. The curved surface considered in our study has been taken from the surface of an armchair (10, 10) CNT where the numbers in the parenthesis represent chiral vectors for the nanotube and this surface has been terminated with H-atom to saturate the dangling bonds. Furthermore, the geometry of this curved surface has been kept frozen in our calculations otherwise on geometry optimization this surface will lead to a planar one like that of graphene and thus missing the effect of surface-curvature. The charge transferred to the cluster has been computed as the sum of Mulliken charges.

4.4: Summary of the Work

To summarize the first section of this chapter, the electronic structure and properties of pristine gold clusters Au_n as well as the alkali metal and hydrogen atom doped clusters $Au_{n-1}X$, where n=2-8, X=Li, Na and H, have been investigated. The dopant atoms are interesting from the perspective that they have similar outer electronic configuration in the form of single valence electron like the gold atom. Electronic properties such as ionization potential, electron affinity, binding energy, HOMO-LUMO gap and hardness parameter are found to exhibit a regular odd-even oscillatory pattern with variation of the cluster size. Our results reveal that the role of hydrogen atom in modulating the structural and electronic properties of gold clusters is antagonistic to that of the alkali metal atoms. The HOMO-LUMO gaps for the hydrogen doped gold clusters are found to be much higher than the pristine as well as alkali metal atom doped clusters. In addition, we have also made an extensive study to investigate the important role of the impurity atoms, viz. hydrogen and alkali metal atoms, on the adsorption of CO molecules by the doped gold clusters. Enhancement of CO-adsorption energy has been observed for the gold clusters doped with hydrogen atom rather than for the corresponding alkali metal doped clusters and the enhancement is observed to be more pronounced for the higher clusters in the series. An interesting observation is that there is as high as fivefold increase in the interaction energy of CO with Au_7H cluster as compared to its pristine counterpart Au_8. Our findings may give new impetus to the investigation of catalysis by gold nano clusters which are suitable candidates in the arena of green chemistry. The novelty of this concept and prospect of doping can also be explored for gold clusters of other sizes and other reactions being catalyzed by gold nano clusters. Furthermore, we have only considered gold clusters doped with single dopant atom and the possibility can be extended to more than one dopant atom per cluster. Further studies addressing these issues and their ramifications on real world of catalysis can be of great interest.

In the latter section of this chapter, to understand the effect of surface of carbon nanomaterials on the adsorption of gold clusters we have considered three model surfaces. These surfaces namely planar, convex and concave essentially represent the surfaces of graphene, nanotube exterior and interior respectively. The gold clusters considered in the present study are pristine cluster Au_8 and its H-atom doped counterpart Au_7H. Towards the first step to adjudicate the efficacy of these nanomaterial-cluster systems for catalytic oxidation of CO and sensory applications, we have studied CO adsorption on these systems. In our valuable findings, we conclude that the adsorption of bare clusters is favored for concave surfaces. Notably, the adsorption energy for the cluster Au_8 is almost doubled as we move from convex to concave surface. This observation signifies the importance of nanotube interior acting as a surface conducive for adsorption of clusters as compared to the exterior surface. However, regarding doping the cluster with H-atom, we find the adsorption energy of clusters with the surface is slightly higher for the doped cluster. Most interestingly, the combined effect of the nature of the surface and effect of H-atom doping is reflected in the adsorption energy of CO on these systems. The value of E_{ads} for the doped cluster is always observed to be enhanced as compared to that of the undoped cluster. The enhancement is as high as threefold for planar and concave surfaces for the cluster Au_7H as compared to that of Au_8. For the undoped cluster the nature of the surface plays some role in deciding the CO adsorption energy as we find that for convex surface, i.e. on top of the CNT, the value of E_{ads} is doubled as compared to the other two variants of model surfaces. On the other hand, for the doped cluster Au_7H, the effect of doping outweighs the effect of nature of surface curvature as the adsorption energy of CO molecule is nearly the same for three surfaces. Considering the charge transferred to clusters, we have tried to rationalize our findings. It is found that a lower negative charge on clusters favors efficient CO binding. Based on these findings, in a very broad qualitative sense it can be put forward that as compared to the surface of graphene, CNT can be a better choice as a support for CO oxidation reaction and also a better sensor for CO. Also, doping gold clusters with H-atoms may help boost the catalytic reaction. Our study underpins the effect of nature of surface of carbon nanomaterials and effect of doping on adsorption of CO molecule which have broader implications in the field of catalysis and sensors. More exploration of detailed catalytic process of CO oxidation on cluster assisted carbon nanomateral surfaces are however needed to consolidate our study which is likely to stimulate further interest.

CHAPTER 5

Tuning the Electronic Properties of Gold Clusters for Efficient Catalysis: CO oxidation as a Case Study

Chapter 5: Tuning the Electronic Properties of Gold Clusters for Efficient Catalysis: CO oxidation as a Case Study

In this chapter, we have delved into the details of the catalytic properties of small gold clusters. The catalytic reaction we have chosen is oxidation of CO to CO_2. This chapter is broadly divided into three sections. In the first section, we have discussed the effect of a single H-atom substitution in a gold cluster Au_8 and its ramifications on the catalytic efficiency of the clusters. In the second part of the chapter, we have made an attempt to identify the factors that primarily govern the catalytic properties of gold clusters. By considering gold clusters doped with several types of impurity atoms which vary in their electronegativity values, we put forward some important governing factors. The last section of this chapter deals with designing composite nanostructures consisting of DNA bases and gold clusters. We propose that the DNA base-gold cluster complexes can be an potential model nanostructure for CO oxidation.

5.1: Importance of Hydrogen in Gold Clusters

Since antiquity, the shine and sheen of gold have been a cause of irresistible temptation for everyone. On the flip side of this shinning glory, being hailed as the noblest of all metals in the bulk form of matter, gold has also been regarded as a poor catalyst in heterogeneous catalysis. Dispelling the myth of inertness of gold, it was the path-breaking report of Haruta et al.[180] which showed that nanoscale gold can be catalytically active. It has been shown that supported gold clusters catalyze several chemical reactions; the most notable is the environmentally important reaction of combustion of CO to CO_2 at temperatures far below the room temperature.[25] Following these initial reports, investigations of structure and reactivity of gold clusters and their relevance to heterogeneous catalysis have emerged as one of the hottest trends in contemporary research. Some of the factors that predominantly govern the catalytic activity of these clusters are shape and size of the cluster, charge state, nature of the support material and more importantly doping of the cluster. Interestingly, for gold clusters of size ~1-nm or even sub-nanometer, the significance of quantum size effects for CO oxidation has recently been demonstrated.[248] The effect of doping[219] is of special importance to the field of catalysis from the perspective of modulating the structure and electronic properties of gold clusters and also from the cost-economy point of view where the dopant atom is essentially a cheaper element.

Hydrogen in gold has a special relevance considering the so-called gold-hydrogen analogy as established by Kiran et al.[249-251] where the chemistry of gold atom resembles that of a single hydrogen atom. Extending a step further, this Au/H analogy initially reported for mono and disilicon gold clusters have also been extended to trisilicon gold clusters by the same authors.[252] Adding new dimensions to this intriguing and expanding chemistry of gold, Zhai et al.[253] have demonstrated that Au mimics H in its bonding to boron in a manner similar to Au-Si bonding. Interestingly, a recent study by Zhai et al.[254] also sheds light on the analogy between a BO unit and Au atom in cluster systems $B_{11}O^-$ and $B_{10}Au^-$. Fortifying the idea that gold behaves as hydrogen, Ghanty[207] has shown a unique one-to-one correspondence between AuBX (X=F, Cl, Br) and HBX radicals. All these reports essentially provide a fertile background to widen up further explorations in the burgeoning field of gold clusters and their fascinating chemistry. In order to investigate the temperature and quantum effects towards the stability of pure and doped gold nanowires, the *ab initio* molecular dynamics simulations of Hobi Jr. et al.[255] have concluded that doping atomically thin gold nanowires with light impurity atoms like H leads to stabilization of the wires. In a very fascinating findings, Buckart et al.[214] from their photoelectron spectra of bare Au_n^- and $Au_{n-1}H^-$ clusters that exhibit surprising similarities, have concluded that H-atom in gold clusters behaves like metal. Interestingly, both gold and hydrogen have closely similar electronegativity value and similar electronic configuration in the form of a single valence electron. Therefore, if there is any modulation in the properties of gold clusters by doping a cheaper element and a dopant like H helps boost their catalytic activity, it can be regarded as an added advantage from the point of view of cost. These results prompted us to explore the effect of H-atom doping on the structural and electronic properties of gold clusters in a detailed manner. From our previous study[68] on the effect of doping alkali atoms along with hydrogen in the small gold clusters, we have found that indeed H-doping of gold clusters stabilizes the cluster which is reflected from the increased binding energy per atom values obtained for the H-atom doped clusters as compared to the pristine ones. Furthermore, as a first step to help understand the catalytic properties of these clusters, we have also studied the adsorption of a single CO molecule on these clusters, where we have observed significant enhancement of adsorption energy for the H-doped gold cluster as compared to their pristine counterparts.[68] Most notably, it is for the cluster Au_7H where the CO adsorption energy was found to be nearly five times that of the pristine cluster Au_8. Moreover, Au_8 cluster has special significance as it has been previously shown that an eight-atom gold cluster is the smallest one to catalyze CO oxidation.[256] Hence Au_8 cluster can be suitably taken as a model cluster system for the investigation of electronic structure and properties as well as the catalytic activity of gold clusters.

In order to have an assessment of how efficient is the strategy of H-atom doping in gold clusters, our density functional theory (DFT) based investigation sheds light on the adsorption of O_2 molecule on the clusters Au_8 and Au_7H as well as the computation of barrier heights for the oxidation of CO to CO_2 on these clusters. In this context, it is worthwhile to mention that describing molecular oxygen interaction with Au_n clusters is intriguing from two considerations. Firstly, the structures of small gold clusters are known to be fluxional and interestingly Au_8 cluster lies at the borderline where a transition of cluster geometry from planar to a 3D structure takes place.[213] Employing coupled cluster methods (CCSD(T)), Olson et al.[213] have concluded that for Au_8, a non-planar geometry with T_d symmetry is the lowest energy structure. Accordingly, our starting geometry for Au_8 cluster also has the similar geometry. Secondly, the predictions of energetics of binding of O_2 on the gold clusters as predicted by DFT and CCSD(T) methods are sometimes conflicting. In an earlier study, Varganov et al.[257] have demonstrated that O_2 binding with Au_n (n=2, 3) clusters depends sensitively on the method, where DFT and CCSD(T) methods differ in their qualitative predictions. However, they have asserted that for smaller clusters (n=2, 3) although DFT could not reproduce the experimental observations, the results significantly improve for larger clusters. A related study by Ding et al.[258] based on DFT methods have concluded that the molecular oxygen adsorption behavior on Au_n (n=1-6) clusters match with that of experimental results quite satisfactorily. Taking the above facts into account, we have employed several functionals in our study (details mentioned later in Computational Details section). Our study demonstrates that, the effect of H-atom doping helps in activation of O_2 molecules favorably as compared to the undoped clusters. To have molecular level insights into the effect of H-atom doping in gold clusters on their catalytic activity we have considered a well-studied reaction, viz. the oxidation of CO to CO_2. We have computed the activation barrier heights for this reaction where both the reactants are adsorbed on the pristine as well as the H-atom doped cluster. Our results also indicate that there is a decrease in the reaction barrier height on the doped cluster as compared to that on the pristine cluster.

5.1.1: A Step Beyond Gold-Hydrogen Analogy: Doping Gold Cluster with H-atom for O_2 Activation and Efficient CO Oxidation

In this section of the chapter we have discussed our results pertaining to adsorption of oxygen molecule on two clusters Au_8 and Au_7H and the subsequent CO oxidation reaction taking place on these clusters. The optimized structure of pristine Au_8 and its doped counterpart Au_7H presented in Figure 5.1 are similar to the ones reported in our previous study. [68] We first focus on the binding of O_2 with the above two clusters as binding and activation of O_2 are the necessary elementary steps in the CO oxidation process. [259-261] Moreover, for supported gold clusters, it has been established that binding of O_2 is strongly dependent on the cluster size which is in contrast to the adsorption energy of CO which is higher than that of O_2 and is relatively insensitive to the cluster size. [219] The optimized geometries of O_2 adsorbed on clusters Au_8 and Au_7H have also been presented in Figure 5.1 (we explored several possible adsorption sites on these two clusters and the lowest energy structures are presented here).

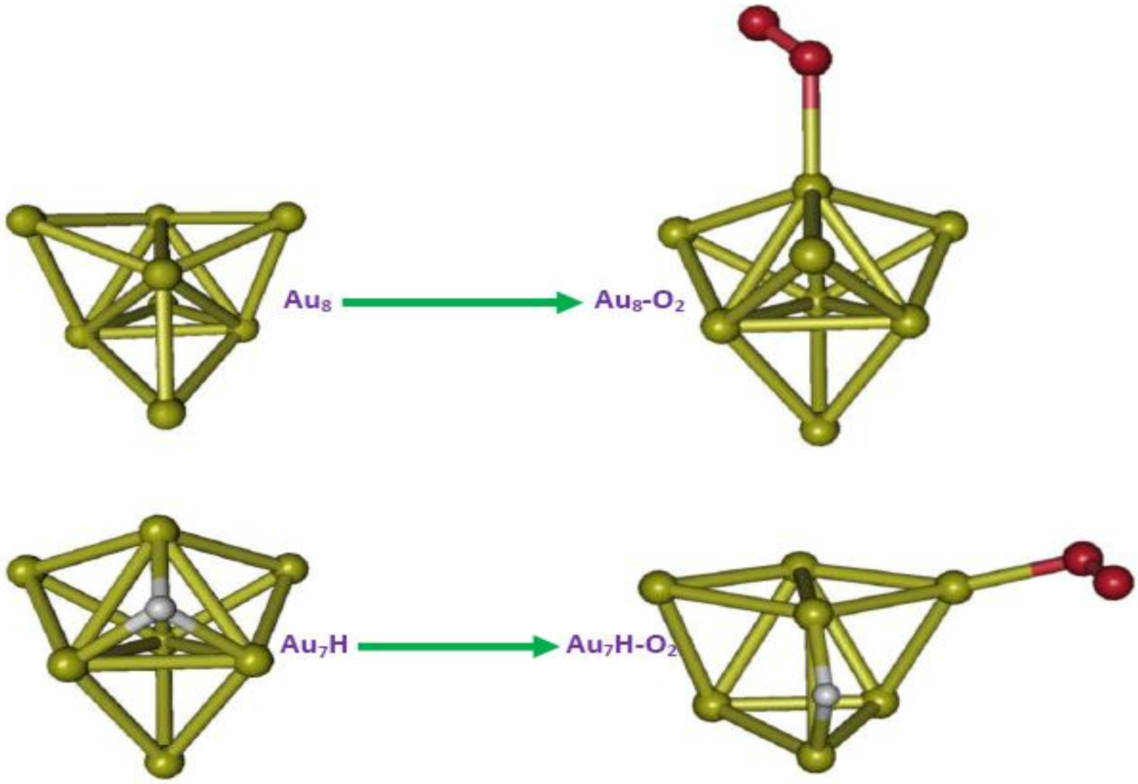

Figure 5.1: Optimized geometries of gold clusters Au_8 and Au_7H along with their complexes with adsorbed O_2 molecule.

The geometries shown in the above figure are essentially obtained from BP86 functional and in our discussion, unless otherwise specified, our results correspond to this functional. It is important to mention that optimized geometries obtained by using PBE and TPSS functionals differ marginally from that of BP86 geometries and the relevant geometrical parameters like O-O bond length ($d_{O\text{-}O}$) and closest Au-O distance ($d_{Au\text{-}O}$) obtained from all the functionals have also been summarized in Table 5.1. Looking at the geometries of the O_2 adsorbed species, it is apparent that Au-O-O bond angle (here Au represents the atom in the cluster that is directly bonded to the CO/O_2 molecule) is nearly 120^0 unlike the case with CO where Au-C-O bond angle is close to 180^0. This is the first difference in the mode of binding of CO and O_2 molecule to the gold clusters. It is reported that even numbered neutral Au_n clusters are closed shell ones and form only weakly bonded physisorbed complexes with O_2.[262] In an excellent demonstration of synergy between photoelectronic spectroscopy and high level *ab initio* calculations, Zhai et al.[263] have established the non bonding behavior of O_2 molecule with closed shell gold clusters. Therefore it is inferred that these clusters are really unimportant from the catalysis point of view as they do not activate O_2. Our computed O_2 adsorption energies (E_b-O_2) with both the pristine as well as H-atom doped clusters obtained from different density functionals have been presented in Table 5.1. Irrespective of the method, it can be clearly seen that the pristine cluster Au_8 binds molecular oxygen very weakly. Our estimation of O_2 adsorption energy (E_b-O_2) for Au_8 as -0.06 eV obtained from BP86 functional is in exact agreement with earlier result by Molina and Hammer.[264] Our result is also in the same line as that of Yoon et al.[262] which concludes that the neutral and cationic gold clusters bind oxygen very weakly and do not induce O-O bond activation. On the contrary, we observe significant enhancement in E_b-O_2 for the cluster Au_7H which is irrespective of the nature of the functional used. For instance, the oxygen binding energy (BP86 result) for H-doped gold cluster is -0.57 eV as compared to -0.06 eV for the pristine cluster. These excellent observations of enhancement in E_b-O_2 on account of H-atom doping in the gold cluster vividly indicates enormous activation of the O_2 molecule.

The binding of oxygen molecule to the gold clusters can be qualitatively rationalized in terms of frontier orbital model.[265,266] The oxygen molecule is a one-electron acceptor and binds strongly to gold clusters with odd number of electrons and the binding is weaker for clusters having even number of electrons. Both the clusters Au_8 and Au_7H are closed shell ones with even number of electrons as both the atoms are monovalent. The weaker binding to Au_8 cluster is justified based on the above arguments. However, for the cluster Au_7H this logic fails. In some recent work on the activity of hydrated anionic gold clusters towards O_2 adsorption, it has been demonstrated that the behavior of OH group being electron withdrawing in nature, it activates the clusters for stronger binding of oxygen molecule. [266]

Table 5.1 : Oxygen binding energy, O-O distance, shortest Au-O distance and O-O stretching frequencies computed for oxygen adsorbed complexes with Au_8 and Au_7H clusters employing different functionals.

Method		E_b O_2 (eV)	$d_{O\text{-}O}$ (A^0)	$d_{Au\text{-}O}$ (A^0)	$\nu_{O\text{-}O}$ (cm^{-1})
BP86	Au_8O_2	-0.06	1.236	2.425	1402
	Au_7HO_2	-0.57	1.248	2.237	1336
PBE	Au_8O_2	-0.12	1.234	2.418	1410
	Au_7HO_2	-0.6	1.247	2.236	1347
TPSS	Au_8O_2	-0.09	1.237	2.401	1395
	Au_7HO_2	-0.55	1.251	2.220	1321

Similar explanations[267] have also been offered for the cooperative binding of oxygen molecules to anionic silver clusters where the first O_2 molecule adsorbed being weaker electron acceptor in nature subsequently promotes the binding of a second O_2 molecule. Resorting to an analogous reasoning (as in the preceding lines), the role of H-atom in our case can be interpreted as electron withdrawing in nature, which is inferred from a natural population analysis that shows the charge on H atom to be -0.27 e. Hence, the origin of activation of the cluster Au_7H for preferential O_2 adsorption lies in the activation of the cluster induced by the electron withdrawing nature of H-atom present in the cluster. We also looked at the O-O bond lengths for the O_2 adsorbed complexes as presented in Table 5.1 for the pristine and doped clusters. Two interesting observations can be made from the results presented in Table 5.1. Firstly, the H-atom doping facilitates favorable interaction of oxygen molecule with this cluster which is exemplified from the shortening of $d_{\text{Au-O}}$ for the doped species as compared to the pristine one. Secondly, the activation of oxygen molecule can also be adjudged from the lengthening of $d_{\text{O-O}}$ for the doped cluster. To quantify this activation further, we have also computed the O-O stretching frequencies which are presented in Table 5.1. As a clear indication of significant activation of O_2 molecule, we observe an appreciable red shift (~70 cm^{-1}) in stretching frequency for Au_7H-O_2 cluster complexes. Results from different functionals unequivocally predict this trend. These observations are really encouraging as although there are interesting insights from photoelectronic spectra[268] of O_2 activation by even/odd numbered anionic gold clusters, our results indicate that the closed shell neutral gold cluster (Au_7H) can also significantly activate O_2 molecule. It is well known that the closed shell structure of these gold clusters imparts remarkably greater stability to them which can be rationalized from the odd-even oscillatory nature of their electronic properties like the binding energy per atom[68] as a function of cluster size. Indications that these stable closed shell gold clusters can activate oxygen molecule can be considered as an added advantage from the perspective of nanocatalysis.

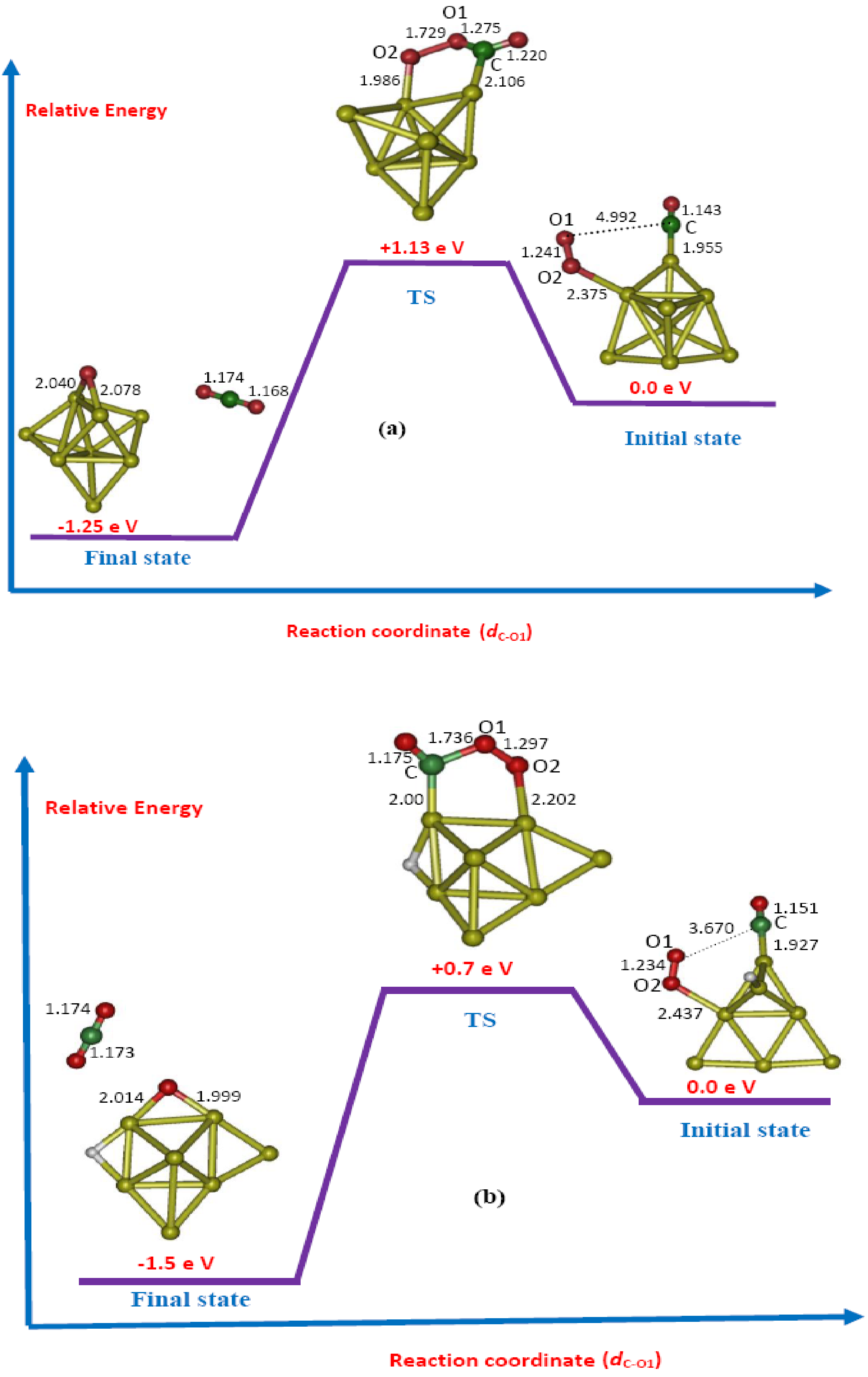

Figure 5.2: Reaction profiles showing the initial state, TS and final states of CO oxidation on clusters (a) Au_8 and (b) Au_7H.

We will now focus our discussion on the CO combustion on these clusters. Temperature programmed reaction (TPR) experiments and extensive *ab initio* calculations for Au_8 supported on MgO reveal a Langmuir-Hinshelwood (L-H) type of reaction mechanism[261] where the activated O_2 molecule and CO molecule are simultaneously adsorbed on the cluster. We have also considered similar situations where both the oxygen and carbon monoxide molecules are adsorbed on the clusters. We have computed the barrier heights for the oxidation of CO to CO_2 for the pristine as well as doped clusters. The structures of the reactant (cluster+O_2+CO), the transition state (TS) and the final product have been presented in Figure 5.2. Looking at all the geometries presented in the above figure, we conclude that for the pristine cluster case, the geometries of reactant, TS and the product do not change appreciably. In contrast, for the doped cluster case, the geometry of the TS differs significantly from that of the reactant and the product tends to adopt a planar geometry. We attribute this fluxionality in the structure of the doped cluster to the effect of hydrogen doping which is in agreement with our earlier results.[68] Our estimation of barrier height for CO oxidation on Au_8 cluster is 1.13 eV. Very interestingly, the barrier height for the cluster Au_7H has been calculated to be 0.7 eV. This observation clearly demonstrates that activation of oxygen molecule as observed for the doped cluster case is manifested in terms of reduction of reaction barrier height. In quantifiable terms, we claim that the effect of introduction of a single H-atom in the gold cluster, apart from activation of molecular oxygen, facilitates the CO combustion.

5.2: In Search of Some Generalized Factors that Decide the Efficiency of CO Oxidations on Gold Clusters

Contingent upon the findings that a single H-atom in gold cluster can significantly promote the CO oxidation process in the previous section, we have made an attempt to find out the possible origin of this activation by making a generalized approach.

5.2.1: Factors Governing CO Oxidation on Gold Clusters

The CO oxidation reaction has been a favorite prototypical reaction to probe several important aspects of heterogeneous catalysis.[269] The performance of wide range of catalyst systems are tested employing this process as a universal probe. In its most illustrative form, CO oxidation finds its application in the automobile exhaust system which is very important from the perspective of environmental chemistry. However, the relevance of this seemingly simple reaction is, by far, wide ranging. By its very chemical nature, CO is poisonous and cannot be released to the atmosphere. In the petrochemical processing industries, the removal of CO from the gas streams is an important requirement which prompted early research to devise strategies to oxidize it with reactive forms of oxygen at low temperatures. In the context of electrochemistry, this reaction is of great important in fuel cell applications where the CO poisoning is a critical issue.[269]

In recent years, noble metal supported CO oxidation is at commonplace among the community leading to a plethora of literature in the related field. Gold clusters supported on a wide range of metal oxides supports viz. MgO, TiO_2, Al_2O_3 , Fe_2O_3, Co_3O_4 , and NiO, etc. have been tested for the CO oxidation reaction with observations of high catalytic efficiency/activity.[270] The cluster size and charge state seems to play a major role in deciding the rate of reaction of Au_n clusters and gas molecules.[271] The discerning role of the charge state of gold clusters towards their interaction with CO and O_2 has been demonstrated on the basis of different catalytic activity observed for supported gold clusters on defect poor and defect rich MgO(100) surface.[256] A number of theoretical and experimental studies have been devoted in deciphering the role of metal oxide supports and the mechanism of CO oxidation on gold clusters. [216,272,266,262,273-275] However, a very relevant question in the form of whether O_2 binds molecularly or dissociatively still persists. DFT study of Noskov and co-workers[273] reveals two different pathways; one with O_2 being dissociated and the other where it is adsorbed in molecular form, whereas experimental findings of Stolcic et al.[275] suggests only molecular oxygen adsorption on anionic gold clusters. Although researchers have been intensely endeavored to elucidate the origin of this activity and factors that influence it, [276-281] there has not been any overreaching consensus to account for all the diverse observations. The divergence of reports can be judged from the fact that some conclude metallic Au to be the active site,[25] some propose Au cations in the absence of metallic Au to be catalytically active[282] while some other report suggests an ensemble Au clusters having Au cations at the perimeter, to be the preferred active site.[283] All the wealth of information, although, illuminates several facets of our understanding on catalysis involving gold clusters, a generalized atomic-level picture of origin of its catalytic activity still belies our understanding. For instance, Mitric et al.[284] have demonstrated that reactivity promoting criterion for Au_6 and Ag_6 anionic clusters can be internal vibrational energy redistribution. Such reports promulgating some fundamental concepts that can be useful in the understanding as well as designing of catalysts are indeed scarce in the literature.

Table 5.2: Natural Charges q_X (e^-), binding energies of BE of CO and O_2 (eV), vibrational frequency ν of CO and O_2 (cm^{-1}), barrier height (eV) for CO oxidation and HL (eV) for different clusters.

Cluster	q_X	BE_{CO}	BE_{O2}	ν_{CO}	ν_{O2}	BH	HL
Au_6		-0.57	-0.14	2062	1363	1.13	2.19
Au_6^-		-0.68	-0.14	1982	1274	0.54	0.38
Au_5F	-0.68	-1.27	-0.17	2106	1362	1.85	1.94
Au_5Cl	-0.48	-0.87	-0.13	2102	1378	1.22	2.14
Au_5N	-0.75	-1.91	-0.58	2075	1293	0.29	0.18
Au_5B	-0.47	-1.20	-0.12	2078	1335	1.00	1.65
Au_5C	-1.34	-1.61	-0.09	2087	1320	1.62	0.30
Au_5Li	0.70	-0.72	-0.12	2070	1374	0.95	2.22
Au_5Na	0.79	-0.66	-0.12	2064	1367	1.06	2.16
Au_5K	0.88	-0.65	-0.13	2058	1356	1.31	2.12
Au_{20}		-0.42	-0.08	2047	1370	0.94	1.91
$Au_{19}N$	-1.12	-1.34	-0.11	2044	1317	0.69	0.33
$Au_{19}C$	-1.04	-0.97	-0.10	2034	1338	0.65	0.27

5.2.1.1: Tuning of Local Electronic Environment of Gold Clusters and its Effect on CO Oxidation Activity

In the current investigation, we have endeavored to rationalize our DFT based findings in terms of how the local electronic environments of gold clusters play a decisive role in governing the CO oxidation. The governing factors are highly driven by local electrostatic effects for effective activation of CO and O_2, along with quantum size effects like HOMO-LUMO gap (HL) of the cluster. Gold cluster Au_6 which has a well characterized D_{3h} symmetry with a close-packed planar triangular structure has been chosen as a model cluster. Moreover, this cluster can be thought of as a small piece of Au (111) surface serving as an ideal model for ctatalytic surface with apex and edge sites only. [285] We have modulated the local electrostatic environment of the cluster by introducing several impurity atoms of varying electronegativity viz. B, C, N, F, Cl, Li, Na, K in the cluster. These impurities induce varying degree of electrostatic effects on the adjacent gold atom. Employing DFT based methods, we have computed the binding of CO and O_2 to these clusters and also their efficacy in terms of activating the cluster by calculation of the activation barrier for the CO oxidation reaction. The observations that the local electrostatic effect is of paramount importance has been unequivocally established by considering different cluster sizes. More importantly, it has been demonstrated that impurities like N and C which have strong electron withdrawing tendency in the environment of gold clusters strongly activate O_2 molecule and promote the catalytic efficiency.

In the previous section, we have demonstrated that H atom in gold cluster leads to O_2 activation and facile CO oxidation as compared to the pristine gold clusters. The origin has been shown to be the negative charge on H atom in gold clusters. This promoted us to investigate the larger role of modulation of local environment around active sites of gold clusters in a generalized perspective. Accordingly we have taken several cluster systems

(Au_5X) with impurity atoms (X) like B, C, N, F, Cl, Li, Na, K in small gold cluster Au_6. The primary objective is that these impurities are of varying electronegativity and likely to influence the local environment of gold clusters accordingly.

Extensive *ab initio* calculations complemented by temperature programmed reaction experiments reveal that the CO oxidation reaction on gold, preferentially follows a Langmuir-Hinshelwood (L-H) kinetics. [261] This essentially requires that both the reactants, CO and O_2 should be adsorbed to the active sites of the cluster simultaneously. Thus, the adsorption of CO and O_2 on the clusters is the foremost important step in the overall process. The clusters considered in the current study are planar Au_6 along with the doped counterparts Au_5X. The optimized structure of Au_6 (Figure 5.3) has two positions for the dopant, vertex and edge. It is observed that the lowest energy optimized structures for X= F, Cl, N, B, C prefer the vertex position whereas for X= Li, Na, K, edge position is preferred. One important observation is that the former set of impurity atoms are electron-withdrawing (EW) in environment of gold clusters whereas the latter ones are electron-donating (ED). From our Natural population analysis, the natural charges on atom X have been presented in Table 5.2. Broadly, these two different classes of impurity atoms manifest two different kinds of modulation in the local electronic environment of gold clusters. When X is EW, they acquire negative charges and induce highly positively charged center on the immediate adjacent atom. Conversely, for the case of ED impurity, negatively charged center is produced on the nearest gold atom. The implications of the modulation of the local electrostatic environment on the adsorption of CO and O_2 are dramatic.

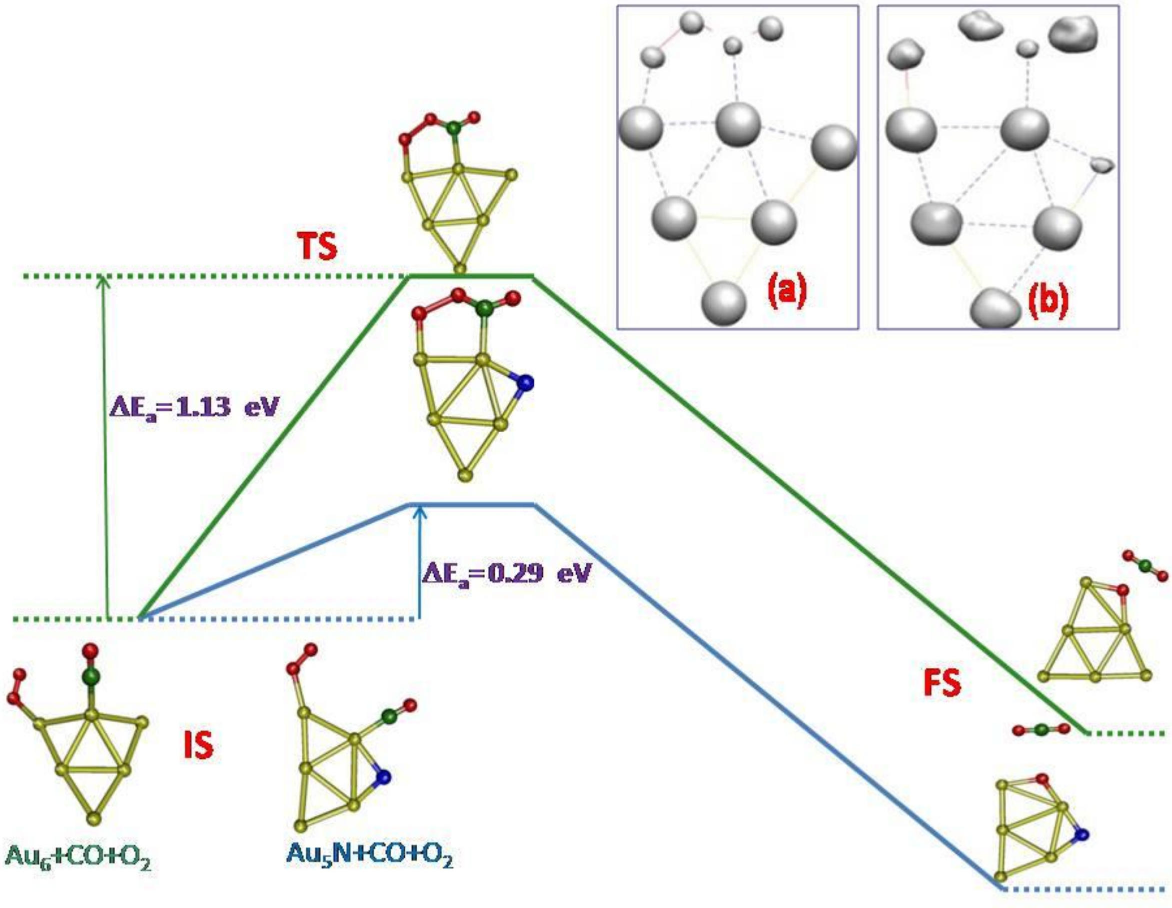

Figure 5.3: Optimized geometries of the initial state (IS), transition state (TS) and final state (FS) of CO oxidation on clusters Au_6 and Au_5N. Inset figures show the total electron density plot of the TS for clusters Au_6 (a) and Au_5N (b). (Highly polarized TS for (b) is noteworthy).

One point which is of paramount importance is that the CO molecule prefers a positively enriched center for binding and O_2 preferentially bind to a gold center having higher negative charge values. Accordingly we will demonstrate that this fundamental electrostatic origin is of paramount importance to the CO oxidation reaction. The binding energies of CO and O_2 separately at the most preferred binding sites according to the preceding rationale have been reported in Table 5.2 along with corresponding stretching frequencies, natural charges on the atom X and H-L gaps. Let us now analyze the results presented in Table 5.2 from a generalized perspective of local electrostatics. The large negative charges (q_X) on EW atoms induce the positive charge centre which is a governing factor for the binding energy of CO molecule (BE_{CO}).

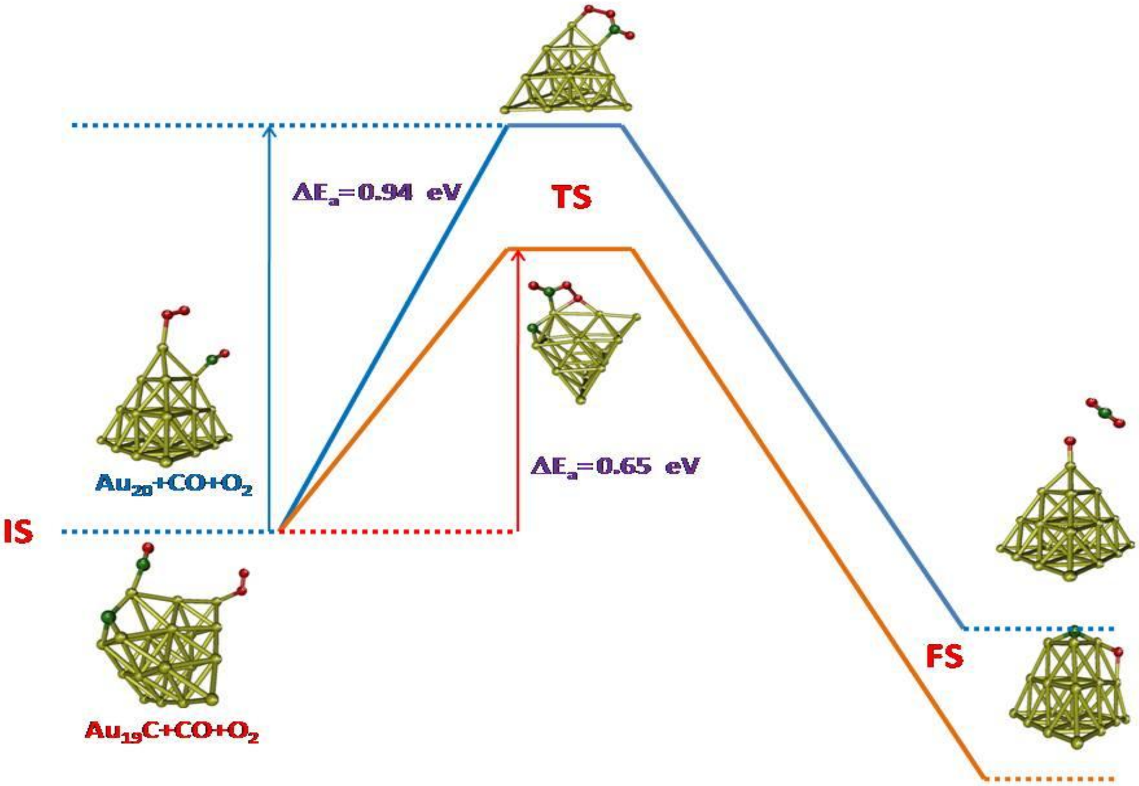

Figure 5.4: Optimized geometries of the initial state (IS), transition state (TS) and final state (FS) of CO oxidation on clusters Au_{20} and $Au_{19}C$.

Concomitantly, significant enhancement in BE_{CO} for cluster with X= N and C, as compared to the pristine one Au_6 is a glaring indication of electrostatics driven CO adsorption. More interestingly, for all the clusters with X having EW nature, the appreciable enhancement in BE_{CO} unequivocally supports the above logic. The previous reports of cationic gold as active sites can, therefore, be attributed to electrostatically favoured CO adsorption. For ED impurities, the adjacent gold atom with partial negative charge is the preferred site of interaction of oxygen molecule and the next nearest gold centre having partial positive charge is the preferred site of CO adsorption. Slight enhancement in BE_{CO} for the case of ED impurities (compared to Au_6) also justifies the role of electrostatics, although it is not prominent for impurities with higher positive character. Careful observation of the BE_{O2}, however, tells us that unlike CO, the electrostatic effect is less prominent. However, we observe that for highly negatively charged impurity, particularly for N, the binding energy of oxygen is also remarkably enhanced as compared to the case of Au_6.

Let us now consider the activation of oxygen molecule which is a crucial step in the oxidation process. Vibrational frequency of the O_2 molecule is a sensitive indicator of its activation marked by a noticeable red shift in the frequency. We observe, remarkable red shift in oxygen vibrational frequency for clusters Au_5N (1293 cm^{-1}) and Au_5C (1320 cm^{-1}) as compared to Au_6 (1363 cm^{-1}). This emphatically demonstrates the activation of di-oxygen for the reaction. For anionic cluster Au_6^- we observe maximum activation of oxygen molecule (1274 cm^{-1}), an effect which is very much similar to that of the cluster Au_5N. In view of recently experimental demonstration[263] that anionic gold clusters induce significant activation in the oxygen molecule, our interpretation of the current observation is that the impurities like N and C apart from inducing favorable CO binding to the clusters, also renders negatively charge centers on the cluster akin to the anionic clusters and thus activate the O2 molecule. The underlying importance of local electrostatic effect in dictating the CO oxidation reaction is thus demonstrated. The actual efficacy of these clusters can also be judged from the calculation of barrier heights (BH) for the oxidation reaction. The initial state (IS), transition state (TS) and the final state (FS) of the CO oxidation reaction have been demonstrated in SI and as an exemplary case the corresponding states for clusters Au_5N and Au_6 have been presented in Figure 5.3. More interestingly, in fine tune with the governing role of electrostatics factors as put forward in the preceding lines, the barrier for CO oxidation on Au_5N (0.29 eV) is significantly reduced against the barrier height of 1.13 eV obtained for Au_6. The fact that electrostatic effect is a key player can also be ascertained from the total electron density plots of the TS (inset of Figure 5.3) for clusters Au_5N and Au_6 with the former having a highly polarizable distribution of electron density involving O-O-C-O atoms, which in turn manifest in significant reduction of barrier of the reaction. Even, the cluster Au_5N turns out to be more effective in bringing down the barrier height as compared to anionic cluster Au_6^- (0.54 eV). Experimentally it has been established that moisture in the reactant gas greatly influence the CO oxidation and it has also been proposed that moisture activates the O_2 molecule.[286] The electron withdrawing nature of OH groups has been shown to be the guiding factor for O_2 activation.[266] Keeping these important observations in coherence with our observation that ED impurities like C and N distinctly influence the CO oxidation reaction, the role of electrostatics that underpin all these effects can be firmly realized.

One of the attributes of well known quantum size effects in these small gold clusters, the HL is also an indicator of the reactivity of the clusters. The trend of HL for all the clusters (Table 5.2) vividly demonstrates the high reactivity of the clusters Au_5N and Au_5C in the form of greatly reduced HL values as compared to the other clusters including Au_6. A point worthy to mention here is that we get the barrier height estimation for cluster Au_5C as 1.62 eV which is larger and seems to be at loggerheads with the preceding arguments of reactivity of this cluster. However, we asserted that the geometry of the IS of this cluster is highly fluxional and assumes a pseudo tetrahedral geometry with C atom at the centre and the two reactant species CO and O2 are spatially separated by a larger distance as compared to any of the other clusters where both the reactants are held fairly close to each other. In a reassuring attempt that our observations of higher reactivity of clusters with impurities like N and C are not only limited to this particular cluster size which is primarily planar in geometry, but also translate to larger cluster size with 3D geometry, we have considered T_d gold cluster Au_{20} alongside clusters Au_5N and Au5C. The IS, TS and FS for these three clusters is presented in

Figure 5.4. Enhancement in BE_{CO}, sizeable activation of oxygen molecule, significant reduction in HL and BH for the latter two clusters (Table 5.2), unequivocally conform the guiding principles as laid in our discussions. More pragmatically, some recent observations [287] of facilitation of catalysis by subsurface C fortify our interpretation and rationale.

5.3: DNA Base-Gold Cluster Complexes as a Model Catalyst System for CO Oxidation

In the first two sections of this chapter we have discussed the activity of gold clusters for CO oxidation in terms of doping of the cluster by other atoms. In the last section of this chapter, we will focus on strategies for promoting the CO oxidation process by complexation of the gold clusters with DNA bases which can act as an ideal support material for gold.

5.3.1: DNA-Au System and Its Importance in Nanotechnology

The larger aim of nanotechnology, apart from enriching our scientific knowledge in terms of providing detailed insights into the structure, property and phenomena at the nanoscale, is to render viable and sustainable technologies to the society for the betterment of our life. To this end, DNA based nano-bio technology has undergone an unprecedented advancement in recent years. The emergence of DNA as a "programmable assembler" for the bottom-up synthesis of materials has attracted the lure and fascination of material chemists.[288] The possibilities of employing DNA as a template have opened up new avenues for the synthesis of nanomaterials pushing down the cost and size limit imposed by the conventional top-down approaches like optical lithography. The interaction of DNA with metal nanoparticles finds diverse applications in the recent developments of nano-bio technology. [289-298] Of particular interest is the DNA-gold interaction which forms the basis of several diagnostics applications involving DNA detection employing techniques, viz. surface plasmon resonance spectroscopy (SPRS), surface enhanced Raman Spectroscopy (SERS), electrochemical, colorimetric detection etc.[299-301] DNA molecule adsorbed on Au films, Auelectrodes or DNA coated Au nanoparticles have been reported to have applications in the field of electronics, sensors, drug delivery, chips, imaging, etc.[302-304] For all these diverse applications, understanding the binding of DNA bases, Adenine (A), Thymine (T), Guanine (G), and Cytosine (C) with gold is of central importance. Storhoff et al. have demonstrated that the binding and stabilities of deoxynucleosides to gold nanoparticles is highly sequence dependent.[303] From combined Fourier transform infrared (FTIR) spectroscopy and X-ray photoelectron spectroscopy (XPS), Whitman and co-workers have inferred that the adsorption affinity of DNA bases on Au-surface follows the trend as $A > C \geq G > T$.[304] Using temperature-programmed desorption studies, Demers et al. have quantitatively estimated the energetics of this fundamental interaction of DNA bases with gold.[302] Hence the very nature of interaction of DNA bases, nucleosides or oligonucleotide sequences with Au forms the basis for all the versatile applications of the DNA-Au system.

In sharp contrast to the attribute of bulk gold as the noblest of metals, an interesting variant, the nanoscale gold, has come into the limelight by virtue of exhibiting pronounced catalytic activity particularly promoting the low temperature CO oxidation which was recognized by Haruta et al. nearly two decades ago.[187] More importantly, this reaction, apart from being a very important reaction dealing with the constituent of the automobile exhaust systems, where the oxidation of poisonous CO is imperative, serves as a prototype reaction for the larger spectrum of heterogeneous catalysis community.[305] The nature of the support (mostly oxides) for the catalyst can also play a decisive role on the oxidation of CO. It has been demonstrated that charging effects due to presence of F-center rich MgO surface greatly facilitate the CO oxidation on supported gold clusters.[306] The related literature pertaining to noble metal supported catalysis has also witnessed an unprecedented expansion on the studies underpinning several aspects of nanoscale gold, including its varied structure and electronic properties as well as their applications in nanocatalysis, thus prompting some authors to call it "nanocatalysis beyond the gold rush era".[307]

Using small gold clusters as catalytic models, the essential aspects of the structural, energetic and mechanistic details of many important chemical reactions, apart from CO oxidation, can be gleaned through with the help of computational methods.[308] Kryachko et al. have theoretically demonstrated a unique feature of the complexes between DNA bases and small gold clusters Au_3 and Au_4, namely a nonconventional N-H···Au hydrogen bonds.[309] Interestingly, these clusters are strongly bound to DNA bases primarily by an N-Au or O-Au anchor bond along with the above mentioned hydrogen bond.[309] This DNA base-Au cluster complex forms an ideal model for investigating the catalytic activity of the clusters, consequent upon the formation of stable complexes. Our objective for the current investigation is, to employ density functional theory (DFT) based method for investigating the (1) binding ability of DNA base-Au_3 cluster complex (2) interaction of CO/O_2 with gold cluster bound to the DNA bases and (3) mechanism and energetics of CO oxidation reaction on these complexes. On comparison with the results obtained for a bare Au_3 clusters, we are able to put forward an important observation that the complexes of DNA base-Au_3 facilitate the oxidation reaction by reducing the activation barrier. These observations can be taken as a first step towards designing promising heterogeneous catalyst systems with DNA as a basic building block or an active support.

5.3.1.1: CO Oxidation on Au_3-DNA Base Complex: Mechanistic Details and Energetics

In the following sections of the chapter, we will elaborate our results on the CO oxidation process on Au_3-DNA base complex.

5.3.1.2: Binding of Gold Cluster Au_3 with DNA Bases

We begin our discussion by considering the complexes of DNA bases (A, T, G, and C) with the gold cluster Au_3. For a particular DNA base, there can be several possible positions where the cluster Au_3 can bind with the base via an anchor bond and a non conventional hydrogen bond.[309] We, however, have only considered the DNA base-Au_3 complex which is having the highest binding energy for a given base-cluster complex. For instance, for A, Au_3 bound via N3, H9 (anchor bond and hydrogen bond respectively), as shown in Figure 5.5, corresponds to the complex having highest binding energy. Similarly, for T, G, and C the most preferred binding sites for the cluster Au_3 are O2, H1; N3, H9; and N3, H4 respectively (Figure 5.5). We have computed the binding energy of the cluster with the bases by employing B3LYP functional as well as BP86 functional, and the results are presented in Table 5.3. It is important to note that the former functional predicts the binding energy which is very close to experimentally obtained heat of desorption of DNA bases on Au films that fall in the range of 26.3-34.9 kcal mol^{-1}.[302] In our previous studies pertaining to CO oxidation on small gold clusters, we have shown that the performance of the functional BP86 is reasonably better in comparison to some other functionals.[310] Hence, in our subsequent discussion we present results obtained exclusively by using this functional. The optimized geometries of the complexes along with some important geometrical parameter such as anchor bond length ($d_{\text{Au-N}}/d_{\text{Au-O}}$), H-bond length ($d_{\text{Au-H}}$) and N/O-Au-Au bond angle, have been presented in Figure 5.5. The relative affinities of gold cluster-DNA base complexes follow the order $A \geq C > G > T$. This trend closely matches with the experimental results of $A > C \geq G > T$ obtained by Kimura-Suda et al.[304] These cluster-DNA base complexes form the basis for our subsequent investigations of CO oxidation reactions on the gold clusters.

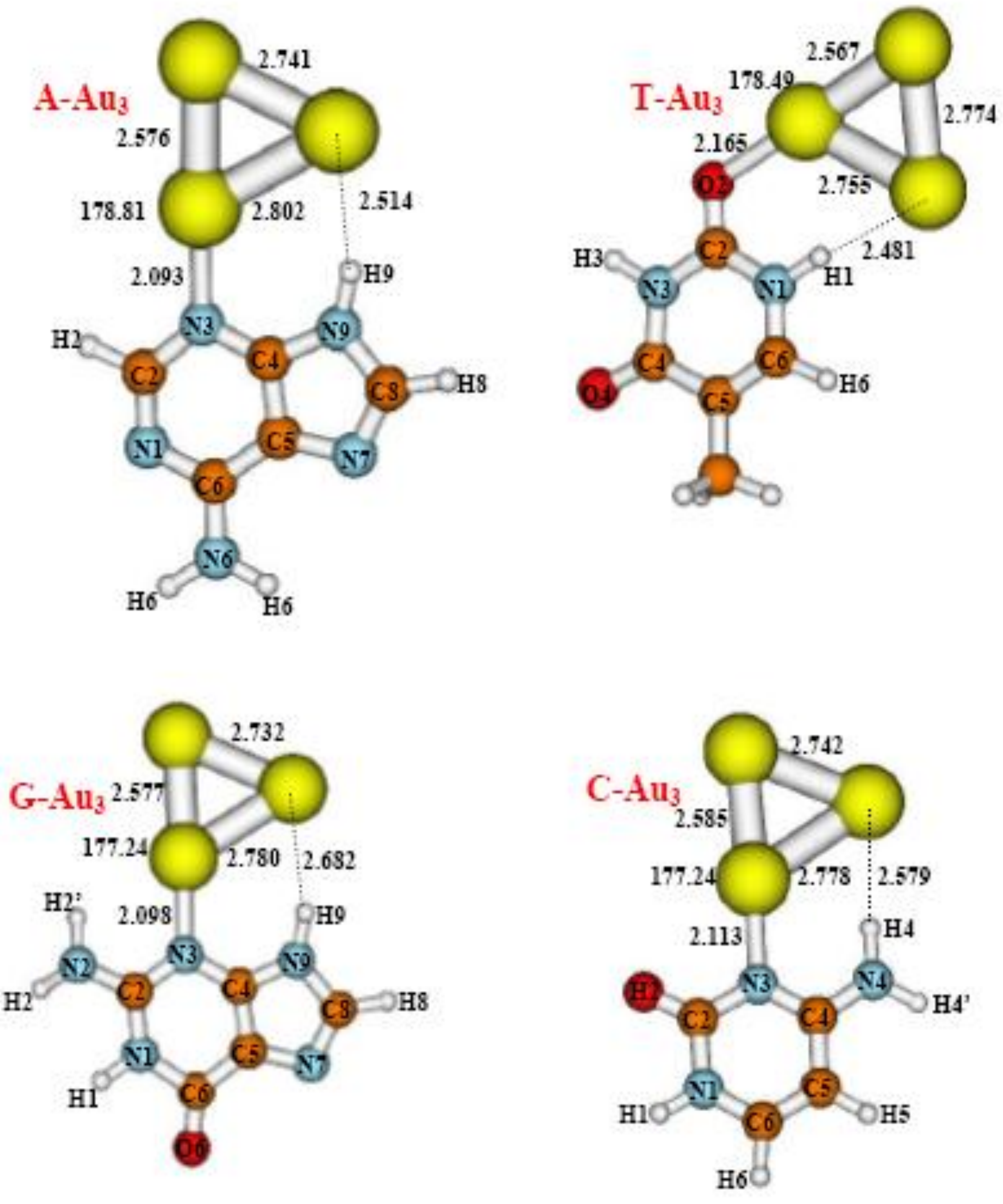

Figure 5.5: The most stable complexes of DNA base-Au_3 cluster with some important geometrical parameters.

Table 5.3: Binding energy of DNA bases with Au_3, activation barrier (ΔE_a) and heat of formation (ΔH_f) of CO oxidation reaction on Au_3 and DNA base- Au_3 complexes. (* BP86 results)

Cluster-complex	E_b (BP86) (kcal mol^{-1})	E_b (B3LYP) (kcal mol^{-1})	$\Delta E_a^{*\,ER}$ (kcal mol^{-1})	$\Delta H_f^{*\,ER}$ (kcal mol^{-1})	q_{Au3} (e)
Au_3			46.81	-39.76	0.0
Au_3-A	-37.74	-32.16	36.20	-57.93	-0.110
Au_3-T	-24.24	-21.73	38.74	-51.27	-0.048
Au_3-G	-34.35	-28.75	37.35	-54.63	-0.122
Au_3-C	-37.56	-31.73	35.97	-54.61	-0.098

5.3.1.3: CO Oxidation

Gold nanoclusters are becoming overwhelmingly important on account of their importance in heterogeneous catalysis, a brief introduction of which has been discussed already. The important reaction of CO combustion on supported gold proceeds through two different mechanisms, viz. Langmuir-Hinshelwood (L-H) and Eley-Rideal (E-R). [261] In the L-H mechanism, both the reactants (CO and O_2) are pre-adsorbed on the gold cluster in the IS. On the contrary, the E-R mechanism proceeds with the adsorption of only one of the reactant species in the IS. Before we start our discussion on DNA base-Au_3 complex, we will first consider CO oxidation on a pristine Au_3 cluster. On a bare Au_3 cluster, the CO oxidation can take place via either of the two possible mechanisms (E-R and L-H). The optimized geometries of IS, TS and FS for the CO combustion on Au_3 by the above two mechanisms have been presented in Figure 5.6. For the E-R mechanism, in the IS geometry only CO molecule is adsorbed on the cluster, although it is important to note that in the IS geometry for E-R type of mechanism, oxygen can also be adsorbed on the bare cluster. However, here we have considered only CO adsorbed on the pristine cluster because in the case of Au_3 bound to DNA bases we find only the CO and not O_2 getting adsorbed on the cluster. Hence for the sake of comparison, we have only considered the case of CO adsorbed on the cluster rather than O_2 in the IS geometry. It is also pertinent to mention that the binding of CO to small gold clusters is always favorable as compared to that of O_2 which has been discussed previously in several studies. [204] Likewise, for L-H type of CO oxidation on Au_3, both CO and O_2 are adsorbed on the cluster. We have calculated the barrier heights (ΔE_a) for CO oxidation reaction as well as the heats of formation of the final product (ΔH_f).

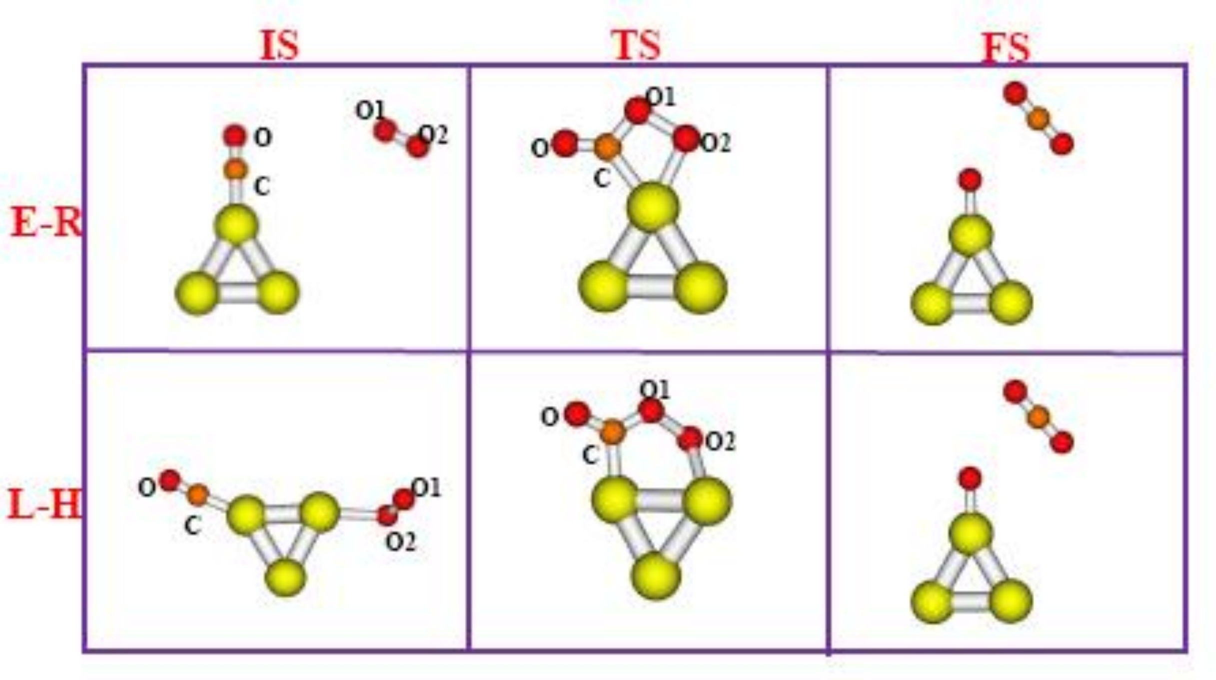

Figure 5.6: Oxidation of CO on an Au_3 cluster via two possible mechanisms (L-H, and E-R) showing the IS, TS and the FS.

The calculated ΔE_a and ΔH_f for L-H mechanism are 42.43 and -39.61 kcal mol^{-1}, while for E-R mechanism these are 46.81 and -39.76 kcal mol^{-1} respectively. It is interesting to note that on a pristine cluster Au_3, CO oxidation can preferentially take place by a L-H mechanism which is having lesser ΔE_a (42.43 kcal mol^{-1}) as compared to E-R mechanism (46.81 kcal mol^{-1}). Some previous reports of CO oxidation on Au_8/MgO(100) system also discuss the existence of two different type of reaction pathways based on Temperature Programmed Reaction (TPR) spectra and extensive *ab initio* calculations which support our findings that L-

H mechanism can be a favorable channel for this reaction.[261] In the FS as shown in Figure 5.6, the CO_2 molecule is formed along with O-atom adsorbed on the cluster. From the values of ΔH_f for the CO oxidation we infer that the reaction is highly exothermic with a net heat of formation of ~ -39 kcal mol^{-1}.

Let us now turn our attention to CO oxidation taking place on an Au_3 cluster bound to the DNA bases. Before studying the CO oxidation process, we attempted to study the adsorption of individual reactant species on different sites of the cluster. There are three possible binding sites for the individual CO or O_2 molecule on the cluster, namely the Au atom involved in the anchor bond (Au_A), Au atom involved in the H-bond (Au_H), and the remaining Au atom flanked by Au_A and Au_H (central Au, Au_C). We tried to optimize O_2 adsorbed on the above three possible binding sites, but found in all cases the oxygen molecule to drift apart from cluster suggesting its weak interaction with cluster-DNA base complexes. However, in case of CO molecule, we find the favorable binding site as Au_C. This observation suggests that in the IS only one reactant (CO) is adsorbed on the cluster and consequently the mechanism for CO oxidation is E-R type. The geometries corresponding to IS, TS and FS for all the four DNA base-Au_3 complexes have been presented in Figure 5.7. As a requirement for the E-R type of mechanism, we find that in the IS, the CO molecule is adsorbed on the gold cluster and the oxygen molecule approaches the CO molecule. The TS for the reaction, involves a 4-member O-C-O1-O2 structure adsorbed on the cluster. The FS of the reaction is characterized by an O atom bound to the Au_3 cluster and CO_2 being released. It is interesting to add that the atomic oxygen adsorbed on the gold cluster is also involved in H-bonding with one of the DNA-base H atoms. The energetics for the oxidation process has been summarized in Table 5.3. Most notably, we find that for all DNA base-Au_3 complexes, the barrier height is reduced as compared to that of the pristine cluster (E-R and L-H values).

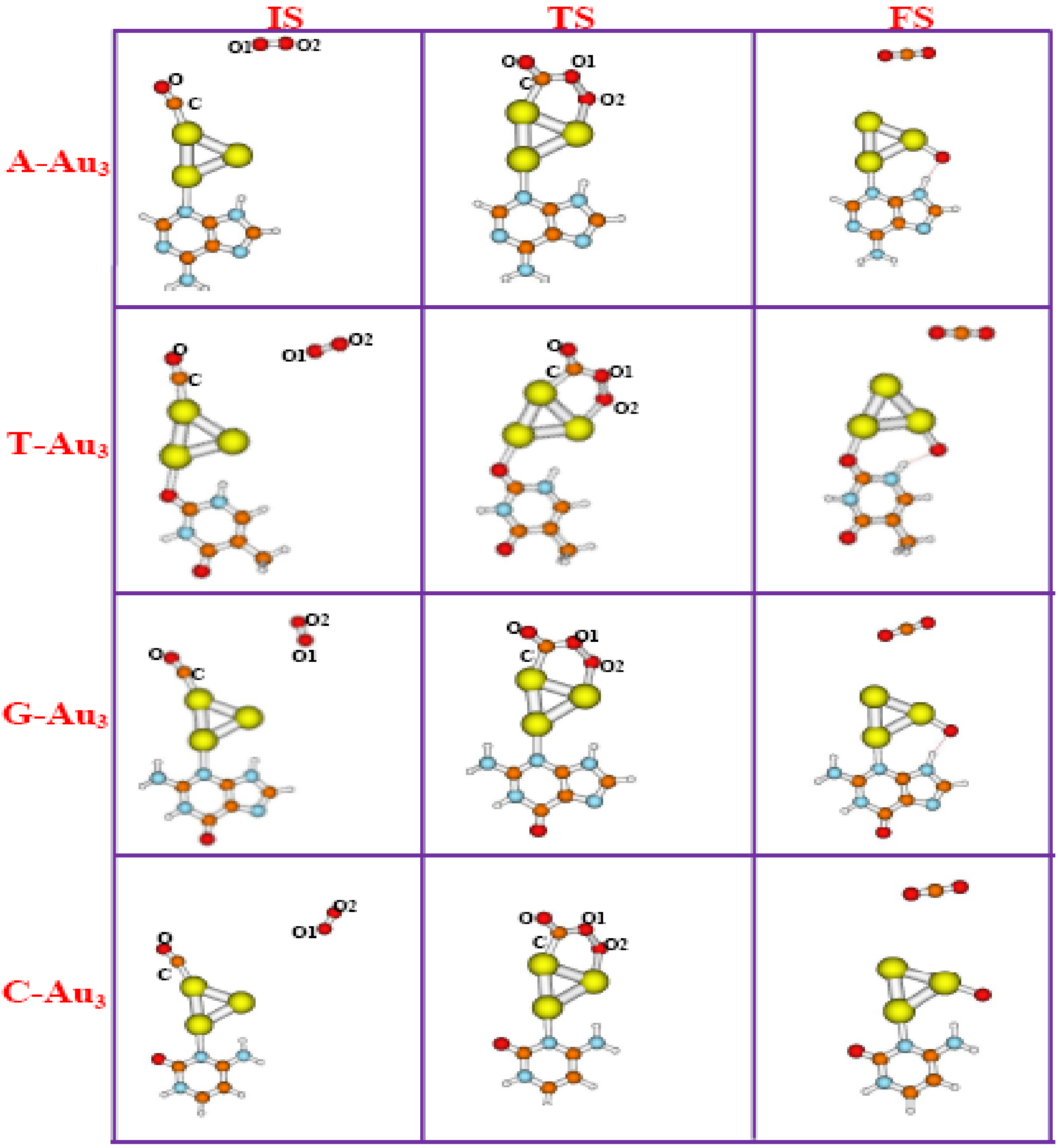

Figure 5.7: Oxidation of CO on an Au_3 cluster via two possible mechanisms (L-H, and E-R) showing the IS, TS and the FS.

For instance, the barrier height for CO oxidation on Au_3-C is the minimum (35.97 kcal mol^{-1}) as compared to the corresponding value of 46.81 kcal mol^{-1} for the pristine cluster. Thus, these amounts to be ~20 % reduction in the activation energy for the reaction which is quite significant. For the different base-cluster complex, the trend in the ΔE_a follows the order: T >

G > A > C. It is, however, noted that the barrier height for the CO oxidation reaction taking place on the four different base-cluster complexes varies within a range of ~3 kcal mol^{-1}. For T-Au$_3$ system the barrier is the highest as compared to its counterparts. This observation is explained on the basis of binding ability of bases with the cluster where the T-Au$_3$ system has the lowest binding energy as the Au-O anchor bond is relatively weaker than the stronger Au-N bond. Moreover, the weaker binding energy for the former complex also has minimum effect on the charging of the cluster (q_{Au3} from Table 5.3). The observation that gold cluster bound DNA bases appreciably reduce the activation barrier for CO oxidation as compared to the bare cluster, suggests that the cluster is activated by virtue of forming stable complexes with DNA bases. The heat of formation of the final product corresponds to highly endothermic situation. It can clearly be noticed from Table 1, that the final states for the DNA base-Au$_3$ system is more stabilized as compared to that for a bare Au$_3$ cluster. This suggests that CO oxidation on gold cluster bound to a DNA base is more facile as compared to a pristine gas phase cluster.

The reduction in ΔE_a for CO oxidation for DNA base-Au$_3$ complex can be attributed to the charging of the cluster. We have computed the total charge transferred from the DNA base to the cluster from a natural population analysis the results of which have also been presented in Table 5.3. The net charge transferred to the gold cluster is always negative suggesting the fact that the cluster becomes anionic when it forms complexes with DNA bases. It is already reported in the literature that anionic gold clusters are more active for CO oxidation as compared to their neutral counterparts.[204] In this context, the role of DNA bases assumes significance from two counts: (1) they form stable complexes with gold cluster, and (2) they help in the charging of the cluster which in turn manifests in activation of the cluster for CO oxidation. The role of charging of Au clusters and their effect on CO oxidation have previously been stressed upon in the literature.[306] Yoon et al. in their seminal work have demonstrated that charging of Au_8 cluster on MgO surface can play a discerning role on the CO oxidation.[306] Two major advantages of oxides or surfaces of carbon nanomaterials like graphene or carbon nanotubes etc. which are commonly employed as substrates are (1) they provide strong adherence for the nanoparticles and (2) they modulate the electronic environment of active nanoparticles to facilitate catalysis. To this end, we assert that DNA base–gold complex can also be an ideal substitute for the well explored oxide-gold system. The potential role of DNA as an ideal template for nano-assembling can be important in designing active heterogeneous catalyst system.

5.4: Computational Details

For the first study dealing with adsorption of O_2 and subsequent CO oxidation on Au_8 and Au_7H, All the calculations have been performed using computational chemistry package TURBOMOLE[179] (v6.0). For gold atom, the core electrons are treated with relativistically corrected ECP-60-MWB and valence electrons of gold as well as all other atoms are treated with def2-TZVP basis sets as implemented in TURBOMOLE. We have considered several DFT functionals such as the generalized gradient approximation (GGA) based BP86 and PBE. Apart from that we have also employed meta-GGA functional TPSS.[311] The rational for using different functional stems basically from the fact that the difficulty of DFT methods to correctly predict oxygen binding with clusters which has been explained in our text. We indeed found that the three different functionals are quite consistent in their prediction of binding energy of O_2 with gold clusters. The binding energies of oxygen adsorbed complexes have been computed as the difference in the total energy of the complex and the constituents (cluster and O_2 molecule). The barrier height for the CO oxidation has been computed using only BP86 functional because we found all the functionals to reproduce closely similar quantitative results. For the calculation of barrier heights, the reaction coordinate has been chosen to be the distance ($d_{C\text{-}O1}$) between C atom of CO and O1 atom of O_2 molecule. We have carried out constrained optimizations by varying the distance $d_{C\text{-}O1}$ and the point with highest energy along the scan has been taken as the initial guess for TS optimization. The TS has been characterized by a single imaginary frequency. The vibrational analysis has been carried out by using analytical force constant calculations.

For this second work, we have used BP86 functional. The other details of the computational methods employed for this work is similar to that of the previous section.

In the third section of this chapter dealing with DNA-Au complexes, the initial geometries of the complexes of Au_3 with DNA bases have been optimized by employing two different functionals namely B3LYP and BP86. To study the oxidation of CO on the Au_3-DNA base complexes, the initial state (IS), transition state (TS) and the final state (FS) have been optimized with BP86 functional. The transition state search has been carried out by choosing the distance between C and O1 (C of CO molecule and O1 of O_2 molecule, described by O1-O2), $d_{C\text{-}O1}$ as the reaction coordinate for the CO oxidation reaction. We have carried out constrained optimizations by varying $d_{C\text{-}O1}$ as the reaction coordinate and generating the initial guess structures for the TS. The optimized TS is characterized with a single negative vibrational frequency as obtained from the hessian calculation. The barrier height (ΔE_a) for the CO oxidation reaction is calculated as the difference between the energies of TS and IS. Similarly, the enthalpy of formation of the product (ΔH_f) is computed as the difference in the energies of the FS and IS.

5.5: Summary of the Work

In summary of the first section of this chapter, our DFT calculations shed light on the effect of doping a single hydrogen atom in gold cluster Au_8 on the adsorption of oxygen molecule. Inching a step further in the direction of the so called Au/H analogy that entails the similarity in the behavior of a gold atom and a hydrogen atom in several cluster systems, we demonstrate that a single H-atom doped cluster, Au_7H preferentially activates an oxygen molecule as compared to the pristine cluster Au_8. The binding energy for O_2 molecule on the cluster Au_7H is remarkably higher than that on Au_8. Lengthening of O-O bond and red shift in stretching frequency are supportive of the activation of oxygen molecule on the doped cluster. Although both the clusters have closed shell electronic configuration and are expected to exhibit weaker binding with O_2 molecule, favorable interaction in case of H-doped gold cluster can be rationalized in terms of electron withdrawing nature of H-atom and subsequent activation of this cluster. The higher stability of closed shell gold clusters in conjunction with their preferential activation of oxygen molecule sounds encouraging, considering the overwhelmingly important contributions of gold clusters to nanocatalysis. Our estimation of barrier height for the oxidation of CO on these clusters shows reduction in the reaction barrier for the doped cluster case. These observations indicate that impurities like H-atom in gold clusters can be an efficient and cost-effective catalyst as compared to the pristine gold cluster. Our results can have broader consequences to the field of heterogeneous catalysis by gold and stimulate further research.

In section two of this chapter our density functional theory based study uniquely demonstrated that local electrostatic effects primarily govern the oxidation of CO on small gold clusters. Through suitable modulation of the local electronic environment, by introducing impurities like C and N atoms which are highly electronegative, effects similar to highly active anionic gold clusters can be produced for facile CO oxidation reaction. Moreover, quantum size effect like HL can also be a discerning parameter in designing suitable catalyst. Our reports can be potentially pertinent in charting out road map for effective noble metal based catalysts and spark off further interest.

Finally, to summarize the third and last section of this chapter, we have explored, by employing DFT based method, the possibilities of using DNA base-Au_3 cluster complexes as a catalytic model system for the CO oxidation reaction. These complexes are energetically stable and our calculated interaction energies match closely with that of experimentally obtained desorption energies of DNA bases on Au-film. We have demonstrated that on a pristine Au_3 cluster, the CO oxidation can take place by two different mechanisms such as E-R and L-H. On the contrary, on an Au_3 cluster bound to DNA bases, the mechanism is exclusively E-R. Our estimation of the activation barrier for the oxidation reaction suggests that in all the DNA base-gold cluster complexes, the CO oxidation is more facile with a lesser ΔE_a as compared to the bare gold cluster. Moreover, this reaction also becomes more endothermic for the case of base-cluster system in comparison to that of the pristine cluster. The charging of the cluster on account of complex formation can be of importance in deciding the catalytic activity of the cluster. Our results seem to be interesting in the light of the fact that DNA-nanoparticle complexes serve as an ideal route to the assembling of nanomaterials. The role of DNA can be analogous to that of oxides or carbon nanomaterials which are exhaustively explored as substrates for heterogeneous catalysis. As evinced from our interpretations, apart from the conventional diagnostic applications of DNA-gold systems where the thrust has been centered on so far, these systems can also act as active catalytic centers for several other reactions. Our results are likely to stimulate further interest in this direction.

CHAPTER 6

Nanomaterials for Energy Applications related to Water Splitting and Hydrogen Storage

Chapter 6: Nanomaterials for Energy Applications related to Water Splitting and Hydrogen Storage

The generation of clean and green energy is one of the most-sought after areas of research being pursued world-wide very intensively and actively. Depletion of fossil fuel and CO_2 induced climate change has spearheaded the need for green energy sources. To this end, hydrogen holds a promise as a potential energy carrier. Direct thermal splitting of water, $H_2O \rightarrow H_2 + (1/2)\ O_2$, although seems promising as it does not generate CO_2 and produce hydrogen, this process is associated with large kinetic barrier requiring temperatures in excess of 2000^0C. [312,313] Similarly, the electro-catalysis of water is energy intensive with very low yield and also requires expensive catalysts. [313]

The interaction of water with metals is of central importance in fields such as catalysis, electrochemistry, corrosion etc. In several industrially relevant catalytic processes, viz. water gas shift reaction, steam reforming etc., the formation and dissociation of water is a vital step. It is, therefore, of fundamental interest to study water interaction with metal surfaces which can help us improve the performance of catalysts relevant to these processes.

In recent years, there have been several theoretical and experimental studies on transition metal based nanostructures for high-capacity hydrogen storage and catalysts for water dissociation.[313-318] Pathak et al. [315] have discussed the adsorption and dissociation of a water monomer on (111) surfaces of several transition metals such as Cu, Au, Pt, Pd, and Ni. The first principle calculations of Pozzo et al. [317] shed light on the dissociation of water on Rh(111) and Ni(111) surfaces. They have calculated the barrier for water dissociation on Rh and Ni surfaces to be 0.92 and 0.89 eV respectively.

In the introductory chapter, we have briefly mentioned the importance of CNT and their possible applications. Development of methodologies or strategies for designing functional materials by assembling/incorporating the nanotubes into functional structures is the need of the hour. The hydrogen storage capacity of carbon based nanostructures has generated immense interest in recent years and a flurry of related literature is available[319-324]. Lei et al. [316] have discussed the initial stages of interaction of water molecules on Ti-doped CNTs. They have calculated the barrier for dissociation of a single water molecule to be ~ 0.4 eV and the subsequent barrier for splitting of the second water molecule which in turn releases H_2 is shown to be as low as 0.1 eV[316]. Similarly, Liu et al. [318] have proposed Ti-decorated C_{60} as a prototypical nanostructure for water dissociation. Hence, it follows from our preceding discussions that metal-based catalysts along with carbon based nanostructures (CNTs, C_{60} fullerenes etc.) are ideal nano-systems to investigate two important aspects associated with hydrogen energy, viz. (1) splitting of water to generate hydrogen and (2) storage of molecular hydrogen for portable application.

This chapter is primarily divided into two parts. The first part deals with different nanomaterials that can be employed as nano-catalyst systems for splitting of water. In second part of this chapter we have discussed some molecular systems which can be potential candidates for molecular hydrogen storage.

6.1: Nanomaterials for Water Splitting: A Computational Quest

At the outset of this chapter, the role of hydrogen as a sustainable source of energy has been emphasized alongside the need for exploring suitable nanomaterials that can act as catalysts for splitting of water to generate hydrogen. In this part of the thesis, we will focus on two nanocatalyst systems. The first study pertains to dissociation of water on gold clusters. The other nanomaterials that we have considered as catalyst for water splitting is Ti atom decorated BN nanotube (BNT). Through computational investigations, we explore the energetics of water dissociation reaction on these model catalysts.

6.1.1: Water Dissociation on a Gold Cluster Au_8 Supported on Carbon Nanostructures

In the previous chapters we have delved into the structure and electronic properties of gold nanoclusters and their role in catalysis. In the introductory part of the present chapter, we have underlined the importance of interaction of water with metals which plays a crucial role in several industrially relevant processes. The manifestations of nanoscale gold as catalytically active materials, particularly for CO oxidation reaction, have been elaborated at length in the previous chapters of this thesis. Consideration of gold nanoclusters as a nanocatalyst for water dissociation is an unexplored realm and it is therefore interesting to study the catalytic properties of small gold clusters with reference to water splitting reaction. With this objective, we have chosen the cluster Au_8, having the highly symmetric T_d geometry, as a catalytic model. We have considered the water dissociation on the pristine gas phase cluster as well as two important surfaces of carbon nanostructure namely planar graphene and curved CNT which are having a single vacancy site as defect. These two surfaces can be considered as ideal anchoring media for the nanoparticles and can modulate the catalytic properties of the nanoparticles by tuning the electronic environment of the active catalyst.

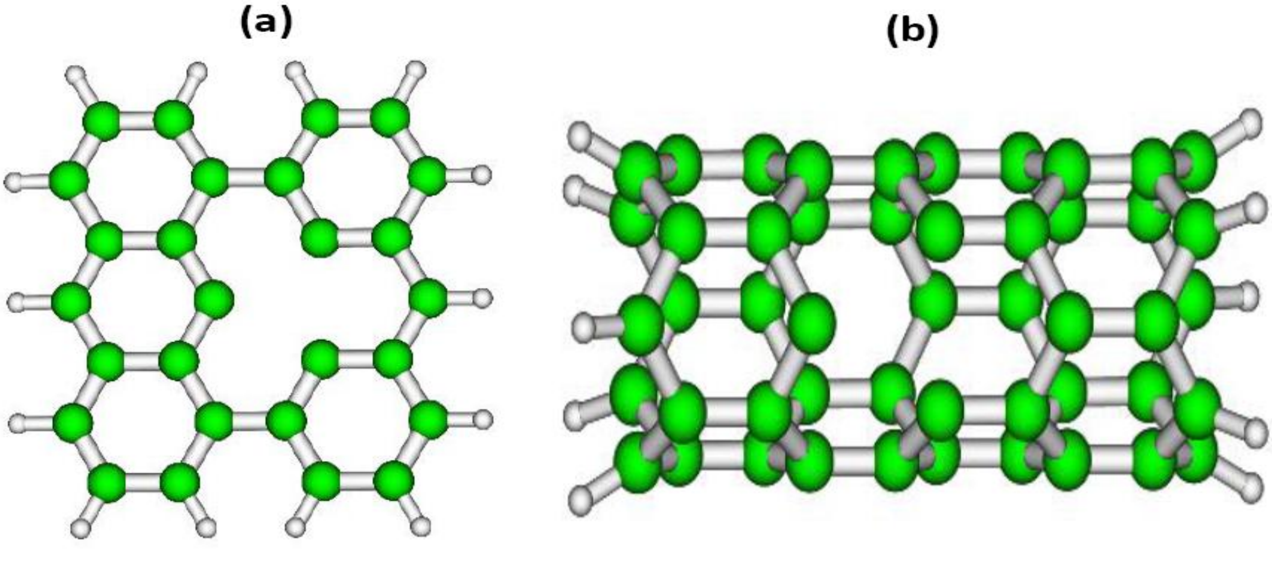

Figure 6.1: Graphical representations of two model carbon nanostructure surfaces; (a) defective graphene and (b) defective CNT(5,0).

6.1.1.1: Results and Discussions

Let us begin our discussion with the consideration of water dissociation reaction on a gas phase Au_8 cluster. The initial geometry for the gold cluster has T_d symmetry and serves as an ideal model gold cluster which is having exceptionally higher stability. [213] The water molecule can interact with this highly symmetric gold cluster at two types of symmetry unique gold atoms (differing in coordination number) in the cluster. It is found that a single water molecule favorably interacts with the low-coordinated gold atom, as presented in Figure 6.2 (IS). The binding of the water molecule with the gold cluster is favorable and the binding energy is calculated to be -0.37 eV. In the IS geometry, the Au (interacting with O-atom of H_2O)-O bond distance is found to be 2.455 Å. Similarly the O-H distance of the bound water molecule is 0.974 Å and the H-O-H angle is 105.27^0. The potential energy surface for the dissociation of water molecule has been generated by choosing one of the O-H bonds as the reaction coordinate. The optimized TS is also presented in Figure 6.2. It is noted that in the TS structure, one of the O-H bond distances (the reaction coordinate) is found to be 1.929 Å whereas the other O-H distance remains unaltered (0.978 Å). In the FS geometry, the water molecule is completely dissociated into H and OH which are bound to gold atoms through a bridging mode. The estimated barrier or water dissociation is 2.04 eV. Let us analyze our results more carefully by comparing with some earlier reported results for water dissociation. The dissociation of water on the (111) surfaces of Rh and Ni have been previously examined by DFT methods. [317] These metals are important from the viewpoint of their utility as catalysts in several industrially relevant processes. A comparison, therefore, can give us important insights into the performance of these catalysts.

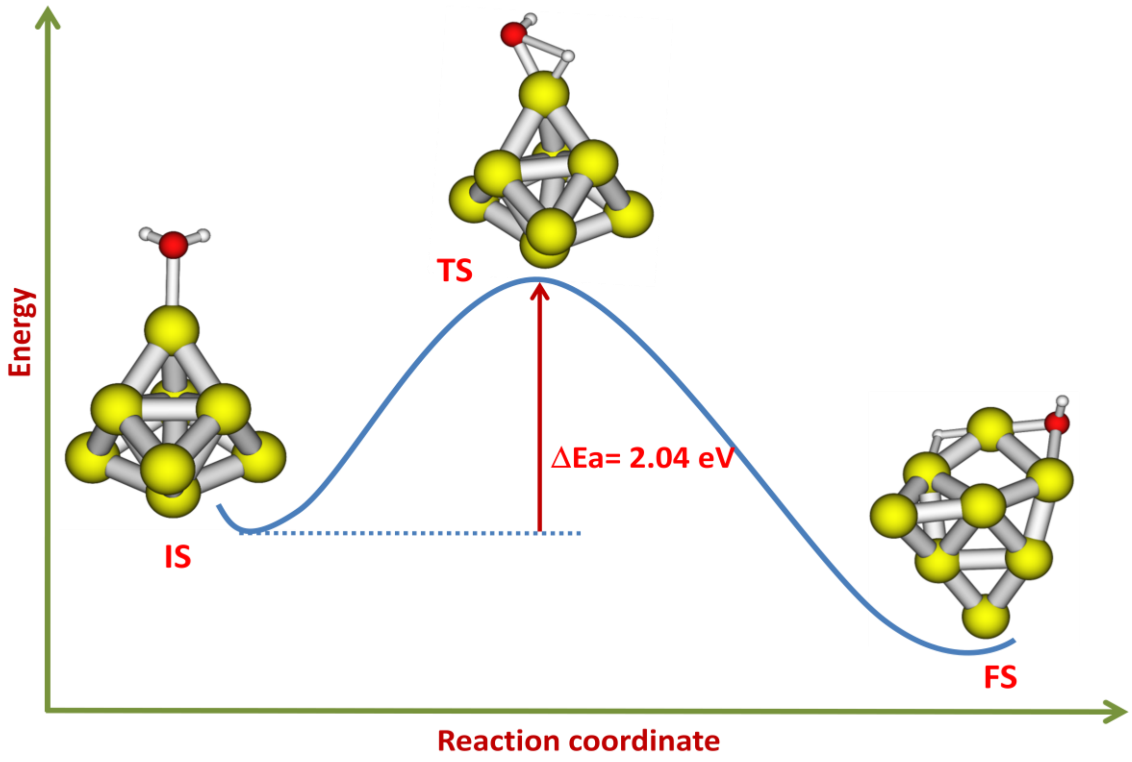

Figure 6.2: The reaction pathway showing IS, TS and FS for the dissociation of a single water molecule on Au_8 cluster.

The estimated binding energies of a water molecule on Rh and Ni surfaces are reported to be 0.35 eV and 0.25 eV respectively. [317] Our calculated binding energy (0.37 eV) matches closely with the above results. Thus it is inferred that, water can favorably interact with nanoscale gold and the interaction energies can be comparable with that of other metals like Rh and Ni. The barrier for water dissociation on the above two surfaces have been reported to be 0.92 eV and 0.89 eV respectively for Rh and Ni. [317] Our result for the barrier of water dissociation (2.04 eV) is much higher as compared to the above results. We, thus infer that although the water molecule binds to the gold cluster favorably, the barrier towards dissociation of water into H and OH is larger as compared to other common metals employed in catalysis. To bring down this high barrier, suitable substrates can be chosen. We have considered two model carbon nanostructure surfaces, viz. graphene and CNT which can be promising candidates as substrates.

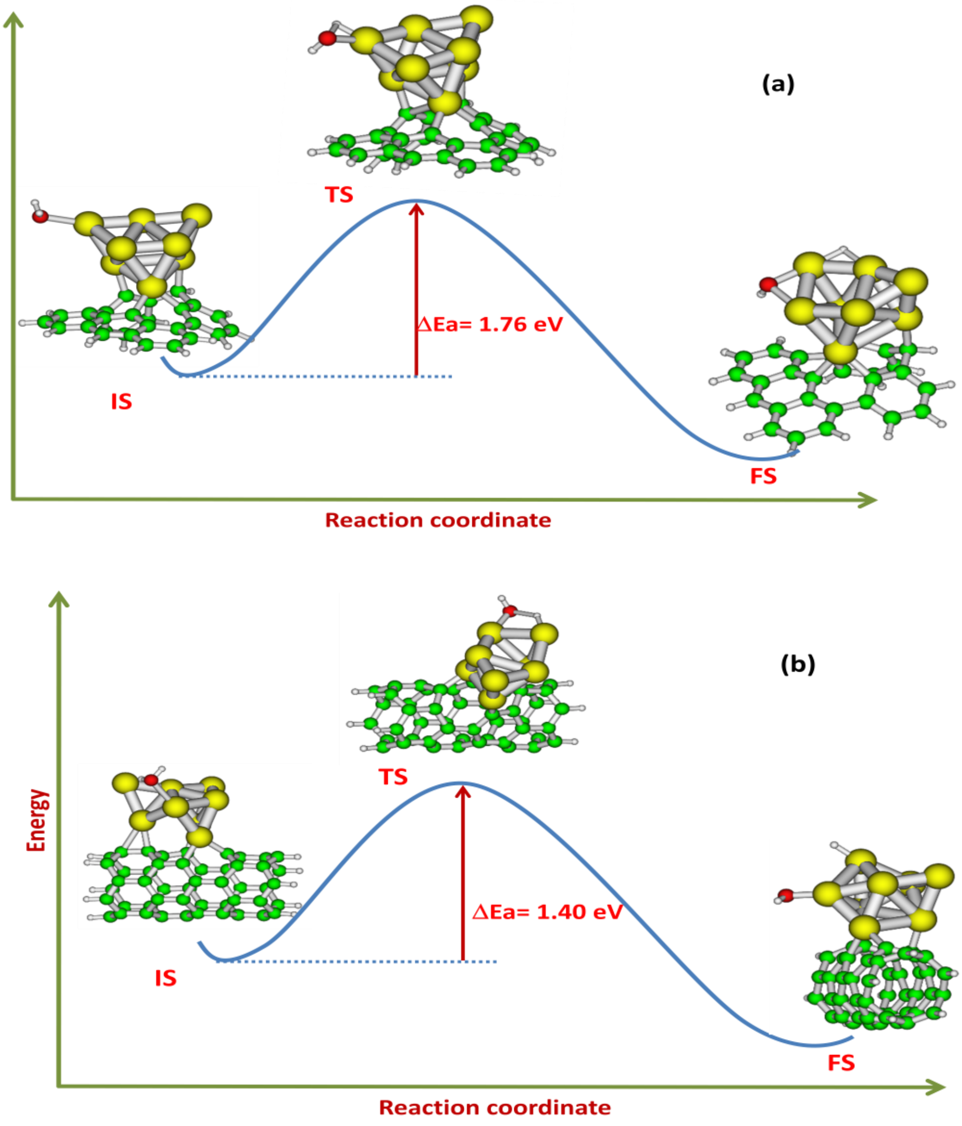

Figure 6.3: Water dissociation pathways on (a) Au_8-defective graphene and (b) Au_8-CNT systems.

These two surfaces have a single vacancy in the form of defect. It is noted that the interaction of perfect graphene/CNT with Au cluster is very weak. For better adherence and effective tuning of electronic environment of the active catalyst, the surface vacancy can be a useful concept. Recently Kauffman et al. have explored the sensory applications of Au decorated CNT. [325] They have shown that the binding of gold cluster at the vacancy site is stronger and the sensing property for gases like CO is also significantly modulated by the presence of vacancy site on the CNT surface. [325] Hence, considering gold cluster adsorbed atop a vacancy site on graphene or CNT can be a proper choice of nanostructure for water dissociation. The water dissociation pathways (IS, TS and FS) on the defective graphene and CNT surfaces have been presented in Figures 6.3 (a) and (b) respectively. Let us first discuss the results for water dissociation on Au_8 adsorbed on defective graphene. Due to the presence of vacancy site, the adsorption energy of the cluster Au_8 on the graphene surface is found to be -2.39 eV which is significantly higher as compared to the adsorption of the same cluster on a non-defective planar graphene (~0.3 eV). This signifies that the vacancy site on the surface of graphene can, in principle, help in strong adherence of the gold nano clusters and act as active sites for the catalysis. This strong binding also helps in significant charging of the cluster Au_8 which is found to have charge q_{Au8}=0.73 in atomic units, as calculated from a natural population analysis. Interestingly, the binding energy of water molecule to the supported cluster (IS of Figure 6.3 (a)) is also considerably higher (-1.42 eV) as compared to that of a gas phase Au_8 cluster (-0.37 eV) discussed already. The H_2O molecule prefers to bind to a low-coordinated Au-atom through O-atom, similar to the case of bare Au_8 cluster. The optimized Au-O distance is 2.423 Å which is slightly shorter than the same for gas phase cluster case. The O-H bond distances (0.974 Å and 0.973 Å) and H-O-H bond angle (105.62^0) for graphene-Au_8-H_2O system however does not vary appreciably as compared to the case of Au_8-H_2O system. In the TS geometry (Figure 6.3 (a)), the O-H bond lengths are 0.977 Å and 0.973 Å (reaction coordinate). Also, there is significant shortening of Au-O bond distance (2.129 Å) as compared to the corresponding IS geometry. The barrier for dissociation of water for this system is computed to be 1.76 eV. Thus, we observe that the activation barrier for water dissociation is reduced for graphene-Au_8-H_2O system than the corresponding bare cluster case. This reduction can be attributed to the significant charging of the cluster in the case of defective graphene as the substrate. Otherwise the reaction proceeds with high activation barrier in the case of pristine gold cluster. Let us now turn our attention to the case of water dissociation taking place on Au_8 adsorbed on defective CNT (Figure 6.3 (b)). The binding energy of Au_8 on top of defective CNT is -3.53 eV. This binding energy is considerably higher than that in the case of defective graphene (-2.39 eV). These two surfaces differ only by their inherent surface curvature. This observation shows that a curved surface like CNT can provide better adherence for the nanoclusters and can be helpful in promoting the catalysis. The charge on the cluster Au_8 is found to be 1.06 (in atomic units) which is even higher than the case of graphene-Au_8. The favorable binding and charging of the cluster seem to show correlation with the increase in curvature of the surface of carbon nanostructure. A curved CNT surface can manifest stronger binding as well as charging of the clusters. In the IS geometry, the Au-O bond distance is 2.433 Å, O-H bond distances are 0.993 Å and 0.975 Å, and H-O-H bond angle is 104.19^0. The binding energy of water molecule to gold cluster in this case is found to be -0.44 eV. In the optimized TS geometry, the Au-O bond length is shortened to 2.079 Å from the initial value of 2.433 Å. The O-H bond distances are 0.976 Å and 1.979 Å (reaction coordinate). The barrier for water splitting is this case is computed to be 1.40 eV. This barrier height is lower than the previous two cases, viz. the pristine gold cluster and the graphene-gold cluster system. This observation clearly demonstrates the effect of substrate in tuning the efficiency of water dissociation on the gold cluster. The important conclusion we derive from the preceding discussions is that, while water dissociation on a bare gold cluster proceeds through a higher activation barrier, the same can be significantly reduced by considering suitable substrates. Defective graphene and CNT can be good choices for the substrate. The latter is a better candidate in terms of providing stronger binding of the cluster to the surface as well as significantly reducing the barrier height. It is also worthwhile to mention that the electronic properties of small gold clusters is significantly size dependent. Hence several possibilities like proper choice of nanoclusters size, choice of substrate, presence of defects on the surface etc. are of paramount importance for the design of nanostructures for effective water splitting.

6.1.2: Water Dissociation on a Ti Decorated BN Nanotube

In the beginning of this chapter, we have given a brief overview of the importance of carbon nanomaterials for water splitting and hydrogen storage. In analogy to the CNTs, BN nanotubes (BNT) can be considered as the cylindrical structures resulting from the wrapping of a single honeycomb hexagonal sheet of BN (*h*-BN). [326] BNTs are emerging as technologically important materials following their successful synthesis in last two decades. [327,328] One of the most fascinating aspect of BNTs is that they belong to a class of semiconductors and the band gap is independent of the tube chirality, unlike the CNTs where chirality decisively determines the band gaps of the CNTs. [329-331] In the early 1970s, the seminal work of Fujishima and Honda has opened up a new avenue for employing semiconducting TiO_2 as a photocatalyst for water splitting. [332] The possibility of coating CNT with Ti has been demonstrated both theoretically and experimentally. [333,334] Very recently, Tang et al. have demonstrated improved photocatalytic reduction properties of TiO_2 when nano composites of this material are functionalized on the surface of BNTs. [335]

With this initial motivation, in the present study, we have considered the dissociation of water on a BNT decorated with a single Ti atom. From our calculations, we have demonstrated that the dissociation of water to H and OH fragments is extremely facile. Further, we have also shown that a second water molecule may also interact with the product from the splitting of the first water molecule. Interestingly, the splitting of the second water molecule proceeds with extremely small barrier leading to the evolution of one H_2 molecule.

6.1.2.1: Results and Discussions

We begin our discussion by considering the adsorption of a single Ti atom on top of BNT. Ti atom prefers to adsorb above the center of BN hexagon as compared to other binding possibilities like on top of B atom, N atom or a bridged site between B-N bond. We have considered a BNT with smaller diameter having chirality (4, 4) to minimize the computational cost arising out of consideration of wider tubes with more number of atoms. It has already been mentioned in the previous section that the band gap energy of BNT is independent of the selection of chirality (n, m). On the contrary, for CNTs the selection of chiral vectors (semiconducting (n, 0); metallic (n, n)) can influence the electronic properties. The binding energy of Ti atom on a (4, 4) BNT is found to be -1.03 eV. This Ti adatom on the surface of BNT also acquires significant partial positive charge (0.497 e) as obtained from a Mulliken population analysis. To evaluate the effect of surface curvature of BNT on the binding energy of Ti atom, we have also considered two more variants of BNT, viz. (5, 5) and (6, 6). The diameters of the three BNTs (4, 4), (5, 5) and (6, 6) follow an increasing trend and the surface curvature follow an inverse trend. The binding energy of Ti atom on (5, 5) and (6, 6) BNTs are -0.79 eV and -0.65 eV respectively. We, therefore, infer that the adsorption of Ti is more favorable for highly curved (smaller diameter) nanotubes. The optimized geometry (IS) of water adsorbed on Ti decorated BNT (4, 4) has been presented in Figure 6.4 (a). The binding energy of a single water molecule is calculated to be -1.78 eV. This high binding energy suggests that water adsorption on a Ti-BNT system is a favorable process. We have also presented the dissociation of this water molecule bound to Ti-BNT system in Figure 6.4 (a). The barrier for the splitting of the water molecule atop Ti adatom is computed to be 0.12 eV. Lei et al. have estimated the barrier for water dissociation to be ~0.4 eV on a Ti-CNT system. [316] Our observation of extremely lower barrier can be pertinent in the design of nanostructures for splitting of water. In the FS, we find that one of the product (OH fragment) is adsorbed on Ti adatom whereas the other (H) is held by a bridged bond between the Ti adatom and one of the B atoms on the BNT surface. The overall heat of formation of the product is calculated to be -2.89 eV. This suggests that spitting of water molecule on a Ti-BNT system is extremely exothermic. With this initial observation that the dissociation of first water molecule on a Ti adatom on BNT surface is highly facile, we have attempted to investigate the subsequent dissociation of the second water molecule. The dissociation process of the second water molecule is pictorially presented in part (b) of Figure 6.4. The binding energy of the second water molecule on the Ti (shown in IS of Figure 6.4 (b)) adatom is found to be -3.94 eV which is higher than that of the first water molecule (-1.78 eV). This indicates that, even after the splitting of the first water molecule, Ti adatom can still act as a catalytic active center for subsequent interaction of water molecule. The higher binding energy of the second water molecule can be attributed to the formation of a hydrogen bond (O-H….N) between one of the H atoms of the second water molecule and one of the surface N atoms. The corresponding O-H bond is considered as the reaction coordinate for the generation of the potential energy surface. Further, we have estimated the barrier height for the splitting of the second water molecule to be 0.01 eV. This observation emphatically demonstrates that the splitting of the second water molecule is almost barrierless. This extremely low barrier for splitting of the second water molecule can, in principle, be ascribed to the stabilization of the TS structure (Figure 6.4 (b)) through hydrogen bonding. The O-H bond distance (reaction coordinate) is increased from its initial value of 1.002 Å in the IS geometry to 1.230 Å in the TS. Similar to the case of the IS structure, the hydrogen bonding involving O-H….N is still intact in the TS structure and this stabilization is the possible reason for barrier-less nature of the second step. Lei et al. have shown the barrier height for the dissociation of the second water molecule for a Ti-CNT system to be 0.12 eV. [316] BNT and CNT manifest quite different behavior as substrates and in terms of their interaction with water. While the surface of CNT is essentially hydrophobic, the BNT surface can act as hydrophilic and the N-atoms on the latter's surface may facilitate hydrogen bonding with water molecules. Our observations based on this rationale make Ti-BNT system a promising candidate for water splitting. Another point which is worth mentioning is that, in the product state two OH fragments are bonded to Ti adatom with the liberation of one H_2 molecule. Moreover, the heat of formation of the product is estimated to be -0.97 eV which indicates the exothermicity of this step. The preceding discussions, therefore, lead us to conclude that water dissociation on a Ti-BNT nanostructure is an extremely favorable process. The dissociation of first molecule of water is a process with minimal barrier and subsequent dissociation of the second water molecule which in turn leads to the formation of hydrogen molecule is almost barrierless. Some of the interesting innate properties of BNT, such as their semiconducting nature irrespective of their chirality, the hydrophilic nature of the surface, etc. can make Ti-BNT system as an effective nanostructure for water splitting and generation of hydrogen.

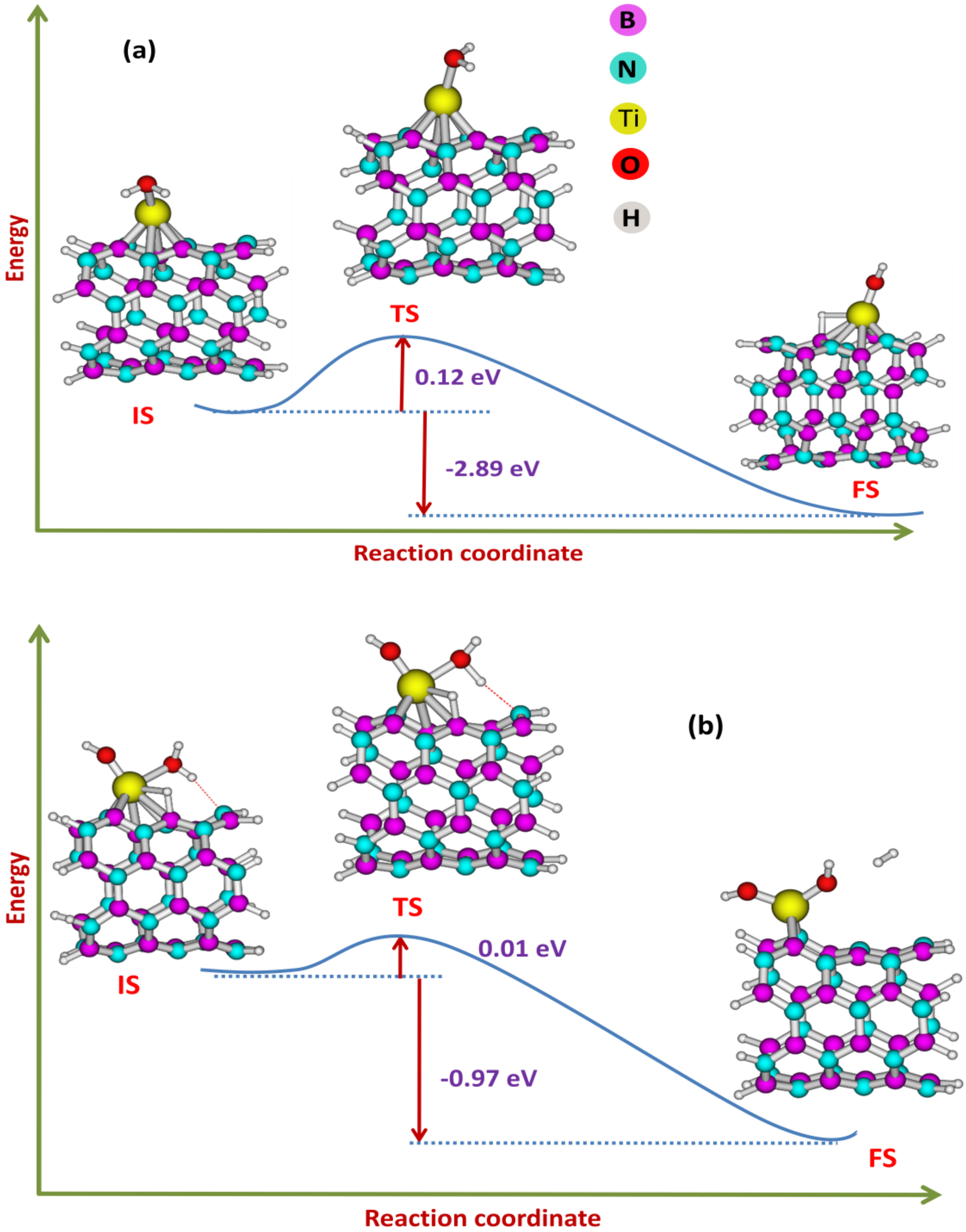

Figure 6.4: The schematic potential energy surface for splitting of first water molecule (a) and second water molecule (b) on a Ti-decorated BNT.

6.2: Nanomaterials for Molecular Hydrogen Storage

In this section of the chapter, we will discuss our computational investigations on the hydrogen storage properties of some nanomaterials, particularly the binary clusters of Si-Li.

6.2.1: Hydrogen Adsorption in Silicon-Lithium Binary Clusters

To meet the ever increasing energy demands for the world at large, hydrogen in recent years has emerged as a preferred candidate for an alternate source of energy. [336-338] The choice of hydrogen energy is obviated from considerations like high utilization efficiency and more importantly being a green and environmental friendly clean source of energy. Realization of this goal, however, rests on the design and development of novel materials for hydrogen storage. [339,340] The bottleneck for designing these kinds of materials is the requirement of high gravimetric and volumetric density, fast sorption kinetics and favourable thermodynamics. Moreover, the hydrogen interaction energy should be somewhere in-between that of chemisorption and physisorption, typically in the range of 5.0 to 9.0 kcal/mol for room temperature applications. [341,342] Though a large number of materials have been studied for hydrogen storage, none of the presently existing materials satisfies all the requirements to reach the target of 6.5 weight % and 62 kg/m^3 volume density set by the Department of Energy (DOE). Hence, exploration of new hydrogen storage materials for onboard hydrogen storage is an essential and active area of research.

Last few years have witnessed an active research, both theoretically and experimentally, addressing the rational development of materials for hydrogen storage. These materials span the wide range of metal hydrides, porous materials like zeolites and metal organic frame works (MOFs), carbon based nano materials starting from graphene to fullerenes and also nanotubes etc. [89,320,343-352] These nanomaterials, in their pristine as well as metal doped forms have been explored in all its lengths and depths in recent years. Transition metal atom decorated fullerenes and nanotubes are shown to be effective hydrogen adsorbing materials. [321,323] However, later it has been shown that transition metals aggregate to form clusters at high temperatures which diminishes their hydrogen storage capacity. [353] In an interesting work, Chandrakumar et al. [44] have shown that alkali metal atom doped C_{60} fullerenes can be a high capacity hydrogen storage materials. In the transition metal decorated nanomaterials, H_2 binds to the metal centres by Kubas interactions whereas in the alkali metal decorated systems the H_2 binds through ion-quadrupole and ion-induced dipole interactions. Apart from extended systems like MOFs, graphenes and nanotubes, molecular systems having the desired properties of hydrogen storage are equally important. Molecular systems from the main group elements having interesting structures and properties have not been widely explored from the point of view of hydrogen storage. Recently, Srinivasu et al. have explored the possibilities of hydrogen storage by Li-doped *closo*-boranes and proposed an extended 3D network for this application. [354]

In one of the earlier studies, Srinivasu et al. showed that alkali metal ion decorated $C_5H_5^-$ can adsorb molecular hydrogen with 12 wt% of H_2 and discussed the role of aromaticity in stabilising these systems. [246] Jemmis et al. studied the structure and stability of $C_3Li_3^+$ and showed that the Li atoms form bond to C-C edges. [355] Minkin et al. proposed the structure and stability of a series of perlithioannulenes C_nLi_n ($n = 3$–6). [356] An interesting 3D molecular star like structures such as $Si_5Li_n^{n-6}$ (n=5-7), have been reported very recently by Tiznado et al. where they have shown that the central unit of Si_5^{6-} ring interacts with Li cations. [357] These fascinating molecular structures which essentially contain lighter elements like Si and Li can be important for hydrogen storage with higher gravimetric result. Moreover, alkali metal atoms like Li, which is present in these systems favourably bind multiple hydrogen molecules. These attractive features have prompted us to undertake extensive *ab initio* theoretical investigations of hydrogen storage by these systems.

6.2.1.1: Results and Discussions

Let us first discuss the structure and energetics of silicon-lithium clusters. The equilibrium geometries of the possible isomers of the three different silicon-lithium binary clusters, $Si_5Li_5^-$, Si_5Li_6 and $Si_5Li_7^+$, optimized at MP2/6-31++G(2d 2p) level of theory, are given in Fig. 1. $Si_5H_5^-$ can be considered as the analogue of $C_5H_5^-$ which is known to be aromatic and form stable Ferrocene like complexes. If all the protons are replaced with Li ions, it generates the $Si_5Li_5^-$ binary cluster and can be expected to have a geometry similar to that of $C_5H_5^-$. However, the planar D_{5h} geometry of $Si_5Li_5^-$ shown in Figure 6.5 (a-iv) is found to be a higher energy isomer as compared to the lowest energy isomer (a-i) with an energy difference of 60.69 kcal/mol. The lowest energy isomer is found to have two different types of lithium sites with C_{2v} symmetry shown in Figure 6.5 (a-i). Two of the five lithium atoms are found to occupy the axial positions, with one below and one above the Si_5 plane and the remaining three are bonded to the Si-Si edges with an average Si-Si bond distance of 2.38 Å. The Si-Li distance for the axial Li is found to be 2.56 Å whereas the same is 2.41 Å for the equatorial lithium atoms. From the calculated atomic charges, it is found that the axial Li sites carry a positive charge of 0.78 while the equatorial Li has a charge of 0.44 which shows that the axial Li sites are more ionic in nature. The second lowest energy isomer (a-ii) is found to have C_{2v} symmetry with three adjacent bridge bonds and two axial lithium atoms which is just 3.19 kcal/mol higher in energy as compared to the lowest energy isomer. The next higher energy isomer (a-iii) with one axial lithium and four equatorial Li is 28.6 kcal/mol higher in energy as compared to the lowest energy isomer. In this isomer, the equatorial lithium atoms are not in the Si_5 plane, but have moved towards the axial Li with bridge Li-axial Li distance of 3.5 Å.

In the case of Si_5Li_6, two different isomers are geometry-optimized and the minimum energy structure is found to be the one with four equatorial Li and two axial Li as shown in

Figure 6.5 (b-i). The optimized geometry of this isomer has the symmetry C_{2v} with an average Si-Si bond length of 2.35 Å. The calculated atomic charges on the axial Li and equatorial Li are found to be 0.92 and 0.63 respectively. The next higher energy isomer (b-ii) with one axial Li and five equatorial Li is found to have 27.66 kcal/mol more energy and the symmetry C_{5v}. In the case of $Si_5Li_7^+$, we have optimized only one isomer with two axial Li and the remaining five equatorial Li are bridged to all the five edges of Si_5 ring and is found to have D_{5h} symmetry as shown in Figure 6.5 (c). In this case, as all the edges are bonded to Li, all the Si-Si bonds are equivalent and the Si-Si bond distance is found to be 2.33 Å. The calculated atomic charge on axial Li is found to be 1.1 and that on the equatorial Li is 0.81. All the minimum energy structures of $Si_5Li_5^-$, Si_5Li_6 and $Si_5Li_7^+$ are in good agreement with the earlier reported global minima by Tiznado et al. [357] For all the isomers considered here, we calculated the Hessian at MP2/6-31++G(2d 2p) level of theory and found none of them to have imaginary frequencies indicating that all these structures correspond to the local minima on their respective potential energy surfaces. The minimum vibrational frequencies are also found to be considerably large to ensure the stability of the binary clusters considered.

We will now discuss about the hydrogen adsorption properties of Si_5Li_6 and $Si_5Li_7^+$. Although molecular hydrogen does not have a permanent dipole moment, it has a large quadrupole moment and polarizability and hence, when it approaches a charged site it can bind to that site through ion-quadrupole and ion- induced dipole interactions. First, we discuss the hydrogen adsorption properties of Si_5Li_6 with different number of molecular hydrogen adsorbed as shown in Figure 6.6 and the corresponding results are reported in Table 6.1. In the case of $Si_5Li_6(H_2)_6$ where each Li site binds one molecular hydrogen, the average adsorption energy per H_2 calculated at MP2/6-31++G(2d 2p) level of theory is found to be -3.63 kcal/mol.

(a) $Si_5Li_5^-$

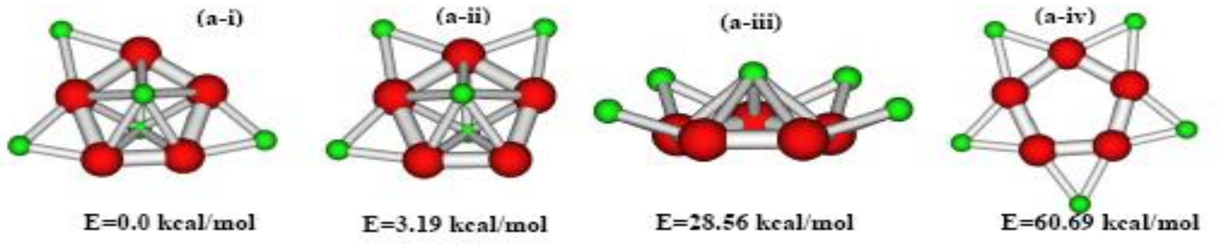

(b) Si_5Li_6

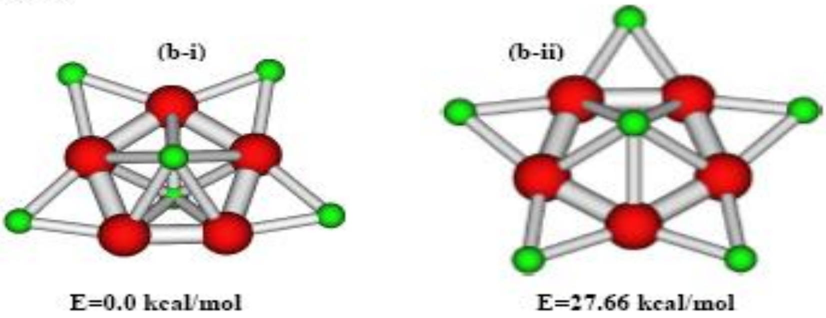

(c) $Si_5Li_7^+$

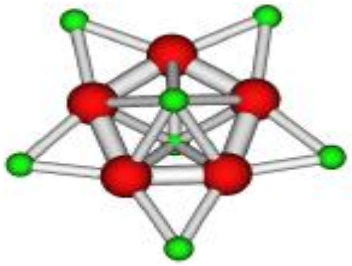

Figure 6.5: Equilibrium geometries of (a) $Si_5Li_5^-$, (b) Si_5Li_6 and (c) $Si_5Li_7^+$.

The Li-H_2 distance in the case of axial Li is found to be 1.98 Å which is shorter as compared to that in the case of bridged Li-H_2 (2.1 Å) distance which can be attributed to the relatively higher charge on axial Li as compared to that on bridged Li. This difference in Li-H bond distance shows that H_2 molecules bonded to axial Li are more strongly bonded as compared to others bonded to equatorial Li. When the second H_2 molecule approaches each Li site, the axial Li sites cannot trap the second H_2 and thus two of the twelve H_2 in $Si_5Li_6(H_2)_{12}$ move away from the binary cluster as shown in Figure 6.6 which might be attributed to the steric repulsion from molecular hydrogen already adsorbed. Hence, we re-optimized the structure by removing the two H_2 molecules which are not bound as $Si_5Li_6(H_2)_{10}$ and the structure is shown in Figure 6.6. The interaction energy per molecular hydrogen in this case is found to be -3.03 kcal/mol.

In the case of $Si_5Li_6(H_2)_{14}$ the interaction energy per molecular hydrogen is found to be -2.47 kcal/mol. As we have seen in our earlier studies, each Li site can adsorb up to a maximum of three molecular hydrogens. Also from the optimized geometry of $Si_5Li_6(H_2)_{14,}$ one can see that the adsorbed hydrogen molecules are already crowded and introduction of further hydrogen molecules is difficult. Hence, we have studied up to a maximum of three H_2 per Li with a total number of 14 molecular hydrogen adsorbed resulting into $Si_5Li_6(H_2)_{14,}$ with the gravimetric density of 13.33 wt% of hydrogen.

The next binary cluster studied for hydrogen adsorption is $Si_5Li_7^+$ and the optimized geometries of the corresponding hydrogenated species with different number of molecular hydrogen are given in Figure 6.7 with the results reported in Table 1. The average interaction energy per molecular hydrogen in $Si_5Li_7^+(H_2)_7$ calculated at MP2/6-31++G(2d 2p) is found to be -4.3 kcal/mol and the optimized structure is found to have C_s symmetry. The adsorption energy of molecular hydrogen in this cluster is found to be more than that in the Si_5Li_6 case as the Li sites here are more ionic in nature as compared to the Li sites in Si_5Li_6. Similar to the earlier case, on introduction of two molecular hydrogen, two of the 14 H_2 move away from $Si_5Li_7^+(H_2)_{14}$ as shown in Figure 6.7 and hence we optimized the structure again with 12 H_2 as $Si_5Li_7^+(H_2)_{12}$ and the interaction energy per molecular hydrogen is found to be -3.79 kcal/mol. In the case of $Si_5Li_7^+(H_2)_{17}$, the five bridged Li adsorb 15 H_2 molecules and two axial Li adsorb two H_2 which corresponds to a gravimetric density of 15.25 wt%. The adsorption energy per molecular hydrogen is found to be -2.98 kcal/mol and the optimized structure is found to have C_s symmetry.

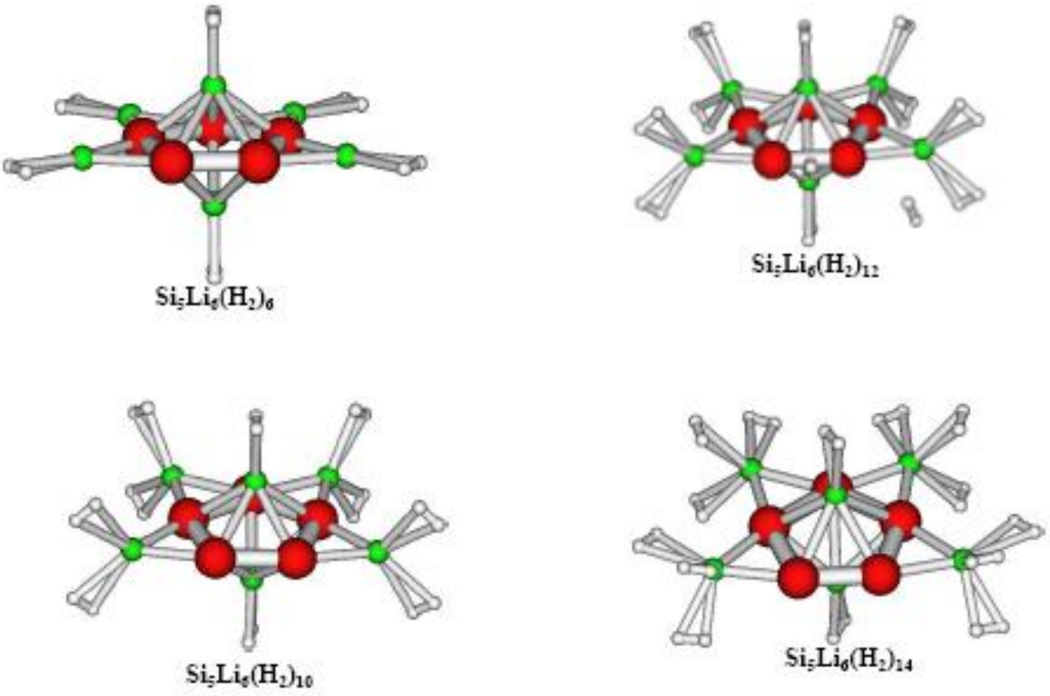

$Si_5Li_6(H_2)_6$ $Si_5Li_6(H_2)_{12}$ $Si_5Li_6(H_2)_{10}$ $Si_5Li_6(H_2)_{14}$

Figure 6.6: Equilibrium geometries of $Si_5Li_6(H_2)_n$.

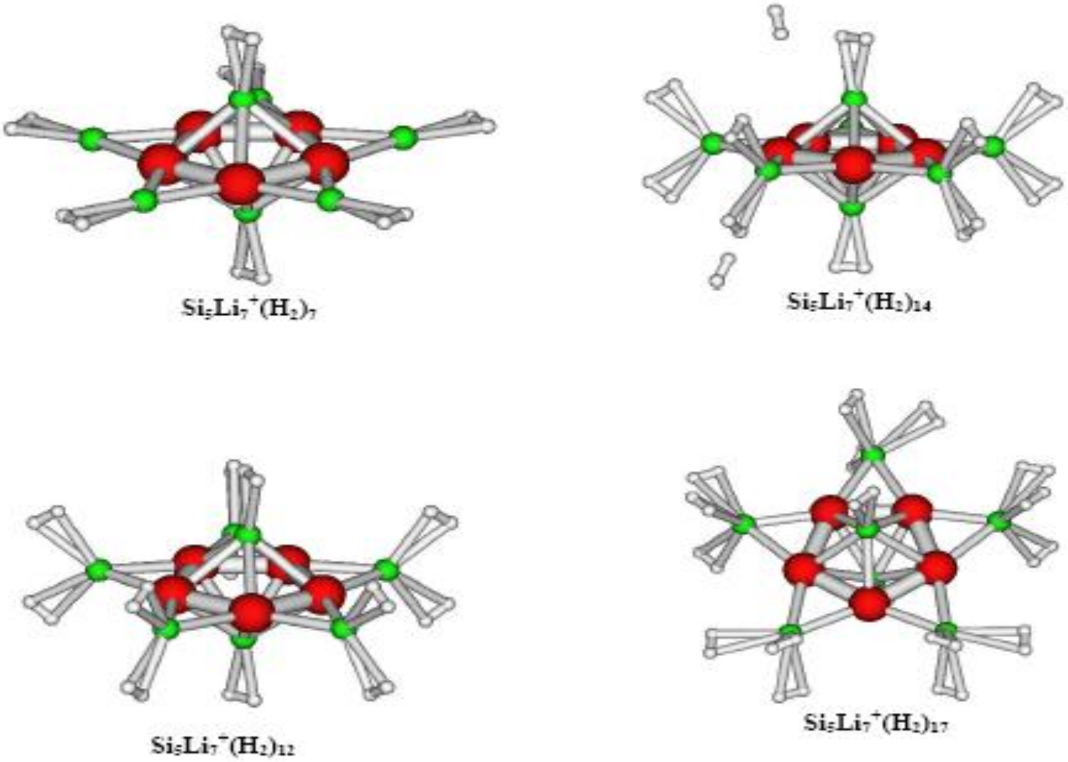

$Si_5Li_7^+(H_2)_7$ $Si_5Li_7^+(H_2)_{14}$ $Si_5Li_7^+(H_2)_{12}$ $Si_5Li_7^+(H_2)_{17}$

Figure 6.7: Equilibrium geometries of $Si_5Li_7^+(H_2)_n$.

The interaction energies calculated by MP2 method are found to be larger than the corresponding PW91 results as is evident from results reported in Table 1. This kind of observation with the correlated methods giving improved results as compared to the commonly used DFT functionals, is well known in the literature, particularly in the case of weakly interacting systems. In all the hydrogenated clusters, the adsorbed hydrogen is mainly in molecular form and the bond length in adsorbed H_2 is little elongated to 0.743 Å from 0.736 Å in the free molecular hydrogen optimized at the same level of theory. The calculated HOMO-LUMO gaps for all the hydrogenated clusters are reported in Table 6.1 and all of them are found to have large HOMO-LUMO gaps which are an indication for their stability.

Table 6.1: Hydrogen interaction energy, charge on lithium atom and HOMO-LUMO gaps of hydrogenated Si_5Li_6 and $Si_5Li_7^+$ binary clusters.

System	Interaction energy (kcal/mol)		Charge on Li (a.u)		HOMO-LUMO gap (eV)		η (eV)	ω (eV)
	PW91	MP2	PW91	MP2	PW91	MP2		
Si_5Li_6			0.89	0.92	1.96	5.49	4.93	0.79
Si_5Li_6-$6H_2$	-2.613	-3.632	0.789	0.958	2.03	5.44	5.54	0.69
Si_5Li_6-$10H_2$	-2.511	-3.032	0.637	0.743	1.97	5.30	5.36	0.67
Si_5Li_6-$14H_2$	-2.361	-2.472	0.556	0.635	2.15	5.21	5.50	0.68
$Si_5Li_7^+$			1.07	1.10	2.51	6.71	6.22	2.43
$Si_5Li_7^+$-$7H_2$	-3.238	-4.300	0.975	1.069	2.45	7.06	6.12	2.22
$Si_5Li_7^+$-$12H_2$	-2.881	-3.788	0.818	0.848	2.41	6.98	6.02	2.11
$Si_5Li_7^+$-$17H_2$	-2.725	-2.979	0.450	0.618	2.39	6.92	5.83	2.20

In addition, in Table 6.1, we also report the calculated values of the electrophilicity (ω) as well as hardness parameters. It is observed that there is a gradual decrease in electrophilicity with increase in the number of hydrogen molecules adsorbed per metal site, in line with the minimum electrophilicity principle. The hardness (η) values are found to show trends quite similar to the HOMO-LUMO gap values, reaffirming the conclusion about the stability of the hydrogenated species. It may be interesting to further investigate the role of the principles of maximum hardness in this context. This trend demonstrates the stability of the hydrogenated metal clusters. We have also calculated the Hessian for all the hydrogenated clusters at MP2/6-31++G(2d 2p) level of theory and found only real frequencies which shows that these structures are at the local minima on their respective potential energy surfaces. As all the lithium sites in these star like binary clusters are positively charged, it might be possible to design three dimensional materials by choosing a proper ligand. It is also possible to construct multidecker sandwich type of materials which are well known in the case of $C_5H_5^-$ (Cp^-).

6.3: Computational Details

For the first work of the first part of this chapter (CNT-Au system), all the calculations have been performed using the electronic structure software TURBOMOLE. We have employed def2-SVP basis set for the atoms of the substrate (graphene and CNT) and def2-TZVP for all other atoms. Relativistic corrected effective core potential ecp-mwb has been used for 60 core electrons of Au atom. The PBE density functional has been used for all the calculations. The model graphene surface consists of 27 C-atoms with a vacancy site and the peripheral carbon atoms saturated by 14 H-atoms (Figure 6.1 (a)). Likewise, to model the CNT surface, we have considered a small segment of CNT(5,0) with a single vacancy site and the terminal C-atoms saturated by H-atoms (Figure 6.1 (b)). The potential energy surface for water dissociation reaction on Au_8 adsorbed on these surfaces is computed by considering one of the O-H bond in water molecule as the reaction coordinate. The geometry corresponding to maxima on the potential energy surface is taken as the initial guess for the transition state (TS) optimization. The optimized TS is confirmed by a hessian calculation where only one imaginary frequency is observed. The barrier for water dissociation (ΔE_a) is calculated by subtracting the energy of the TS and initial state (IS).

The calculations for the second section of the first part (BNT-Ti system) of this chapter have been carried out by using the computational chemistry software TURBOMOLE. We have used the density functional PBE in conjunction with def2-SV(P) basis set for all the atoms. The BNT has been modeled by considering a small segment of BNT(4, 4) where the terminal B and N atoms have been saturated with H atoms. One of the O-H bonds of the water molecule is chosen as the reaction coordinate and the potential energy surface for water dissociation has been generated from several single point calculations. The highest point on the potential energy surface is taken as the initial guess geometry for TS optimization.

In the concluding section of this chapter (Si-Li system), all the energy calculations and structural optimization of the cluster systems have been carried out by using the electronic structure theory based GAMESS software. [50] We have employed the density functional theory (DFT) with the Perdew-Wang (PW91) exchange correlation functionals. [358] Since the molecular hydrogen interaction is weak in nature, it is important to include proper electron correlation effects. Although the performance of the DFT based exchange-correlation functionals is reasonably good in some of the cases, most of the existing functionals like B3LYP are not good enough for the description of weak interactions. Hence, we have also carried out all the calculations using the second order Moller-Plesset (MP2) perturbation method. We have used the extensive split-valence basis sets with diffuse and polarization functions, 6-31++G(2d,2p). The highest occupied molecular orbital (HOMO)-lowest unoccupied molecular orbital (LUMO) gaps are calculated as the energy difference between the corresponding orbitals. The initial geometries and all the reported structures have been obtained using the graphical software MOLDEN. [359] The adsorption energy per molecular hydrogen on the Si-Li clusters is calculated using the relation

$$\Delta E(H_2) = \{E[Si_5Li_m(H_2)_n]-[E(Si_5Li_m) + n\,E(H_2)]\}/n\ .$$

We have also calculated the chemical hardness (η) and electrophilicity (ω) values to verify the stability of the systems using molecular electronic structure principles like the principle of maximum hardness and minimum electrophilicity principle. [360] [361] [362] The hardness and electrophilicity parameters are calculated using the formulae

$$\eta = I - A$$

and

$$\omega = \frac{\mu^2}{2\eta} = \frac{\chi^2}{2\eta},$$

where I is the vertical ionization potential and A is the vertical electron affinity values calculated for an N electron system as $I = E(N-1) - E(N)$ and $A = E(N) - E(N+1)$.

6.4: Summary of the Work

The broad objective of this chapter has been computational investigations of nanostructures for water dissociation and hydrogen storage and accordingly we have discussed our results in two main sections.

In the first study of the first part of this chapter, we have considered water dissociation on bare as well as supported gold cluster Au_8. Two important carbon nanostructures namely graphene and CNT have been chosen as the surfaces. These two surfaces have defects on them in the form of a single vacancy site. It is observed that the water dissociation on the pristine gold cluster is a process with higher barrier with calculated barrier height as 2.04 eV. This barrier height, however, is reduced to 1.76 eV and 1.40 eV for graphene-Au_8 and CNT-Au_8 systems respectively. The vacancy on the surface of graphene/CNT provides stronger adherence to the cluster. The binding energy of the cluster on the curved CNT surface is more than that of the planar graphene surface, indicating the CNT as a better choice for the surface. The charging of the cluster on these two surfaces is also found to play a key role in deciding the catalytic efficiency. It is proposed that CNT decorated gold clusters can be a potential catalyst for water splitting. Factors like nature of CNT, shape and size of gold clusters can be influential in fine-tuning the efficiency of these nanostructures for water dissociation.

In the second study related to the splitting of water under part one of this chapter, we have considered Ti-decorated BNT as a model nanostructure. Our results demonstrate that adsorption of Ti atom on a BNT surface depends on the surface curvature of the latter. We find that for a more curved BNT (with smaller diameter), the binding energy of Ti adatom is higher. We have computed the barriers for successive splitting of two water molecules on a Ti-BNT nanostructure. The barrier for splitting of the first water molecule is found to be 0.12 eV whereas the barrier for the second step is marginally smaller (0.01 eV). Stabilization of the TS structure by hydrogen bond involving O-H….N, for the second water splitting step is the possible reason for the barrierless nature of this process. The dissociation of two water molecules finally leads to the formation of H_2 molecule. We propose Ti-decorated BNT system to be a potentially promising nanostructure for splitting of water and generation of hydrogen.

In the second part of this chapter where we have discussed nanostructures for hydrogen storage applications, we have investigated the hydrogen adsorption properties of silicon-lithium binary clusters. We have shown here that silicon can form perlithioannulene type of structures with the general formula $Si_5Li_n^{n-6}$ (n=5-7). Three dimensional structures with two axial lithium and remaining (n-2) lithium in the Si_5 plane are found to be more stable structures. We have considered three different clusters viz. $Si_5Li_5^-$, Si_5Li_6 and $Si_5Li_7^+$ and for each cluster, the geometries of different possible isomers are optimized. In all the minimum energy isomers of the three clusters considered, two of the lithium atoms are found to be situated in the axial positions and the remaining lithium atoms are in the equatorial position in the Si_5 plane. The lithium atoms which are in Si_5 plane are bonded to the Si-Si edge through a bridge bonding instead of a corner of the Si_5 ring. From the calculated atomic charges, it is found that there is a charge transfer from lithium to silicon leaving a partial positive charge on the Li atoms and the axial lithium atoms are more charged as compared to the remaining lithium atoms. In the case of Si_5Li_6 and $Si_5Li_7^+$, the Li sites can trap a total of 14 and 17 H_2 molecules respectively, with each bridge bonded Li site adsorbing three H_2 molecules and each axial Li adsorbing one H_2 molecule which corresponds to a gravimetric density of 13.33 wt% and 15.25 wt% respectively. We propose that, the multidecker sandwich type of materials using these $Si_5Li_n^{n-}$ binary clusters as building units can be a promising candidate for molecular hydrogen storage.

CHAPTER 7

Outlook and Future Explorations

Chapter 7: Outlook and Future Explorations

In this concluding chapter, we will discuss some of the possible extensions of the work that can stem out from our discussions in the preceding chapters, i.e. from chapter 2-6. The detailed understanding and finer rationale that has been obtained in the course of our investigations on the diverse structural and electronic properties as well as reactivity of a broad range of nanomaterials discussed so far can, in principle, serve as a fertile background for many new paradigms of research.

In chapter 2, we have made an attempt to understand the electronic properties and reactivity of CNTs by using model systems. These kinds of models enable us to derive much insightful information on the electronic properties of CNT with minimum computational cost. As a possible extension of these investigations, we look forward to consider actual CNTs which can indeed give us more accurate and useful information on the structure and reactivity of these systems. In the context of investigating the behavior of water inside the CNT, we have come to some important conclusions on the properties of water under confinement. One such observation has been the critical dependence of blue and red shifting of the normal vibrational modes of water (as compared to that of the free water molecule) on the confinement distance and nanoscale curvature. The importance of detailed exploration of the properties of water in the confined region has been emphasized. There are reports of extremely facile flow of water inside CNT. [81] It has also been reported that inside the cylindrical confined space of CNT, there can be at least nine different phases of ice and some of them have been determined experimentally. [363] The mechanism of fast proton transfer along a one-dimensional chain of water confined in a narrow CNT has been elucidated by Cao et al. [364] Their results reveal that the fast proton transfer inside CNT occurs via a "Zundel ($H_5O_2^+$)-Zundel" mechanism in contrast to "Zundel-Eigen ($H_9O_4^+$)" mechanism observed in bulk water. [364] Motivated by such reports, we are interested to explore further the proton transfer process for nanoconfined systems. Computing the barrier for proton transfer inside CNTs as a function of the tube diameter can provide fundamental insights into how the confinement effect plays a crucial role. Precisely, considering CNTs with varying diameter, we intend to study the proton transfer process and want to shed light on the role of confinement on this process. The confined medium of CNT can be considered as a nanoscale reactor to promote several catalytic processes. The seminal work of Pan et al. [237] has demonstrated that nanoparticles deposited inside the confined region of CNT leads to enhanced production of ethanol. Contingent upon such reports, we are planning to explore several other chemical reactions under the confinement of CNTs.

In chapter 3, we have dealt with some of the possible applications of fullerenes which is firmly based on the interesting and diverse chemistry of fullerenes. We have discussed the role of azafullerenes as potentially important structures for applications based on their NLO. We have also discussed the functionalization of fullerenes for effective binding of uranyl cation. These kinds of studies can be extended further by considering fullerene functionalized with several other functional groups. The well-established chemistry of fullerenes gives us a viable route to synthesize fullerenes with any desired functionality as well as fullerene based materials by assembling several such units. We can possibly extend their applicability to study the binding affinity of several other actinyl cations which are commonly present in nuclear wastes. In the last two decades, the physico-chemical properties of carbon nanostructures have been explored extensively and we have outlined these aspects in the previous chapters. The use of carbon nanostructures in nuclear waste management is rather a pristine and relatively unexplored domain as compared to their other probable applications. [365] Hence, to widen the scope of applications of carbon nanostructures for nuclear waste management processes many new protocols can be standardized.

In Chapter 4, we have discussed our findings on the investigations on structural and electronic properties of small gold clusters. We have demonstrated the importance of doping alkali atoms as well as hydrogen which resemble gold in their outer electronic configuration. The approach of introducing impurity atoms or other inexpensive dopant atoms in gold clusters can lead to significant tuning of their catalytic efficiency. In this line of thought, there have been reports of bimetallic clusters as active catalytic agents compared to pristine gold clusters. [366] Hence the entire gamut of studies related to pristine gold clusters can further be extended to bimetallic clusters and their potential role in catalysis.

The oxidation of CO to CO_2 being an extremely important chemical process, we have explored the catalytic role of gold clusters in promoting the above reaction in chapter 5. Although CO oxidation gold is one of the most explored reactions, there can be other chemical reactions which are catalyzed by nanoscale gold. The water gas shift reaction is an important and industrially relevant reaction which is promoted by gold catalysts. [367] Hence, we can extend our studies on the gold clusters to other pertinent catalytic processes such as the water gas shift reaction. One important aspect of gold catalysis is the dominant role of substrate materials. As a step ahead, we can extend our computational investigations on gold catalysis by considering a wide range of support materials like oxides and carbon nanostructures and try to gain newer insights into this subject.

The search for non-polluting and renewable energy sources as one of the major challenges of the scientific fraternity have been briefly outlined in chapter 6. The increasing interest in the use of hydrogen energy as an alternate energy source is based on some of the unique features of hydrogen which has already been discussed. We have also discussed the possible bottlenecks involved in the generation of hydrogen by splitting of water and the need for the storage of hydrogen for practical applications. Two main important objectives that we tried to address are (i) design of catalyst for water splitting and (ii) design of materials for hydrogen storage. In spite of the availability of plethora of reports in the literature related to the above two areas, intense explorations are still needed to bring about robust technologies for real life applications from the pool of existing knowledge. Several catalysts for water splitting have been proposed in recent years which include metal oxides, semiconducting nanoparticles, molecular organometallic catalysts etc. [368] Molecular water splitting catalysts are considered to be more efficient than the metal oxides as the latter have poor stability because of the oxidation of organic ligands by the reaction intermediates which ultimately limits the performance. [368] Hence, it is highly desirable to look for efficient molecular catalysts and investigate the detailed mechanism of several such catalysts which has been proposed in recent years by employing computational investigations. On the design of materials for hydrogen storage front, although many novel materials have been proposed based on *ab initio* theoretical calculations, very few of them have made it into the realm of practical utility. Investigations on the hydrogen desorption process, which is a very important consideration for hydrogen storage materials, are still rather few. The role of computational approaches still occupies a central position in the rational design of new materials as well as to screen many potentially important candidates.

REFERENCES

(1) Drexler, K. E. *Engines of Creation*; Garden City, Anchor Press/Doubleday: New York, 1986.

(2) Kroto, H. W.; Heath, J. R.; O'Brien, S. C.; Curl, R. F.; Smalley, R. E. *Nature* **1985**, *318*, 162.

(3) Kratschmer, W.; Lamb, L. D.; Fostiropoulos, K.; Huffman, D. R. *Nature* **1990**, *347*, 354.

(4) Haddon, R. C.; Brus, L. E.; Raghavachari, K. *Chem. Phys. Lett.* **1986**, *125*, 459.

(5) Echegoyen, L.; Echegoyen, L. E. *Acc. Chem. Res.* **1998**, *31*, 593.

(6) Arias, F.; Echegoyen, L.; Wilson, S. R.; Lu, Q.; Lu, Q. *J. Amer. Chem. Soc.* **1995**, *117*, 1422.

(7) Bruno, C.; Doubitski, I.; Marcaccio, M.; Paolucci, F.; Paolucci, D.; Zaopo, A. *J. Amer. Chem. Soc.* **2003**, *125*, 15738.

(8) Dagotto, E. *Science* **2001**, *293*, 2410.

(9) Hebard, A. F.; Rosseinsky, M. J.; Haddon, R. C.; Murphy, D. W.; Glarum, S. H.; Palstra, T. T. M.; Ramirez, A. P.; Kortan, A. R. *Nature* **1991**, *350*, 600.

(10) Lappas, A.; Prassides, K.; Vavekis, K.; Arcon, D.; Blinc, R.; Cevc, P.; Amato, A.; Feyerherm, R.; Gygax, F. N.; Schenck, A. *Science* **1995**, *267*, 1799.

(11) Haddon, R. C.; Perel, A. S.; Morris, R. C.; Palstra, T. T. M.; Hebard, A. F.; Fleming, R. M. *App. Phys. Lett.* **1995**, *67*, 121.

(12) Narymbetov, B.; Omerzu, A.; Kabanov, V. V.; Tokumoto, M.; Kobayashi, H.; Mihailovic, D. *Nature* **2000**, *407*, 883.

(13) Allemand, P. M.; Khemani, K. C.; Koch, A.; Wudl, F.; Holczer, K.; Donovan, S.; Gruner, G.; Thompson, J. D. *Science* **1991**, *253*, 301.

(14) Hirsch, A.; Brettreich, M. *Fullerenes: Chemistry and Reactions*; Wiley: New York, 2005.

(15) Iijima, S. *Nature* **1991**, *354*, 56.

(16) Hernandez, E.; Goze, C.; Bernier, P.; Rubio, A. *Phys. Rev. Lett.* **1998**, *80*, 4502.

(17) Khang, D. Y.; Xiao, J.; Kocabas, C.; MacLaren, S.; Banks, T.; Jiang, H.; Huango, Y. Y.; Rogers, J. A. *Nano Lett.* **2008**, *8*, 124.

(18) Taylor, K. J.; Pettiette-Hall, C. L.; Cheshnovsky, O.; Smalley, R. E. *J. Chem. Phys.* **1992**, *96*, 3319.

(19) Herrmann, A.; Leutwyler, S.; Schumacher, E.; Woste, L. *Chem. Phys. Lett.* **1977**, *52*, 418.

(20) Herrmann, A.; Schumacher, E.; Woste, L. *J. Chem. Phys.* **1978**, *68*, 2327.

(21) Knight, W. D.; Clemenger, K.; De Heer, W. A.; Saunders, W. A. *Phys. Rev. B* **1985**, *31*, 2539.

(22) Knight, W. D.; Monot, R.; Dietz, E. R.; George, A. R. *Phys. Rev. Lett.* **1978**, *40*, 1324.

(23) Parent, D. C.; Anderson, S. L. *Chem. Rev.* **1992**, *92*, 1541.

(24) Haruta, M. *Catalysis Today* **1997**, *36*, 153.

(25) Valden, M.; Lai, X.; Goodman, D. W. *Science* **1998**, *281*, 1647.

(26) Bond, G. C.; Thompson, D. T. *Catalysis Reviews - Science and Engineering* **1999**, *41*, 319.

(27) Haruta, M.; Date, M. *App. Catal. A* **2001**, *222*, 427.

(28) Abelson, P. H. *Science* **2000**, *288*, 269.

(29) Meyer, R.; Lemire, C.; Shaikhutdinov, S. K.; Freund, H. J. *Gold Bulletin* **2004**, *37*, 72.

(30) Novoselov, K. S.; Geim, A. K.; Morozov, S. V.; Jiang, D.; Zhang, Y.; Dubonos, S. V.; Grigorieva, I. V.; Firsov, A. A. *Science* **2004**, *306*, 666.

(31) Sofo, J. O.; Chaudhari, A. S.; Barber, G. D. *Phys. Rev. B* **2007**, *75*, 153401.

(32) Popov, V. N. *Mater. Sci. Eng. R: Reports* **2004**, *43*.

(33) Lui, C. H.; Liu, L.; Mak, K. F.; Flynn, G. W.; Heinz, T. F. *Nature* **2009**, *462*, 339.

(34) Kociak, M.; Kasumov, A. Y.; Gueron, S.; Reulet, B.; Khodos, I. I.; Gorbatov, Y. B.; Volkov, V. T.; Vaccarini, L.; Bouchiat, H. *Phys. Rev. Lett.* **2001**, *86*, 2416.

(35) Tang, Z. K.; Zhang, L. Y.; Wang, N.; Zhang, X. X.; Wang, J. N.; Li, G. D.; Li, Z. M.; Wen, G. H.; Chan, C. T.; Sheng, P. *Synthetic Metals* **2003**, *133-134*, 689.

(36) Jeong, J. S.; Lee, H. W. *Phys. Rev. B* **2009**, *80*.

(37) Pereira, V. M.; Castro Neto, A. H. *Phys. Rev. Lett.* **2009**, *103*, 046801.

(38) Zheng, G.; Wang, Z.; Irle, S.; Morokuma, K. *J. Amer. Chem. Soc.* **2006**, *128*, 15117.

(39) Mahesh Kumar, R.; Elango, M.; Subramanian, V. *J. Phys. Chem. A*, *114*, 4313.

(40) Li, J.; Jia, G.; Zhang, Y.; Chen, Y. *Chem. Mater.* **2006**, *18*, 3579.

(41) Lu, X.; Chen, Z. *Chem. Rev.* **2005**, *105*, 3643.

(42) Peralta-Inga, Z.; Lane, P.; Murray, J. S.; Boyd, S.; Grice, M. E.; O'Connor, C. J.; Politzer, P. *Nano Lett.* **2003**, *3*, 21.

(43) Haddon, R. C. *Science* **1993**, *261*, 1545.

(44) Chandrakumar, K. R. S.; Ghosh, S. K. *Nano Lett.* **2008**, *8*, 13.

(45) Guo, G. Y.; Chu, K. C.; Wang, D. S.; Duan, C. G. *Phys. Rev. B* **2004**, *69*, 205416.

(46) Benedict, L. X.; Louie, S. G.; Cohen, M. L. *Phys. Rev. B* **1995**, *52*, 8541.

(47) Guo, G. Y.; Chu, K. C.; Wang, D. S.; Duan, C. G. *Comp. Mater. Sci.* **2004**, *30*, 269.

(48) Kudin, K. N.; Car, R.; Resta, R. *J. Chem. Phys.* **2005**, *122*, 1.

(49) Brothers, E. N.; Izmaylov, A. F.; Scuseria, G. E.; Kudin, K. N. *J. Phys. Chem. C* **2008**, *112*, 1396.

(50) Schmidt, M. W.; Baldridge, K. K.; Boatz, J. A.; Elbert, S. T.; Gordon, M. S.; Jensen, J. H.; Koseki, S.; Matsunaga, N.; Nguyen, K. A.; Su, S.; Windus, T. L.; Dupuis, M.; Montgomery, J. A. *J. Comp. Chem.* **1993**, *14*, 1347.

(51) Zhao, Y.; Truhlar, D. G. *Theor. Chem. Acc.* **2008**, *120*, 215.

(52) Zhao, Y.; Truhlar, D. G. *Acc. Chem. Res.* **2008**, *41*, 157.

(53) Zhao, Y.; Truhlar, D. G. *J. Phys. Chem. C* **2008**, *112*, 4061.

(54) Zhao, Y.; Truhlar, D. G. *Phys. Chem. Chem. Phys.* **2005**, *7*, 2701.

(55) Ahlrichs, R.; Bar, M.; Haser, M.; Horn, H.; Kolmel, C. *Chem. Phys. Lett.* **1989**, *162*, 165.

(56) Allouche, A. R. 2007.

(57) Cohen, H. D.; Roothaan, C. C. J. *J. Chem. Phys.* **1965**, *43*, S34.

(58) Karakas, A.; Unver, H.; Elmali, A. *Journal of Molecular Structure: THEOCHEM* **2006**, *774*, 67.

(59) Ouyang, M.; Huang, J. L.; Lieber, C. M. *Acc. Chem. Res.* **2002**, *35*, 1018.

(60) Chen, C. W.; Lee, M. H. *Nanotechnology* **2004**, *15*, 480.

(61) Shan, B.; Cho, K. *Phys. Rev. Lett.* **2005**, *94*, 1.

(62) Su, W. S.; Leung, T. C.; Li, B.; Chan, C. T. *App. Phys. Lett.* **2007**, *90*.

(63) Buonocore, F.; Trani, F.; Ninno, D.; Di Matteo, A.; Cantele, G.; Iadonisi, G. *Nanotechnology* **2008**, *19*.

(64) Zhan, C. G.; Nichols, J. A.; Dixon, D. A. *J. Phys. Chem. A* **2003**, *107*, 4184.

(65) Melnikov, D. V.; Chelikowsky, J. R. *Phys. Rev. B* **2004**, *69*, 113305.

(66) Torrens, F. *Nanotechnology* **2004**, *15*, S259.

(67) Galano, A. *Chem. Phys.* **2006**, *327*, 159.

(68) Jena, N. K.; Chandrakumar, K. R. S.; Ghosh, S. K. *J. Phys. Chem. C* **2009**, *113*, 17885.

(69) Lucas, A. A.; Lambin, P. H.; Smalley, R. E. *J. Phys. Chem. Sol.* **1993**, *54*, 587.

(70) Sawada, S. i.; Hamada, N. *Solid State Comm.* **1992**, *83*, 917.

(71) Yaghobi, M. *Int. J. Nanosci.* **2010**, *9*, 531.

(72) Lu, J.; Nagase, S.; Zhang, X.; Wang, D.; Ni, M.; Maeda, Y.; Wakahara, T.; Nakahodo, T.; Tsuchiya, T.; Akasaka, T.; Gao, Z.; Yu, D.; Ye, H.; Mei, W. N.; Zhou, Y. *J. Amer. Chem. Soc.* **2006**, *128*, 5114.

(73) Gulseren, O.; Yildirim, T.; Ciraci, S. *Phys. Rev. Lett.* **2001**, *87*, 116802/1.

(74) Schlichting, I.; Berendzen, J.; Chu, K.; Stock, A. M.; Maves, S. A.; Benson, D. E.; Sweet, R. M.; Ringe, D.; Petsko, G. A.; Sligar, S. G. *Science* **2000**, *287*, 1615.

(75) Taraphder, S.; Hummer, G. *J. Amer. Chem. Soc.* **2003**, *125*, 3931.

(76) De Groot, B. L.; Grubmuller, H. *Science* **2001**, *294*, 2353.

(77) Hub, J. S.; De Groot, B. L. *Proc. Natl. Acad. Sci. USA* **2008**, *105*, 1198.

(78) Jensen, M. O.; Dror, R. O.; Xu, H.; Borhani, D. W.; Arkin, I. T.; Eastwood, M. P.; Shaw, D. E. *Proc. Natl. Acad. Sci. USA* **2008**, *105*, 14430.

(79) Hinds, B. J.; Chopra, N.; Rantell, T.; Andrews, R.; Gavalas, V.; Bachas, L. G. *Science* **2004**, *303*, 62.

(80) Holt, J. K.; Park, H. G.; Wang, Y.; Stadermann, M.; Artyukhin, A. B.; Grigoropoulos, C. P.; Noy, A.; Bakajin, O. *Science* **2006**, *312*, 1034.

(81) Hummer, G.; Rasaiah, J. C.; Noworyta, J. P. *Nature* **2001**, *414*, 188.

(82) Waghe, A.; Rasajah, J. C.; Hummer, G. *J. Chem. Phys.* **2002**, *117*, 10789.

(83) Maibaum, L.; Chandler, D. *J. Phys. Chem. B* **2003**, *107*, 1189.

(84) Ghosh, S.; Sood, A. K.; Kumar, N. *Science* **2003**, *299*, 1042.

(85) Koga, K.; Gao, G. T.; Tanaka, H.; Zeng, X. C. *Nature* **2001**, *412*, 802.

(86) Ball, P. *Nature* **1993**, *361*, 297.

(87) Alexiadis, A.; Kassinos, S. *Chem. Rev.* **2008**, *108*, 5014.

(88) Mahesh Kumar, R.; Elango, M.; Subramanian, V. *J. Phys. Chem. A* **2010**, *114*, 4313.

(89) Chandrakumar, K. R. S.; Srinivasu, K.; Ghosh, S. K. *J. Phys. Chem. C* **2008**, *112*, 15670.

(90) Wang, L.; Zhao, J.; Li, F.; Fang, H.; Lu, J. P. *J. Phys. Chem. C* **2009**, *113*, 5368.

(91) Sharma, M.; Donadio, D.; Schwegler, E.; Galli, G. *Nano Lett.* **2008**, *8*, 2959.

(92) Coudert, F. X.; Vuilleumier, R.; Boutin, A. *ChemPhysChem* **2006**, *7*, 2464.

(93) Ahlrichs, R.; Bar, M.; Hoser, M.; Horn, H.; Kolmel, C. *Chem. Phys. Lett.* **1989**, *162*, 165.

(94) Walters, E. A.; Grover, J. R.; White, M. G.; Hui, E. T. *J. Phys. Chem.* **1985**, *89*, 3814.

(95) Levitt, M.; Perutz, M. F. *J. Mol. Bio.* **1988**, *201*, 751.

(96) Suzuki, S.; Green, P. G.; Bumgarner, R. E.; Dasgupta, S.; Goddard Iii, W. A.; Blake, G. A. *Science* **1992**, *257*, 942.

(97) Rozas, I.; Alkorta, I.; Elguero, J. *J. Phys. Chem. A* **1997**, *101*, 9457.

(98) Prakash, M.; Gopal Samy, K.; Subramanian, V. *J. Phys. Chem. A* **2009**, *113*, 13845.

(99) Zhao, Y.; Tishchenko, O.; Truhlar, D. G. *J. Phys. Chem. B* **2005**, *109*, 19046.

(100) Jenness, G. R.; Jordan, K. D. *J. Phys. Chem. C* **2009**, *113*, 10242.

(101) Franks, F. *Water: A Comprehensive Treatise*; Plenum: New York, 1972.

(102) Rasaiah, J. C.; Garde, S.; Hummer, G. In *Ann. Rev. Phys. Chem.* 2008; Vol. 59, p 713.

(103) Marti, J.; Gordillo, M. C. *Phys. Rev. B* **2001**, *63*, 1654301.

(104) Feng, C.; Zhang, R. Q.; Dong, S. L.; Niehaus, T. A.; Frauenheim, T. *J. Phys. Chem. C* **2007**, *111*, 14131.

(105) Sharma, S. C.; Singh, D.; Li, Y. *J. Raman Spect.* **2005**, *36*, 755.

(106) Kondratyuk, P.; Yates Jr, J. T. *Acc. Chem. Res.* **2007**, *40*, 995.

(107) Ramachandran, C. N.; Sathyamurthy, N. *Chem. Phys. Lett.* **2005**, *410*, 348.

(108) Hehre, W. J.; Radom, L.; R., S. P. v.; Pople, J. A. *Ab initio Molecular Orbital Theory*; Wiley: New York, 1986.

(109) Shameema, O.; Ramachandran, C. N.; Sathyamurthy, N. *J. Phys. Chem. A* **2006**, *110*, 2.

(110) Kroto, H. W. *Nature* **1987**, *329*, 529.

(111) Dresselhaus, M. S.; Dresselhaus, G.; Eklund, P. C. *Science of fullerenes and carbon nanotubes*; Academic Press: NewYork, 1996.

(112) Guo, T.; Jin, C.; Smalley, R. E. *J. Phys. Chem.* **1991**, *95*, 4948.

(113) Hummelen, J. C.; Knight, B.; Pavlovich, J.; Gonzalez, R.; Wudl, F. *Science* **1995**, *269*, 1554.

(114) Hultman, L.; Stafstrom, S.; Czigany, Z.; Neidhardt, J.; Hellgren, N.; Brunell, I. F.; Suenaga, K.; Colliex, C. *Phys. Rev. Lett.* **2001**, *87*, 225503/1.

(115) Xie, R. H.; Bryant, G. W.; Zhao, J.; Smith Jr, V. H.; Di Carlo, A.; Pecchia, A. *Phys. Rev. Lett.* **2003**, *90*, 206602/1.

(116) Xie, R. H.; Bryant, G. W.; Sun, G.; Kar, T.; Chen, Z.; Smith Jr, V. H.; Araki, Y.; Tagmatarchis, N.; Shinohara, H.; Ito, O. *Phys. Rev. B* **2004**, *69*, 201403.

(117) Yang, W.; Fellinger, T.-P.; Antonietti, M. *J. Amer. Chem. Soc.* **2011**, *133*, 206.

(118) Qu, L.; Liu, Y.; Baek, J.-B.; Dai, L. *ACS Nano* **2010**, *4*, 1321.

(119) Jin, X.; Balasubramanian, V. V.; Selvan, S. T.; Sawant, D. P.; Chari, M. A.; Lu, G. Q.; Vinu, A. *Angew. Chem. Int. Ed.* **2009**, *48*, 7884.

(120) Zhu, Z. H.; Hatori, H.; Wang, S. B.; Lu, G. Q. *J. Phys. Chem. B* **2005**, *109*, 16744.

(121) Xia, Y.; Walker, G. S.; Grant, D. M.; Mokaya, R. *J. Amer. Chem. Soc.* **2009**, *131*, 16493.

(122) Wang, L.; Yang, R. T. *J. Phys. Chem. C* **2009**, *113*, 21883.

(123) Glenis, S.; Cooke, S.; Chen, X.; Labes, M. M. *Chem. Mater.* **1994**, *6*, 1850.

(124) Pradeep, T.; Vijayakrishnan, V.; Santra, A. K.; Rao, C. N. R. *J. Phys. Chem.* **1991**, *95*, 10564.

(125) Lamparth, I.; Nuber, B.; Schick, G.; Skiebe, A.; Grosser, T.; Hirsch, A. *Angew. Chem. Int. Ed.* **1995**, *34*, 2257.

(126) Czigany, Z.; Brunell, I. F.; Neidhardt, J.; Hultman, L.; Suenaga, K. *App. Phys. Lett.* **2001**, *79*, 2639.

(127) Neidhardt, J.; Hultman, L.; Abendroth, B.; Gago, R.; Moller, W. *J. App. Phys.* **2003**, *94*, 7059.

(128) Yu, R.; Zhan, M.; Cheng, D.; Yang, S.; Liu, Z.; Zheng, L. *J. Phys. Chem.* **1995**, *99*, 1818.

(129) Sjostrom, H.; Stafstrom, S.; Boman, M.; Sundgren, J. E. *Phys. Rev. Lett.* **1995**, *75*, 1336.

(130) Otero, G.; Biddau, G.; Sanchez-Sanchez, C.; Caillard, R.; Lopez, M. F.; Rogero, C.; Palomares, F. J.; Cabello, N.; Basanta, M. A.; Ortega, J.; Mendez, J.; Echavarren, A. M.; Perez, R.; Gomez-Lor, B.; Martin-Gago, J. A. *Nature* **2008**, *454*, 865.

(131) Wang, S.-H.; Chen, F.; Fann, Y. C.; Kashani, M.; Malaty, M.; Jansen, S. A. *J. Phys. Chem.* **1995**, *99*, 6801.

(132) Kurita, N.; Kobayashi, K.; Kumahora, H.; Tago, K. *Phys. Rev. B* **1993**, *48*, 4850.

(133) Chen, Q.; Li, J. *Chin. J. Struct. Chem.* **1997**, *16*, 445.

(134) Chen, Q.; Li, J.; Li, L.; Chen, H. *Chin. J. Struct. Chem.* **1998**, *17*, 417.

(135) Chen, Z.; Zhao, X.; Tang, A. *J. Phys. Chem. A* **1999**, *103*, 10961.

(136) Stafstrom, S.; Hultman, L.; Hellgren, N. *Chem. Phys. Lett.* **2001**, *340*, 227.

(137) Manaa, M. R.; Sprehn, D. W.; Ichord, H. A. *J. Amer. Chem. Soc.* **2002**, *124*, 13990.

(138) Xie, R.-H.; Bryant, G. W.; Jensen, L.; Zhao, J.; Smith, J. V. H. *J. Chem. Phys.* **2003**, *118*, 8621.

(139) Hou, J. Q.; Kang, H. S. *J. Phys. Chem. A* **2006**, *110*, 12241.

(140) Riad Manaa, M. *Chem. Phys. Lett.* **2003**, *382*, 194.

(141) Ewels, C. P. *Nano Lett.* **2006**, *6*, 890.

(142) Sharma, H.; Garg, I.; Dharamvir, K.; Jindal, V. K. *J. Phys. Chem. A* **2009**, *113*, 9002.

(143) Hoffmann, R.; Schleyer, P. V. R.; Schaefer Iii, H. F. *Angew. Chem. Int. Ed.* **2008**, *47*, 7164.

(144) Liu, H.; Chen, J. *Physica Status Solidi (B) Basic Research* **2003**, *237*, 575.

(145) Gu, F. L.; Chen, Z.; Jiao, H.; Tian, W. Q.; Aoki, Y.; Thiel, W.; Schleyer, P. V. R. *Phys. Chem. Chem. Phys.* **2004**, *6*, 4566.

(146) Antoine, R.; Dugourd, P.; Rayane, D.; Benichou, E.; Broyer, M.; Chandezon, F.; Guet, C. *J. Chem. Phys.* **1999**, *110*, 9771.

(147) Matsuzawa, N.; Dixon, D. A. *J. Phys. Chem.* **1992**, *96*, 6241.

(148) Moore, C. E.; Cardelino, B. H.; Wang, X.-Q. *J. Phys. Chem.* **1996**, *100*, 4685.

(149) Lovley, D. R.; Phillips, E. J. P.; Gorby, Y. A.; Landa, E. R. *Nature* **1991**, *350*, 413.

(150) Lefevre, G.; Noinville, S.; Fedoroff, M. *Journal of Colloid and Interface Science* **2006**, *296*, 608.

(151) Shanbhag, P. M.; Choppin, G. R. *Journal of Inorganic and Nuclear Chemistry* **1981**, *43*, 3369.

(152) Giacalone, F.; Martin, N. *Chem. Rev.* **2006**, *106*, 5136.

(153) Claridge, S. A.; Castleman Jr, A. W.; Khanna, S. N.; Murray, C. B.; Sen, A.; Weiss, P. S. *ACS Nano* **2009**, *3*, 244.

(154) Lamparth, I.; Hirsch, A. *Chem. Comm.* **1994**, 1727.

(155) Guldi, D. M.; Hungerbuehler, H.; Asmus, K. D. *J. Phys. Chem.* **1995**, *99*, 13487.

(156) Yamakoshi, Y. N.; Yagami, T.; Fukuhara, K.; Sueyoshi, S.; Miyata, N. *Chem. Comm.* **1994**, 517.

(157) Vallet, V.; Wahlgren, U.; Schimmelpfennig, B.; Szabo, Z.; Grenthe, I. *J. Amer. Chem. Soc.* **2001**, *123*, 11999.

(158) Schreckenbach, G.; Hay, P. J.; Martin, R. L. *J. Comp. Chem.* **1999**, *20*, 70.

(159) Kaltsoyannis, N. *Chem. Soc. Rev.* **2003**, *32*, 9.

(160) Buhl, M.; Diss, R.; Wipff, G. *J. Amer. Chem. Soc.* **2005**, *127*, 13506.

(161) Craw, J. S.; Vincent, M. A.; Hillier, I. H.; Wallwork, A. L. *J. Phys. Chem.* **1995**, *99*, 10181.

(162) Schreckenbach, G.; Shamov, G. A. *Acc. Chem. Res.* **2010**, *43*, 19.

(163) Hagberg, D.; Karlstrom, G.; Roos, B. O.; Gagliardi, L. *J. Amer. Chem. Soc.* **2005**, *127*, 14250.

(164) Austin, J. P.; Sundararajan, M.; Vincent, M. A.; Hillier, I. H. *Dalton Trans.* **2009**, 5902.

(165) Hay, P. J.; Martin, R. L.; Schreckenbach, G. *J. Phys. Chem. A* **2000**, *104*, 6259.

(166) Vazquez, J.; Bo, C.; Poblet, J. M.; De Pablo, J.; Bruno, J. *Inorg. Chem.* **2003**, *42*, 6136.

(167) Sundararajan, M.; Ghosh, S. K. *J. Phys. Chem. A* **2011**, *115*, 6732.

(168) Jayapal, P.; Sundararajan, M.; Rajaraman, G.; Venuvanalingam, P.; Kalagi, R.; Gadre, S. R. *J. Phys. Org. Chem.* **2008**, *21*, 146.

(169) Soto-Guerrero, J.; Havel, J. *Polyhedron* **2003**, *22*, 1085.

(170) Colsenet, R.; Gardiennet, C.; Henry, B.; Tekely, P. *Angew. Chem. Int. Ed.* **2002**, *41*, 4743.

(171) Rao, L.; Jiang, J.; Zanonato, P.; Di Bernardo, P.; Bismondo, A.; Garnov, A. Y. *Radiochimica Acta* **2002**, *90*, 581.

(172) Zhang, Y.; Collison, D.; Livens, F. R.; Helliwell, M.; Heatley, F.; Powell, A. K.; Wocadlo, S.; Eccles, H. *Polyhedron* **2002**, *21*, 81.

(173) Lee, C.; Yang, W.; Parr, R. G. *Phys. Rev. B* **1988**, *37*, 785.

(174) Schleyer, P. v. R.; Maerker, C.; Dransfeld, A.; Jiao, H.; Hommes, N. J. R. v. E. *J. Amer. Chem. Soc.* **1996**, *118*, 6317.

(175) Chen, Z.; Wannere, C. S.; Corminboeuf, C. m.; Puchta, R.; Schleyer, P. v. R. *Chem. Rev.* **2005**, *105*, 3842.

(176) ADF2007.01, S., Theoretical Chemistry; Vrije Universiteit: Amsterdam, The Netherlands, http://www.scm.com.

(177) Schreckenbach, G.; Ziegler, T. *J. Phys. Chem.* **1995**, *99*, 606.

(178) MOPAC2009, J. J. P. S., Stewart Computational Chemistry, Colorado; Springs, C., USA, HTTP://OpenMOPAC.net 2009.

(179) Ahlrichs, R.; Bar, M.; Haser, M.; Horn, H.; Kolmel, C. *Chem. Phys. Lett.* **1989**, *162*, 165.

(180) Haruta, M.; Kobayashi, T.; Sano, H.; Yamada, N. *Chem. Lett.* **1987**, 405.

(181) Herzing, A. A.; Kiely, C. J.; Carley, A. F.; Landon, P.; Hutchings, G. J. *Science* **2008**, *321*, 1331.

(182) Rousseau, R.; Marx, D. *J. Chem. Phys.* **2000**, *112*, 761.

(183) Hakkinen, H.; Landman, U. *Phys. Rev. B* **2000**, *62*, R2287.

(184) Gronbeck, H.; Andreoni, W. *Chem. Phys.* **2000**, *262*, 1.

(185) Seminario, J. M.; Tour, J. M. *Int. J. Quantum Chem.* **1997**, *65*, 749.

(186) Kruger, D.; Fuchs, H.; Rousseau, R.; Marx, D.; Parrinello, M. *J. Chem. Phys.* **2001**, *115*, 4776.

(187) Haruta, M.; Yamada, N.; Kobayashi, T.; Iijima, S. *J. Catal.* **1989**, *115*, 301.

(188) Hayashi, T.; Tanaka, K.; Haruta, M. *J. Catal.* **1998**, *178*, 566.

(189) Boccuzzi, F.; Chiorino, A.; Manzoli, M.; Andreeva, D.; Tabakova, T. *J. Catal.* **1999**, *188*, 176.

(190) Haruta, M. *Gold Bulletin* **2004**, *37*, 27.

(191) Thompson, D. T. *Topics in Catalysis* **2006**, *38*, 231.

(192) Lee, S.; Molina, L. M.; Lopez, M. J.; Alonso, J. A.; Hammer, B.; Lee, B.; Seifert, S.; Winans, R. E.; Elam, J. W.; Pellin, M. J.; Vajda, S. *Angew. Chem. Int. Ed.* **2009**, *48*, 1467.

(193) Pyykko, P. *Angew. Chem. Int. Ed.* **2004**, *43*, 4412.

(194) Pyykko, P. *Angew. Chem.* **2004**, *116*, 4512.

(195) Stephen, A.; Hashmi, K.; Hutchings, G. J. *Angew. Chem* **2008**, *118*, 8064.

(196) Pyykko, P.; Runeberg, N. *Angew. Chem. Int. Ed.* **2002**, *41*, 2174.

(197) Li, X.; Kiran, B.; Li, J.; Zhai, H. J.; Wang, L. S. *Angew. Chem. Int. Ed.* **2002**, *41*, 4786.

(198) Zhai, H. J.; Li, J.; Wang, L. S. *J. Chem. Phys.* **2004**, *121*, 8369.

(199) Gao, Y.; Bulusu, S.; Zeng, X. C. *ChemPhysChem* **2006**, *7*, 2275.

(200) Wang, L. M.; Bulusu, S.; Zhai, H. J.; Zeng, X. C.; Wang, L. S. *Angew. Chem. Int. Ed.* **2007**, *46*, 2915.

(201) Wang, L. M.; Bulusu, S.; Huang, W.; Pal, R.; Wang, L. S.; Xiao, C. Z. *J. Amer. Chem. Soc.* **2007**, *129*, 15136.

(202) Chen, M. X.; Yan, X. H. *J. Chem. Phys.* **2008**, *128*, 1743051.

(203) Gao, Y.; Bulusu, S.; Zeng, X. C. *J. Amer. Chem. Soc.* **2005**, *127*, 15680.

(204) Coquet, R.; Howard, K. L.; Willock, D. J. *Chem. Soc. Rev.* **2008**, *37*, 2046.

(205) Kiran, B.; Li, X.; Zhai, H. J.; Wang, L. S. *J. Chem. Phys.* **2006**, *125*, 1332041.

(206) Gagliardi, L.; Pyykko, P. *Phys. Chem. Chem. Phys.* **2004**, *6*, 2904.

(207) Ghanty, T. K. *J. Chem. Phys.* **2005**, *123*, 1.

(208) Hakkinen, H.; Yoon, B.; Landman, U.; Li, X.; Zhai, H. J.; Wang, L. S. *J. Phys. Chem. A* **2003**, *107*, 6168.

(209) Fernandez, E. M.; Soler, J. M.; Garzon, I. L.; Balbas, L. C. *Phys. Rev. B* **2004**, *70*, 165403.

(210) Hakkinen, H.; Moseler, M.; Landman, U. *Phys. Rev. Lett.* **2002**, *89*, 334011.

(211) Balasubramanian, K.; Liao, M. Z. *J. Chem. Phys.* **1987**, *86*, 5587.

(212) Xiao, L.; Tollberg, B.; Hu, X.; Wang, L. *J. Chem. Phys.* **2006**, *124*, 114309/1.

(213) Olson, R. M.; Varganov, S.; Gordon, M. S.; Metiu, H.; Chretien, S.; Piecuch, P.; Kowalski, K.; Kucharski, S. A.; Musial, M. *J. Amer. Chem. Soc.* **2005**, *127*, 1049.

(214) Buckart, S.; Gantefor, G.; Kim, Y. D.; Jena, P. *J. Amer. Chem. Soc.* **2003**, *125*, 14205.

(215) Wallace, W. T.; Whetten, R. L. *J. Phys. Chem. B* **2000**, *104*, 10964.

(216) Wallace, W. T.; Whetten, R. L. *J. Amer. Chem. Soc.* **2002**, *124*, 7499.

(217) Wu, X.; Senapati, L.; Nayak, S. K.; Selloni, A.; Hajaligol, M. *J. Chem. Phys.* **2002**, *117*, 4010.

(218) Fernandez, E. M.; Ordejon, P.; Balbas, L. C. *Chem. Phys. Lett.* **2005**, *408*, 252.

(219) Hakkinen, H.; Abbet, S.; Sanchez, A.; Heiz, U.; Landman, U. *Angew. Chem. Int. Ed.* **2003**, *42*, 1297.

(220) Jena, P.; Fradin, F. Y.; Ellis, D. E. *Phys. Rev. B* **1979**, *20*, 3543.

(221) Alefeld, G.; Volkl, J. *Hydrogen in Metals I, II, Topics in Applied Physics* **1978**.

(222) Doll, R.; Hammer, L.; Heinz, K.; Bedurftig, K.; Muschiol, U.; Christmann, K.; Seitsonen, A. P.; Bludau, H.; Over, H. *J. Chem. Phys.* **1998**, *108*, 8671.

(223) Wim, W. L.; Kluner, T. *J. Catal.* **2008**, *254*, 349.

(224) Novoselov, K. S. *Electrochemical Society Interface* **2011**, *20*, 45.

(225) Novoselov, K. S. *Nature Physics* **2009**, *5*, 862.

(226) Novoselov, K. S.; Geim, A. K.; Morozov, S. V.; Jiang, D.; Zhang, Y.; Dubonos, S. V.; Grigorieva, I. V.; Firsov, A. A. *Science* **2004**, *306*, 666.

(227) Valentin N, P. *Materials Science and Engineering: R: Reports* **2004**, *43*, 61.

(228) Zou, J.; Tran, B.; Zhai, L. *International Journal of Smart and Nano Materials* **2011**, *2*, 92.

(229) Charinpanitkul, T.; Lorturn, P.; Ratismith, W.; Viriya-Empikul, N.; Tumcharern, G.; Wilcox, J. *Materials Research Bulletin* **2011**, *46*, 1604.

(230) Shin, J. Y.; Kim, Y. S.; Lee, Y.; Shim, J. H.; Lee, C.; Lee, S. G. *Chemistry - An Asian Journal* **2011**, *6*, 2016.

(231) Ivanshina, O. Y.; Tamm, M. E.; Gerasimova, E. V.; Kochugaeva, M. P.; Kirikova, M. N.; Savilov, S. V.; Yashina, L. V. *Inorganic Materials* **2011**, *47*, 618.

(232) Li, X.; Fan, Y.; Watari, F. *Biomedical Materials* **2010**, *5*.

(233) Umasankar, Y.; Thiagarajan, S.; Chen, S. M. *Sensors* **2008**, *8*, 7191.

(234) Ohara, S.; Hatakeyama, Y.; Umetsu, M.; Tan, Z.; Adschiri, T. *Advanced Powder Technology* **2011**, *22*, 559.

(235) Pyrzynska, K. *TrAC - Trends in Analytical Chemistry* **2010**, *29*, 718.

(236) Kauffman, D. R.; Sorescu, D. C.; Schofield, D. P.; Allen, B. L.; Jordan, K. D.; Star, A. *Nano Lett.* **2010**, *10*, 958.

(237) Pan, X.; Fan, Z.; Chen, W.; Ding, Y.; Luo, H.; Bao, X. *Nat Mater* **2007**, *6*, 507.

(238) Jena, N. K.; Chandrakumar, K. R. S.; Ghosh, S. K. *J. Phys. Chem. C* **2009**, *113*, 17885.

(239) Jena, N. K.; Chandrakumar, K. R. S.; Ghosh, S. K. *J. Phys. Chem. Lett.* **2011**, *2*, 1476.

(240) Schmidt, M. W.; Baldridge, K. K.; Boatz, J. A.; Elbert, S. T.; Gordon, M. S.; Jensen, J. H.; Koseki, S.; Matsunaga, N.; Nguyen, K. A.; Su, S. J.; Windus, T. L.; Dupuis, M.; Montgomery, J. A. *J. Comput. Chem.* **1993**, *14*, 1347.

(241) Wadt, W. R.; Hay, P. J. *J. Chem. Phys.* **1985**, *82*, 284.

(242) Hay, P. J.; Wadt, W. R. *J. Chem. Phys.* **1985**, *82*, 299.

(243) Hay, P. J.; Wadt, W. R. *J. Chem. Phys.* **1985**, *82*, 270.

(244) Parr, R. G.; Yang, W. *Density Functional Theory of Atoms and Molecules* **1989**.

(245) Parr, R. G.; Pearson, R. G. *J. Amer. Chem. Soc.* **1983**, *105*, 7512.

(246) Srinivasu, K.; Chandrakumar, K. R. S.; Ghosh, S. K. *ChemPhysChem* **2009**, *10*, 427.

(247) Allouche, A. R. *Gabedit-2.0.11* **2007**.

(248) Lopez-Acevedo, O.; Kacprzak, K. A.; Akola, J.; Hakkinen, H. *Nature Chemistry* **2010**, *2*, 329.

(249) Kiran, B.; Li, X.; Zhai, H. J.; Cui, L. F.; Wang, L. S. *Angew. Chem. Int. Ed.* **2004**, *43*, 2125.

(250) Zhai, H. J.; Kiran, B.; Wang, L. S. *J. Chem. Phys.* **2004**, *121*, 8231.

(251) Li, X.; Kiran, B.; Wang, L. S. *J. Phys. Chem. A* **2005**, *109*, 4366.

(252) Kiran, B.; Li, X.; Zhai, H. J.; Wang, L. S. *J. Chem. Phys.* **2006**, *125*.

(253) Zhai, H. J.; Wang, L. S.; Zubarev, D. Y.; Boldyrev, A. I. *J. Phys. Chem. A* **2006**, *110*, 1689.

(254) Zhai, H. J.; Miao, C. Q.; Li, S. D.; Wang, L. S. *J. Phys. Chem. A* **2010**, *114*, 12155.

(255) Hobi, E.; Fazzio, A.; Da Silva, A. J. R. *Phys. Rev. Lett.* **2008**, *100*.

(256) Sanchez, A.; Abbet, S.; Heiz, U.; Schneider, W. D.; Hakkinen, H.; Barnett, R. N.; Landman, U. *J. Phys. Chem. A* **1999**, *103*, 9573.

(257) Varganov, S. A.; Olson, R. M.; Gordon, M. S.; Metiu, H. *J. Chem. Phys.* **2003**, *119*, 2531.

(258) Ding, X.; Li, Z.; Yang, J.; Hou, J. G.; Zhu, Q. *J. Chem. Phys.* **2004**, *120*, 9594.

(259) Eichler, A.; Hafner, J. *Phys. Rev. B* **1999**, *59*, 5960.

(260) Allers, K. H.; Pfnur, H.; Feulner, P.; Menzel, D. *J. Chem. Phys.* **1994**, *100*, 3985.

(261) Arenz, M.; Landman, U.; Heiz, U. *ChemPhysChem* **2006**, *7*, 1871.

(262) Yoon, B.; Hakkinen, H.; Landman, U. *J. Phys. Chem. A* **2003**, *107*, 4066.

(263) Zhai, H. J.; Burgel, C.; Bonacic-Koutecky, V.; Wang, L. S. *J. Amer. Chem. Soc.* **2008**, *130*, 9156.

(264) Molina, L. M.; Hammer, B. *J. Chem. Phys.* **2005**, *123*, 1.

(265) Lee, T. H.; Ervin, K. M. *J. Phys. Chem.* **1994**, *98*, 10023.

(266) Wallace, W. T.; Wyrwas, R. B.; Whetten, R. L.; Mitric, R.; Bonacic-Koutecky, V. *J. Amer. Chem. Soc.* **2003**, *125*, 8408.

(267) Hagen, J.; Socaciu, L. D.; Le Roux, J.; Popolan, D.; Bernhardt, T. M.; Woste, L.; Mitric, R.; Noack, H.; Bonacic-Koutecky, V. *J. Amer. Chem. Soc.* **2004**, *126*, 3442.

(268) Huang, W.; Zhai, H. J.; Wang, L. S. *J. Amer. Chem. Soc.* **2010**, *132*, 4344.

(269) Freund, H.-J.; Meijer, G.; Scheffler, M.; Schlögl, R.; Wolf, M. *Angew. Chem. Int. Ed.* **2011**, *50*, 10064.

(270) Haruta, M. *Chemical Record* **2003**, *3*, 75.

(271) Cox, D. M.; Brickman, R. O.; Creegan, K.; Kaldor, A. *MRS Proceedings* **1990**, *206*, 43.

(272) Hakkinen, H.; Landman, U. *J. Amer. Chem. Soc.* **2001**, *123*, 9704.

(273) Lopez, N.; Norskov, J. K. *J. Amer. Chem. Soc.* **2002**, *124*, 11262.

(274) Molina, L. M.; Hammer, B. *Phys. Rev. Lett.* **2003**, *90*, 206102/1.

(275) Stolcic, D.; Fischer, M.; Gantefor, G.; Kim, Y. D.; Sun, Q.; Jena, P. *J. Amer. Chem. Soc.* **2003**, *125*, 2848.

(276) Grunwaldt, J. D.; Kiener, C.; Wogerbauer, C.; Baiker, A. *J. Catal.* **1999**, *181*, 223.

(277) Park, E. D.; Lee, J. S. *J. Catal.* **1999**, *186*, 1.

(278) Boccuzzi, F.; Chiorino, A.; Manzoli, M.; Lu, P.; Akita, T.; Ichikawa, S.; Haruta, M. *J. Catal.* **2001**, *202*, 256.

(279) Wolf, A.; Schuth, F. *App. Catal. A* **2002**, *226*, 1.

(280) Date, M.; Ichihashi, Y.; Yamashita, T.; Chiorino, A.; Boccuzzi, F.; Haruta, M. *Catalysis Today* **2002**, *72*, 89.

(281) Zanella, R.; Giorgio, S.; Shin, C. H.; Henry, C. R.; Louis, C. *J. Catal.* **2004**, *222*, 357.

(282) Fierro-Gonzalez, J. C.; Gates, B. C. *J. Phys. Chem. B* **2004**, *108*, 16999.

(283) Costello, C. K.; Kung, M. C.; Oh, H. S.; Wang, Y.; Kung, H. H. *App. Catal. A* **2002**, *232*, 159.

(284) Mitric, R.; Burgel, C.; Bonacic-Koutecky, V. *Proc. Natl. Acad. Sci. USA* **2007**, *104*, 10314.

(285) Zhai, H. J.; Kiran, B.; Dai, B.; Li, J.; Wang, L. S. *J. Amer. Chem. Soc.* **2005**, *127*, 12098.

(286) Date, M.; Okumura, M.; Tsubota, S.; Haruta, M. *Angew. Chem. Int. Ed.* **2004**, *43*, 2129.

(287) Vines, F.; Loschen, C.; Illas, F.; Neyman, K. M. *J. Catal.* **2009**, *266*, 59.

(288) Storhoff, J. J.; Mirkin, C. A. *Chem. Rev.* **1999**, *99*, 1849.

(289) Tarlov, M. J., Steel, A. B. *Biomolecular Films: Design, Function, and Applications*; Marcel Dekker: New York, 2003; Vol. 111.

(290) Bashir, R. *Superlattices and Microstructures* **2001**, *29*, 1.

(291) Moller, R.; Csoki, A.; Kohler, J. M.; Fritzsche, W. *Nucleic acids research* **2000**, *28*.

(292) Pirrung, M. C. *Angew. Chem. Int. Ed.* **2002**, *41*, 1276.

(293) Liu, T.; Tang, J.; Jiang, L. *Biochem. Biophys. Res. Comm.* **2004**, *313*, 3.

(294) Nakao, H.; Shiigi, H.; Yamamoto, Y.; Tokonami, S.; Nagaoka, T.; Sugiyama, S.; Ohtani, T. *Nano Lett.* **2003**, *3*, 1391.

(295) Niemeyer, C. M. *Angew. Chem. Int. Ed.* **2001**, *40*, 4129.

(296) Niemeyer, C. M.; Ceyhan, B. *Angew. Chem. Int. Ed.* **2001**, *40*, 3685.

(297) Bielinska, A.; Eichman, J. D.; Lee, I.; Baker Jr, J. R.; Balogh, L. *J. Nanoparticle Res.* **2002**, *4*, 395.

(298) Woffendin, C.; Yang, Z. Y.; Udaykumar; Xu, L.; Yang, N. S.; Sheehy, M. J.; Nabel, G. J. *Proc. Natl. Acad. Sci. USA* **1994**, *91*, 11581.

(299) Rasmussen, A., V. Deckert *J. Raman Spectrosc.* **2006**, *37*, 311.

(300) Domke, K. F., D. Zhang, B. Pettinger *J. Am. Chem. Soc.* **2007**, *129*, 6708.

(301) Bell, S. E. J., N. M. S. Sirimuthu *J. Am. Chem. Soc.* **2006**, *128*, 15580.

(302) Demers, L. M.; Ostblom, M.; Zhang, H.; Jang, N.-H.; Liedberg, B.; Mirkin, C. A. *J. Am. Chem. Soc.* **2002**, *124*, 11248.

(303) Storhoff, J. J.; Elghanian, R.; Mirkin, C. A.; Letsinger, R. L. *Langmuir* **2002**, *18*, 6666.

(304) Kimura-Suda, H.; Petrovykh, D. Y.; Tarlov, M. J.; Whitman, L. J. *J. Amer. Chem. Soc.* **2003**, *125*, 9014.

(305) Freund, H.-J.; Meijer, G.; Scheffler, M.; Schlögl, R.; Wolf, M. *Angew. Chem. Int. Ed.*, *50*, 10064.

(306) Yoon, B.; Hakkinen, H.; Landman, U.; Worz, A. S.; Antonietti, J.-M.; Abbet, S. p.; Judai, K.; Heiz, U. *Science* **2005**, *307*, 403.

(307) Grabow, L. C.; Mavrikakis, M. *Angew. Chem. Int. Ed.* **2008**, *47*, 7390.

(308) Wells Jr, D. H.; Delgass, W. N.; Thomson, K. T. *J. Catal.* **2004**, *225*, 69.

(309) Kryachko, E. S.; Remacle, F. *Nano Lett.* **2005**, *5*, 735.

(310) Jena, N. K.; Chandrakumar, K. R. S.; Ghosh, S. K. *J. Phys. Chem. Lett.*, *2*, 1476.

(311) Tao, J.; Perdew, J. P.; Staroverov, V. N.; Scuseria, G. E. *Phys. Rev. Lett.* **2003**, *91*, 146401.

(312) Turner, J. A. *Science* **2004**, *305*, 972.

(313) Henderson, M. A. *Surface Science Reports* **2002**, *46*, 1.

(314) Thiel, P. A.; Madey, T. E. *Surface Science Reports* **1987**, *7*, 211.

(315) Phatak, A. A.; Delgass, W. N.; Ribeiro, F. H.; Schneider, W. F. *J. Phys. Chem. C* **2009**, *113*, 7269.

(316) Lei, Y.; Guo, Z. X.; Zhu, W.; Meng, S.; Zhang, Z. *App. Phys. Lett.* **2007**, *91*.

(317) Pozzo, M.; Carlini, G.; Rosei, R.; Alfe, D. *J. Chem. Phys.* **2007**, *126*, 164706.

(318) Liu, Y.; Huang, L.; Gubbins, K. E.; Nardelli, M. B. *J. Chem. Phys.*, *133*, 084510.

(319) Schlapbach, L.; Zuttel, A. *Nature* **2001**, *414*, 353.

(320) Dillon, A. C.; Jones, K. M.; Bekkedahl, T. A.; Kiang, C. H.; Bethune, D. S.; Heben, M. J. *Nature* **1997**, *386*, 377.

(321) Yildirim, T.; Iniguez, J.; Ciraci, S. *Phys. Rev. B* **2005**, *72*, 153403.

(322) Durgun, E.; Ciraci, S.; Yildirim, T. *Phys. Rev. B* **2008**, *77*, 085405.

(323) Zhao, Y.; Kim, Y.-H.; Dillon, A. C.; Heben, M. J.; Zhang, S. B. *Phys. Rev. Lett.* **2005**, *94*, 155504.

(324) Chan, S.-P.; Chen, G.; Gong, X. G.; Liu, Z.-F. *Phys. Rev. Lett.* **2001**, *87*, 205502.

(325) Kauffman, D. R.; Sorescu, D. C.; Schofield, D. P.; Allen, B. L.; Jordan, K. D.; Star, A. *Nano Lett.*, *10*, 958.

(326) Charlier, J.-C.; Blase, S.; Roche, S. *Rev. Mod. Phys.* **2007**, *79*, 677.

(327) Chopra, N. G.; Luyken, R. J.; Cherrey, K.; Crespi, V. H.; Cohen, M. L.; Louie, S. G.; Zettl, A. *Science* **1995**, *269*, 966.

(328) Loiseau, A.; Willaime, F.; Demoncy, N.; Hug, G.; Pascard, H. *Phys. Rev. Lett.* **1996**, *76*, 4737.

(329) Arenal, R.; Stephan, O.; Kociak, M.; Taverna, D.; Loiseau, A.; Colliex, C. *Phys. Rev. Lett.* **2005**, *95*, 127601.

(330) Wirtz, L.; Marini, A.; Rubio, A. *Phys. Rev. Lett.* **2006**, *96*, 126104.

(331) Park, C. H.; Sparatu, C. D.; Louie, S. G. *Phys. Rev. Lett.* **2006**, *96*, 126105.

(332) Fujishima, A.; Honda, K. *Nature* **1972**, *238*, 37.

(333) Dag, S.; Durgun, E.; Ciraci, S. *Phys. Rev. B.* **2004**, *69*, 121407(R).

(334) Zhang, Y.; Franklin, N. W.; Chen, R. J.; Dai, H. *Chem. Phys. Lett.* **2000**, *331*, 35.

(335) Tang, C.; Li, J.; Y., B.; Zhi, C.; Golberg, D. *Chem. Asian J.* **2010**, *5*, 1220

(336) Schlapbach, L.; Zuttel, A. *Nature* **2001**, *414*, 353.

(337) Coontz, R.; Hanson, B. *Science* **2004**, *305*, 957.

(338) Lewis, N. S.; Nocera, D. G. *Proc. Natl. Acad. Sci. USA* **2006**, *103*, 15729.

(339) Dresselhaus, M. S.; Thomas, I. L. *Nature* **2001**, *414*, 332.

(340) Eberle, U.; Felderhoff, M.; Schuth, F. *Angew. Chem. Int. Ed.* **2009**, *48*, 6608.

(341) Lochan, R. C.; Head-Gordon, M. *Phys. Chem. Chem. Phys.* **2006**, *8*, 1357.

(342) Jena, P. *J. Phys. Chem. Lett.* **2011**, *2*, 206.

(343) Orimo, S. I.; Nakamori, Y.; Eliseo, J. R.; Zuttel, A.; Jensen, C. M. *Chem. Rev.* **2007**, *107*, 4111.

(344) Chattaraj, P. K.; Bandaru, S.; Mondal, S. *J. Phys. Chem. A*, *115*, 187.

(345) Rowsell, J. L. C.; Millward, A. R.; Park, K. S.; Yaghi, O. M. *J. Amer. Chem. Soc.* **2004**, *126*, 5666.

(346) Klontzas, E.; Tylianakis, E.; Froudakis, G. E. *Nano Lett.*, *10*, 452.

(347) Patchkovskii, S.; Tse, J. S.; Yurchenko, S. N.; Zhechkov, L.; Heine, T.; Seifert, G. *Proc. Natl. Acad. Sci. USA* **2005**, *102*, 10439.

(348) Barman, S.; Sen, P.; Das, G. P. *J. Phys. Chem. C* **2008**, *112*, 19963.

(349) Prakash, M.; Elango, M.; Subramanian, V. *International Journal of Hydrogen Energy*, *36*, 3922.

(350) Srinivasu, K.; Chandrakumar, K. R. S.; Ghosh, S. K. *Phys. Chem. Chem. Phys.* **2008**, *10*, 5832.

(351) Maark, T. A.; Pal, S. *International Journal of Hydrogen Energy*, *35*, 12846.

(352) Blomqvist, A.; Araujo, C. M.; Srepusharawoot, P.; Ahuja, R. *Proc. Natl. Acad. Sci. USA* **2007**, *104*, 20173.

(353) Sun, Q.; Wang, Q.; Jena, P.; Kawazoe, Y. *J. Amer. Chem. Soc.* **2005**, *127*, 14582.

(354) Srinivasu, K.; Ghosh, S. K. *J. Phys. Chem. C*, *115*, 1450.

(355) Jemmis, E. D.; Subramanian, G.; Kos, A. J.; Schleyer, P. V. R. *J. Amer. Chem. Soc.* **1997**, *119*, 9504.

(356) Minkin, V. I.; Minyaev, R. M.; Starikov, A. G.; Gribanova, T. N. *Russian Journal of Organic Chemistry* **2005**, *41*, 1289.

(357) Tiznado, W.; Perez-Peralta, N.; Islas, R.; Toro-Labbe, A.; Ugalde, J. M.; Merino, G. *J. Amer. Chem. Soc.* **2009**, *131*, 9426.

(358) Perdew, J. P.; Wang, Y. *Phys. Rev. B* **1992**, *45*, 13244.

(359) Schaftenaar, G.; Noordik, J. H. *Journal of Computer-Aided Molecular Design* **2000**, *14*, 123.

(360) Parr, R. G.; Chattaraj, P. K. *J. Amer. Chem. Soc.* **1991**, *113*, 1854.

(361) Ayers, P. W.; Parr, R. G. *J. Amer. Chem. Soc.* **2000**, *122*, 2010.

(362) Chamorro, E.; Chattaraj, P. K.; Fuentealba, P. *J. Phys. Chem. A* **2003**, *107*, 7068.

(363) Takaiwa, D.; Hatano, I.; Koga, K.; Tanaka, H. 2008; Vol. 105, p 39.

(364) Cao, Z.; Peng, Y.; Yan, T.; Li, S.; Li, A.; Voth, G. A. *J. Amer. Chem. Soc.* **2010**, *132*, 11395.

(365) Belloni, F.; Kutahyali, C.; Rondinella, V. V.; Carbol, P.; Wiss, T.; Mangione, A. *Environ. Sci. Tech.* **2009**, *43*, 1250.

(366) Wang, F.; Zhang, D.; Ding, Y. *J. Phys. Chem. C* **2010**, *114*, 14076.

(367) Williams, W. D.; Shekhar, M.; Lee, W.-S.; Kispersky, V.; Delgass, W. N.; Ribeiro, F. H.; Kim, S. M.; Stach, E. A.; Miller, J. T.; Allard, L. F. *J. Amer. Chem. Soc.* **2010**, *132*, 14018.

(368) Sala, X.; Romero, I.; Rodriguez, M.; Escriche, L.; Llobet, A. *Angew. Chem. Int. Ed.* **2009**, *48*, 2842.

List of Publications

1 **Naresh K. Jena**, K. R. S. Chandrakumar, and Swapan K. Ghosh, "Theoretical Investigation on the Structure and Electronic Properties of Hydrogen- and Alkali-Metal-Doped Gold Clusters and Their Interaction with CO: Enhanced Reactivity of Hydrogen-Doped Gold Clusters", *J. Phys. Chem. C* **2009,** *113*, 17885-17892.

2 **Naresh K. Jena**, K. R. S. Chandrakumar, and Swapan K. Ghosh, "Beyond the gold-hydrogen analogy: Doping gold cluster with H-atom - O2 activation and reduction of reaction barrier for CO oxidation", *J. Phys. Chem. Lett.* **2011**, *2,* 1476-1480.

3 **Naresh K. Jena,** K Srinivasu and Swapan K Ghosh, "Computational investigation of hydrogen adsorption in silicon-lithium binary clusters", *J. Chem. Sci.* **2012**, *124,* 255-260.

4 **Naresh K. Jena**, Manoj K. Tripathy, K. R. S. Chandrakumar, Alok K Samanta, and Swapan K. Ghosh, "Water molecule encapsulated in carbon nanotube model systems: Effect of confinement and curvature", *Theor. Chem. Acc.* **2012**, *131,* 1205.

5 **Naresh K. Jena**, Mahesh Sundarajan, and Swapan K. Ghosh, "On the Interactions of Uranyl with Functionalized Fullerenes: A DFT investigation" *RSC Advances* **2012**, *2,* 2994–2999.

6 **Naresh K. Jena**, K. R. S. Chandrakumar, and Swapan K. Ghosh, "DNA Base-Gold Nano Cluster Complex as a Potential Catalyzing Agent: An Attractive Route for CO Oxidation Process" *J. Phys. Chem. C* **2012**, *116,* 17063-17069.

7 **Naresh K. Jena**, K. R. S. Chandrakumar, and Swapan K. Ghosh, "Water Dissociation on Gold Cluster: Effect of Carbon Nanostructures as Substrate" *RSC Advances* **2012**, doi:10.1039/C2RA21032K.

8 K. Srinivasu, **Naresh K. Jena**, and Swapan K. Ghosh, "Electronic structure, Stability and Non-linear Optical Properties of Aza-fullerenes $C_{60-2n}N_{2n}$(n=1-12)", (Submitted to *AIP Advances* **2012**)

9 **Naresh K. Jena**, K. R. S. Chandrakumar, and Swapan K. Ghosh, "Governing Role of Nanoscale Curvature on the Electronic Properties and Reactivity of Carbon Nanotubes", (To be Submitted).

10 **Naresh K. Jena**, K. R. S. Chandrakumar, and Swapan K. Ghosh, "Dissociation of Water on a Ti-decorated BN Nanotbe: Insights from DFT Study", (To be Submitted).

11 **Naresh K. Jena**, K. R. S. Chandrakumar, and Swapan K. Ghosh, "Guiding Principles for CO oxidation on Gold Clusters", (To be Submitted).

This never marks an End,

For, in the path of wisdom

“Means” mean more than “End”….